

NORTHWESTERN UNIVERSITY

Structure-Mechanical Property Relationships  
in Porous SiC Derived from Wood

A DISSERTATION

SUBMITTED TO THE GRADUATE SCHOOL  
IN PARTIAL FULFILLMENT OF THE  
REQUIREMENTS

for the degree

DOCTOR OF PHILOSOPHY

Field of Materials Science and Engineering

By

Vikram S. Kaul

EVANSTON, ILLINOIS

June 2007

© Copyright by Vikram S. Kaul 2006  
All Rights Reserved

## ABSTRACT

### Structure-Mechanical Property Relationships in Porous SiC Derived from Wood

Vikram S. Kaul

Biomorphic silicon carbide (bioSiC) is a novel porous ceramic material derived directly from wood precursors. This material is fabricated by pyrolysis of a natural wood precursor in an inert atmosphere leaving an amorphous carbon scaffold. The amorphous carbon is infiltrated with molten Si in vacuum at elevated temperature, which reacts with the scaffold to form SiC. Finally, any residual Si is removed using an acid solution producing a porous SiC material with a microstructure that is analogous to the wood precursor.

In order to understand mechanical behavior and identify this material for potential applications, fundamental structure-mechanical property relationships in bioSiC were established. This was accomplished by analysis of bioSiC from five different wood precursors, which covered a range of pore volumes, pore sizes, and pore size distributions. The structure and phase composition of these materials were characterized and coupled to mechanical behavior conducted by mechanical testing and finite-element analysis.

In addition to volume of porosity and orientation, mechanical properties were found to be a function of phase composition and structure. All bioSiC materials were found to have unreacted carbon that had a deleterious effect on compressive strength ( $\sigma_{comp}$ ) and elastic modulus ( $E$ ) but no significant effect on fracture toughness ( $K_{IC}$ ). A procedure was developed to quantify the fraction of unreacted carbon in bioSiC, and results showed that materials with a higher fraction of small pores contained higher amounts of this phase. Additionally,

misalignment of tubular pores was found to lower  $\sigma_{comp}$  and  $E$  in axial compression, and random pore arrangement and misorientation of tubular pores with elliptical cross-sections were found to lower  $\sigma_{comp}$  and  $E$  in transverse compression.

Analysis also revealed preferred crack paths in planes parallel to the axial direction. Cracks likely initiate from nodes and curved areas in tubular pores of bioSiC, which act as stress concentrators. Additionally, wood features such as rays and growth rings that manifest themselves as density gradients in bioSiC served as crack deflectors.

Approved by:

---

Professor Katherine T. Faber  
Department of Materials Science and Engineering  
Robert R. McCormick School of Engineering and Applied Science  
Northwestern University  
Evanston, Illinois

June 2007

## Acknowledgments

There are many people that I need to thank for their support through this whole process and throughout my life. The first person I must thank is my advisor, Prof. Katherine Faber. Her door has always been open when I had a question and she always seems to see the silver lining in every situation. Thank you.

I'd also like to thank the other members of my committee. Prof. Catherine Brinson who was on my qualifying committee and Prof. Yip-Wah Chung and Prof. David Dunand who were on both my qualifier committee and my thesis defense committee, thank you for your time. I'd especially like to thank Dr. Edwin Fuller Jr. for all of his help with OOF and for agreeing to be a part of my thesis defense committee on relatively short notice. I should also thank the National Science Foundation (grant # 0244258) for funding my research. Thank you.

I want to thank all of the people inside and outside the department who were always willing to help. Mark Seniw, Kathleen Stair, Peggy Adamson, and Joanna Gwinn always kept things running smoothly in the department. Thanks also to Dr. Chris Warren for supplying materials and Dr. Andrew Reid for OOF advice. Thank you.

Next, I have to thank past and present members of the Faber Group. David Hovis, John Montgomery, Chris Weyant, Kristen Pappacena, Tom Wilkes, Bryan Harder, Michelle Seitz, Noah Shanti, and Harold Hsiung have been great colleagues and even better friends. Thanks for movie nights, crosswords, funfetti, rides when it was raining, fearful leadership, Tom approves, silver-shield glove, Seinfeld references, soccer injuries, ribs in Cincinnati, the Rusty Scupper,

and ridiculous coffee hours. Thanks also to our collaborators in Spain, especially Ranier Enrique Sepulveda Ferrer who showed me the best time in Sevilla and always let it rain. Thank you.

I also have to thank all the other grad students in the department for great parties and IM sports. I finally got my T-shirt! They always made the department feel like a community. All of my friends here and everywhere else, I thank you. Especially Prashant Velagaleti, Vivek Thakkar, Sunaina Velagaleti, and Amit Patel who were all always up for a good time. Thank you.

Finally, I want to thank those people that mean the most to me. Thanks to my brother Raj for his easy going spirit and ambition, he's wiser than he knows. Thanks to my wonderful fiancée Shivani for being so supportive and making me feel so lucky I almost feel guilty. I can't wait until March! Thanks to my Mom and Dad, Kirti and Karan Kaul, they have always encouraged me without pushing and I am everything I am or ever will be because of them. Thank you.

## Table of Contents

List of Figures .....	10
List of Tables .....	18
1. Introduction.....	20
1.1. Scope and Objectives.....	22
2. Background.....	24
2.1. Porous Materials .....	24
2.1.1. Classification of Porous Materials .....	24
2.1.2. Properties and Processing of Porous Ceramics.....	29
2.1.3. Natural Templates .....	39
2.2. Wood.....	42
2.2.1. Solid Phase of Wood.....	44
2.2.2. Structure of Wood.....	49
2.2.3. Classification of Wood .....	56
2.3. Biomorphic Silicon Carbide .....	59
2.3.1. Processing of BioSiC .....	59
2.3.2. State of Research of Biomorphic Materials .....	71
2.4. Summary.....	73
3. Characterization of Microstructure and Phase Composition in Biomorphic Silicon Carbide.....	74

3.1. Evolution of Structure and Phase Composition During Processing .....	74
3.1.1. Evolution of Microstructure.....	75
3.1.2. Evolution of Phase Composition .....	82
3.2. Porous SiC from Several Precursors.....	84
3.2.1. Wood Precursors.....	84
3.2.2. Carbon and BioSiC Structures .....	87
3.2.3. Synthetic SiC Honeycomb.....	91
3.3. Porosity and Solid Phase Analysis by Density Measurements.....	95
3.3.1. Porosity and Apparent Density of Pyrolyzed Carbon and BioSiC .....	95
3.3.2. Solid Phase Analysis.....	101
3.4. Porosity and Pore Measurements by Image Analysis.....	103
3.4.1. Pore Size Distribution.....	103
3.5. Unreacted Carbon Content .....	113
3.5.1. Quantification of Unreacted Carbon.....	113
3.5.2. Presence of Unreacted Carbon.....	118
3.6. Summary.....	128
4. Mechanical Properties of Biomorphic Silicon Carbide .....	129
4.1. Experimental Procedures.....	129
4.1.1. Nanoindentation.....	130
4.1.2. Compressive Strength and Elastic Modulus .....	134
4.1.3. Fracture Toughness.....	136

4.2. Nanoindentation Results and Discussion.....	138
4.2.1. Nanoindentation Results .....	139
4.2.2. Nanoindentation Discussion .....	145
4.3. Compressive Strength and Bulk Elastic Modulus Results and Discussion .....	145
4.3.1. Compressive Test Results .....	146
4.3.2. Compressive Test Discussion .....	151
4.4. Fracture Toughness Results and Discussion.....	169
4.4.1. Fracture Toughness Results .....	169
4.4.2. Fracture Toughness Discussion .....	173
4.5. Summary.....	178
5. Finite-Element Analysis of Mechanical Behavior in Biomorphic Silicon Carbide.....	179
5.1. Object-Oriented Finite-Element Analysis .....	179
5.1.1. Creation of Finite-Element Mesh.....	180
5.1.2. Virtual Mechanical Testing.....	182
5.1.3. Materials Analysis by OOF .....	184
5.2. Experimental Plan.....	184
5.3. Mechanical Behavior of BioSiC in Axial Compression.....	185
5.3.1. Effective Axial Elastic Modulus.....	186
5.3.2. Pore Channel Misalignment.....	197
5.3.3. Stress Distribution and Fracture of BioSiC in Axial Compression .....	200
5.4. Mechanical Behavior of BioSiC in Transverse Compression .....	206

- 5.4.1. Effective Transverse Elastic Modulus .....206
- 5.4.2. Pore Effects on Transverse Properties .....215
- 5.4.3. Stress Distribution and Fracture of BioSiC in Transverse Compression.....227
- 5.5. Summary.....233
  
- 6. Summary and Conclusions .....234
  - 6.1. Summary.....234
  - 6.2. Conclusions.....239
  - 6.3. Suggestions for Future Work.....242
  
- References.....244

## List of Figures

Figure 2.1. Examples of a) honeycomb, b) open-pore foam, and c) closed-pore foam materials. (Gibson and Ashby 1997) .....	26
Figure 2.2. Chart showing optimum pore size, volume fraction, and interconnectivity for various applications of porous materials (Kelly 2006).....	28
Figure 2.3. Schematic representation of possible processing routes for forming ceramics with controlled porosity (Studart et al. 2006) .....	30
Figure 2.4. Microstructures of porous Al <sub>2</sub> O <sub>3</sub> fabricated using a) corn starch (Montgomery and Faber 2005) and b) camphene (Shanti et al. 2006) sacrificial templates .....	32
Figure 2.5. Micrographs of a) graphite (Gaies and Faber 2002), and b) Al <sub>2</sub> O <sub>3</sub> (Sepulveda and Binner 1999) formed by direct foaming .....	35
Figure 2.6. Scanning electron micrographs of porous a) Al <sub>2</sub> O <sub>3</sub> with b) hollow struts (Green and Colombo 2003) and c) SiC (Fitzgerald and Mortensen 1995) formed by the replica method .....	38
Figure 2.7. Scanning electron micrographs of a) natural coral and b) replicated hydroxyapatite (Ben-Nissan 2003), and c) natural butterfly wing scale and d) replicated ZnO (Zhang et al. 2006).....	40
Figure 2.8. Examples of natural porous materials including a) balsa wood, b) cork, c) plant stem, and d) trabecular bone (Gibson 2005) .....	41
Figure 2.9. Schematic representing the convention used to refer to principle directions in wood.....	43
Figure 2.10. a) Axial and b) transverse projections of crystalline cellulose with planar sheets parallel to the axial direction (Gardener and Blackwell 1974).....	46
Figure 2.11. Molecular structures of a) hemicellulose and b) lignin (Greil 2001).....	47

Figure 2.12. Multi-layer composite structure of wood after Greil (1998).....	50
Figure 2.13. Scanning electron micrograph of pyrolyzed beech exhibiting the shoneycomb-type structure of wood .....	51
Figure 2.14. Scanning electron micrographs of axial planes of a) pyrolyzed sapele (hardwood) and b) pyrolyzed cedar (softwood) showing examples of four primary wood cells.....	53
Figure 2.15. Micrographs of a) Douglas fir after Dinwoodie (1989) and b) pyrolyzed red oak showing macroscopic features in the axial plane of wood .....	55
Figure 2.16. Range of densities for various softwoods and hardwoods (Dinwoodie 1989).....	57
Figure 2.17. Scanning electron micrographs of the axial plane of a) diffuse porous (poplar) and b) ring porous (red oak) pyrolyzed hardwoods.....	58
Figure 2.18. Flow chart giving the processing steps necessary to fabricate bioSiC.....	61
Figure 2.19. Diagrammatic representation of the 4-stage breakdown of wood during pyrolysis (Tang and Bacon 1964).....	63
Figure 2.20. X-ray diffraction of poplar wood during pyrolysis showing only limited crystallinity because of the non-graphitizable nature of wood carbon (Byrne and Nagle 1997b).....	64
Figure 2.21. Thermogravimetric analysis of red oak wood showing weight changes corresponding to 1) loss of absorbed water, 2) hemicellulose decomposition, 3) initial cellulose and lignin decomposition, 4) rapid cellulose and lignin decomposition, and 5) continued lignin decomposition (Byrne and Nagle 1997a) .....	66
Figure 2.22. Transmission electron micrograph of nano-grain, coarse-grain SiC, and residual C in bioSiC derived from beech wood (Zollfrank and Sieber 2004).....	69

- Figure 3.1. Scanning electron micrographs of the a) axial plane and b) a transverse plane of a typical carbon scaffold resulting from the pyrolysis of a hardwood precursor .....76
- Figure 3.2. Scanning electron micrographs of the a) axial plane and b) a transverse plane of bioSi/SiC resulting from the molten Si infiltration of a pyrolyzed carbon scaffold.....78
- Figure 3.3. Scanning electron micrographs of the a) axial plane and b) a transverse plane of bioSiC following the removal of residual Si by acid etching .....80
- Figure 3.4. Porous and polycrystalline bioSiC resulting from the dissolution/precipitation dominated reaction between molten Si and the amorphous carbon scaffold.....81
- Figure 3.5. XRD patterns showing the evolution of composition from amorphous carbon to  $\beta$ -SiC.....83
- Figure 3.6. SEM micrographs of the axial planes of (a-e) pyrolyzed carbon and (f-j) bioSiC from five different hardwood precursors (Kaul et al. 2006).....88
- Figure 3.7. SEM micrographs of the transverse planes of (a-e) pyrolyzed carbon and (f-j) bioSiC from five different hardwood precursors .....89
- Figure 3.8. Optical micrographs of the a) axial and b) transverse plane of synthetic SiC honeycomb along with a c) SEM micrograph showing closer detail .....93
- Figure 3.9. XRD pattern from synthetic SiC honeycomb showing the presence of  $\beta$  and  $\alpha$ -SiC.94
- Figure 3.10. Schematic showing how SEM micrographs were converted to black and white images to measure porosity and fit with ellipses to measure pore sizes using image analysis....105
- Figure 3.11. Pore size distributions for UDP and NUDP bioSiC after Kaul et al. (2006) .....110
- Figure 3.12. a) Optical micrograph of SiC honeycomb and b) the corresponding image used for image analysis.....112

- Figure 3.13. Schematic showing how small pores with thick pore walls can be closed as a result of volume expansion upon conversion of pyrolyzed carbon to bioSiC.....121
- Figure 3.14. Schematic representation of a single pore in bioSiC.....122
- Figure 3.15. SEM micrographs of pyrolyzed carbon showing the variation of pore size and pore wall thickness between late and early wood .....124
- Figure 3.16. SEM micrographs and EDS maps of a,c) UDP poplar bioSiC and b,d) NUDP red oak bioSiC showing large patches of unreacted carbon in dense areas of the NUDP material...125
- Figure 3.17. a) SEM micrograph and b) EDS map of red oak bioSiC showing dense area of SiC and porous areas of unreacted carbon .....127
- Figure 4.1. Typical load-displacement curve from nanoindentation of a ceramic material showing regions of (I) surface flexure recovery and (II) indentation depth recovery where  $S$  is stiffness 133
- Figure 4.2. Schematic of experimental setup used for compressive testing .....135
- Figure 4.3. Schematic of experimental setup used for fracture toughness testing.....137
- Figure 4.4. Single nanoindentation made using a Berkovich indenter on fused quartz.....141
- Figure 4.5. As-processed interior of a vessel pore in red oak bioSiC.....142
- Figure 4.6. Compressive strength as a function of porosity for (a) axial and (b) transverse bioSiC and SiC honeycomb .....147
- Figure 4.7. Elastic modulus as a function of porosity for (a) axial and (b) transverse bioSiC and SiC honeycomb.....148

Figure 4.8. Plot of E as a function of porosity in the axial direction with gray bars showing the upper and lower bound MSA values when unreacted carbon is accounted for using the rule of mixtures.....156

Figure 4.9. Bulk elastic modulus as a function of solid phase elastic modulus for constant porosity (50%) as predicted by the MSA model.....159

Figure 4.10. Plot of E as a function of porosity in the transverse direction with gray bars showing the upper and lower bound MSA values when unreacted carbon is accounted for using the rule of mixtures.....162

Figure 4.11. SEM micrographs of fracture surfaces of UDP (poplar) and NUDP (sapele) axial bioSiC samples tested in compression.....164

Figure 4.12. SEM micrographs of fractured compression samples of (a) poplar, (b) mahogany, (c) beech, and (d) red oak bioSiC (arrows point to fracture surfaces).....165

Figure 4.13. SEM micrographs of fracture surfaces from transverse (a) poplar and (b) red oak bioSiC samples tested in compression.....166

Figure 4.14. SEM micrographs of (a) fracture surface and (b) profile of SiC honeycomb samples tested in compression.....168

Figure 4.15. Fracture toughness of bioSiC and SiC honeycomb (axial and transverse orientations) as a function of porosity.....170

Figure 4.16. Schematics of axial and transverse bioSiC fracture toughness samples .....171

Figure 4.17. SEM micrographs of fracture surfaces of axial (a) beech and (b) mahogany, and transverse (c) poplar and (d) sapele bioSiC fracture toughness samples.....175

Figure 4.18. SEM micrograph of fracture surface of axial fracture toughness red oak bioSiC sample .....176

Figure 4.19. SEM micrographs of fracture surface of (a) axial and (b) transverse SiC honeycomb fracture toughness samples .....177

Figure 5.1. Sequence used to create a finite-element mesh in OOF beginning with a a) digitized image to which a b) threshold is applied followed by the c) assignment of properties. Finally a d) grid is created forming a e) coarse finite-element mesh that is adapted to the image resulting in the f) final mesh .....181

Figure 5.2. SEM micrographs of transverse bioSiC planes and corresponding finite-element meshes for analysis of axial mechanical behavior .....187

Figure 5.3. SEM micrographs of bioSiC fiber and tracheid porosity in the transverse plane and the corresponding finite-element meshes.....189

Figure 5.4. SEM micrographs and corresponding stress distributions of axial red oak bioSiC samples compressed in the Y direction (pore space shown in blue).....194

Figure 5.5. SEM micrograph and idealized image of red oak bioSiC compressed in the Y direction with corresponding stress distributions (pore space shown in blue) .....196

Figure 5.6. Idealized microstructures of tubular pores at various alignment angles .....198

Figure 5.7. Plot of relative elastic modulus as a function of angle of alignment to stress axis from OOF data and equation 2 .....199

Figure 5.8. SEM micrographs and corresponding stress distributions ( $\sigma_{xx}$ ) of axial bioSiC samples compressed in the X direction (pore space shown in blue, scale from -33.06 to 5.55 MPa).....201

Figure 5.9. SEM micrographs and corresponding stress distributions ( $\sigma_{yy}$ ) of axial bioSiC samples compressed in the X direction (pore space shown in blue, scale from -15.00 to 10.00 MPa).....202

Figure 5.10. SEM micrographs and corresponding stress distributions ( $\sigma_{xy}$ ) of axial bioSiC samples compressed in the X direction (pore space shown in blue, scale from -10.00 to 13.00 MPa).....	203
Figure 5.11. SEM micrographs and corresponding virtual fracture images of axial bioSiC compressed in the X direction (black elements are fractured).....	205
Figure 5.12. SEM micrographs of axial bioSiC planes and corresponding finite-element meshes for analysis of transverse mechanical behavior .....	207
Figure 5.13. SEM micrographs of bioSiC fiber and tracheid porosity in the axial plane and the corresponding finite-element mesh.....	208
Figure 5.14. SEM micrographs and finite-element meshes illustrating the procedure used to determine Eeffective for dense and porous bands of red oak bioSiC .....	212
Figure 5.15. Idealized microstructures and relative elastic moduli used to analyze the effect of pore size on mechanical behavior .....	216
Figure 5.16. Idealized microstructures to analyze the effect of pore arrangement on mechanical behavior.....	218
Figure 5.17. Plot of relative elastic modulus as a function of porosity for ordered and random porosity .....	220
Figure 5.18. Idealized microstructures to analyze the effect of pore shape and arrangement on mechanical behavior .....	222
Figure 5.19. Idealized microstructures to analyze the effect of elliptical pore orientation on mechanical behavior .....	225
Figure 5.20. Plot of relative elastic modulus as a function of angle of orientation for transverse compression of elliptical pores (P = 50 %).....	226

Figure 5.21. SEM micrographs and corresponding stress distributions ( $\sigma_{yy}$ ) of transverse bioSiC samples compressed in the Y direction (pore space shown in blue, scale from -30.00 to 7.00 MPa).....228

Figure 5.22. SEM micrographs and corresponding stress distributions ( $\sigma_{xx}$ ) of transverse bioSiC samples compressed in the Y direction (pore space shown in blue, scale from -8.00 to 12.00 MPa).....229

Figure 5.23. SEM micrographs and corresponding stress distributions ( $\sigma_{xy}$ ) of transverse bioSiC samples compressed in the Y direction (pore space shown in blue, scale from -9.00 to 11.00 MPa).....230

Figure 5.24. SEM micrographs and corresponding virtual fracture images of transverse bioSiC compressed in the Y direction (black elements are fractured).....232

## List of Tables

Table 2.1. Weight fractions of wood components (Dinwoodie 1989).....	45
Table 3.1. Densities of five hardwood precursors (density calculated by dimensional measurement).....	85
Table 3.2. Result of Archimedes' method and He pycnometry measurements of pyrolyzed carbon and bioSiC (error equals one standard deviation).....	99
Table 3.3. Porosities of pyrolyzed carbon and bioSiC measured by image analysis (error equal to one standard deviation).....	108
Table 3.4. Pore sizes measured by image analysis (error equal to one standard deviation).....	111
Table 3.5. Volume fractions of unreacted carbon in the solid portion of bioSiC (error equal to one standard deviation).....	115
Table 3.6. Normalized data showing the significant difference between the unreacted carbon contents of UDP and NUDP bioSiC.....	117
Table 4.1. Mechanical properties measured by nanoindentation of dense standard samples (error represents one standard deviation).....	140
Table 4.2. Mechanical properties measured by nanoindentation on porous bioSiC phases and SiC honeycomb.....	144
Table 4.3. Normalized (a) compressive strength and (b) elastic modulus data showing significant differences between UDP and NUDP bioSiC.....	152
Table 4.4. Comparison of experimental elastic modulus values for axial bioSiC and values predicted by the MSA model using the rule of mixtures to account for unreacted carbon .....	155

Table 4.5. Comparison of experimental elastic modulus values for transverse bioSiC and values predicted by the MSA model using the rule of mixtures to account for unreacted carbon .....161

Table 5.1. Upper and lower-bound axial elastic moduli calculated with OOF using the rule-of-mixtures values for solid phase elastic modulus.....190

Table 5.2. Experimental and OOF values for axial elastic moduli calculated accounting for all porosity and unreacted carbon content .....191

Table 5.3. Relative axial elastic moduli calculated for each bioSiC using OOF and the MSA model (only vessel porosities shown and used for OOF and MSA  $E/E_0$ ) .....193

Table 5.4. Upper and lower-bound transverse elastic moduli calculated with OOF using the rule of mixtures values for solid phase elastic modulus .....210

Table 5.5. Experimental and OOF values for transverse elastic moduli calculated accounting for all porosity and unreacted carbon content.....211

Table 5.6. Upper and lower bound results for red oak bioSiC bands using rule-of-mixtures to account for unreacted carbon .....214

Table 5.7. OOF results of relative elastic modulus as a function of pore arrangement.....219

Table 5.8. Compiled OOF results of circular and ellipsoidal pores in ordered and random arrangements in  $X$  and  $Y$  orientations.....223

# 1

## Introduction

In recent years, an increasing amount of attention has been focused on the emergence of porous materials for engineering applications. These materials include metals, polymers, and ceramics, and they are utilized in a variety of thermal, electrical, optical, biological, and structural applications (Gibson and Ashby 1997; Kelly 2006). In many cases, the simple incorporation of void space can create a material that possesses a more appropriate combination of properties for a certain application.

The view of porosity in materials as being desirable, and the employment of porous materials in engineering applications, is a reversal in conventional thought as porosity has traditionally been considered an unwanted phase (Green and Colombo 2003; Kelly 2006). This is because porosity is generally viewed as an inclusion which results from poor processing methods and serves to weaken the material. However, materials with controlled porosity can have certain inherent properties such as lower density, lower thermal conductivity, lower dielectric constant, and higher surface area that make them more favorable candidates for certain applications than the equivalent pore free material (Green and Colombo 2003). As a result of these properties, porous materials are often used for thermal insulation, fuel cells, filters, tissue engineering, acoustic damping, catalyst supports, and structural supports (Davis 2002; Kelly 2006).

Porosity in a material is only beneficial if it provides desirable properties and can be controlled. Important aspects of porosity that affect material properties include volume %, pore size, pore shape, and interconnection of pores. Nature provides many examples of porous materials including bone, antler, egg shell, butterfly wings, natural sponges, coral, and wood (Ashby et al. 1995; Ben-Nissan 2003; Gibson 2005; Gibson et al. 1995; Zhang et al. 2006). In these applications, nature uses porosity to create materials that are both tough and lightweight. Natural porous materials generally possess complex microstructures that have been optimized over time by evolution to be multi-functional. The solid constituent of natural materials is generally some kind of ceramic phase such as hydroxyapatite in the case of bone or aragonite in the case of coral (Ben-Nissan 2003; Gibson 2005).

Following nature's lead, synthetic porous ceramics are produced and employed for a variety of applications that take advantage of the properties of both porous materials and those of ceramics which include high melting temperature, high strength, high stiffness, low density, and chemical inertness. Mimicry of natural microstructures in synthetic porous ceramics is often attempted in order to replicate the optimized properties of these materials. However, this is difficult using conventional methods of making porous ceramics and often leads to expensive, multi-step processes that do not always produce robust materials (Ben-Nissan 2003; Zhang et al. 2006).

Although reproduction of natural microstructures in synthetic materials has proven to be difficult, a new class of materials known as biomorphic materials overcomes this by using natural materials themselves to create engineering materials (Chakrabarti et al. 2004; Di et al. 2003; Greil et al. 1998a; Greil et al. 1998b; Herzog et al. 2006; Liu et al. 2005; Ota et al. 2000;

Ota et al. 1995; Rambo et al. 2004). A specific example of this class of materials is biomorphic silicon carbide (bioSiC), which is a novel porous ceramic material derived directly from wood precursors. This material retains the porous microstructure of wood and will be the focus of this document.

### **1.1. Scope and Objectives**

BioSiC was first produced by Ota et al. in 1995 by a process combining pyrolysis and molten Si infiltration of wood. Through this processing method, wood is directly converted into SiC, and the result is a porous silicon carbide material that retains the optimized microstructure of the original wood precursor.

Since its initial development, much work has been conducted on processing and mechanical properties of this material as a function of porosity (Arellano-Lopez et al. 2004; Greil et al. 1998a; Greil et al. 1998b; Martinez-Fernandez et al. 2003; Martinez-Fernandez et al. 2000; Singh and Salem 2002; Varela-Feria et al. 2002). While these are important, these materials are complex and more fundamental relationships between properties and microstructure must also be established in order to truly characterize the material and identify it for potential applications. To this end, the characterization of fundamental structure-mechanical property relationships in bioSiC will be the focus of this document.

In order to do this, a research plan was developed. This consisted of several elements, beginning with the selection of different wood precursors from several species of trees that covered a range of porosities, pore sizes, and pore size distributions. Each of these precursors was processed and converted into bioSiC, and the structure and chemical composition of the

materials were characterized at various stages through the processing using various analytical methods. These materials were then tested in compression and in bending to evaluate the mechanical properties of bioSiC. Additionally, finite-element analysis was also used to assess the effect of microstructure on mechanical properties. Finally, microstructure-mechanical property relationships in these materials were established. Further details and results of this work will be presented in the following chapters.

# 2

## Background

This chapter provides the background information necessary to understand biomorphic silicon carbide (bioSiC), how it fits into the class of porous materials, and what makes it unique from other materials in this category. In addition to processing methods and properties of porous materials, details on the structure of wood and how it relates to bioSiC will also be provided. Finally, a description of the pyrolysis/reaction-infiltration process used to fabricate bioSiC will be given, along with a review of other work related to this material.

### **2.1. Porous Materials**

A material can be defined as porous if it consists of one or more solid phases and void space. Common examples of porous materials include polymeric foams for impact absorption, metal foams for lightweight structural airplane components, and ceramic foams for molten metal filtration (Davis 2002; Green and Colombo 2003; Saggio-Woyansky et al. 1992). Different types of porous materials are employed in a variety of applications because they combine the properties inherent to the solid constituent and the porous phase.

#### 2.1.1. Classification of Porous Materials

Materials containing porosity can further be classified by the amount and nature of their porosity. Porous materials containing greater than 70% porosity are referred to as cellular

materials (Gibson and Ashby 1997). Unlike porous materials with lower amounts of void space, the mechanical behavior of cellular materials tends to be dominated by interactions between pores. However, because the bulk of this work concerns materials that have less than 70% porosity, the focus of this document will be placed on the behavior of non-cellular porous materials.

In addition to the amount of porosity, materials can also be categorized by the isotropy or dimensionality of porosity. Materials with isotropic, three-dimensional porosity are known as foams. The pores in these materials are polyhedrons and are arranged in three-dimensional arrays (Gibson and Ashby 1997). Materials with anisotropic, two-dimensional porosity are known as honeycombs. The pores in these materials are tubular and aligned with polygonal cross-sections and are arranged in two-dimensional-arrays (Gibson and Ashby 1997). Examples of both foams and honeycombs are shown in figure 2.1. Properties of foams are generally isotropic while those of honeycombs are usually anisotropic as properties in the direction parallel to tubular alignment are different from those in perpendicular directions (Brezny and Green 1990; Gibson and Ashby 1997; Hasselman and Fulrath 1965; Huang and Gibson 1991; Rice 1998).

Porous materials can further be classified by the amount of interconnection between pores. Those materials where porosity is interconnected and unenclosed by solid are said to have open-porosity.

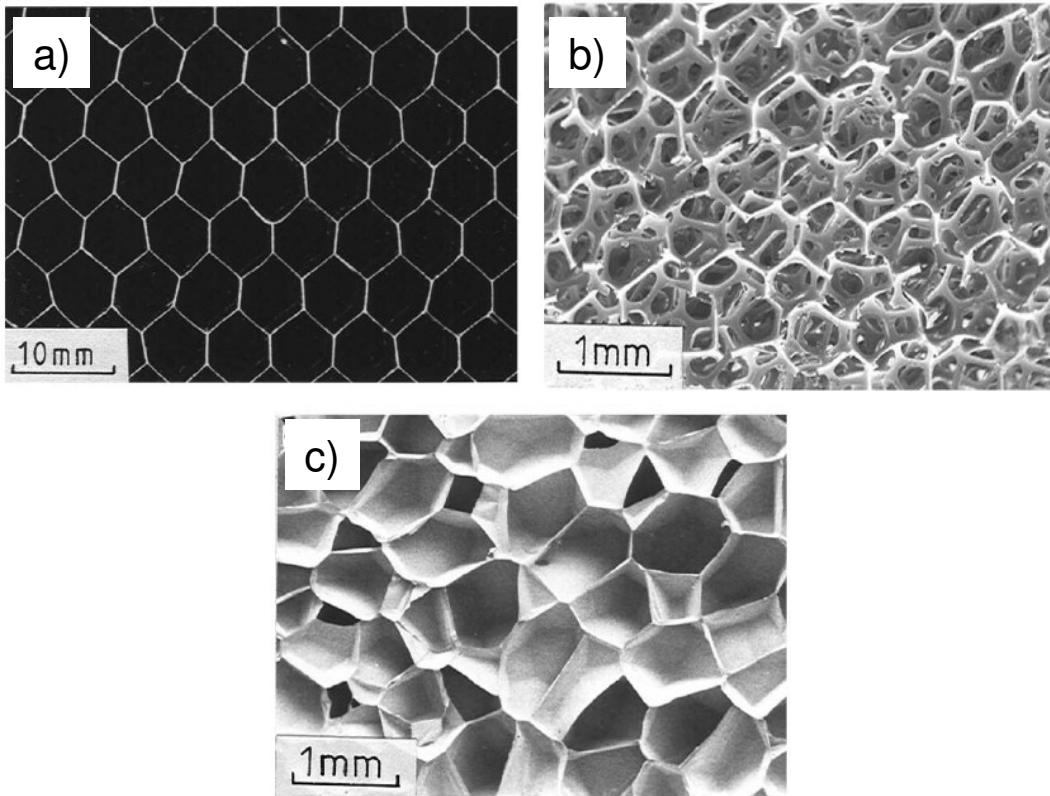


**Figure 2.1. Examples of a) honeycomb, b) open-pore foam, and c) closed-pore foam materials. (Gibson and Ashby 1997).**

Those materials where pores are enclosed by solid and porosity is not interconnected are said to have closed-porosity (Gibson and Ashby 1997). Examples of materials with open and closed-porosity are also shown in figure 2.1. Depending on the application, the choice of open or closed-porous material can be significant. For example, for thermal insulation or acoustic damping, closed-pore materials are generally preferred to inhibit the transmittance of heat or sound through the material. In the case of filters or catalyst carriers, open-porosity is preferred to allow maximum exposed surface area and permeability (Kelly 2006). Figure 2.2 gives more examples of applications where either open or closed-pore materials are more appropriate.

In addition to porosity interconnection, figure 2.2 also gives appropriate pore sizes for these applications. Depending on the purpose for which the material will be employed, pore size is also an important parameter. For example, for filtration, the proper pore size must be chosen based on the size of the species to be filtered. Porosity for tissue engineering is also another place where an appropriate pore size must be chosen as tissue ingrowth will only occur within pores approximately 100  $\mu\text{m}$  in diameter (Black 1999).

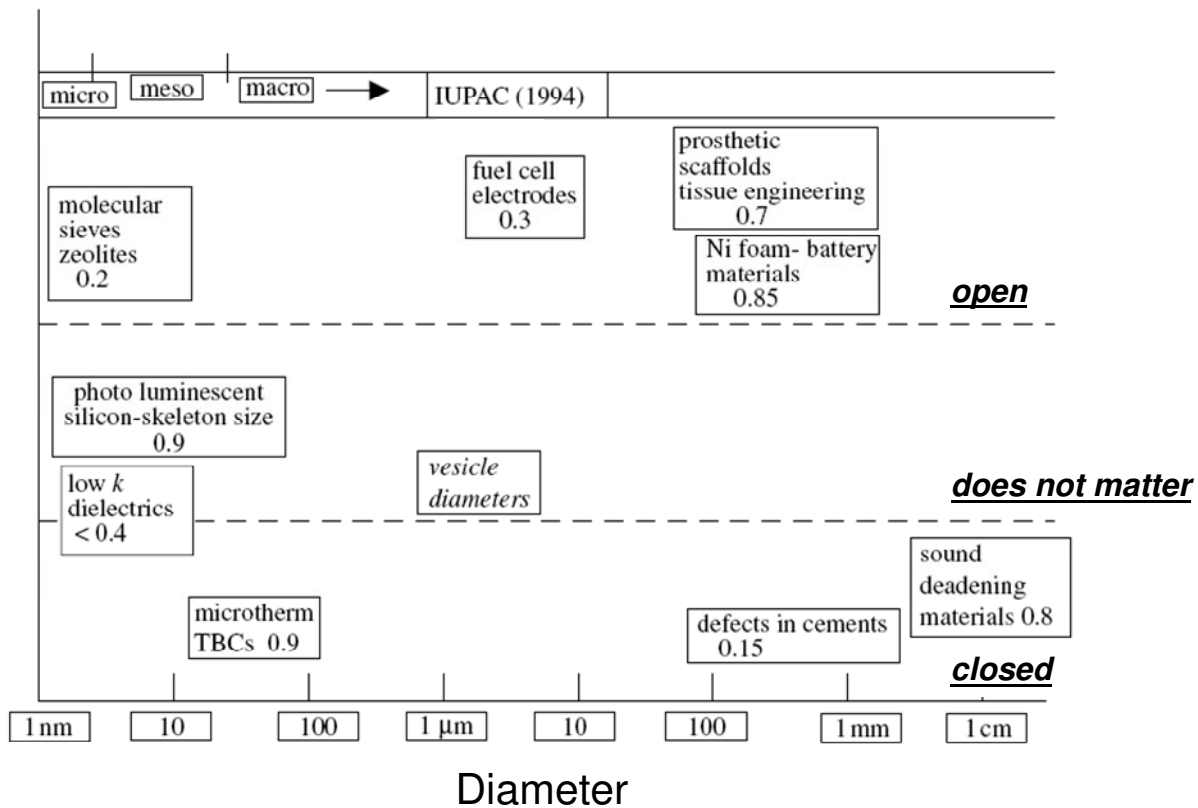


**Figure 2.2.** Chart showing optimum pore size, volume fraction, and interconnectivity for various applications of porous materials (Kelly 2006).

### 2.1.2. Properties and Processing of Porous Ceramics

Porous polymers and metals are widely used because it is relatively easy to fabricate polymers and metals that are robust and have controlled porosity by liquid-phase foaming. In contrast, the introduction of porosity is not as prevalent in ceramics because of difficult and expensive processing and the brittle nature of ceramics. As a result of this brittle nature, pores in ceramics can serve as flaws where cracks may initiate and cause catastrophic failure of the material. However, porous materials with ceramic solid phases are potentially useful in several applications where metals and polymers would not be appropriate. For example, porous ceramics can be used as molten metal filters and catalyst carriers because of their high melting temperatures and resistance to oxidation and corrosion (Green and Colombo 2003; Studart et al. 2006). With the advent of advanced processing methods, it is now possible to create ceramics with controlled porosity for applications where porous metals or polymers are not appropriate.

One simple way of creating porous ceramics is by partial sintering of ceramic powder (Yang et al. 2002). In this method however, pore morphology and size is determined by particle size and is not independently controllable. For this reason, focus in this section of the thesis will be placed on methods where control of porosity is independent of pore size. Processing methods for the fabrication of controlled porous ceramics can be divided into three categories: sacrificial template, direct foaming, and replica (Studart et al. 2006). These processing methods are shown schematically in figure 2.3. Each of these methods allows for the creation of ceramics with controlled porosity. The materials produced by each method also have differing porous morphologies that are a result of the pore forming agent used during processing.

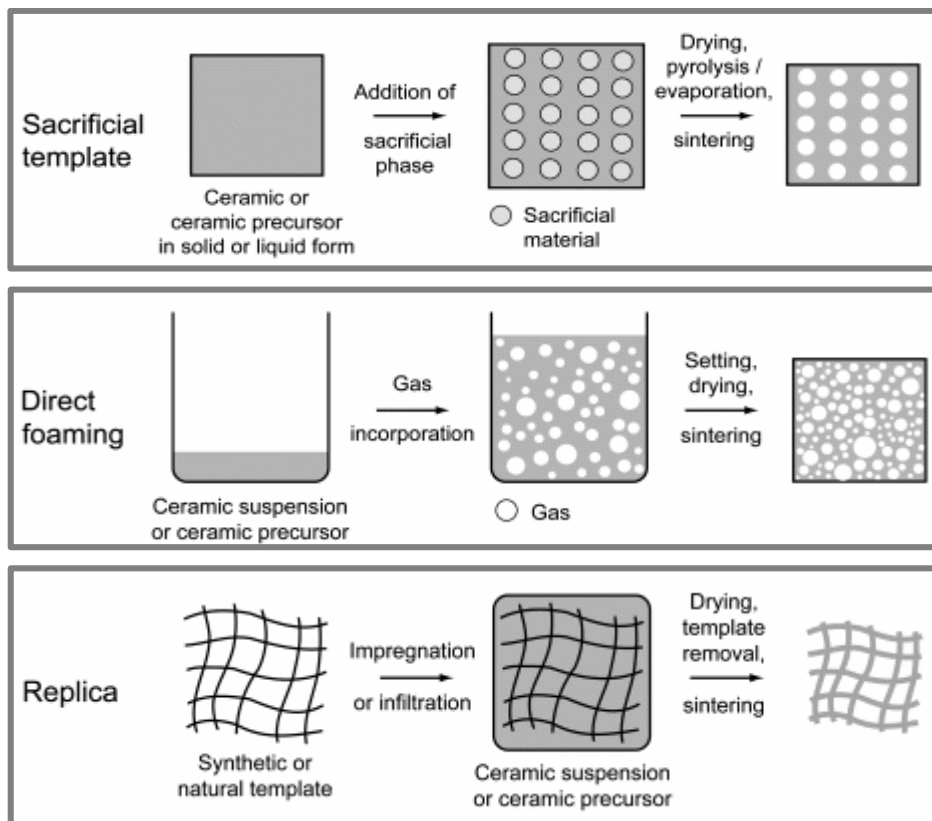


**Figure 2.3. Schematic representation of possible processing routes for forming ceramics with controlled porosity (Studart et al. 2006).**

### *Sacrificial template method*

In the sacrificial template method, a composite material is first created, followed by the removal of a sacrificial phase to create porosity. This method effectively creates a material that is the negative of the sacrificial phase. The three main stages of processing porous ceramics by the sacrificial template method are (I) formation of the green composite material by combining the ceramic or pre-ceramic phase and the sacrificial phase, (II) removal of the sacrificial phase, and (III) sintering of the final porous ceramic material. Common methods for creating the green composite include pressing a mixture of ceramic and sacrificial powder, formation of a liquid suspension of ceramic and sacrificial material which is then cast, and impregnation of a sacrificial material with ceramic slurry. Typical sacrificial phases used are synthetic and natural organics, liquids, and salts. Methods for removing these sacrificial phases include oxidation, sublimation, and chemical leaching (Studart et al. 2006).

Montgomery and Faber gelcast a slurry of alumina ( $\text{Al}_2\text{O}_3$ ) and 5-10  $\mu\text{m}$  corn starch to create flaw tolerant alumina laminates with controlled porosity. In this work, the sacrificial starch was removed by pyrolysis, and a scanning electron micrograph of the sintered microstructure is shown in figure 2.4(a) (Montgomery and Faber 2005). Shanti et al. fabricated porous  $\text{Al}_2\text{O}_3$  using camphene as the sacrificial phase. In this work, a suspension of  $\text{Al}_2\text{O}_3$  and camphene was freeze cast, leading to the formation of dendrites. The camphene was then removed by freeze drying leaving an interconnected porous microstructure as seen in figure 2.4(b) (Shanti et al. 2006).

The main advantage of the sacrificial template method is the ease by which the fugitive phases can be incorporated into the material to create various pore morphologies.

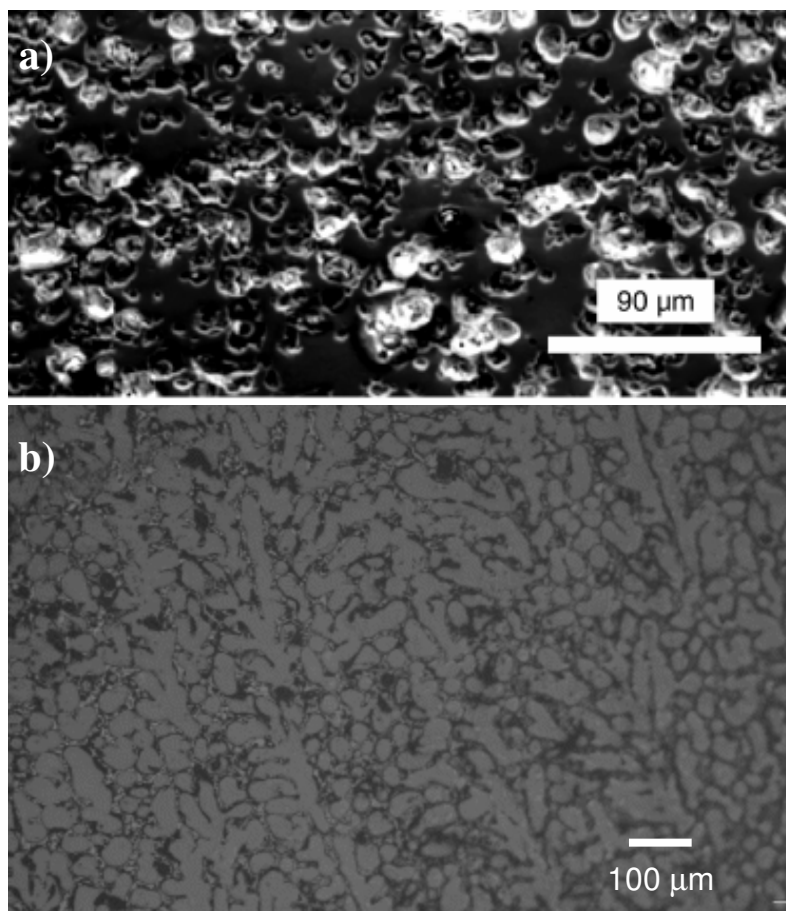


**Figure 2.4. Microstructures of porous  $\text{Al}_2\text{O}_3$  fabricated using a) corn starch (Montgomery and Faber 2005) and b) camphene (Shanti et al. 2006) sacrificial templates.**

The major disadvantage of the method is the often difficult and time consuming removal of the sacrificial phase as strong acids or long heat treatments are often necessary (Studart et al. 2006).

#### *Direct foaming method*

Another processing method for making porous ceramics is by direct foaming, which involves the incorporation of a gaseous phase into a ceramic slurry, precursor or melt to form pores. The main stages of this method are (I) gas incorporation by physical or chemical means into a liquid ceramic slurry, precursor or melt, (II) setting/stabilization of the liquid porous structure, and (III) sintering of the porous ceramic. The liquid ceramic or slurry is generally a ceramic suspension with a surfactant to stabilize the porous structure after foaming, ceramic sol-gel, or a ceramic slurry containing monomers that are polymerized to stabilize the porous microstructure (Studart et al. 2006). Gas incorporation generally takes place by physical, chemical, or thermal methods. Common methods by which this occurs include: physical blowing of a gas to foam a ceramic slurry, mechanical frothing of a ceramic slurry, a chemical reaction in the slurry that produces a gaseous species, or thermal expansion to create and expand a gas in the ceramic slurry (Studart et al. 2006). The amount of porosity is simply controlled by the volume of gas incorporated, and the pore size is controlled by the type of stabilization used.

Klett created porous graphite by foaming carbon pitch. In this process, carbon pitch was heated above its softening temperature while nitrogen gas was introduced. The temperature was then gradually raised, expanding the gas to foam and then harden the carbon pitch. This was followed by heat treatment at 2800 °C to graphitize the foam (Klett 2000). The structure of the final material is shown in figure 2.5(a). Sepulveda and Binner also used foaming to create

porous ceramics. In this work, an aqueous slurry of  $\text{Al}_2\text{O}_3$ , organic monomers, and surfactant was foamed by mechanical stirring. After foaming, the slurry was stabilized by the introduction of an initiator and catalyst to polymerize the organic monomers. The organics were then burned out and the material was sintered resulting in a porous  $\text{Al}_2\text{O}_3$  material shown in figure 2.5(b) (Sepulveda and Binner 1999).

The main advantage of the direct foaming method is the relative ease of pore incorporation in to the material. However, the disadvantages include toxic stabilizing agents and the limitation to spherical porosity.

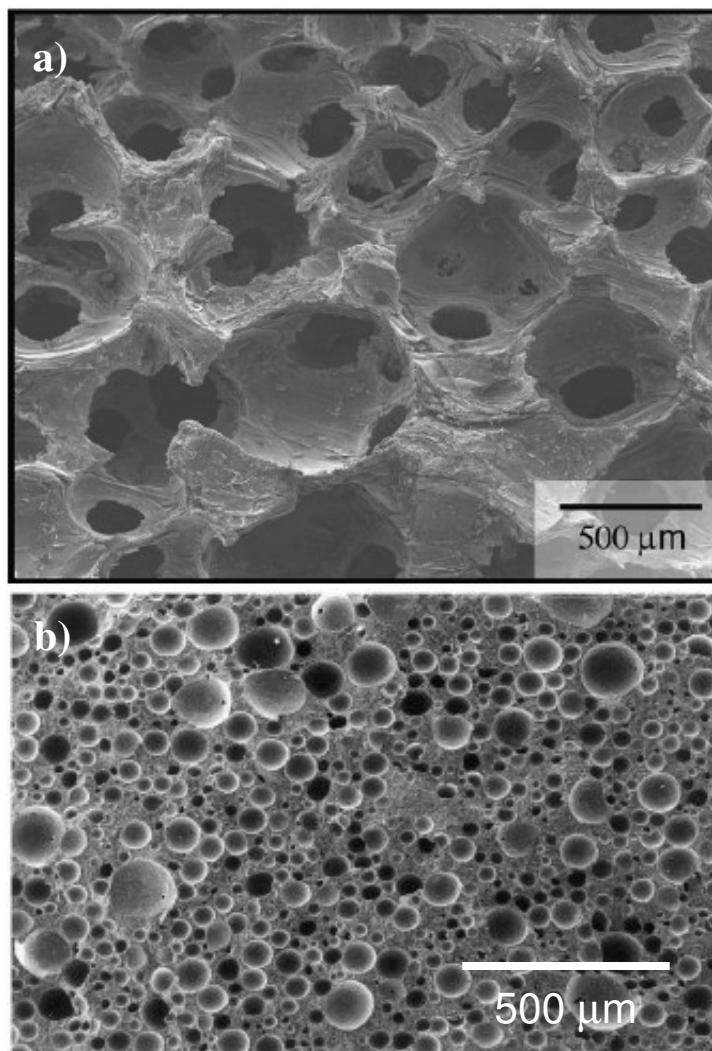


**Figure 2.5. Micrographs of a) graphite (Gaies and Faber 2002), and b) Al<sub>2</sub>O<sub>3</sub> (Sepulveda and Binner 1999) formed by direct foaming.**

### *Replica method*

As the name implies, the replica method is based on the replication of an existing porous material or template to create a porous ceramic. The initial step in this method is (I) infiltration of the template with a ceramic slurry. This is followed by (II) drying and removal of excess green ceramic and the porous template. The final step is (III) sintering of the porous material. This process leads to a porous ceramic with a structure that mimics the structure of the template. In this method, the viscosity of the ceramic slurry must be controlled to allow infiltration of the slurry into the template and adhesion to it without dripping. Binders and plasticizers are also added to the slurry for increased strength and toughness to prevent cracking during template removal (Studart et al. 2006). The template is generally a polymer sponge, and the amount of porosity and pore size of the final ceramic material are determined by the template. For polymer templates, removal is usually accomplished by pyrolysis, which leaves void space within the solid ceramic strut in addition to the porosity in the template structure.

One example of the replica method is the patented procedure developed by Schwartzwalder et al. (1963). Using this procedure, alumina foams can be produced by coating polyurethane foams with  $\text{Al}_2\text{O}_3$  slurry. After drying, the polyurethane foam is removed by pyrolysis resulting in porous  $\text{Al}_2\text{O}_3$  with hollow struts, as shown in figures 2.6(a) and (b) (Schwartzwalder et al. 1963). Fitzgerald and Mortensen produced microcellular SiC foams by a process that combined the sacrificial template and replica methods. Here, a porous sodium chloride compact was infiltrated with polycarbosilane. The compact was then dissolved, leaving a porous polycarbosilane negative. The polycarbosilane was then oxidized and pyrolyzed to

form porous SiC (Fitzgerald et al. 1995). The structure of the foam formed using this process is shown in figure 2.6(c).

The major advantage of the replica method is the control of porosity, pore size and pore morphology provided by using a template. The ease of fabrication of porous polymers provides a variety of templates. The main disadvantage is the voids and cracks that often result from template removal. These voids create additional porosity and often weaken the final porous ceramic (Stuart et al. 2006).

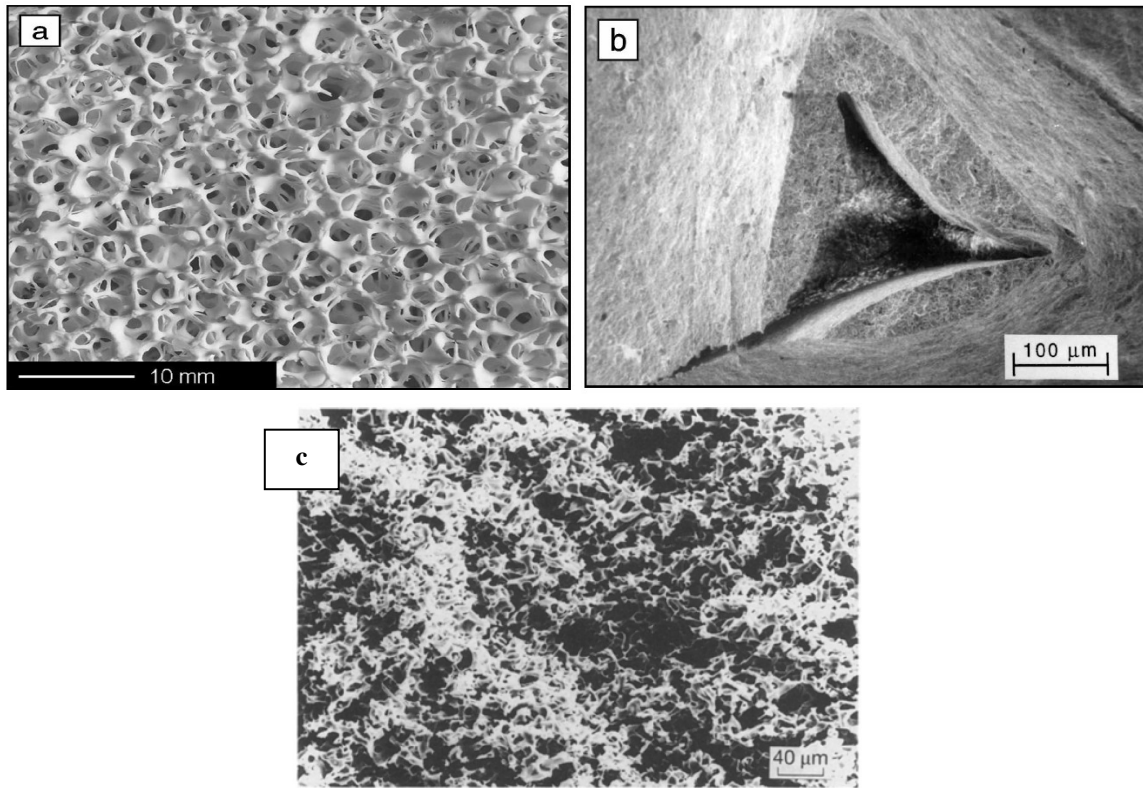


**Figure 2.6. Scanning electron micrographs of porous a)  $\text{Al}_2\text{O}_3$  with b) hollow struts (Green and Colombo 2003) and c) SiC (Fitzgerald and Mortensen 1995) formed by the replica method.**

### 2.1.3. Natural Templates

In addition to synthetic templates, porous materials found in nature can also be used as templates for forming porous ceramics. Ben-Nissan used natural coral as a template to create porous hydroxyapatite for bone grafts using the replica method (2003). Coral is an ideal template for bone grafts because its porosity ranges in size from 150 – 500  $\mu\text{m}$  and it has a structure similar to that of cancellous bone, which is difficult to form artificially. By using replication, the natural structure of coral is retained, and its primarily aragonite (calcium carbonate) solid phase is converted to hydroxyapatite (calcium phosphate) by a two-step reaction (Ben-Nissan 2003). The structure of the natural coral and the porous hydroxyapatite are shown in figures 2.7(a) and (b). As another example, Zhang et al. used the replica method to create porous ZnO from butterfly wings. This was done using a three-step process and the microstructure of the butterfly wing and the resulting porous ZnO are shown in figures 2.7(c) and (d) (Zhang et al. 2006).

In addition to coral and butterfly wing, porous materials appear in many different places in nature, and many of these materials can be used as templates to create porous ceramics. Several examples of natural porous materials are shown in figure 2.8. As mentioned earlier, nature uses complex and hierarchical microstructures to create porous materials for structural applications. These materials are both tough and lightweight, and their complex microstructures are nearly impossible to create artificially.

A natural porous material that has been of particular interest and utility throughout history is wood. Wood has a complex porous microstructure that is replicated in bioSiC, the central material researched for the work presented in this document.

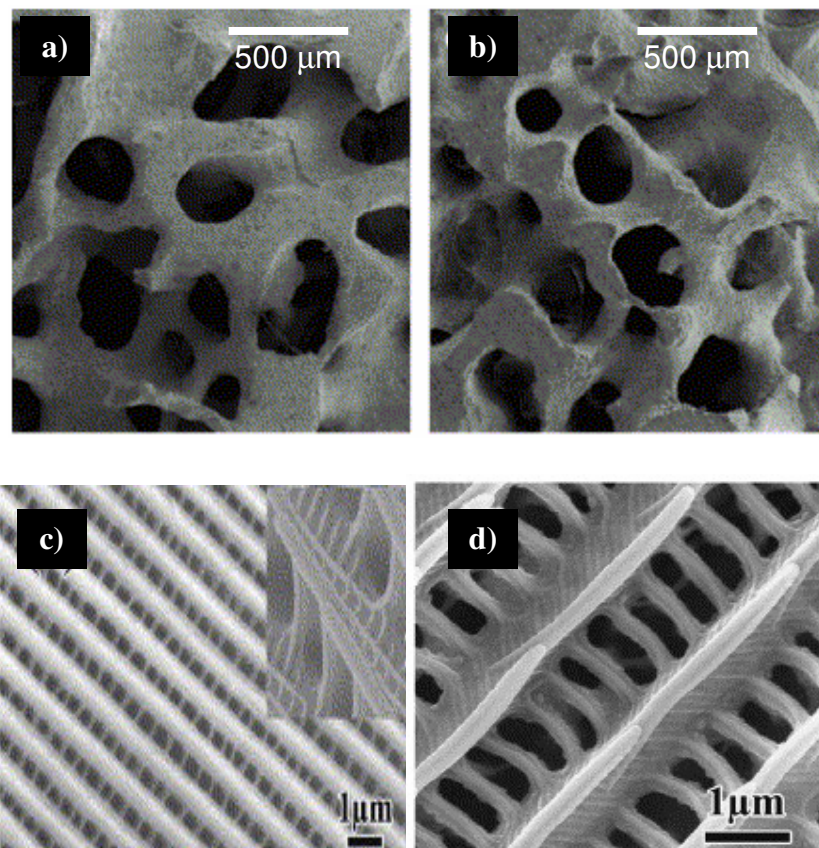


**Figure 2.7. Scanning electron micrographs of a) natural coral and b) replicated hydroxyapatite (Ben-Nissan 2003), and c) natural butterfly wing scale and d) replicated ZnO (Zhang et al. 2006).**

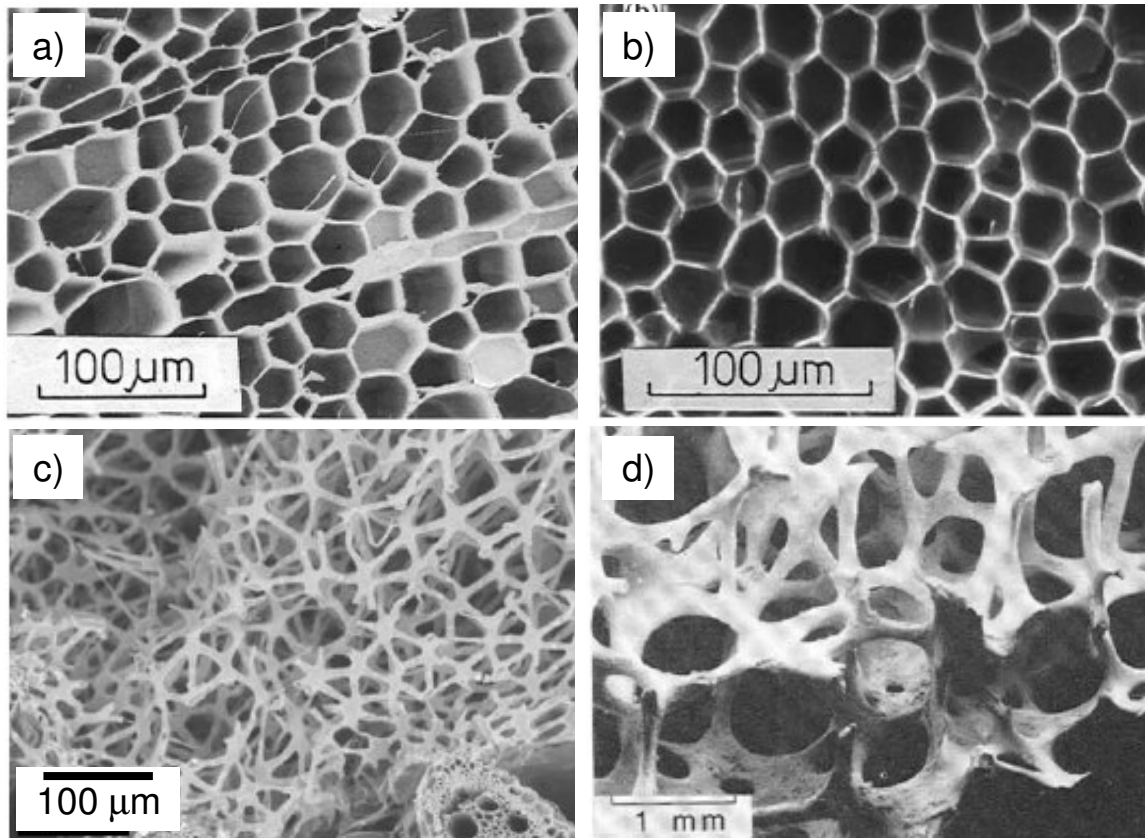


**Figure 2.8. Examples of natural porous materials including a) balsa wood, b) cork, c) plant stem, and d) trabecular bone (Gibson 2005).**

In order to understand and characterize the structure of bioSiC, it is necessary to possess an understanding of the structure of the wood from which it is derived. This will be the subject of the next section.

## **2.2. Wood**

Although many other materials have been developed for structural applications since ancient times, wood continues to be used in some form in everything from the most rudimentary to even the most modern structures. Trees grow virtually everywhere on the planet, making some type of wood available in every nation. In developing countries, wood is an essential structural material because it is readily available and inexpensive. In industrialized nations, even when other materials are easily available, wood is often used for structural applications because it is a tough and durable material with a specific strength (strength/density) greater than steel (Ashby et al. 1995).

In order to characterize the structure and mechanical properties of bioSiC, it is necessary to understand the structure of the wood precursors from which it is fabricated. This precursor structure is retained in bioSiC and it dictates many of the properties of the material. The convention that will be used in this document to refer to the principal directions in wood is shown in figure 2.9. Planes will also be referred to by this convention. For example, the vertical growth direction and the plane perpendicular to it will be referred to as the axial direction and axial plane, respectively. The remainder of this section will serve to describe the structure and composition of wood as they relate to bioSiC.

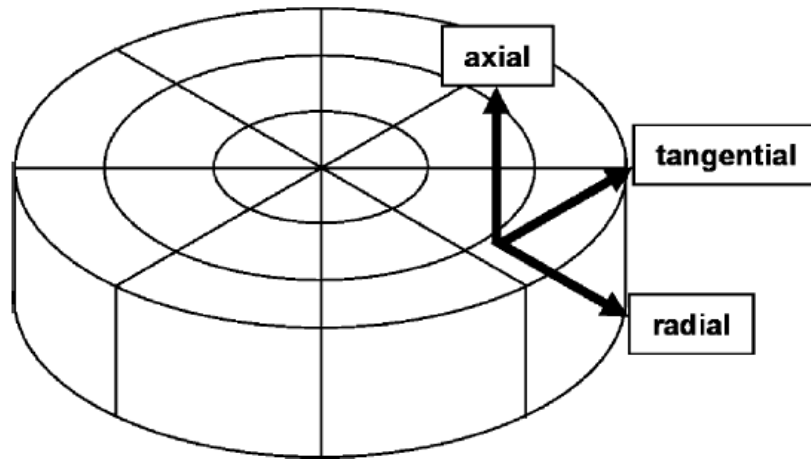


**Figure 2.9. Schematic representing the convention used to refer to principal directions in wood.**

### 2.2.1. Solid Phase of Wood

While there are many differences between different species of wood, the solid material that makes up the pore walls is basically the same (Gibson 1992). This material is essentially a multi-layer polymer fiber-reinforced glass composite and is primarily made of three components: cellulose, hemicellulose, and lignin (Dinwoodie 1989). The weight fractions of each of these components in softwoods and hardwoods are shown in table 2.1.

#### *Wood components*

Cellulose ( $C_6H_{10}O_5$ )<sub>n</sub> is a naturally occurring polymer that is built up within trees from the glucose ( $C_6H_{12}O_6$ ) monomer and has a degree of polymerization of 8000 – 10,000 units. Up to 70% of the cellulose in wood is crystalline, and forms planar sheets (Dinwoodie 1989). These crystalline sheets tend to be stiff and rigid due to strong intermolecular covalent bonds and intramolecular hydrogen bonds (fiber phase in composite analogy). In addition to these strong interplanar bonds, weaker van der Waals' forces are present between crystalline layers (Greil 2001). The crystalline structure of cellulose is shown in figure 2.10.

Another component of wood is hemicellulose. This semi-amorphous organic material has a structure that is very similar to cellulose. However, the degree of polymerization of hemicellulose is approximately one order of magnitude lower than that of cellulose. The structure of hemicellulose is shown in figure 2.11(a). Like cellulose, hemicellulose is meant to provide reinforcement.

**Table 2.1. Weight fractions of wood components (Dinwoodie 1989).**

	<b>Softwoods</b>	<b>Hardwoods</b>
<b>Cellulose</b>	40 – 45 %	45 – 50 %
<b>Hemicellulose</b>	25 – 35 %	21 – 35 %
<b>Lignin</b>	26 – 39 %	22 – 40 %

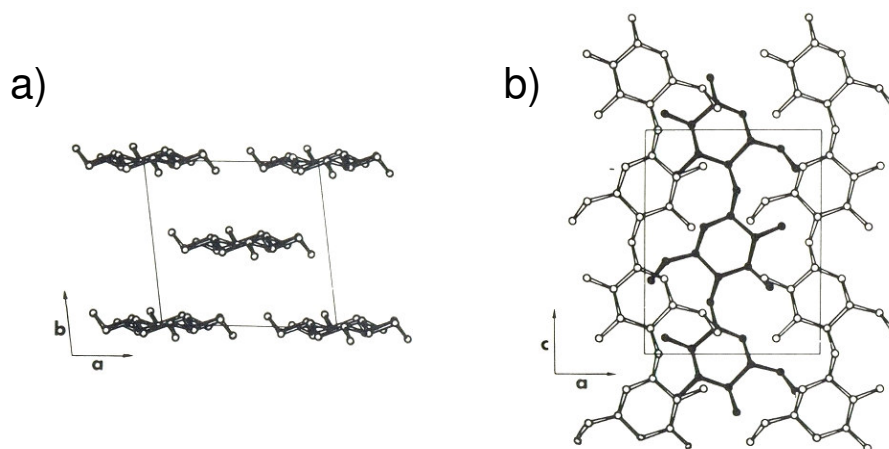


**Figure 2.10. a) Axial and b) transverse projections of crystalline cellulose with planar sheets parallel to the axial direction (Gardener and Blackwell 1974).**

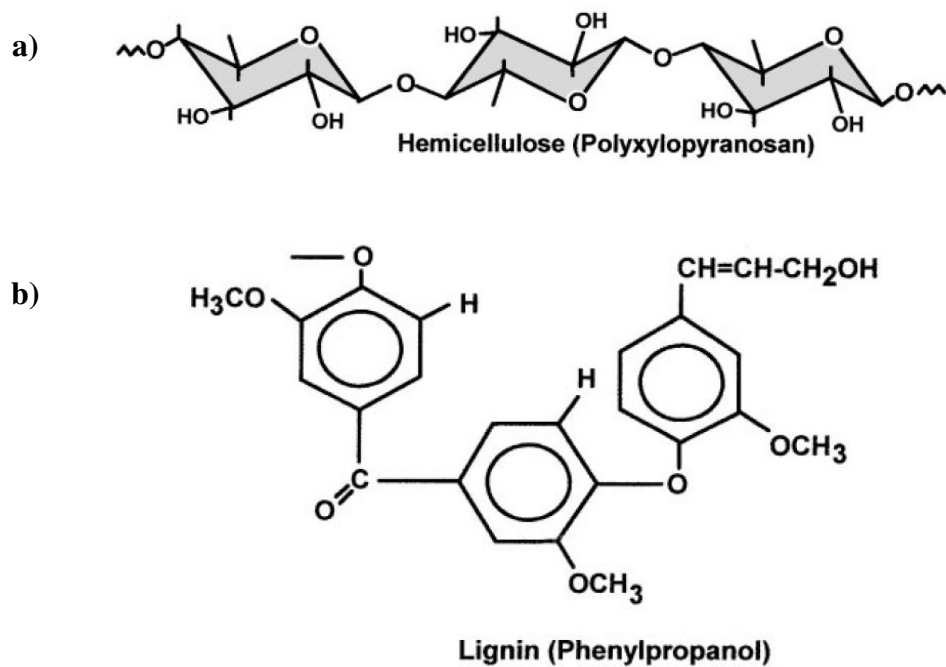


Figure 2.11. Molecular structures of a) hemicellulose and b) lignin (Greil 2001).

The final primary component of wood is lignin. It serves as the coupling agent or glue in wood and is amorphous in nature (analogous to the matrix in a fiber composite) (Dinwoodie 1989). The lignin molecule is relatively large and its structure is shown in figure 2.11(b).

### *Composite Structure of Wood*

The primary wood components of cellulose, hemicellulose, and lignin combine to form a composite material that makes up the pore walls in wood. This naturally optimized material is ordered and multi-layered with differing fiber alignment schemes in each layer.

The wall material that makes up wood is composed of three layers. The outermost layer, known as the middle lamella, is thin and made up of amorphous lignin. In each of the remaining layers, the amorphous matrix is strengthened by the polymer fiber phase in various fiber-architectures. In wood, these polymer fibers are known as fibrils. These fibrils are composed of crystalline cellulose that is surrounded by amorphous cellulose, hemicellulose, and lignin (Dinwoodie 1989). As a result of the strong interlayer bonding in cellulose, these rigid fibers serve as the stiffening component of wood.

Inside the middle lamella is the primary wall. This layer is made up of an amorphous matrix of hemicellulose and lignin with randomly woven fibrils. Inside the primary wall is the secondary wall, which is composed of three sub-layers known as  $S_1$ ,  $S_2$ , and  $S_3$ . In each of these sub-layers, fibrils are arranged in an ordered architecture to strengthen wood. In the  $S_1$  and  $S_3$  sub-layers, fibrils are woven in an ordered mesh while in the  $S_2$  sub-layer, fibrils are unidirectionally aligned in an orientation nearly parallel to the axial direction. A schematic of

this multi-layer arrangement and the fibril architecture in each layer are shown in figure 2.12. This fibril architecture and alignment are responsible for the anisotropic shrinkage that takes place during pyrolysis. The woven networks of these woven fibril networks act as a thermosetting polymer and as a result, the composite pore wall material of wood burns upon pyrolysis (Greil 2001).

### 2.2.2. Structure of Wood

Wood is a honeycomb-type porous material with two-dimensional, anisotropic porosity. This porosity is composed of tubular, elongated pores that are aligned parallel to the axial direction of the tree. An example of this structure is shown in figure 2.13. Depending on the source species of the wood, the volume of porosity can range from 5% for *lignum vitae* to 97% for balsa (Gibson and Ashby 1997). Trees can be massive organisms, and the porous microstructure of wood has been optimized through evolution to have excellent properties in both compression and flexure while remaining lightweight (Ashby et al. 1985; Varela-Feria et al. 2002). Not only does this structure provide mechanical support, it also serves as the vascular system of trees so that water and nutrients can be distributed to all parts of the organism.

When cut perpendicular to the axial direction, the two-dimensional array of pores on the axial plane that is characteristic of honeycomb-type materials becomes apparent. In wood, there are four types of cells or pores that make up this array. These are tracheids, parenchyma, fibers, and vessel elements. These cells all compose the non-living tissue of the tree known as xylem.

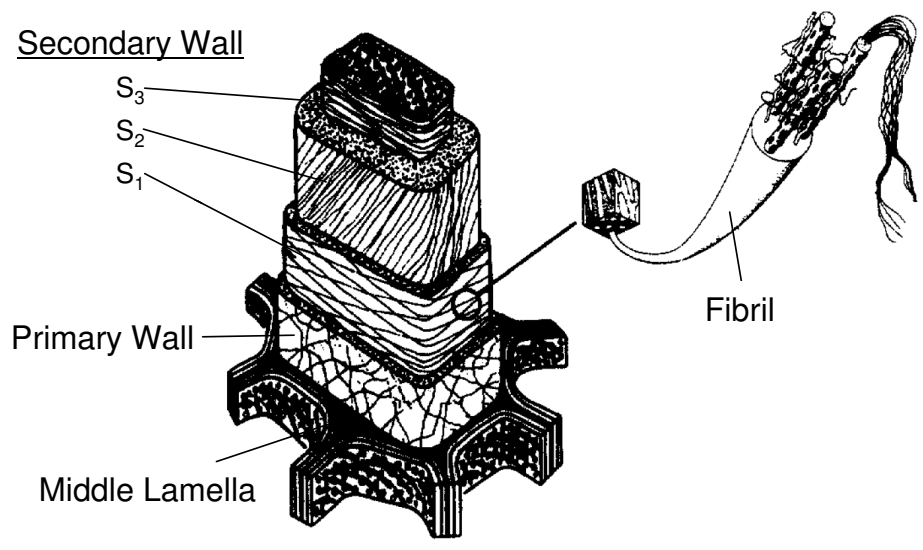
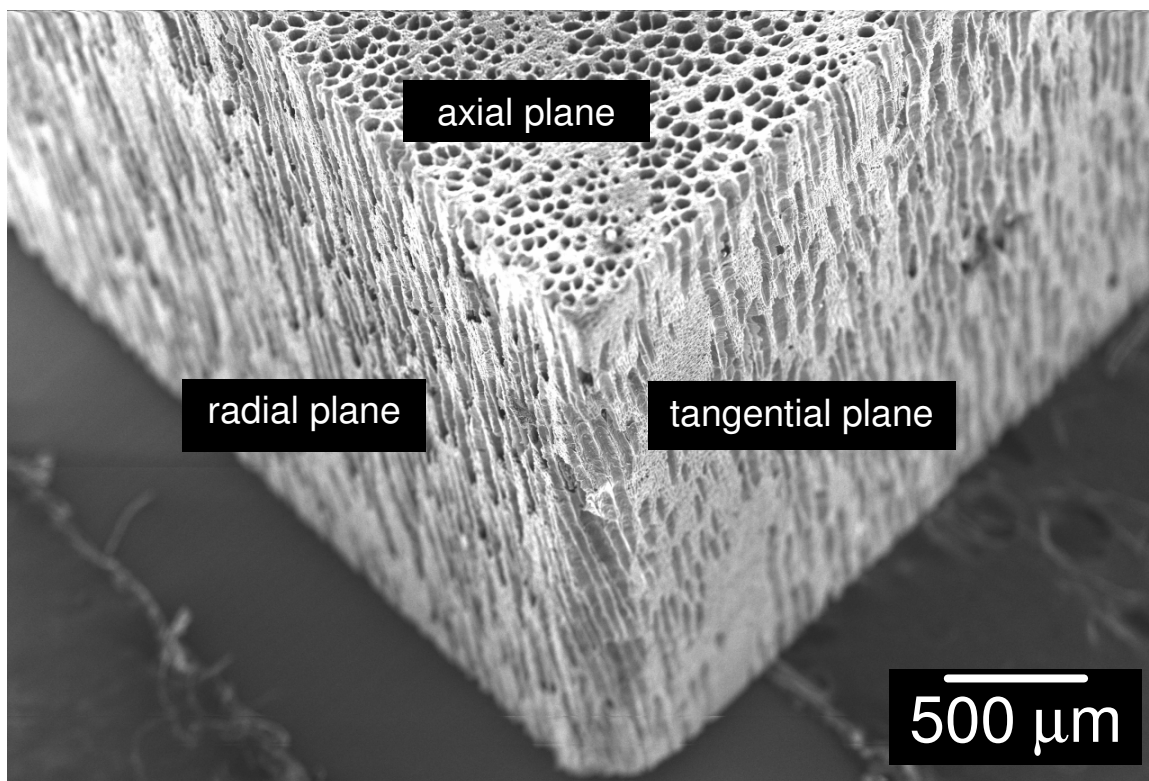


Figure 2.12. Multi-layer composite structure of wood after Greil (1998a).



**Figure 2.13.** Scanning electron micrograph of pyrolyzed beech exhibiting the honeycomb-type structure of wood.

The living portion of trees, known as cambium, comprises only a small circumferential portion of tree and is not part of commercially available timber that was used in this work (Dinwoodie 1989; Raven et al. 1976).

Tracheids are tubular cells with tapered ends that are aligned parallel to the axial direction. The diameters of these cells range between 30-50  $\mu\text{m}$  in softwoods and 50-200  $\mu\text{m}$  in hardwoods (Greil 2001). The length of these cells varies from 2900-4500  $\mu\text{m}$  in softwoods and 100-800  $\mu\text{m}$  in hardwoods. These cells are responsible for both fluid conduction and mechanical support. Parenchyma cells are smaller radially aligned cells that are responsible for food storage and are present in both soft and hardwoods. These cells are approximately 200 x 30  $\mu\text{m}$  (Dinwoodie 1989). Another type of cell present in wood is the fiber. These are tubular cells with tapered ends that are axially aligned and have very similar dimensions to tracheids. These cells are only present in hardwoods and are responsible for mechanical support. The final type of cell present in wood is the vessel element. These are axially aligned drum-like cells that are only present in hardwoods and are responsible for fluid conduction (Canny 1998). The height of these cells is between 200-1000  $\mu\text{m}$  and the width is between 30-500  $\mu\text{m}$  depending on the species of wood and growth conditions. As the tree ages, the ends of these cells dissolve to form continuous tubes for fluid conduction known as a vessels (Dinwoodie 1989). Pores known as pits are also present within the walls of these cells for non-axial conduction between cells. Many of these features of wood are shown in figure 2.14.

These pores also make up macroscopic features in the two-dimensional array of pores. As trees grow outward, the wood toward the center becomes dry and non-conducting. This darker wood is known as heartwood.

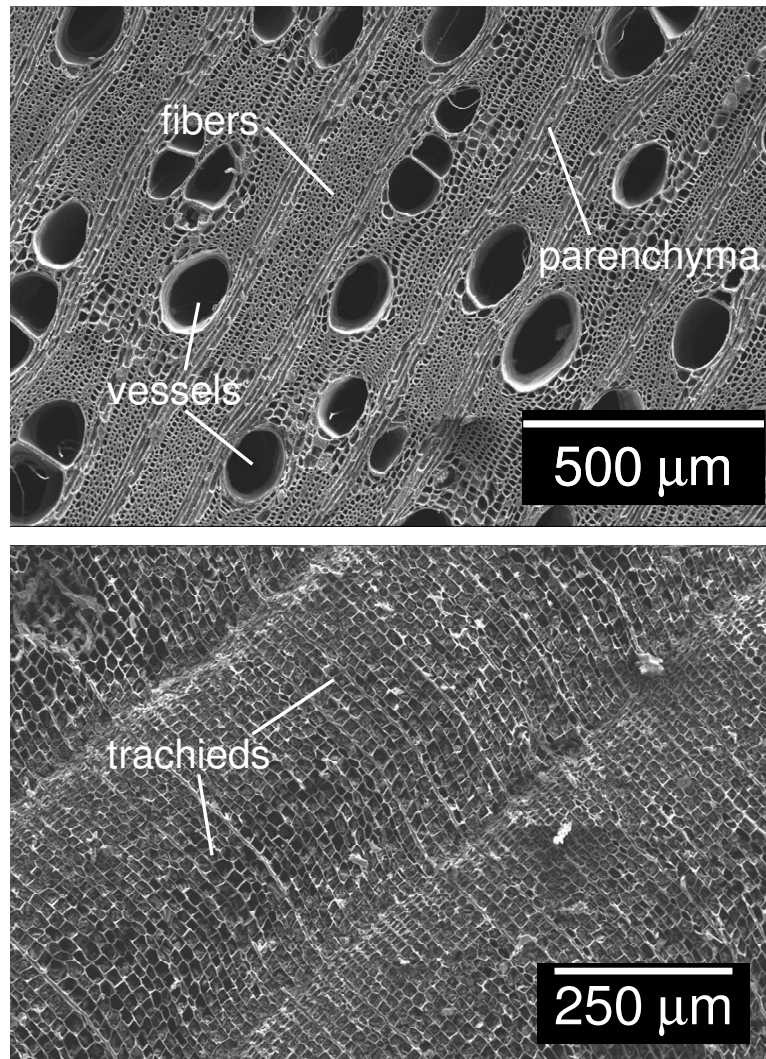


**Figure 2.14. Scanning electron micrographs of axial planes of a) pyrolyzed sapele (hardwood) and b) pyrolyzed cedar (softwood) showing examples of four primary wood cells.**

The lighter, fluid-conducting wood found away from the center is known as sap wood (Raven et al. 1976). While heartwood tends to be more valuable as a building material, a composite of both of these wood phases are found in commercial timber (Dinwoodie 1989).

Also present are growth rings, which are concentric rings of varying pore density that are the result of cyclically changing growth rates due to seasons. These features form because larger thin-walled pores, forming what is known as early wood, grow during the spring and summer when water is more abundant and smaller thick-walled pores, forming late wood, grow during the fall and winter when water is less abundant (Dinwoodie 1989). As their name suggests, growth rings are often used as a way to estimate the age of a tree as one complete ring generally corresponds to one year. Rays are also macroscopic features which are formed by groups of aligned parenchyma that radiate from the center of the tree. Growth rings, rays, early wood, late wood, heart wood, and sap wood are all shown in figure 2.15. Some of these features can be controlled by regulating growth conditions. For example, growth rings can be eliminated by a controlled and constant environment, and vessels can be eliminated by compression of growing wood (Bauer and Eschrich 1997).

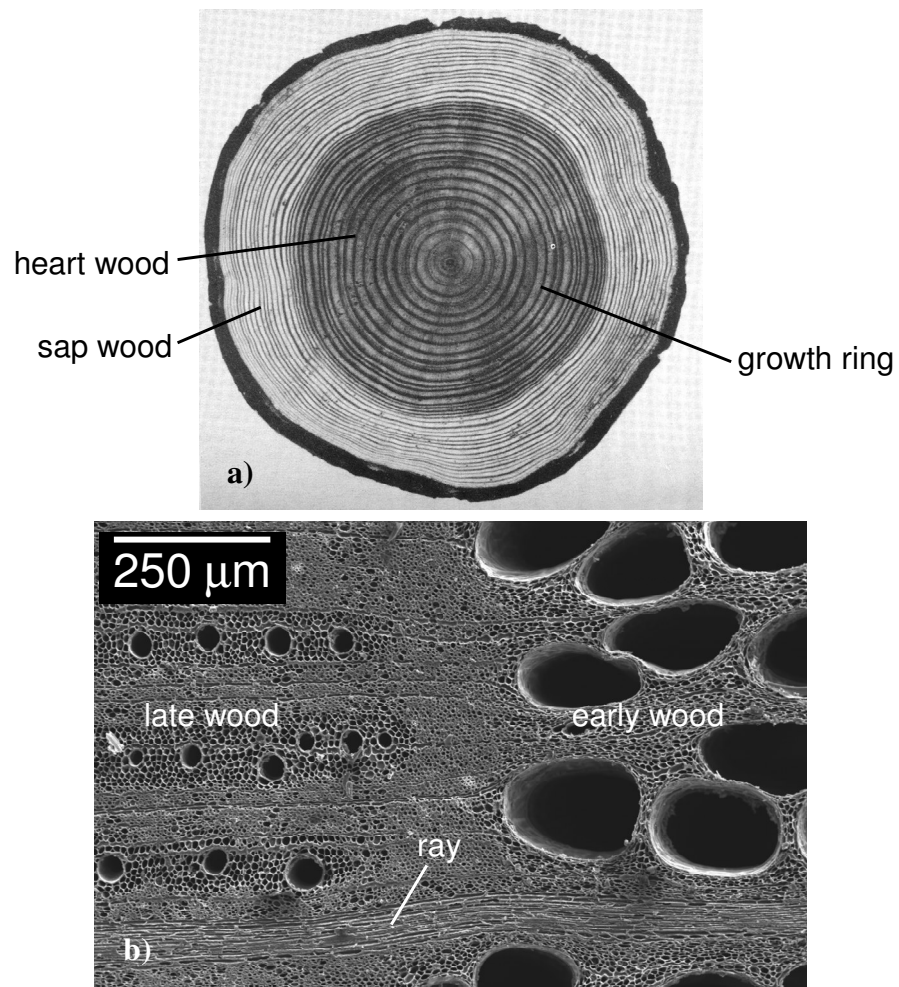


**Figure 2.15. Micrographs of a) Douglas fir after Dinwoodie (1989) and b) pyrolyzed red oak showing macroscopic features in the axial plane of wood.**

### 2.2.3. Classification of Wood

Woods are generally classified as either softwoods (gymnosperms) or hardwood (angiosperms). Gymnosperm comes from the ancient Greek meaning “naked seed” and these are conifers that generally have uncovered seeds within cones. Common examples of softwood trees include pine, cedar, and fir. These trees are characterized by needle-like leaves that remain green throughout the year. Angiosperm comes from the ancient Greek meaning “receptacle seed.” These hardwood trees are known as dicots and common examples include maple, oak, and birch. The leaves of hardwoods are usually broad and fall off annually (Raven et al. 1976). While all woods share common pore wall compositions and pore types, woods cover a very broad range of densities and pore sizes. Examples of woods that span this range are shown in figure 2.16. The range of densities covered by hardwoods is larger than softwoods and for this reason, and because of the easy commercial availability of several species, hardwoods will be the focus of this work.

Hardwoods can further be classified as either diffuse porous or ring porous woods. Diffuse porous woods show little differentiation between early wood and late wood, while ring porous woods show clear segregation and differentiation of late and early woods. Examples of diffuse and ring porous woods are shown in figure 2.17.

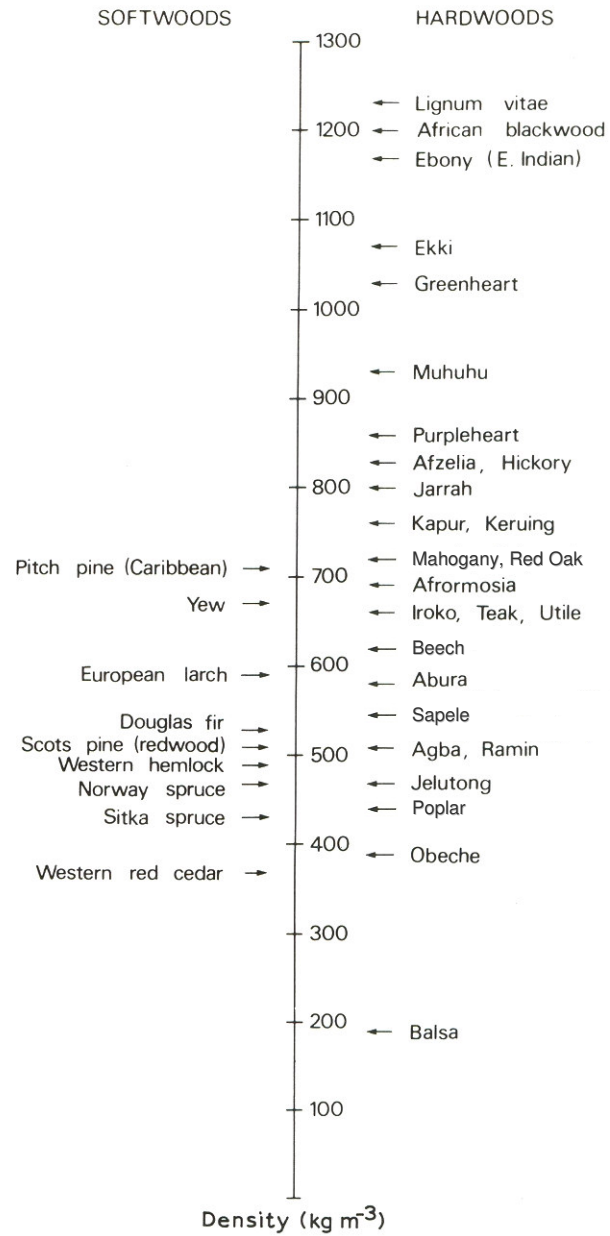


**Figure 2.16. Range of densities for various softwoods and hardwoods (Dinwoodie 1989).**

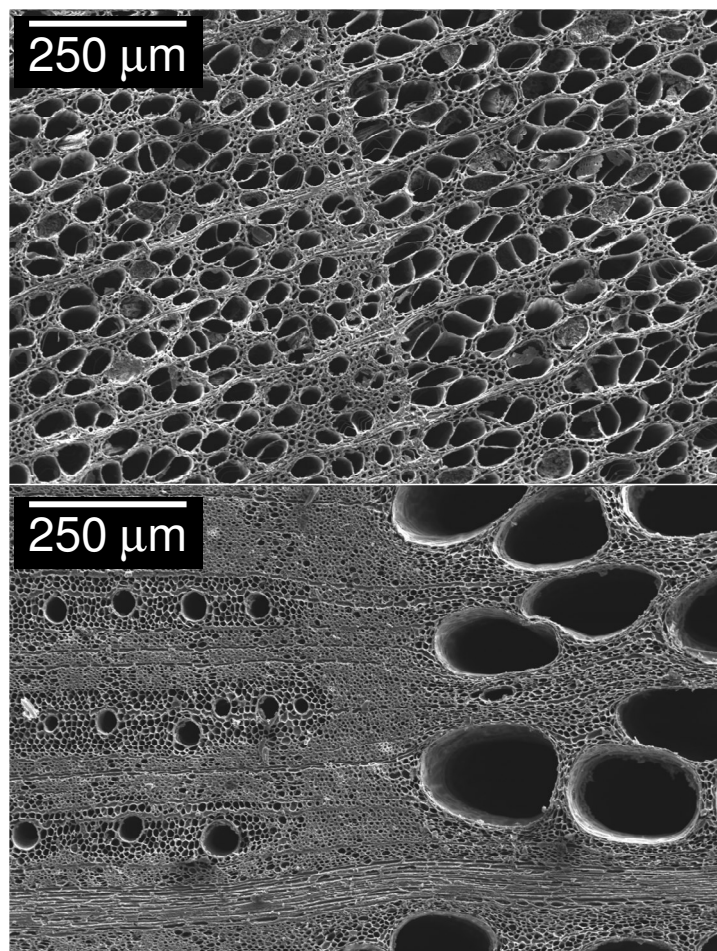


**Figure 2.17.** Scanning electron micrographs of the axial plane of a) diffuse porous (poplar) and b) ring porous (red oak) pyrolyzed hardwoods.

### 2.3. Biomorphic Silicon Carbide

BioSiC is a novel porous silicon carbide material derived directly from wood precursors. As a result, the structure of this material is distinct from those of materials processed by the conventional methods outlined previously. This section will outline the processing procedure used to fabricate bioSiC and how it differs from other methods of forming porous SiC. Previous work on this unique material and other similar materials will also be reviewed. The structure and properties of bioSiC will be the focus of subsequent chapters of this document.

#### 2.3.1. Processing of BioSiC

The unique process used to make bioSiC from natural wood precursors was first introduced by Ota et al. (1995). However, the initial in-depth development of this process and evaluation of the mechanical properties of this material can be credited to Greil et al. (1998a; 1998b). The processing of bioSiC begins with the pyrolysis of the natural wood precursor. These precursors have been dried in ambient air for several weeks to reduce the amount of water that must be desorbed during pyrolysis. The wood is heated in argon (to prevent oxidation) at temperatures between 400 and 800 °C. A relatively slow heating rate must be used to prevent cracking of the carbon structure due to thermal stresses and expansion caused by gas evolution. The result is an amorphous carbon scaffold that retains the porous microstructure of the wood precursor. Following pyrolysis, the carbon is machined to the desired form and placed in a boron nitride-coated crucible with silicon powder that is in stoichiometric excess by a factor of at least 1.5. The boron nitride coating prevents reaction between the alumina and silicon, and the excess silicon is to ensure that all pores are filled to aid complete conversion of the carbon scaffold to

silicon carbide. The materials are heated in vacuum above the melting temperature of Si (1410 °C). During this stage, the scaffold is infiltrated by molten silicon which reacts with the pyrolyzed carbon to form silicon carbide. The processing is then completed by soaking the material for one week in a stirred acid solution to remove the excess silicon. The end result is a porous silicon carbide material with a structure that is analogous to the structure of the wood precursor (Kaul et al. 2006). This processing procedure is essentially a replication method and is summarized in figure 2.18.

This replication process has many features that make it an attractive alternative to other methods of forming porous silicon carbide. Of course, the primary feature of this processing method is the retention of the naturally optimized porous microstructure of wood. Volume of porosity, pore size, and pore distribution in the final SiC material can all be controlled by the choice of precursor wood. This microstructure allows for reduction in weight, as well as open porosity for filtration or reinfiltration of a second phase. Additionally, complex parts can easily be formed by machining the pyrolyzed carbon prior to silicon infiltration and reaction. This is particularly attractive as machining of silicon carbide is difficult and expensive. A final feature of this process is the relatively low processing temperature. The maximum heat treatment temperature of 1550 °C is significantly lower than SiC sintering or hot-pressing techniques that require temperatures of 1800-2000 °C. The remainder of this section will serve to describe in further detail the three main stages of bioSiC processing.

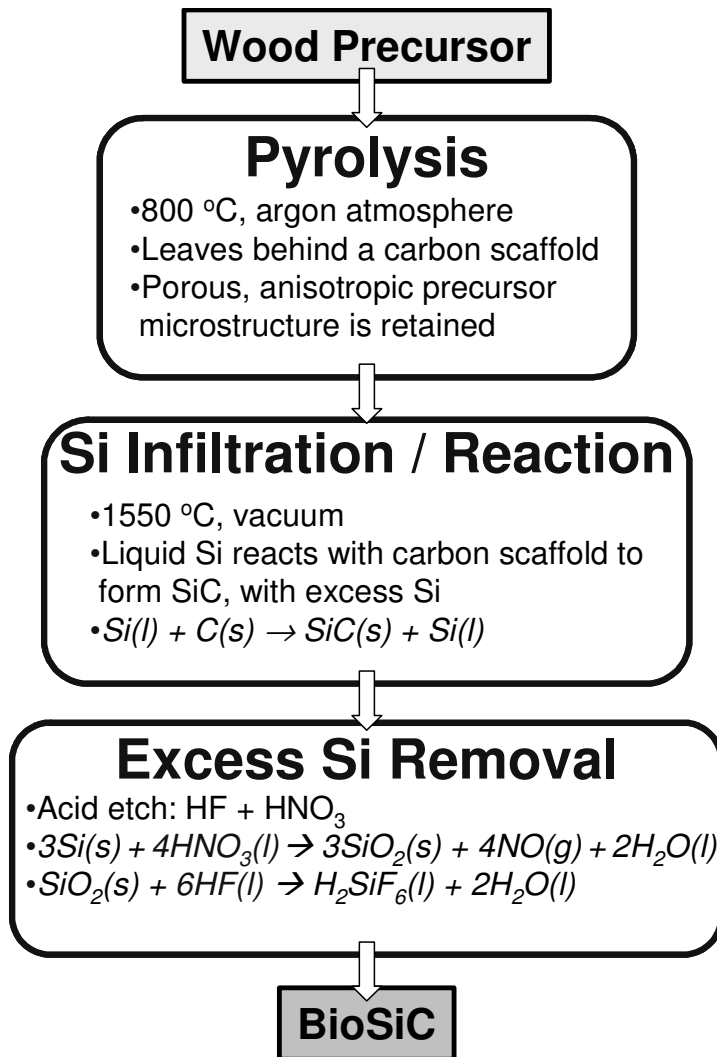


Figure 2.18. Flow chart giving the processing steps necessary to fabricate bioSiC.

### *Pyrolysis of Wood*

In order for wood to be used as a template for forming bioSiC, all the volatiles must be burned off and the organics in wood must be broken down to form a porous carbon scaffold. This is accomplished by pyrolysis of the wood precursor. The widely accepted group of mechanisms responsible for the breakdown of wood during pyrolysis was introduced by Tang and Bacon and involves four main stages (Tang and Bacon 1964).

1. desorption of adsorbed water between ambient temperature and 150 °C
2. splitting off of cellulose structure water between 150 – 240 °C
3. depolymerization, breaking of C-O and C-C bonds, and release of CO and CO<sub>2</sub> between 240 – 400 °C
4. formation of semi-crystalline layers above 400 °C

This process is also shown in figure 2.19. In terms of wood components, hemicellulose is the first to breakdown in stage 2 of the process. This is followed by the breakdown of cellulose and lignin in stage 3 (Byrne and Nagle 1997a).

The end result of pyrolysis is an amorphous carbon scaffold that retains the complex microstructure of the wood precursor, provided the heating rate is below 2 °C/minute. Heating rates higher than this can lead to microcracking resulting from residual stress build up and the rapid release of gaseous species (Byrne and Nagle 1997b; Greil et al. 1998a). Continued heat treatment above 2000 °C leads to some added crystallinity, but full graphitization is not possible as wood carbon is a non-graphitizable or hard carbon (Byrne and Nagle 1997b; Cheng et al. 1999). This is shown by X-ray diffraction patterns taken as a function of temperature in figure 2.20.

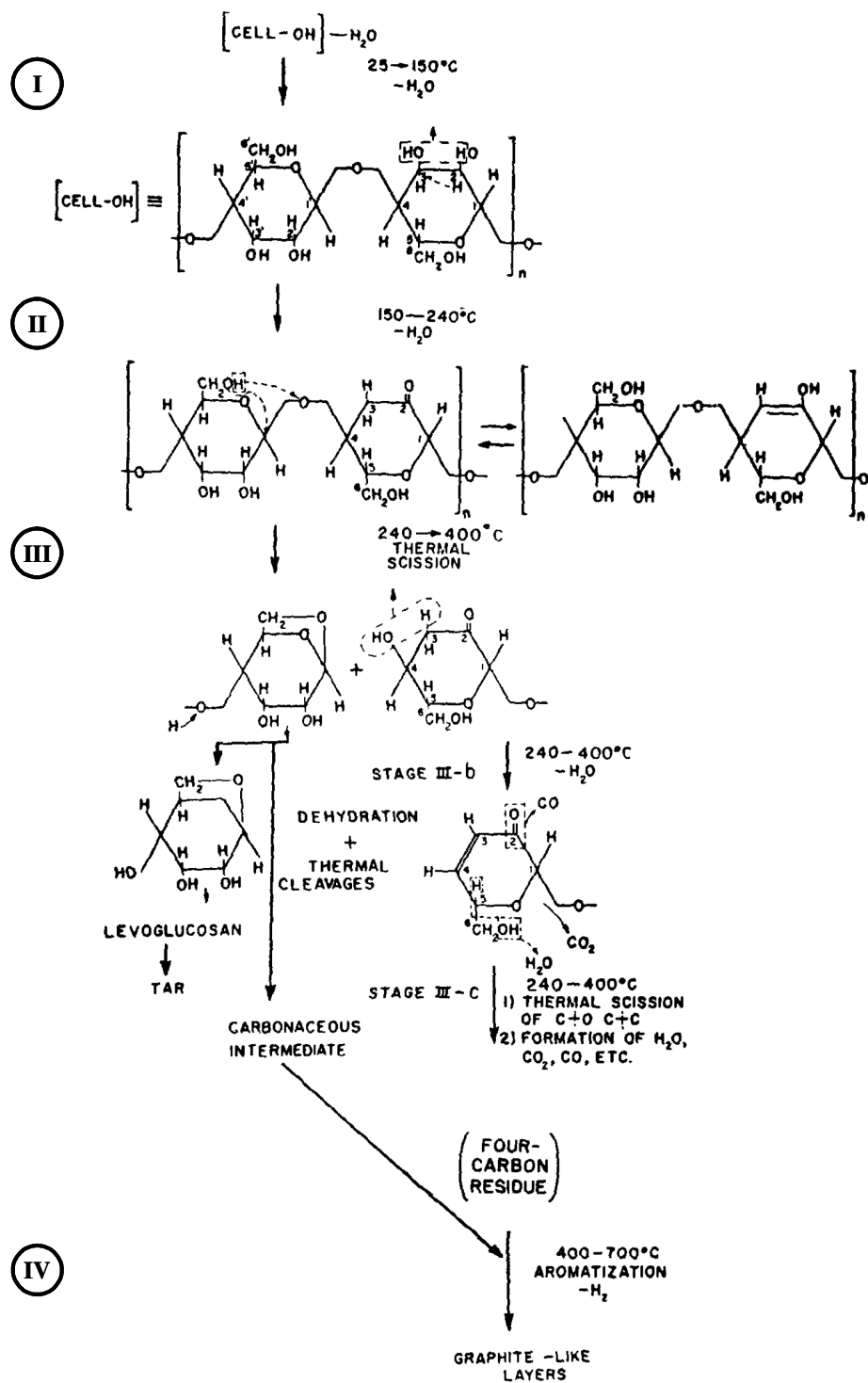


Figure 2.19. Diagrammatic representation of the 4-stage breakdown of wood during pyrolysis (Tang and Bacon 1964).

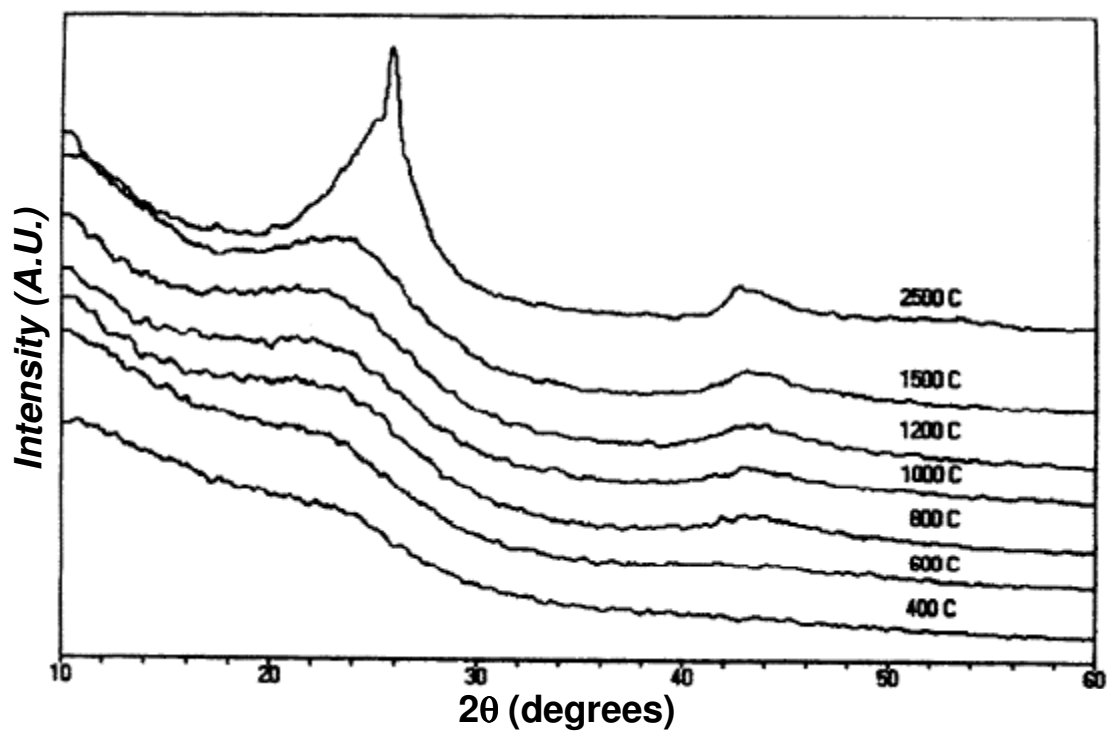


Figure 2.20. X-ray diffraction of poplar wood during pyrolysis showing only limited crystallinity because of the non-graphitizable nature of wood carbon (Byrne and Nagle 1997b).

The crystallinity in these patterns is the result of turbostratic carbon formation and not graphite formation (Paris et al. 2005). Further rearrangement of the crystal structure to form graphite is prevented because of rigid cross-links that form below 1000 °C (Franklin 1951).

In addition to chemical changes, physical changes also take place during pyrolysis. As a result of the elimination of water and breakdown of organics, there is an 18% reduction in bulk density (Greil 2001). Approximately 80% of the weight loss during pyrolysis occurs between 200 – 400 °C where the decomposition of organics occurs as shown by the thermogravimetric analysis plot shown in figure 2.21 (Byrne and Nagle 1997a). The change in specific density, and therefore, porosity tends to be dependent on the specific samples as different woods have varying amounts of organic phases. Anisotropic dimensional changes also occur during pyrolysis. In the axial direction, shrinkage of between 15-22% occurs while shrinkage of between 22-40% occurs in the radial and tangential directions. This anisotropy is due to the alignment of cellulose fibrils in the wood, which will be described in the next section. However, as the heat treatment continues above 300 °C, this alignment is reduced with the breakdown of cellulose fibrils and less than 10 % of this order is retained after pyrolysis (Greil 2001).

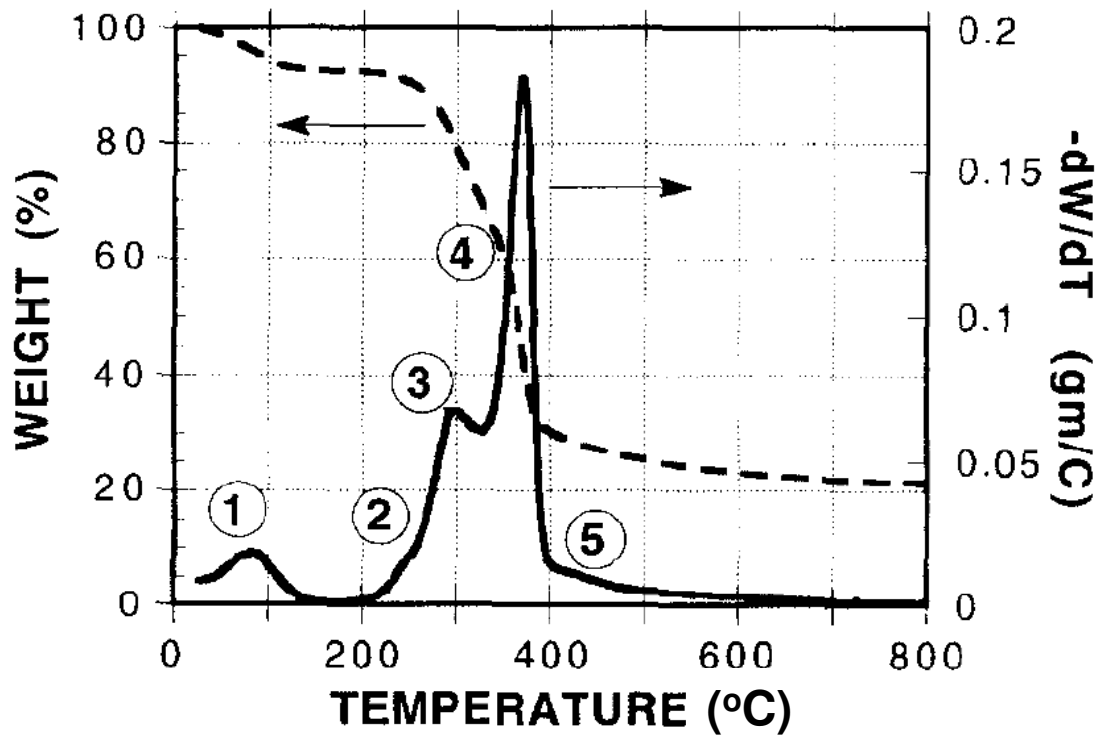


Figure 2.21. Thermogravimetric analysis of red oak wood showing weight changes corresponding to 1) loss of absorbed water, 2) hemicellulose decomposition, 3) initial cellulose and lignin decomposition, 4) rapid cellulose and lignin decomposition, and 5) continued lignin decomposition (Byrne and Nagle 1997a).

### *Silicon Infiltration and Reaction*

The reaction between the carbon scaffold and silicon is complex and occurs via several mechanisms through several stages. This reaction actually begins in the vapor phase and progresses via heterogeneous nucleation, dissolution and precipitation, and diffusion. The end result is solid silicon carbide with a distinctly bimodal morphology. The reaction can be divided into three stages.

1. In vacuum at approximately 1350 °C (below the melting temperature of Si), vapor forms and reacts with the solid carbon scaffold. Grains of SiC, 10-80 nm (nano-SiC), heterogeneously nucleate to form a thin layer on the inside of the pore walls (Zollfrank and Sieber 2005).
2. Upon melting at 1410 °C, molten silicon spontaneously wets and fills the pores of the scaffold (Chiang et al. 1991; Hase et al. 1976; Pampuch et al. 1986; Whalen and Anderson 1975). Li et al. have investigated the reactive wetting of carbon by molten silicon and found that three distinct factors are responsible for reducing contact angle and wetting: dissolution of carbon in silicon, formation of a SiC reaction layer, and the release of free energy as a result of the localized reaction (Li and Hausner 1991; Li and Hausner 1996). Once the molten Si infiltrates the scaffold, Si diffuses through the initial nano-SiC reaction layer and more nano-SiC is nucleated. Depending on the density of the carbon, a volume expansion of approximately 60% occurs upon conversion of the scaffold to SiC (Sangsuwan et al. 2001; Wang et al. 2004), and the reaction is exothermic and can lead to localized temperatures that are hundreds of degrees higher than the

ambient temperature (Chiang et al. 1991; Schulte-Fischedick et al. 2002). These lead to stresses that crack and spall the reaction layer (Hase et al. 1976).

3. As a result of the cracking of the reaction layer, the C scaffold is still exposed to molten Si. In addition to reaction by diffusion, C is dissolved in Si and micro-SiC grains (1-3  $\mu\text{m}$ ) precipitate in cooler areas of the melt (Zollfrank and Sieber 2004). The reaction oscillates between dissolution and precipitation as the dissolution of C in Si is endothermic (heat of solution = 247 kJ/mole (Scace and Slack 1959)) and the precipitation of SiC is exothermic (heat of crystallization = -362 kJ/mole (Pampuch et al. 1986)) (Zollfrank and Sieber 2005).

This reaction continues to progress while the Si is held above the melting temperature. The final microstructure consists of nano and micro-SiC, excess Si, and unreacted C. The unreacted C is a result of choking of the channels due to SiC volume expansion and thick (>5  $\mu\text{m}$ ) pore struts that did not fully react (Zollfrank and Sieber 2005). A transmission electron micrograph of this microstructure is shown in figure 2.22.

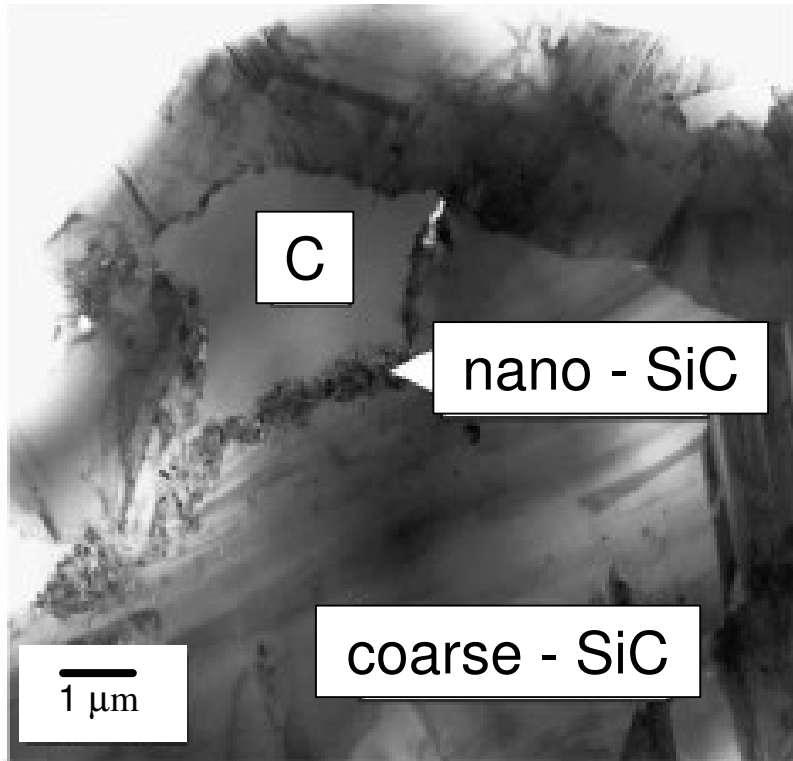
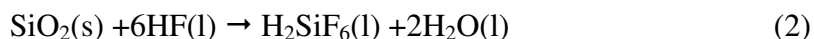


**Figure 2.22. Transmission electron micrograph of nano-grain, coarse-grain SiC, and residual C in bioSiC derived from beech wood (Zollfrank and Sieber 2004).**

### *Removal of Excess Silicon*

Following molten silicon infiltration and conversion of the carbon scaffold to SiC, excess Si still fills pores that are <30  $\mu\text{m}$  in diameter (Greil et al. 1998a). This excess Si must be removed to expose the porous microstructure of bioSiC. This allows for utilization of the naturally optimized porous microstructure and raises the upper temperature limit of the material as Si melts at a temperature well below SiC.

The excess Si is removed by isotropic etching using a 1:1 combination of 49% hydrofluoric (HF) and 69% nitric acid ( $\text{HNO}_3$ ) that is commonly used in the semiconductor industry. This etching takes place in the two stage reaction given by (Robbins and Schwartz 1959)



Here, a cyclical reaction takes place with the  $\text{HNO}_3$  oxidizing the exposed Si followed by the reaction of HF and  $\text{SiO}_2$ . The end result is a porous SiC material that is free of residual Si and has a microstructure that is analogous to the wood precursor.

This material lends itself to a number of applications that utilize the properties of its naturally optimized porous microstructure and those of SiC. Potential applications for bioSiC are: high temperature molten metal filters, composite reinforcements, catalyst carriers, heat exchangers, bioimplants, and lightweight structural materials. These materials have already

found some use as fire resistant joining pins in wooden structures (Arellano-Lopez and Martinez-Fernandez 2004).

### 2.3.2. State of Research on Biomorphic Materials

Since the initial development of this material in the late 1990's, many researchers have analyzed various properties of this material and looked at alternative processing methods. The majority of this work has focused on bioSi/SiC. This material is processed by the same method described previously, but the excess Si is not removed and still fills many of the pores. While this material tends to have better room temperature mechanical properties than bioSiC, much of the natural porous microstructure is filled with Si that limits its use in many of the applications listed above.

The majority of the work with bioSi/SiC has focused on processing of different woods (Esposito et al. 2004; Greil et al. 1998a; Qian et al. 2003; Sieber; Singh and Yee 2004) and measurement of elastic modulus and strength as a function of porosity (Greil et al. 1998b; Martinez-Fernandez et al. 2000; Munoz et al. 2002; Presas et al. 2005; Singh and Salem 2002; Varela-Feria et al. 2002). These researchers have found that elastic modulus and strength of bioSiC both decrease with increasing porosity and that mechanical properties are much higher in the axial direction than the transverse direction. Other work on this material include contributions by Arellano-Lopez and Martinez-Fernandez who found that bioSiC has excellent erosion properties and low strength degradation (Arellano-Lopez et al. 2004), Gonzalez et al. and Carlos et al. who found bioSiC to be biocompatible and conducive to tissue in growth when coated with a bioactive glass for biomedical applications (Carlos et al. 2005; Gonzalez et al.

2004; Gonzalez et al. 2003), Pappacena et al. who found bioSiC to have excellent thermomechanical properties and anisotropic thermal conductivity (Pappacena et al. 2006). Additionally Zollfrank et al., Di et al., and Wilkes et al. produced high strength composites by reinfiltration of this material with a metal phase (Di et al. 2003; Wilkes et al. 2006; Zollfrank et al. 2005).

Alternative processing methods have also been developed to form bioSiC from wood and other cellulose based templates. Si based gas and sol-gel have also been used to form bioSiC. Vogli et al. used Si-vapor and SiO to fabricate bioSiC (Vogli et al. 2001; Vogli et al. 2002). While no residual Si is present, gas phase processing requires longer times and often uses toxic gases. Qian et al. and Vyshnyakova et al. have infiltrated wood with silica sol-gel to produce bioSiC in a process that combines the pyrolysis and reaction steps (Qian et al. 2004a; Qian et al. 2004b; Vyshnyakova et al. 2006). Although it has fewer processing steps, the SiC yield of this method is far lower than that for the molten Si infiltration process. Additionally, biomorphic titania (Ota et al. 2000), alumina (Rambo and Sieber 2005), nickel oxide (Liu et al. 2005), and YSZ (Rambo et al. 2004) have all been formed using wood templates and sol-gel infiltration. Alternative cellulose based templates have also been used with similar processes. For example, Fey et al. fabricated porous SiC from cellulose paper (Fey et al. 2006) and Herzog et al. used a similar process to manufacture SiC from wood-based fiberboard (Herzog et al. 2006).

## 2.4. Summary

Porous ceramics are a class of materials that are increasingly utilized in applications that take advantage of their porous morphologies and the properties inherent to ceramics. One specific example is bioSiC, a material that possesses the properties of SiC as well as a porous microstructure that has been optimized by nature for structural applications. This chapter served to introduce porous ceramics and various processing techniques for their fabrication. Particular attention was focused on the processing of bioSiC and the reactions that take place during this process, as well as the structure of wood which is replicated in bioSiC. This provides the background information necessary for understanding subsequent chapters in this document.

# 3

## Characterization of Microstructure and Phase Composition in Biomorphic Silicon Carbide

In order to establish structure-property relationships in biomorphic silicon carbide (bioSiC), it is necessary to characterize the microstructure and phase composition of the material and how it evolves through processing. A variety of wood precursors was used resulting in bioSiC with differing microstructures, as the structure of the final material is analogous to that of the precursor. Additionally, a synthetic, porous SiC-honeycomb was also analyzed as a control material. Several analytical techniques were utilized for characterization including optical microscopy (OM), scanning electron microscopy (SEM), X-ray diffraction (XRD), energy dispersive spectroscopy (EDS), image analysis, and helium pycnometry. This chapter presents qualitative and quantitative results and conclusions drawn from this characterization.

### **3.1. Evolution of Structure and Phase Composition During Processing**

During the conversion of wood precursors to bioSiC, the naturally optimized organic composite that forms the solid phase of wood is replaced by an inorganic ceramic. While aspects of the final porous ceramic material differ from the precursor, the overall anisotropic porous structure of the original wood is retained. This section will describe the microstructure and phase composition of bioSiC as well as the changes that occur in each step of processing. Characterization will be exemplified using SEM (Hitachi S-3500N VP) and XRD (XDS 2000,

Scintag Inc.) analysis of a single hardwood precursor. The overall evolution of this material is common to all precursors processed.

### 3.1.1. Evolution of Microstructure

The processing of bioSiC begins with a natural wood precursor, which has a honeycomb-type microstructure with anisotropic tubular porosity. This microstructure was described in detail in the previous chapter. All woods have certain common features but each species has unique properties such as pore size distribution and volume of porosity. This section describes features that are altered and those that are retained through each step of processing.

#### *Pyrolyzed Carbon Scaffold*

The natural wood precursor is pyrolyzed in an argon atmosphere. The precursor is heated to 800 °C at 0.5 °C/minute to breakdown the solid organic phase of the wood while still maintaining the porous microstructure inherent in wood. The processes and mechanisms by which this breakdown takes place were outlined in the previous chapter. Due to the elimination of organics and volatiles, there is an increase in porosity upon conversion of the precursor to pyrolyzed carbon. This change is dependent on the composition of the precursor and varies with each type of wood. The result of this pyrolysis is a carbon scaffold that retains the porous microstructure of its wood precursor, as shown in figure 3.1. In this figure, many of the pores/cells common to hardwoods are still visible. These include vessels, fibers, and parenchymas which appear within rays.

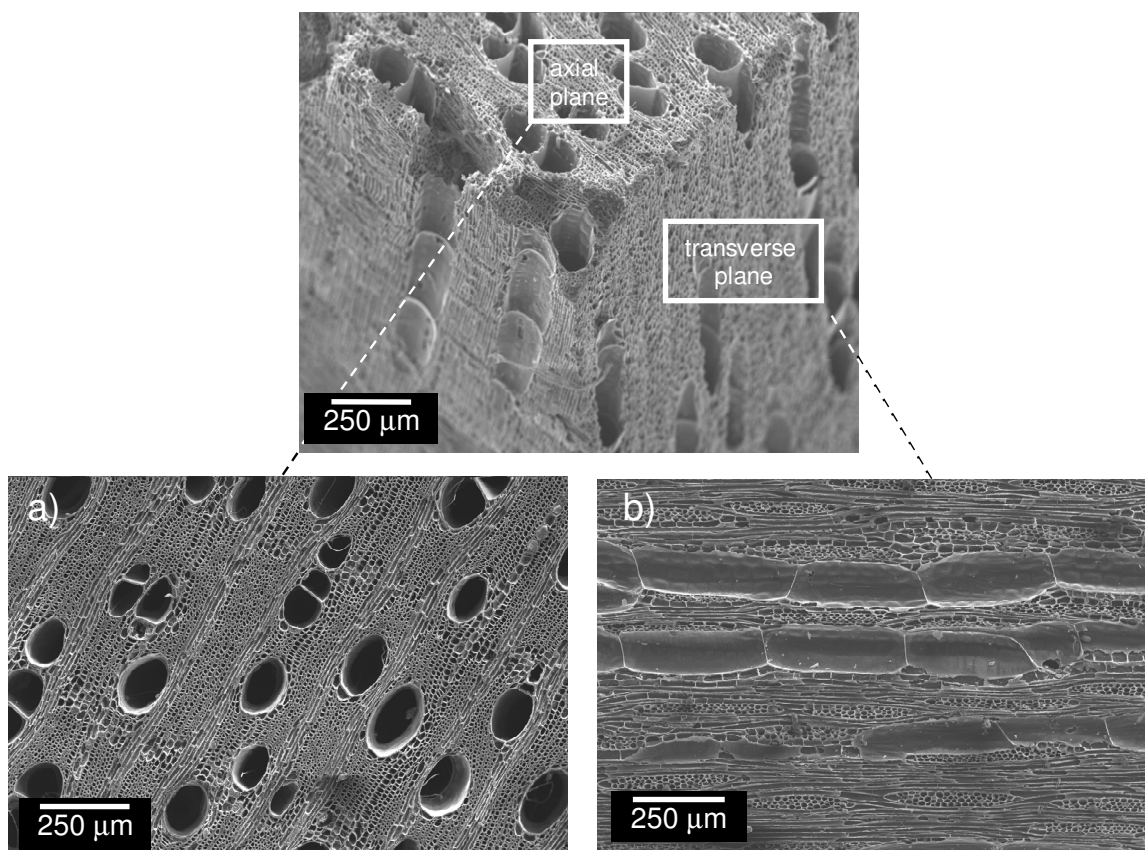


**Figure 3.1. Scanning electron micrographs of the a) axial plane and b) a transverse plane of a typical carbon scaffold resulting from the pyrolysis of a hardwood precursor.**

While these pores do not maintain the same functions as in a living tree, they do affect the properties of the final bioSiC material. This will be illustrated in the following sections.

### *Silicon Infiltrated BioSi/SiC*

Following pyrolysis, the carbon scaffold is converted to SiC via reaction with molten Si. To accomplish this, the carbon scaffold is heated in vacuum with semiconductor-grade Si powder to 1550 °C and held at temperature for 1 hour. The molten Si wets the carbon and the two species react by the mechanisms described in the previous chapter to form SiC. To ensure complete reaction of the carbon scaffold, Si in stoichiometric excess by a factor of at least 1.5 is used. As a consequence, excess Si remains after the reaction stage is complete.

The resulting microstructure is shown in figure 3.2 where it is evident that only large pores (>30  $\mu\text{m}$ ) are free of excess Si and the smaller pores remain filled. These large pores correspond to the vessels of the wood precursor. Due to variation across different types of woods, the amount of free porosity and Si filled porosity is not simply a function of precursor pore volume but also the pore sizes inherent to a specific species. Many of the smaller unfilled pores that are present in figure 3.2 are the result of incomplete infiltration and reaction. This will be discussed in later sections.

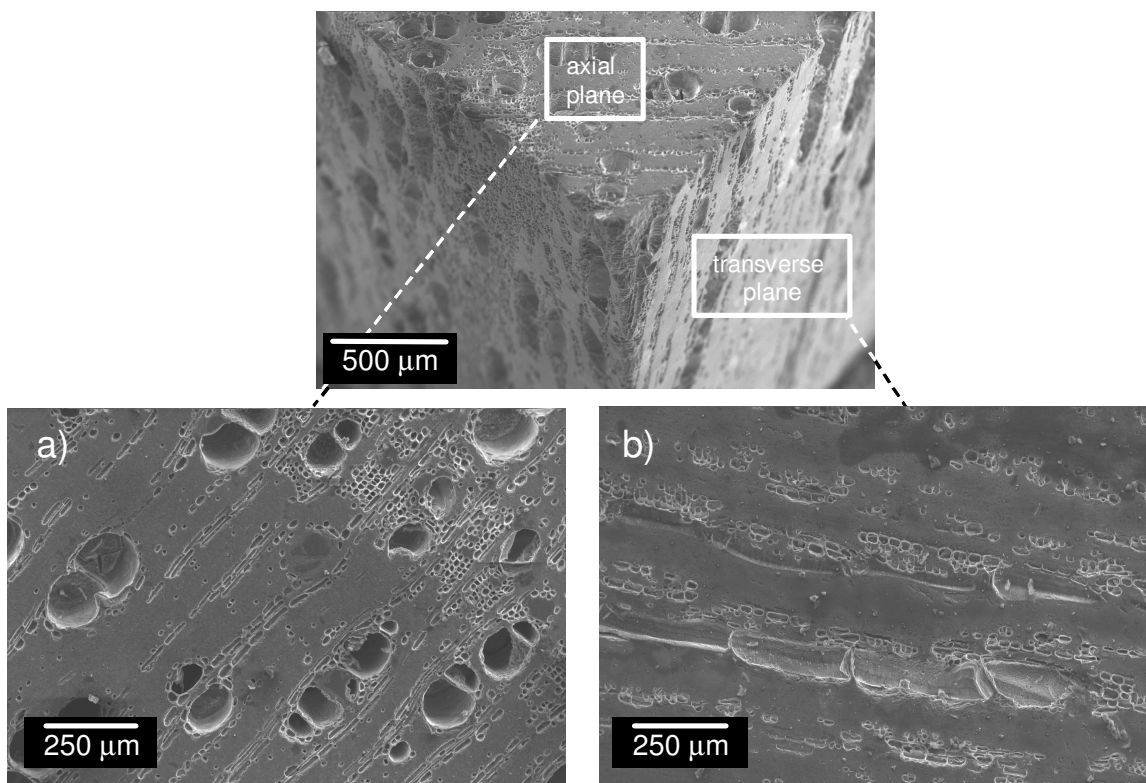


**Figure 3.2.** Scanning electron micrographs of the a) axial plane and b) a transverse plane of bioSi/SiC resulting from the molten Si infiltration of a pyrolyzed carbon scaffold.

### *Biomorphic SiC*

Once the carbon scaffold has been converted to SiC, the excess Si must be removed to fully expose the porous structure. This is accomplished by the two-step reaction between Si and the hydrofluoric and nitric acid solution described in chapter 2. The result is a porous SiC material with a microstructure that mimics that of the wood precursor, as shown in figure 3.3.

In this figure, vessels are still present but many of the smaller fibers and tracheids are not due to the volume expansion that occurs upon conversion of carbon to SiC. Closer inspection of bioSiC (figure 3.4) shows the polycrystalline nature of the SiC produced by the dissolution/precipitation reaction. As shown in this figure, grains of approximately 2-5  $\mu\text{m}$  form by this reaction.

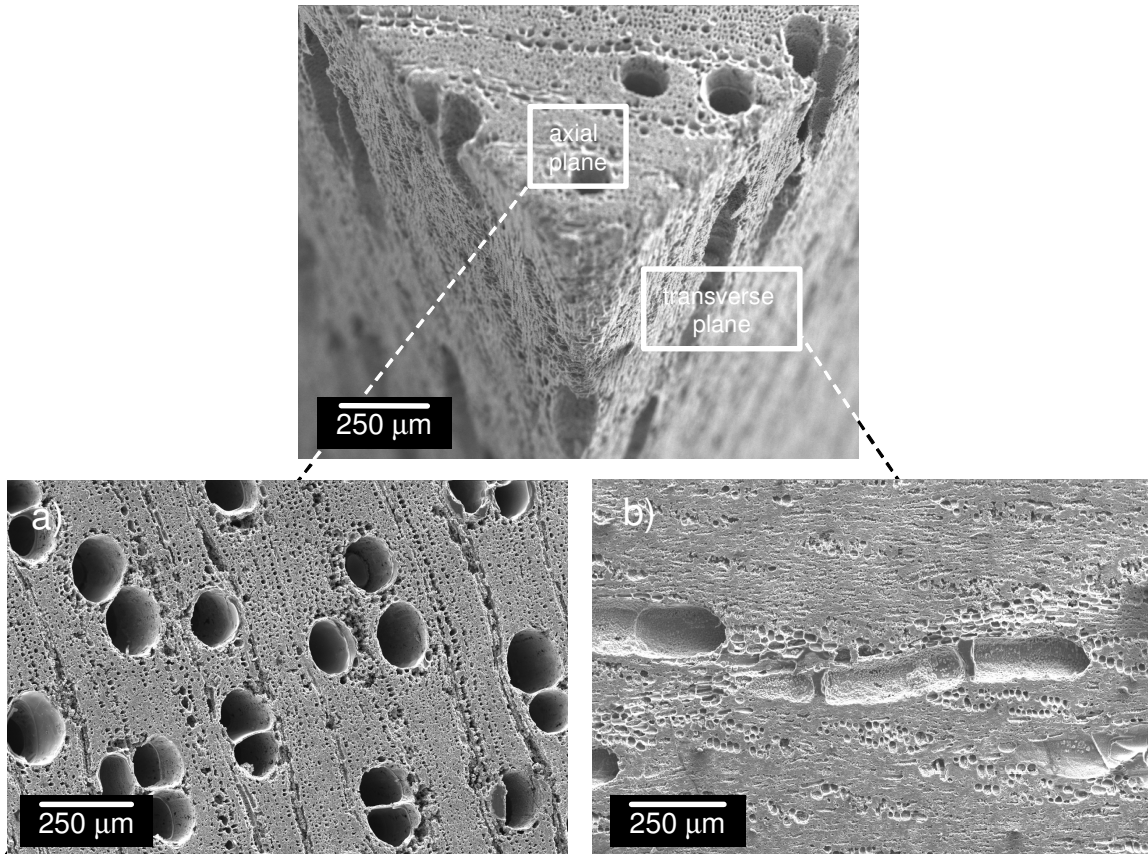


**Figure 3.3. Scanning electron micrographs of the a) axial plane and b) a transverse plane of bioSiC following the removal of residual Si by acid etching.**

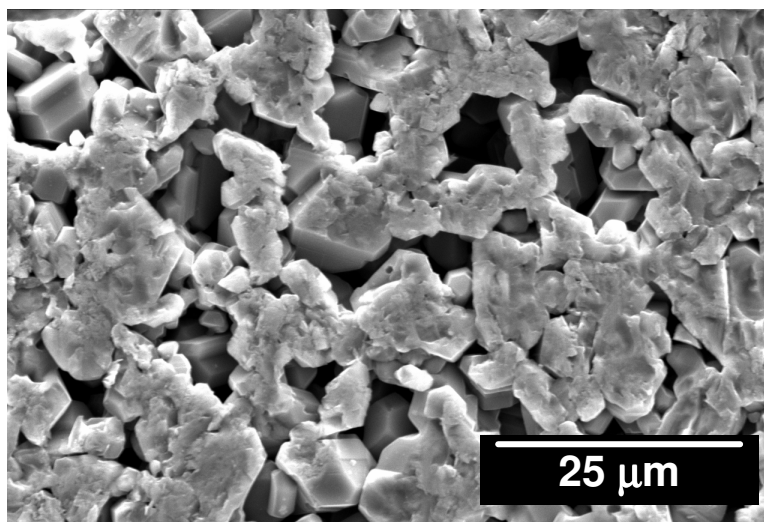


**Figure 3.4. Porous and polycrystalline bioSiC resulting from the dissolution/precipitation dominated reaction between molten Si and the amorphous carbon scaffold.**

### 3.1.2. Evolution of Phase Composition

Along with changes in microstructure, changes in the phase composition of the material also occur during processing. While the porous microstructure of the wood is retained through the process, the chemistry changes from a combustible natural material to an inorganic refractory material. These changes can be followed using X-ray diffraction. Diffraction patterns from each stage of processing were obtained from bulk samples and are shown in figure 3.5.

It is apparent from the carbon XRD pattern in figure 3.5 that the material resulting from the pyrolysis of wood is amorphous in nature. This is consistent with the work of other researchers (Byrne and Nagle 1997; Cheng et al. 1999) and is expected as a pyrolysis temperature of at least 2500 °C is necessary to induce crystallinity (Byrne and Nagle 1997), which is far above the temperature of 800 °C used in this work. In addition, wood carbon is non-graphitizable even at 3000 °C (Cheng et al. 1999). Upon infiltration and reaction of the amorphous carbon scaffold, a Si-SiC composite is formed as evidenced by the Si/SiC XRD pattern in figure 3.5. Following acid etching of this composite material, no significant amount of Si is detectable as shown by the bioSiC XRD pattern in figure 3.5, and only crystalline  $\beta$ -SiC is present. This is the low-temperature phase of SiC and has a zinc blend crystal structure while the most common high-temperature phase,  $\alpha$ -SiC, has a wurtzite crystal structure (Kingery et al. 1976). The high-temperature phase forms above 2000 °C and, although local temperatures can be several hundred degrees higher than ambient due to the exothermic nature of the Si-C reaction, no significant amount of  $\alpha$ -SiC was detected.

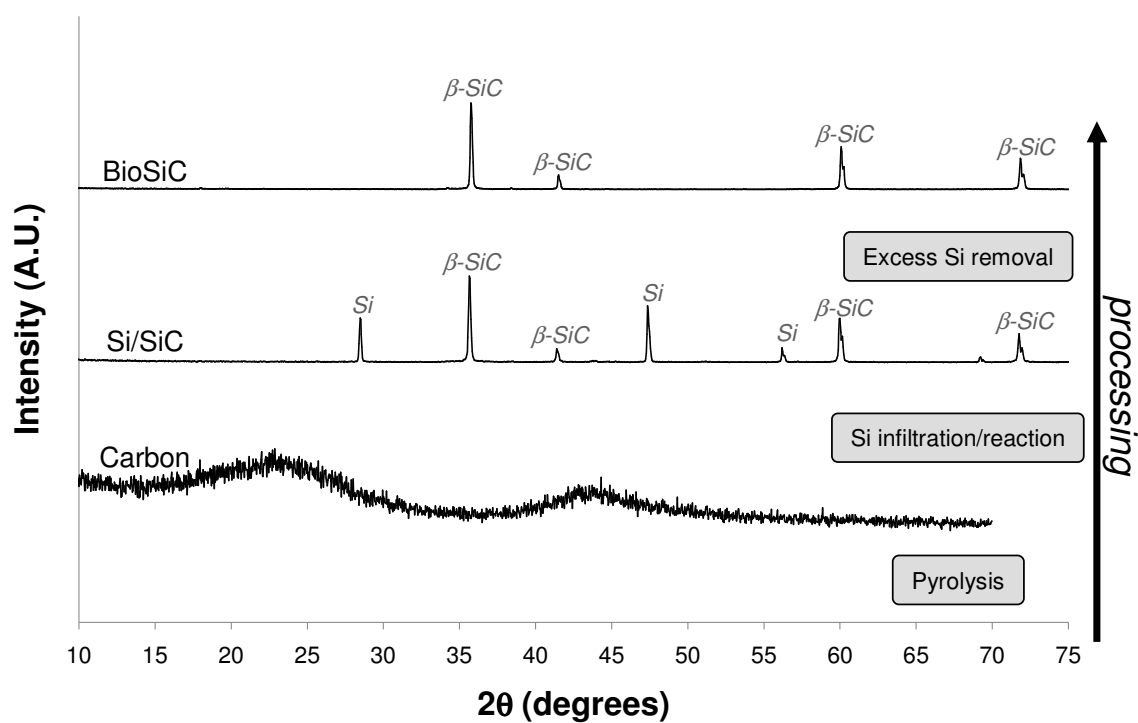


Figure 3.5. XRD patterns showing the evolution of composition from amorphous carbon to  $\beta$ -SiC.

For bioSiC, bulk and powdered samples were analyzed to detect possible texture that may result from any alignment of carbon due to crystalline cellulose sheets present in the precursor.

However, there was no significant difference in the XRD patterns of bulk and powdered samples indicating that no texture is present. This is due to the dissolution/precipitation reaction by which the majority of the SiC is formed. As a result, any carbon alignment remaining after pyrolysis is lost.

### **3.2. Porous SiC from Several Precursors**

In order to gauge the effects of porosity and microstructure on the mechanical properties of bioSiC, several different hardwoods were used as precursors. These woods not only cover a range of porosities, but also a range of pore sizes and pore size distributions. Additionally, these woods are readily available at local retailers. Softwoods were not used because of the narrow range of pore sizes and porosities of commercially available woods. In this section, the hardwood precursors and the bioSiC derived from each will be described.

#### **3.2.1. Wood Precursors**

A total of five hardwoods were used as precursors in this work. These covered a range of densities as shown in table 3.1. Both imported and domestic woods that are utilized in a wide variety of applications were processed.

**Table 3.1. Densities of five hardwood precursors (density calculated by dimensional measurement).**

<b>Wood</b>	<b>Bulk Density (g/cm<sup>3</sup>)</b>
Beech ( <i>Fagus sylvatica</i> )	0.640
Mahogany ( <i>Swietenia macrophylla</i> )	0.723
Poplar ( <i>Liriodendron tulipifera</i> )	0.480
Red Oak ( <i>Quercus rubra</i> )	0.679
Sapele ( <i>Entandrophragma cylindricum</i> )	0.550

*Beech (Fagus sylvatica)*

Beech is a diffuse porous hardwood that is native to North America. The source of most commercial beech timber is the eastern third of the United States and Canada. It is generally described as a heavy and strong wood with excellent shock resistance. Beech is generally used in flooring, furniture, veneer, containers, and railway ties (Forest Products Laboratory 1990).

*Mahogany (Swietenia macrophylla)*

Mahogany is a diffuse porous hardwood that is native to Central and South America, and plantations can be found from southern Mexico to Bolivia. In the 1600's mahogany was the primary wood used in Europe for ship building and fine furniture. Today, it is still used for boats and furniture as well as musical instruments and paneling (Forest Products Laboratory 1990).

*Poplar (Liriodendron tulipifera)*

Poplar is a light diffuse porous hardwood that is used for furniture, interior finishing, musical instruments, and plywood. It is generally described as a uniform and straight grained material. Most commercial poplar is grown domestically in the eastern half of the U.S. from New York to Florida and as far west as Missouri (Forest Products Laboratory 1990).

*Red Oak (Quercus rubra)*

Red oak is a domestically grown ring porous hardwood that is native to the southeast. It is generally described as a heavy wood and is used in railroad ties, mine timbers, fence posts, flooring, furniture, and boats (Forest Products Laboratory 1990).

*Sapele (Entandrophragma cylindricum)*

Sapele is a diffuse porous hardwood that is native to Central African rainforests. It is grown from Sierra Leone to Angola and eastward through Congo and Uganda. The primary uses for sapele include plywood veneer, furniture, and flooring (Forest Products Laboratory 1990).

In addition to these woods, other precursors of higher and lower porosities were processed. However, bioSiC processed from higher porosity woods was found to be very fragile and difficult to handle and Si infiltration was found to be very difficult in materials processed from lower porosity precursors. For these reasons, only the five precursors described above were included in this thesis.

### 3.2.2. Carbon and BioSiC Structures

Each of these precursors was processed using the previously outlined procedure to form five distinct types of bioSiC, and each type will be referred to by its wood precursor. The microstructures of the pyrolyzed carbon and the bioSiC resulting from the processing of each precursor are shown in figures 3.6 and 3.7. These images show many features that are retained from the precursor with some alteration due to the conversion reaction.

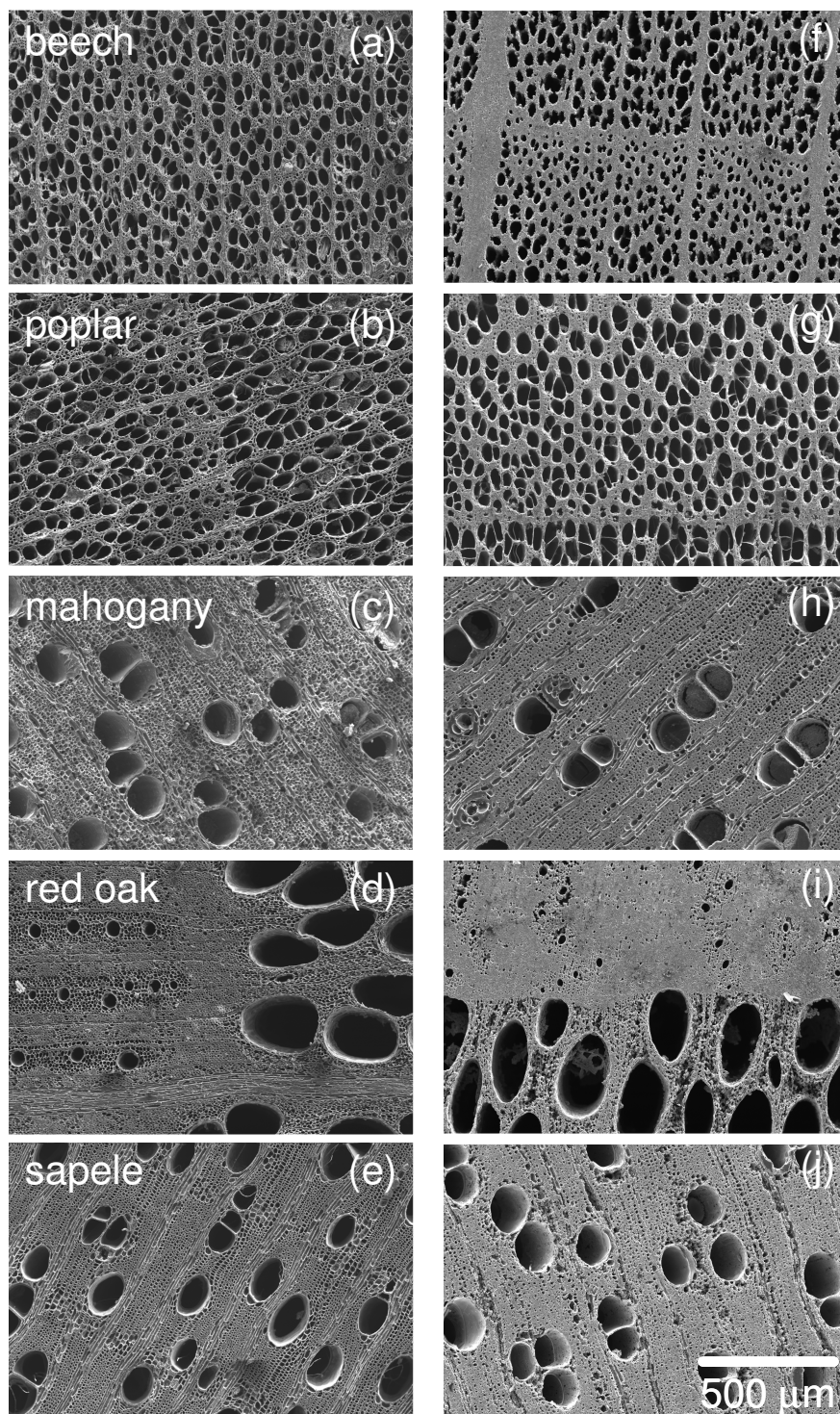
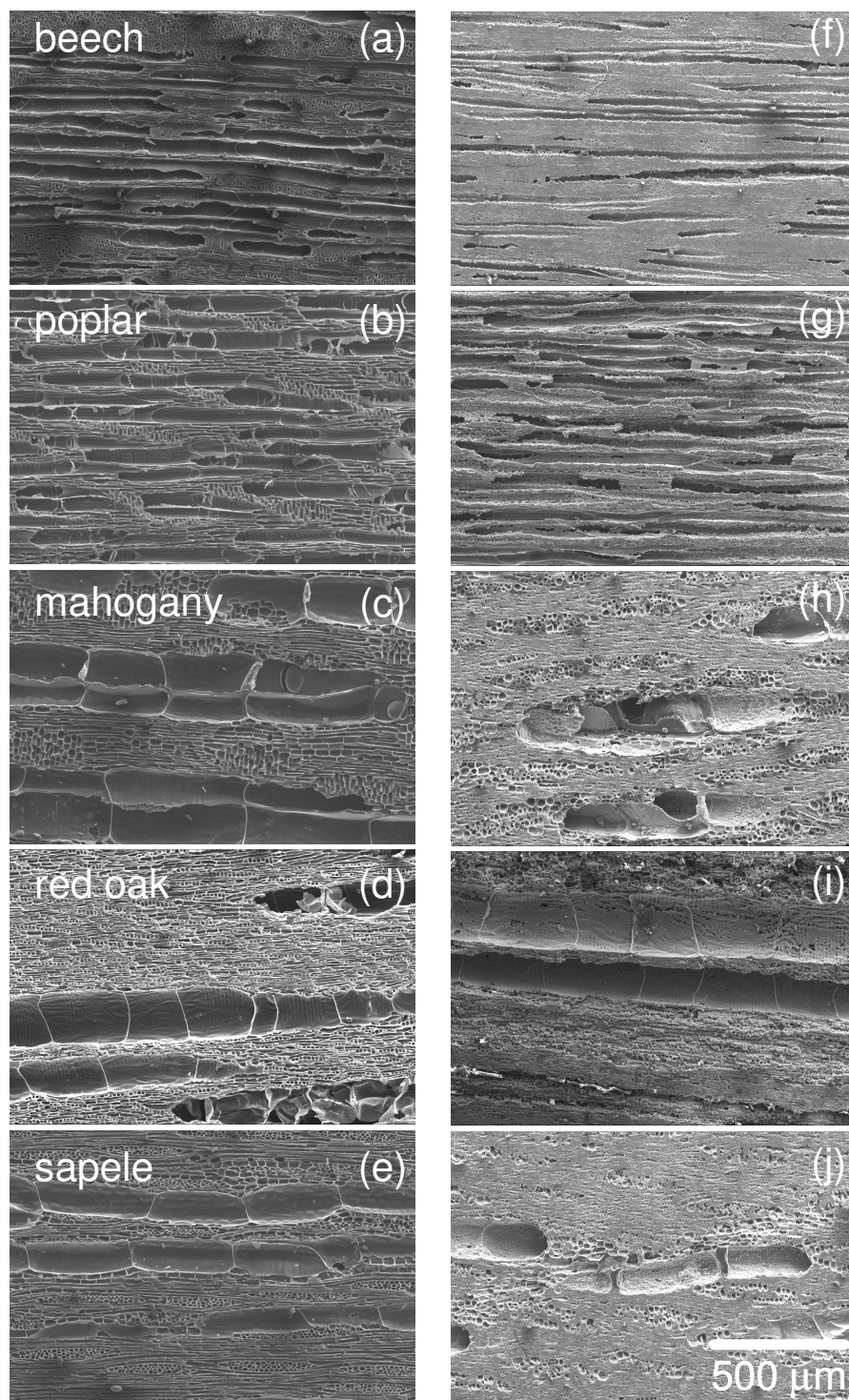


**Figure 3.6.** SEM micrographs of the axial planes of (a-e) pyrolyzed carbon and (f-j) bioSiC from five different hardwood precursors (Kaul et al. 2006).



**3.7. SEM micrographs of the transverse planes of (a-e) pyrolyzed carbon and (f-j) bioSiC from five different hardwood precursors.**

### *Retained Wood Features*

The most obvious change that occurs for each bioSiC upon conversion of the carbon scaffold to SiC is the closure of small pores due to volume expansion. The exterior volume of the samples remains unchanged after conversion indicating that all volume expansion is accommodated by the porosity and decreases the diameter of pores. This volume expansion will be discussed in further detail later.

In addition to large pores corresponding to vessels and small pores corresponding to fibers and tracheids, other features from the wood precursor are also present on the axial plane. Rays formed by horizontally aligned parenchyma cells are also present. The width of these rays however, varies from wood to wood depending on the number of parenchyma cells. For example, red oak rays can be as wide as 100  $\mu\text{m}$  while the rays of the other woods are generally about 30  $\mu\text{m}$  in width. Early and late wood regions are also apparent in some of the micrographs. These features manifest themselves as density gradients in bioSiC, and the role which they play in crack propagation in bioSiC will be illustrated later. Also clearly evident is the ring porous nature of red oak bioSiC. While early and late wood can be distinguished in the other woods, the segregation of pores in red oak is extreme. As a result of this segregation, there are alternating bands of low-porosity regions with small pores and high-porosity regions with large pores. In the transverse images shown in figure 3.7, the tubular nature of wood porosity can be seen. One important factor to note is the curvature of many of the vessel channels. This is mostly due to the non-linear fashion in which a tree may grow and partially due to warping of the material during conversion of wood to carbon.

### *Pore Uniformity*

In addition to the wood features retained in bioSiC, it is important to note the level of uniformity of the pore distribution in each bioSiC. By qualitative observation of the axial (figure 3.6) and transverse (figure 3.7) planes, a distinction can be made between beech and poplar bioSiC and mahogany, red oak, and sapele bioSiC. In the case of beech and poplar bioSiC, the porosity tends to be spatially more uniform and homogeneous than the others studied, as shown in figures 3.6(f, g). In woods, this is often described as even texture. For this reason, beech and poplar bioSiC will be categorized as uniformly distributed pore (UDP) bioSiC. In contrast, mahogany, red oak, and sapele bioSiC (figures 3.6(h-j)) have spatially non-uniform porosity and areas of high porosity and low porosity are present. These types of bioSiC will be referred to as non-uniformly distributed pore (NUDP) bioSiC. The effects of these features and those of other wood features on the properties of bioSiC will be described later.

### 3.2.3. Synthetic SiC Honeycomb

In addition to bioSiC, a porous SiC honeycomb material supplied by Corning Inc. was also analyzed. Corning manufactured this material as a potential catalyst support in diesel engine catalytic converters. This material is fabricated by a proprietary process in which a carbon-containing polymer precursor is reacted in-situ with Si in an inert atmosphere at 1800 °C (Warren 2004). In this process, carbon is in excess of Si and residual carbon is removed by heat treatment in air at 1000 °C. Because of its uniform microstructure and consistent properties, this material was used as a control and as a way to compare material from a natural precursor and material from a synthetic precursor. As shown in figure 3.8, this material consists of a grid of

continuous tubular pores with square cross-sections. An XRD pattern of the synthetic SiC honeycomb is shown in figure 3.9. From the pattern, it is clear that this material differs from bioSiC as the pattern shows both  $\beta$  and  $\alpha$ -SiC. The presence of the high temperature  $\alpha$  phase is most likely due to the higher temperatures used by Corning to process this material.

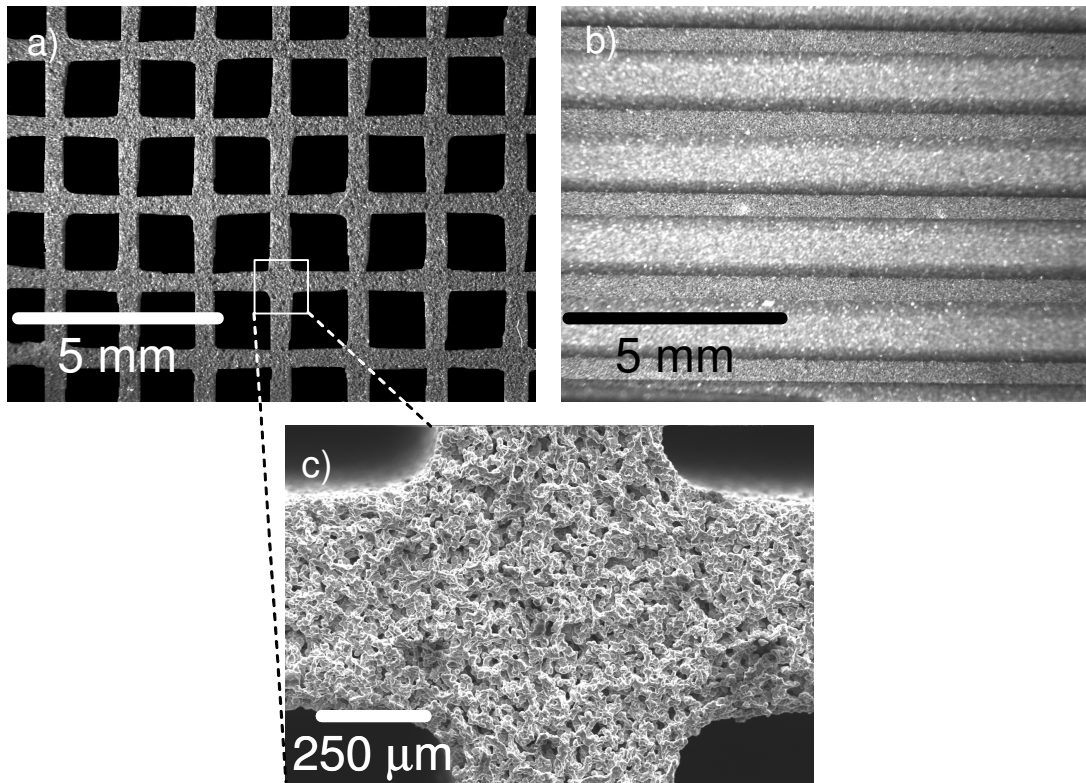


**Figure 3.8. Optical micrographs of the a) axial and b) transverse plane of synthetic SiC honeycomb along with a c) SEM micrograph showing closer detail.**

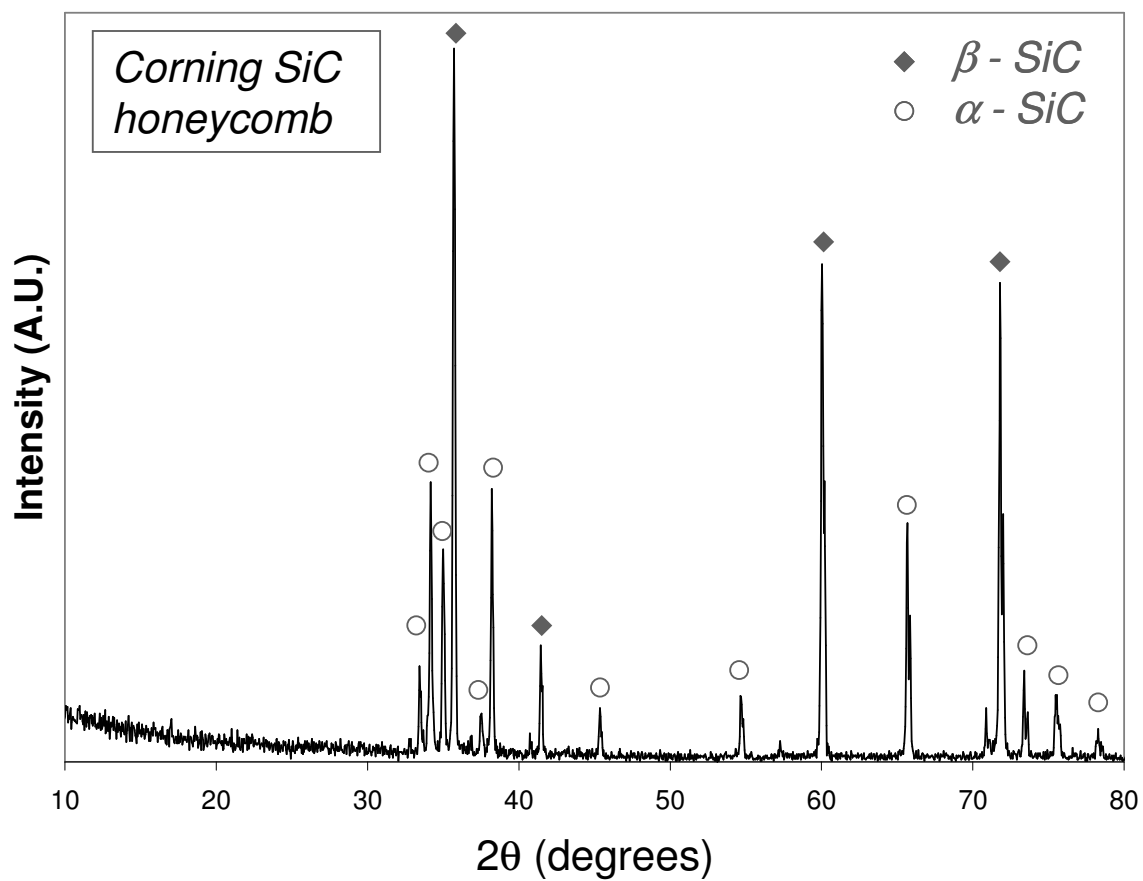


Figure 3.9. XRD pattern from synthetic SiC honeycomb showing the presence of  $\beta$  and  $\alpha$ -SiC.

### 3.3. Porosity and Solid Phase Analysis by Density Measurements

In addition to microscopy and X-ray diffraction, porosities as well as bulk and apparent densities of pyrolyzed carbon and bioSiC were also measured. This was done via Archimedes' method and helium pycnometry. These analyses allow for further characterization of the materials formed from each precursor and the changes that take place during processing.

Samples used were processed from 3 cm x 3 cm x 30 cm pieces of each wood precursor. Following pyrolysis, samples with dimensions of 1 cm x 2 cm x 6 cm were sectioned and infiltrated with molten Si to form bioSiC. These large pieces were then machined into 4 mm x 4 mm x 8 mm samples, followed by the removal of excess Si by acid etching. These dimensions were chosen because, in addition to density measurements, these samples were used for compression testing.

#### 3.3.1. Porosity and Apparent Density of Pyrolyzed Carbon and BioSiC

The Archimedes' method and He pycnometry were used to measure at least 9 samples of pyrolyzed carbon and bioSiC from each precursor. Using these methods, porosity, bulk density, and apparent density could be measured. Here, bulk density is defined as the mass of the sample divided by its exterior volume (includes open pore volume and solid volume), and apparent density is the mass of the sample divided by the volume of the water impervious/solid portion of the material.

### *Archimedes' Method*

The basic procedure outlined in ASTM standard C373-88 (ASTM C373-88 1999) was followed for density measurements using Archimedes' method. The dry mass of each sample was first measured using a balance (Mettler Toledo AB104-S) with a resolution of 0.0001 grams. The dry mass measurement was highly repeatable so only one measurement was used for each sample. Samples were then submersed in boiling deionized (DI) water for 3 hours to promote infiltration of all open porosity with water. The samples were then allowed to sit in still water for at least 12 hours.

Following water infiltration, the suspended and saturated masses of each sample were measured. Suspended mass was measured using a special assembly where the sample is suspended in a wire mesh basket and the suspended mass was measured after the balance was tared with the empty basket. To measure the saturated mass, submerged samples were removed from the water and rolled on a water-soaked, lint-free paper towel. The water-soaked paper towel and special care were used to remove only water on the exterior of the sample in order to avoid removal of water filling the internal pores of the sample. Because these measurements were less repeatable than dry mass measurements, three measurements were taken for each. The standard deviation on these measurements was less than 0.001 grams.

Using the dry ( $D$ ), suspended ( $S$ ), and saturated masses ( $M$ ), the porosity, bulk density, and apparent density could be measured by using equations 1-5 and assuming the density of water at room temperature to be unity.

$$P = \frac{M - D}{V_{\text{exterior}}} \quad (1)$$

$$T = \frac{D}{V_{\text{solid}}} \quad (2)$$

$$B = \frac{D}{V_{\text{exterior}}} \quad (3)$$

$$V_{\text{exterior}} = M - S \quad (4)$$

$$V_{\text{solid}} = D - S \quad (5)$$

Here,  $P$  is volume fraction of porosity,  $T$  is apparent density, and  $B$  is bulk density.

### *Gas Pycnometry*

In addition to Archimedes' method, He pycnometry (Micromeritics AccuPyc 1330) was also used to measure apparent density. This method was used to verify the consistency of the two measurements and as a fast and easy way to measure apparent density. Several samples were measured using both methods and the results were found to be in agreement within 1%.

Gas pycnometry measures apparent density by filling a chamber of known volume with a gas. If the pressure and temperature are known, the volume of solid portion of the sample

occupies in the chamber can be measured, and apparent density can be calculated with the sample mass.

### *Results*

The results of measurements using Archimedes' method and He pycnometry are shown in table 3.2. One obvious and expected change shown in table 3.2 is reduction in porosity due to the volume expansion that takes place during conversion of carbon to SiC. This volume expansion can be calculated by

$$\text{volume expansion} = \frac{V_{SiC} - V_C}{V_C} \quad (6)$$

Here,  $V_x$  is molar volume and is given by

$$V_x = \frac{M_x}{\rho_x} \quad (7)$$

where  $M_x$  is atomic mass ( $M_C = 12.0107$  g/mol and  $M_{SiC} = 40.0962$  g/mol) and  $\rho_x$  is density ( $\rho_{SiC} = 3.21$  g/cm<sup>3</sup>). As shown by table 3.2, the density of carbon from wood pyrolyzed at 800 °C is not constant. At this temperature, carbon density and porosity are inversely related as the decomposition of cellulose is more readily achieved in more porous wood.

**Table 3.2. Result of Archimedes' method and He pycnometry measurements of pyrolyzed carbon and bioSiC (error equals one standard deviation).**

<i>Pyrolyzed Carbon</i>			<i>Precursor</i>	<i>BioSiC</i>		
bulk density (g/cm <sup>3</sup> )	apparent density (g/cm <sup>3</sup> )	porosity (%)		bulk density (g/cm <sup>3</sup> )	apparent density (g/cm <sup>3</sup> )	porosity (%)
0.5210 ± 0.0233	1.8299 ± 0.0133	71.53 ± 1.27	<b><i>Beech</i></b>	1.4264 ± 0.0459	3.0368 ± .0508	53.16 ± 1.29
0.4015 ± 0.0229	1.7106 ± 0.0138	76.53 ± 1.34	<b><i>Mahogany</i></b>	1.3796 ± 0.1093	2.6689 ± 0.2759	48.32 ± 2.39
0.3495 ± 0.0099	1.7391 ± .0305	83.25 ± 0.47	<b><i>Poplar</i></b>	1.2096 ± 0.0698	3.0789 ± 0.0777	60.68 ± 2.44
0.4844 ± 0.0123	1.7364 ± 0.0155	72.10 ± 0.71	<b><i>Red Oak</i></b>	1.6720 ± 0.0915	3.0233 ± 0.1429	46.61 ± 2.23
0.4468 ± 0.0283	1.6971 ± 0.0094	73.67 ± 1.67	<b><i>Sapele</i></b>	1.3117 ± 0.0717	3.0340 ± 0.0860	56.77 ± 2.05

Although the resolution of mass measurements was 0.0001 grams and all measurements were reasonably repeatable, there is still significant variability in the bioSiC apparent density values in table 3.2. This is due to the structure of the wood precursors, which are a function of environment. Depending on factors such as rainfall and temperature, growth rates and porosities in trees vary with faster growth rates of more porous wood during warm rainy periods and slower growth rates of denser wood during dry cold periods (Dinwoodie 1989). As the length of these periods and amount of rainfall is not constant from year to year, some variation in porosity exists within even a single tree. As a result, even though samples for each type of bioSiC were processed from a single piece of precursor wood, there is still significant spread in porosity and density measurements.

The apparent density shown in table 3.2 is the density of the water-impermeable part of the sample. Ideally, the density of this impermeable portion should be  $3.21 \text{ g/cm}^3$ , the theoretical density of SiC. However, these apparent density values indicate that the impermeable portion is not solely dense SiC. In reality, this portion may consist of closed porosity and/or various other phases in addition to SiC. Using the results of Archimedes' method analysis in combination with helium pycnometry, the composition of the solid phase of each bioSiC was determined and quantified.

For SiC honeycomb, values of  $0.89 \pm 0.10 \text{ g/cm}^3$ ,  $71.70 \pm 2.50 \%$ , and  $3.04 \pm 0.2 \text{ g/cm}^3$  were measured for bulk density, porosity, and apparent density of the wall material. Much like bioSiC, the apparent density of the solid portion of SiC honeycomb is below the theoretical density of SiC. Because SiC honeycomb is processed such that no unreacted carbon is present in the final material, this value would indicate that the impervious portion of the material possesses

approximately 5 % closed porosity. When the closed porosity in each sample is accounted for, the total porosity of SiC honeycomb is  $74.04 \pm 2.50$  %.

### 3.3.2. Solid Phase Analysis

As a result of the multi-step process used to fabricate bioSiC and the intricate microstructures of the natural precursors, closed porosity, residual Si, and unreacted carbon may be present in addition to SiC in the solid portion of the final porous material. These phases all affect the mechanical properties of bioSiC and are a function of various factors including precursor density and microstructure. This section presents the procedures used to determine and quantify the phases present in the solid portion of each bioSiC and conclusions that may be drawn from the results.

#### *Closed Porosity*

Along with open porosity, closed porosity may be present in bioSiC and can lead to a reduction in apparent density. The microstructure of wood consists of only open porosity so closed porosity would not be expected to be present in the precursor or pyrolyzed carbon scaffold (Gibson and Ashby 1997). However, because of changes in microstructure through processing, closed porosity may be present in bioSiC. The presence of closed porosity can be determined by combining apparent density measurements made using Archimedes' method and the He pycnometer apparent density measurements.

Bulk samples of poplar, red oak, and mahogany bioSiC were separately ground using a mortar and pestle to a particle size of  $\sim 3$   $\mu\text{m}$ , which was on the order of the size of the large SiC

precipitates. The apparent density of the powdered samples was again measured in the pycnometer. These values were also found to be in agreement with bulk apparent density measurements. This result indicates that there is no significant closed porosity present in the machined bioSiC compression samples, and leads to the conclusion that the phase(s) present in addition to SiC must be residual Si and/or unreacted carbon.

### *Residual Si*

The presence of residual Si in the final bioSiC material was not expected but was possible if the acid etching process was incomplete. Samples were submerged in a stirred solution of HF and HNO<sub>3</sub> for at least one week so insufficient reaction time was not a likely reason for the presence of residual Si. Also, proportions and amounts of the acid were measured in stoichiometric and volumetric excess of what was necessary for the removal all residual Si in the samples so this was also not a plausible cause for the presence of Si. One possible reason for residual Si could be masking of this phase by one of the other solid phases (SiC or carbon) present in bioSiC. However, this is also unlikely as the molten Si infiltrated the porous carbon scaffolds and would be expected to be exposed to the acid etch on the inner walls of the bioSiC pores.

In order to verify the absence of residual Si in the bioSiC sample, it was necessary to eliminate one of the three solid phases (SiC, Si, and C) that could possibly be present. This was done by heat treating the powdered bioSiC in air at 600 °C for 7 hours. This oxidized any residual carbon present in the material, leaving only SiC and residual Si, if present. The powdered samples were used instead of bulk samples to allow for easy oxidation and elimination

of the unreacted carbon as long diffusion distances through the bulk material would require longer heat treatment times or higher temperatures.

Following heat treatment, the apparent density of the powder was again measured and found to be in agreement with the theoretical density of SiC. As the density of Si ( $2.33 \text{ g/cm}^3$ ) and  $\text{SiO}_2$  ( $2.65 \text{ g/cm}^3$ ) are below that of SiC, this result indicated that all residual Si in the samples was removed by the acid etch and that only unreacted carbon and SiC were present in the samples.

### **3.4. Porosity and Pore Size Measurements by Image Analysis**

More quantitative evidence of the differences between each bioSiC and the changes that occur during processing can be obtained by image analysis. This allows for relatively easy measurement of pore size and porosity. ImageJ (version 1.33u) (Rasband 2005), an open-source program developed at the National Institutes of Health (NIH), was chosen for image analysis.

#### **3.4.1. Pore Size Distribution**

In order to quantitatively characterize the porosity of bioSiC, ImageJ was used to measure the pore size distributions from images of SiC and pyrolyzed C from each precursor. ImageJ allowed measurement of hundreds of pores to get accurate distributions.

#### *Procedure*

SEM micrographs of the axial planes of bioSiC and carbon from each precursor were used for image analysis. Because of the tubular nature of wood, these images were taken to be

representative of all cross-sections of the material. Images at magnifications ranging from 40x to 2000x were used in order to efficiently and accurately measure a large number of pores. This was necessary because a large number of vessel pores could only be measured in lower magnification images and fiber and tracheid pores could only be measured accurately in higher magnification images. Only axially aligned pores were measured using this method.

The scale of each image was first set to enable absolute pore size measurements. Using image manipulation tools in ImageJ, each gray-scale SEM micrograph was converted into a black and white image by applying a threshold. This set gray-scale values above the threshold to white and those below it to black. Several pores were then measured manually to ensure that the image was still representative of the micrograph. The “analyze particles” function could then be used to measure porosity based on the fraction of black pixels in the image. This function also fit an ellipse to each pore, and the ellipse areas were used to calculate the pore size distribution. This procedure was used to measure at least 350 pores for each pyrolyzed carbon and each bioSiC, and is shown in figure 3.10.

As shown in figure 3.10, the threshold and minimum pore area to be measured was set such that only vessels were measured in images with magnifications of 40x – 70x and only fibers and tracheids were measured on images with magnifications of 250x – 2000x.

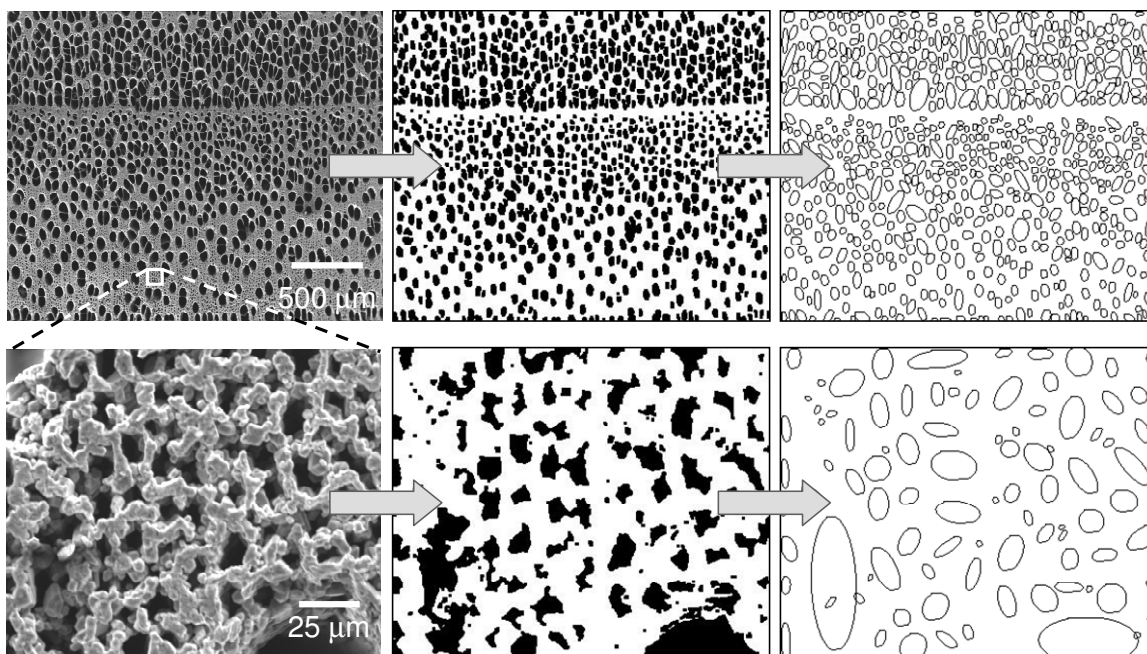


**Figure 3.10. Schematic showing how SEM micrographs were converted to black and white images to measure porosity and fit with ellipses to measure pore sizes using image analysis.**

The area fraction of each pore was calculated by dividing the pore ellipse area by the dimensions of the image, and a histogram was derived from these area fractions. This was done for both vessel pores in low magnification images and fiber and tracheid pores in high magnification images. In the low magnification images, the non-vessel pore area was assumed to consist of solid phase and porosity composed of both fibers and tracheids. The fraction of porosity measured in the high magnification images was normalized by this area fraction so that the contribution of large (vessel) pores and small (fiber and tracheid) pores to the total porosity could be measured. This was necessary because the high magnification images consisted almost entirely of fiber and tracheid pores and were not representative of the overall porosity. Given the tubular nature of the porosity in these materials, the area fraction of porosity in the axial plane was assumed to be equal to the volume fraction of porosity.

Histograms for each type of bioSiC were created from the ellipse areas, and data from high and low magnification images were combined so as to be representative of the vessel and fiber and tracheid porosity. These data were plotted versus pore size to create pore size distributions. The pore size of each pore was taken to be the average of the major and minor axes of each fitted ellipse. Total porosities measured for bioSiC using this method were close to those measured using Archimedes' method. The discrepancies present can be explained by the fact that parenchyma pores, which account for approximately 10% of the total porosity in wood (Gibson and Ashby 1997), were not measured, and further because of the variation in natural materials. In addition to parenchyma porosity and natural variation, pits in pore walls also contribute to porosity in pyrolyzed carbon and these were not accounted for by image analysis. The omission of pits did not have a significant effect on bioSiC porosity measurements because

these are relatively small ( $\sim 2 \mu\text{m}$  (Dinwoodie 1989)) pores and close due to volume expansion upon conversion of carbon to SiC.

### *Results*

Table 3.3 shows porosities measured for both pyrolyzed carbon scaffolds and bioSiC from each precursor. Some difference in porosity between measurement methods is to be expected because of the contribution from parenchyma pores which is not accounted for by image analysis and because of the variability of porosity in the natural precursors. As expected, there is a reduction in porosity upon conversion of carbon to bioSiC due to volume expansion.

Also shown in table 3.3 is the contribution to porosity from large vessel pores and smaller fiber and tracheid pores for each pyrolyzed carbon and bioSiC. The amount of porosity composed of vessel pores and that composed of fiber and tracheid pores are both reduced upon conversion to bioSiC. Much like the qualitative difference between materials made from beech and poplar (UDP) precursors and those made from mahogany, red oak, and sapele (NUDP) precursors seen in SEM micrographs, the contribution to porosity from large and small pores shown in table 3.3 shows a similar difference. The primary source of porosity in materials from UDP precursors is vessel pores while fiber and tracheid pores are the primary source of porosity in materials made from NUDP precursors. It will be shown later that this discrepancy between materials from the two precursor groups affects the phase composition and mechanical properties of the final bioSiC material.

**Table 3.3. Porosities of pyrolyzed carbon and bioSiC measured by image analysis (error equal to one standard deviation).**

<b>Carbon</b>			<b>Precursor</b>	<b>BioSiC</b>		
total porosity (%)	vessel porosity (%)	fiber and tracheid porosity (%)		vessel porosity (%)	fiber and tracheid porosity (%)	total porosity (%)
57.7 ± 1.9	44.0 ± 1.9	13.72 ± 0.0	<b><i>Beech</i></b>	35.8 ± 10.8	18.7 ± 2.5	54.5 ± 13.3
75.9 ± 8.7	44.7 ± 8.3	31.2 ± 0.4	<b><i>Poplar</i></b>	37.4 ± 4.9	19.2 ± 2.2	56.6 ± 7.1
66.5 ± 2.3	16.5 ± 2.1	36.8 ± 0.2	<b><i>Mahogany</i></b>	15.7 ± 0.8	29.7 ± 2.4	45.4 ± 3.2
67.8 ± 5.2	31 ± 2.9	36.8 ± 2.3	<b><i>Red Oak</i></b>	25.1 ± 0.8	22.5 ± 3.2	47.6 ± 4.0
63.7 ± 9.2	26.4 ± 8.5	37.3 ± 0.7	<b><i>Sapele</i></b>	23.2 ± 4.0	39.1 ± 2.3	53.2 ± 6.3

This trend can also be seen in the pore size distributions for poplar and sapele bioSiC plotted in figure 3.11 where the difference in the contribution to porosity from vessel pores and from fiber and tracheid pores is clearly evident. The specific pore sizes for each pyrolyzed carbon and bioSiC measured by image analysis are shown in table 3.4, and there are several important things to note. From the pore size distributions and table 3.4, it is apparent that the vessel pores of the UDP materials are smaller and have a narrower distribution than those of the NUDP materials. Although there is a reduction in porosity due to the volume expansion that occurs upon conversion of pyrolyzed carbon to bioSiC, there is no indication of pore size reduction from image analysis results. This is due to the fact that wood is a natural material subject to changing environments. For example, pore size and pore wall thickness are a function of rainfall with larger pores and thin walls forming during rainy seasons and smaller pores and thicker walls forming during dry seasons (Dinwoodie 1989). In addition, carbon and bioSiC pore size measurements from each wood precursor were conducted on different samples, which would be affected by sample-to-sample variation.

Image analysis was also used to analyze SiC honeycomb. Assuming dense wall material as shown in figure 3.12, the side lengths of the large square channels were measured to be approximately 2 mm and these channels account for a porosity value of 53.5 %. However, the porosity value of  $74.04 \pm 2.50$  % determined by Archimedes' method was much higher. This indicates that more than 20 % of the total porosity is not accounted for by the tubular channels in SiC honeycomb.

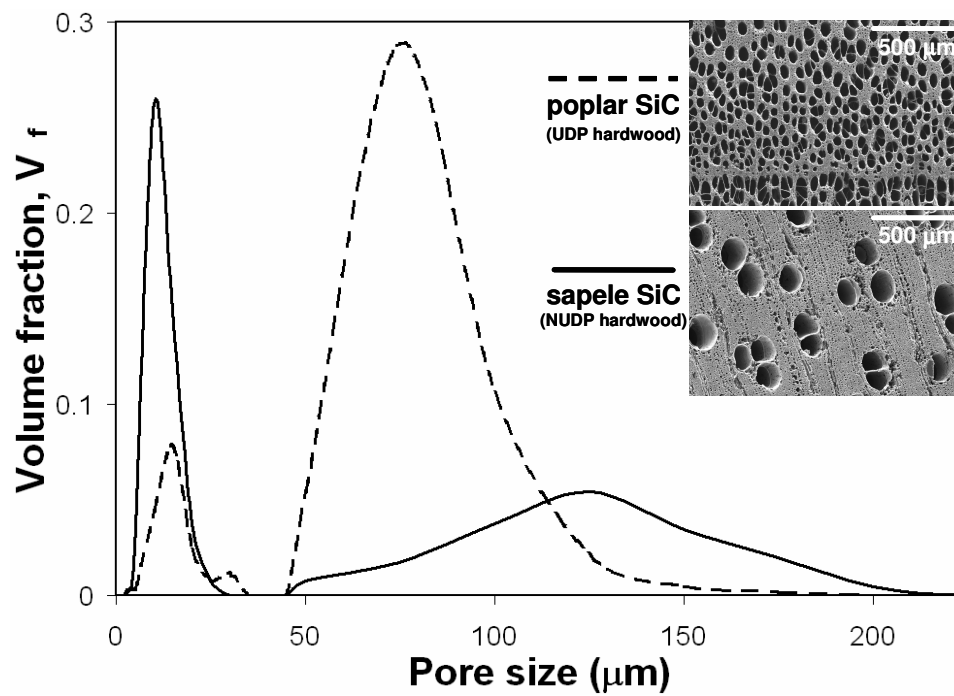
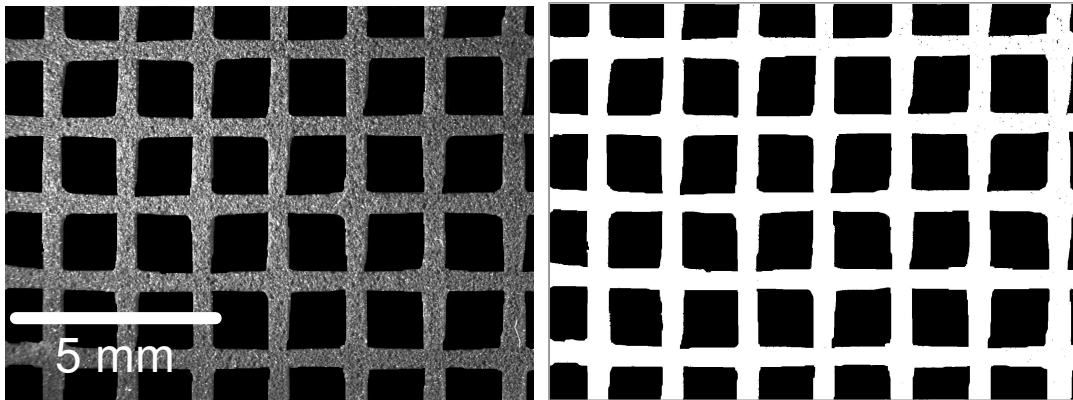


Figure 3.11. Pore size distributions for UDP and NUDP bioSiC (Kaul et al. 2006).

**Table 3.4. Pore sizes measured by image analysis (error equal to one standard deviation).**

<b><i>Carbon</i></b>		<b><i>Precursor</i></b>	<b><i>BioSiC</i></b>	
vessel pore size ( $\mu\text{m}$ )	fiber and tracheid pore size ( $\mu\text{m}$ )		vessel pore size ( $\mu\text{m}$ )	fiber and tracheid pore size ( $\mu\text{m}$ )
54 $\pm$ 13	4 $\pm$ 2	<b><i>Beech</i></b>	58 $\pm$ 12	3 $\pm$ 2
67 $\pm$ 23	10 $\pm$ 7	<b><i>Poplar</i></b>	72 $\pm$ 21	10 $\pm$ 6
121 $\pm$ 36	11 $\pm$ 6	<b><i>Mahogany</i></b>	114 $\pm$ 38	14 $\pm$ 11
112 $\pm$ 97	15 $\pm$ 9	<b><i>Red Oak</i></b>	127 $\pm$ 95	8 $\pm$ 6
107 $\pm$ 53	9 $\pm$ 5	<b><i>Sapele</i></b>	114 $\pm$ 45	9 $\pm$ 4



**Figure 3.12. a) Optical micrograph of SiC honeycomb and b) the corresponding image used for image analysis.**

Knowing that

$$P_{wall} = \frac{P_{total} - P_{channel}}{1 - P_{channel}} \quad (8)$$

it can be calculated that the pore wall material (total volume excluding the square channels) is 44.17 % porous.

### 3.5. Unreacted Carbon Content

From the results of Archimedes' method and He pycnometry measurements, it is evident that only SiC and unreacted carbon are present in the impervious portion of bioSiC. Even though Si in stoichiometric excess was used during processing to promote the conversion of the pyrolyzed carbon scaffold to SiC, the presence of unreacted C in the final bioSiC material is not unexpected. In this section, this unreacted carbon will be quantified and reasons for its presence will be presented.

#### 3.5.1. Quantification of Unreacted Carbon

##### *Procedure*

The theoretical density of  $\beta$ -SiC and the apparent density of unreacted carbon are 3.21 g/cm<sup>3</sup> and 1.80 ± 0.15 g/cm<sup>3</sup> respectively. The value for unreacted carbon was measured by He pycnometry after heat treatment of pyrolyzed carbon samples in vacuum at 1550 °C for 1 hour to

simulate infiltration conditions. After this heat treatment, the apparent density values for each type of carbon were in agreement. Using these density values together with the data from Archimedes' method analysis, the carbon content in each sample can be calculated. Following the determination that there is no significant amount of closed porosity or residual Si in the samples, the solid portion of bioSiC is a simple two-phase material and the volume fraction of unreacted carbon in the solid portion of the material can be calculated from

$$V_C = \frac{\rho_{solid} - \rho_{SiC}}{\rho_C - \rho_{SiC}} \quad (9)$$

Here,  $\rho_{solid}$  is the apparent density as measured by Archimedes' method.

### *Results*

The carbon content of each sample was calculated using equation 9 and the results are shown in table 3.5. It is important to note that while unreacted carbon has been observed by other researchers (Zollfrank and Sieber 2004; Zollfrank and Sieber 2005), this work is the first to quantify and correlate it to microstructural features in the precursor. From these results, one obvious trend is the general increase in carbon content that occurs with decreasing porosity. This is expected as the highest carbon contents would be expected in bioSiC processed from denser (lower porosity) precursors because there is more carbon to convert to SiC.

Although the lower porosity bioSiC materials have higher unreacted carbon contents, the correlation between the two is not the same for each bioSiC.

**Table 3.5. Volume fractions of unreacted carbon in the solid portion of bioSiC (error equal to one standard deviation).**

		<b><i>Precursor</i></b>	<b><i>BioSiC</i></b>		
			vol. frac. carbon (%)	apparent density (g/cm <sup>3</sup> )	porosity (%)
<b>UDP</b>	<b><i>Beech</i></b>		11.54 ± 3.39	3.0368 ± .0508	53.16 ± 1.29
	<b><i>Poplar</i></b>		8.40 ± 5.49	3.0789 ± 0.0777	60.68 ± 2.44
<b>NUDP</b>	<b><i>Mahogany</i></b>		35.41 ± 19.25	2.6689 ± 0.2759	48.32 ± 2.39
	<b><i>Red Oak</i></b>		13.82 ± 8.82	3.0233 ± 0.1429	46.61 ± 2.23
	<b><i>Sapele</i></b>		11.65 ± 6.15	3.0340 ± 0.0860	56.77 ± 2.05

In addition to the qualitative difference described earlier between UDP and NUDP bioSiC, there is also a difference in carbon content. From table 3.5, it is evident that NUDP bioSiC has more unreacted carbon content than UDP. This becomes clearer by using equations 10 and 11 to normalize the carbon content of each bioSiC by porosity and calculate the range of the difference between the carbon contents of UDP and NUDP bioSiC.

$$\text{normalized carbon content} = \frac{V_c}{1-P} \quad (10)$$

$$\begin{aligned} &\text{range of difference} \\ &\text{between two sample} \\ &\text{means} \end{aligned} = \pm t \left( \sqrt{n_{UDP} \sigma_{UDP}^2 + n_{NUDP} \sigma_{NUDP}^2} \right) \left( \sqrt{\frac{n_{UDP} + n_{NUDP}}{n_{UDP} n_{NUDP} (n_{UDP} + n_{NUDP} - 2)}} \right) \quad (11)$$

Here,  $n$  is the sample size,  $\sigma$  is the standard deviation and the  $t$ -value is chosen based on the number of samples and the desired confidence value. The normalized UDP and NUDP bioSiC carbon content data used to calculate the range of the difference between the two sample means is shown in table 3.6. From these data, it can be said with 95% confidence that, for a given porosity, NUDP bioSiC has a higher carbon content than UDP bioSiC.

**Table 3.6. Normalized data showing the significant difference between the unreacted carbon contents of UDP and NUDP bioSiC.**

	$V_{carbon}/(1-P)$	Std. Dev.	n	Confidence Level	Range of Diff. between Sample Means
<b>UDP bioSiC</b>	23%	11	23	95%	13
<b>NUDP bioSiC</b>	39%	30	36		

### 3.5.2. Presence of Unreacted Carbon

The presence of unreacted carbon in bioSiC can be explained via the molten Si infiltration and reaction process used to convert the pyrolyzed carbon scaffold to SiC. As previously outlined, the reaction is a combination of dissolution/precipitation and diffusion-based processes. In order for the carbon to be fully converted to SiC, molten Si must fully infiltrate the scaffold and sufficient time must be allowed for full conversion to take place. When these two requirements are unmet, unreacted carbon remains in the final bioSiC material. Keeping this in mind, there are two primary methods by which unreacted carbon may be present. These are 1) insufficient reaction time and 2) choking or premature closure of uninfiltated channels. In addition to channel choking, areas of the carbon scaffold may be cut off from the Si melt because of collapsed pores (Herzog et al. 2006) and channel diameters of at least 1  $\mu\text{m}$  are required for reasonable reaction times (Greil 2001). This sometimes occurs in wood while drying and is unavoidable in commercially bought wood.

#### *Insufficient Reaction Times*

One of the mechanisms by which the pyrolyzed carbon scaffold is converted to SiC is by diffusion of Si through the reaction formed SiC layer. The effective diffusion coefficient for Si through this reaction formed layer is given by

$$D_{effective} = D_o \exp\left(\frac{-Q}{RT}\right) \quad (12)$$

Here,  $D_o$  is  $2 \times 10^{-6} \text{ cm}^2/\text{s}$ ,  $Q$  is the activation energy (132 kJ/mole) (Greil et al. 1998),  $R$  is the gas constant (8.31 J/mole-K) and  $T$  is temperature making  $D_{effective}$  equal to  $3.29 \times 10^{-10} \text{ cm}^2/\text{s}$  at the reaction temperature of 1550 °C. The reaction depth can then be approximated by

$$d_{SiC} \approx \sqrt{D_{effective}t} \quad (13)$$

where  $t$  is time. Given the speed of the spontaneous molten Si infiltration and the dissolution/precipitation reaction that is also taking place, this diffusion reaction is a rate limiting step by several orders of magnitude. For molten Si infiltration of beech-derived carbon scaffolds, Zollfrank and Sieber found that reaction times of over 5 hours were necessary at 1550 °C for near complete conversion to SiC (Zollfrank and Sieber 2005). Although the conversion of carbon to SiC by this process is still possible on practical time scales because the dissolution/precipitation reaction is the dominant mechanism, some unreacted carbon may remain in thicker pore walls as a result of this rate limiting step because reaction times of 1 hour were used to process these materials.

### *Channel Choking*

During the conversion of carbon to SiC, a volume expansion of approximately 87% occurs. As a consequence of this volume expansion, many of the small channels present in the carbon scaffold are closed or choked with reaction formed SiC. This choking causes portions of the carbon scaffold to be cut-off from the supply of molten Si and remain unreacted in the final bioSiC material.

Figure 3.13 shows a schematic of how channel choking can occur during processing. If volume expansion is assumed to be isotropic, then the linear coefficient for small expansions can be approximated by 29% as shown by (Callister 2003).

$$\Delta l \approx \frac{\Delta V}{3} \quad (14)$$

Using this result and modeling a single pore by the diagram shown in figure 3.14, the pore wall thickness as a function of pore size necessary for channel closure is given by

$$\text{wall thickness} \geq \text{pore size} / \Delta l \quad (15)$$

This equation indicates that a pore wall thickness to pore diameter ratio greater than 3.45 would result in channel choking. Given the structure and pore size distribution of the carbon scaffold, this ratio is most likely to be eclipsed in dense areas of small pores and thick pore walls.

#### *UDP v. NUDP*

As previously mentioned, for a given porosity, NUDP bioSiC tends to have a higher content of unreacted carbon than UDP bioSiC. While a portion of this comes from insufficient reaction times, the primary source of unreacted carbon and the source of the discrepancy between UDP and NUDP bioSiC is channel choking.

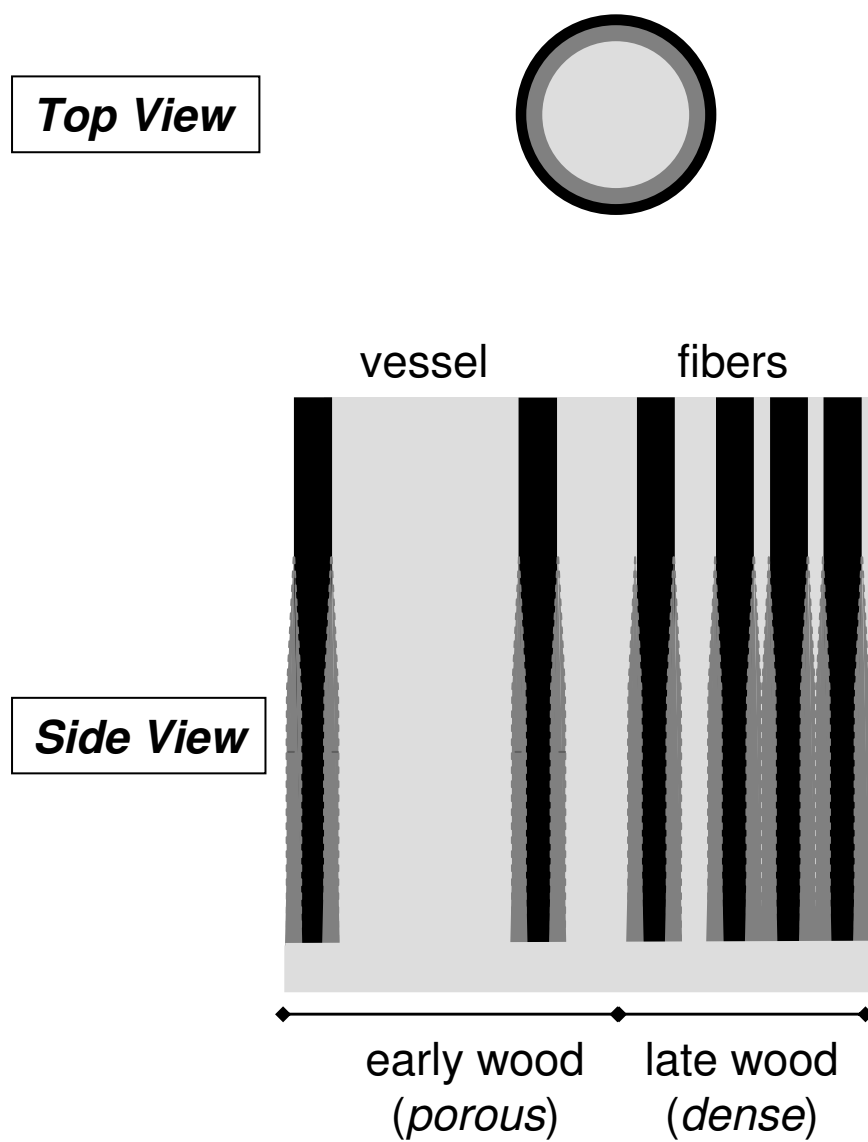


**Figure 3.13. Schematic showing how small pores with thick pore walls can be closed as a result of volume expansion upon conversion of pyrolyzed carbon to bioSiC.**

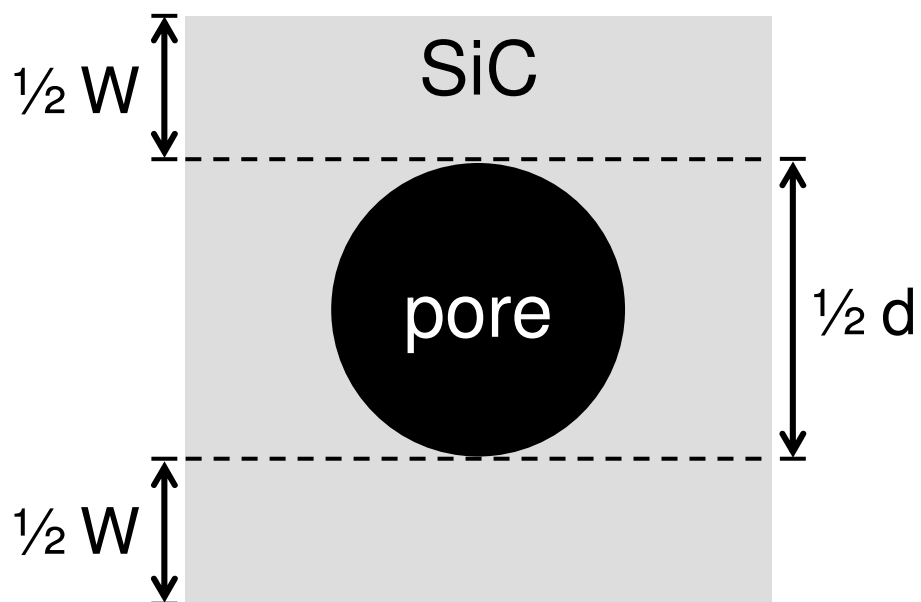


**Figure 3.14.** Schematic representation of a single pore in bioSiC.

As mentioned earlier, channel choking is most likely to occur in regions of small pore size. It is apparent from the pore size distributions in figure 3.11 and from SEM micrographs that regions of this description are more prevalent in NUDP bioSiC than in UDP bioSiC. In addition to small pore sizes, relatively large wall thicknesses are also necessary for channel choking. This occurs in dense regions corresponding to late wood regions in the wood precursors. This dependence of wall thickness on region for both NUDP and UDP bioSiC is illustrated in figure 3.15. It is important to note that the ends of fiber pores in wood are tapered, and they are most likely to be closed due to volume expansion at these ends. From figure 3.15, it is again clear that the likelihood of channel choking is much higher in NUDP materials. Experimental observations were in agreement as large patches of unreacted carbon were often observed in materials processed from NUDP precursors and not in those from UDP precursors.

Using EDS (PGT Energy Dispersive X-ray analyzer), areas of unreacted carbon can be identified. EDS elemental maps of UDP and NUDP bioSiC are shown in figure 3.16. From this figure, it is clear that the distribution of Si and carbon is uniform in UDP poplar bioSiC. This indicates near full conversion of the carbon scaffold to SiC and the absence of unreacted carbon from channel choking. Unreacted carbon from insufficient reaction times may be present but is not observed by EDS. In contrast, the EDS maps of NUDP red oak show large patches of unreacted carbon that are free of Si. These areas occur in dense late wood regions while more porous early wood regions still show uniform Si content indicating near complete conversion. These dense regions are consistent with the requirements for channel choking and unreacted carbon.

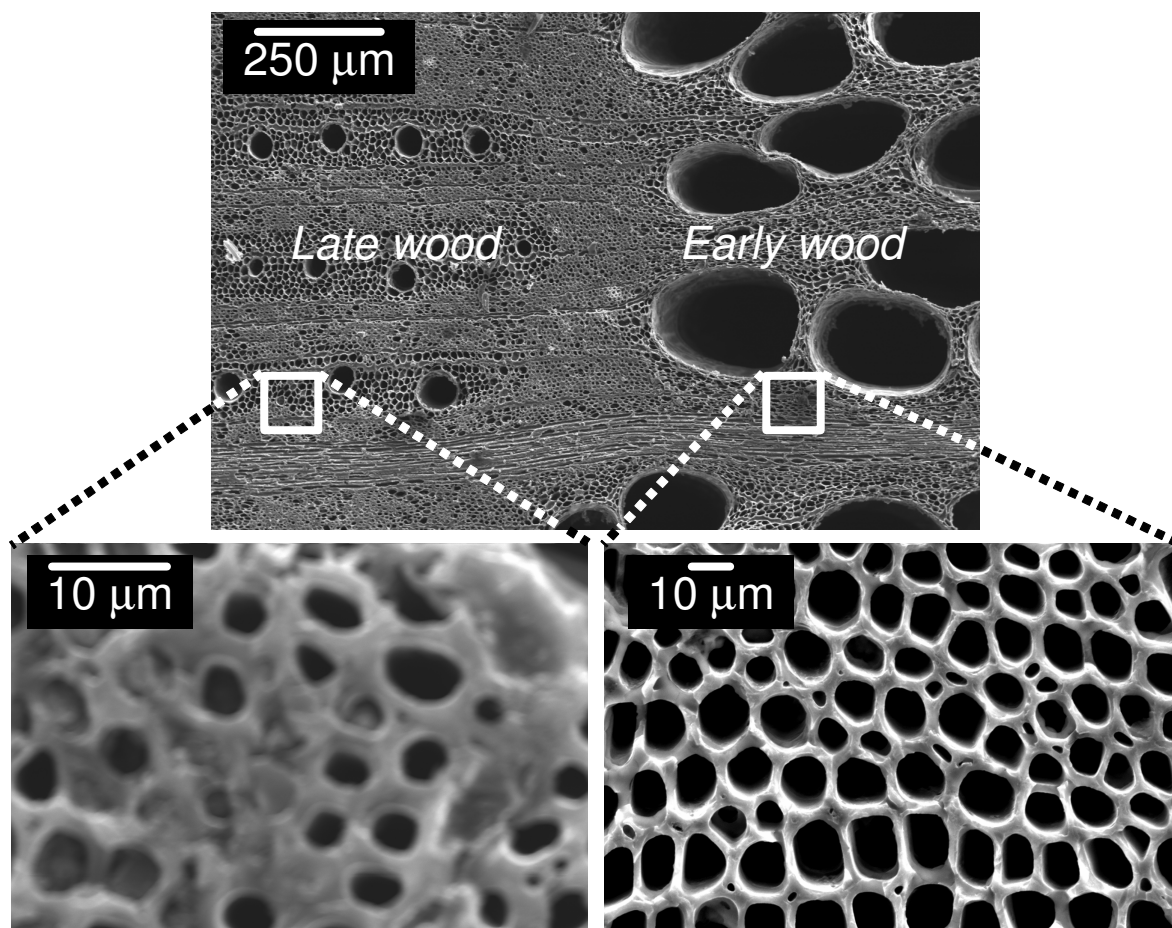
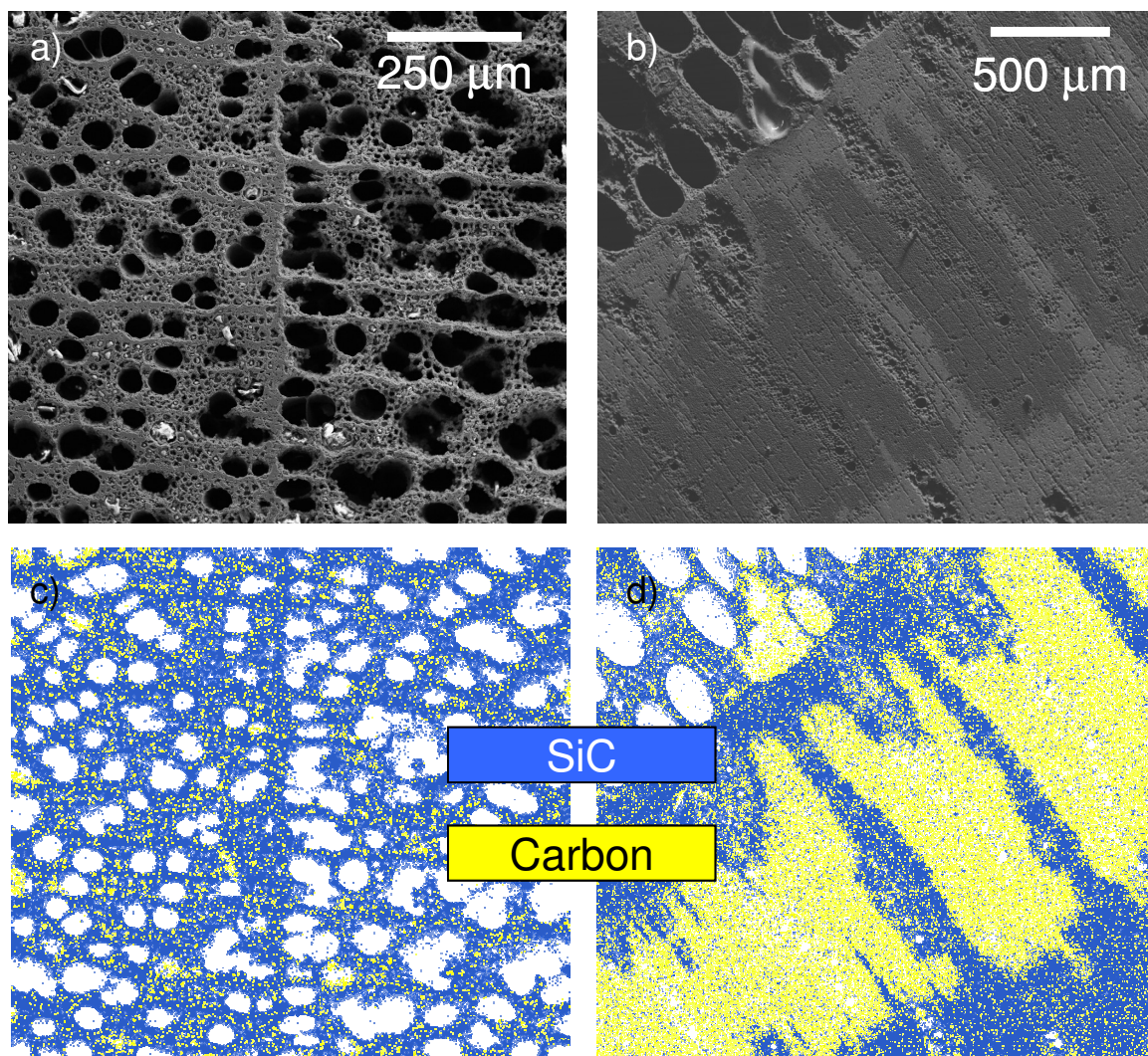


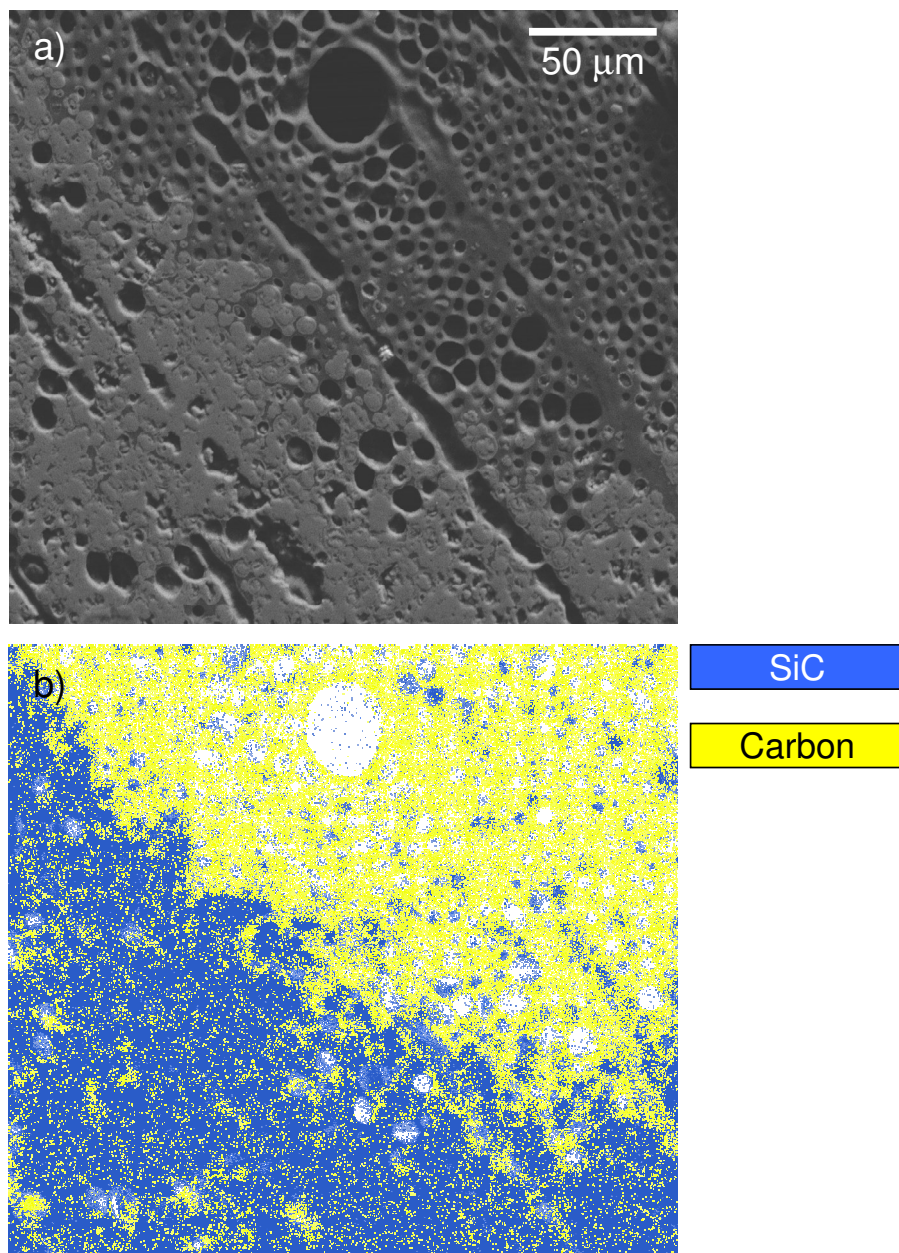
**Figure 3.15.** SEM micrographs of pyrolyzed carbon showing the variation of pore size and pore wall thickness between late and early wood.



**3.16. SEM micrographs and EDS maps of a,c) UDP poplar bioSiC and b,d) NUDP red oak bioSiC showing large patches of unreacted carbon in dense areas of the NUDP material.**

Closer inspection in figure 3.17 shows that the porous structure of the pyrolyzed carbon scaffold is maintained in these unreacted regions.

While insufficient reaction time leads to thin areas of unreacted carbon within pore walls, channel choking results in large patches of completely unreacted material. This closure of channels and large patches of unreacted material would indicate closed porosity which was not detected by previous measurements. This is due to the fact that small samples (4 mm x 4 mm x 8 mm) were used for density measurements and these samples were smaller than most of the carbon patches due to channel choking. Effectively, the small measured sample had no closed porosity but closed porosity was present in the bulk samples from which they were fabricated. In the UDP samples, unreacted carbon generally makes up approximately 10 volume % of the solid phase. However, this value ranged from 5 to 50 volume % for the NUDP samples, further indicating the heterogeneous or patchy distribution of the unreacted carbon resulting from channel choking.



**3.17. a) SEM micrograph and b) EDS map of red oak bioSiC showing dense area of SiC and porous areas of unreacted carbon.**

### 3.6. Summary

While all woods are porous materials with certain common features, each species has a unique characteristic volume of porosity, pore size distribution, and microstructure. To gauge the effect of these characteristic features, five different wood precursors were chosen and processed. In addition to bioSiC, a porous SiC honeycomb material from a synthetic precursor was also analyzed. These woods were categorized into two groups (UDP and NUDP) based on the uniformity of their pore distributions and the major constituent of porosity. In this chapter, the analysis of structure and phase composition of each of these woods in each processing step presented. While the general structure of the wood precursor is retained, the amount of porosity and phase composition change during processing and is found to be dependent on the choice of precursor. Porosity was found to decrease upon conversion of carbon to SiC, and this volume expansion was found to be the major cause of unreacted carbon in the final material. The amount of unreacted carbon was quantified and found to higher in NUDP bioSiC than UDP bioSiC.

# 4

## Mechanical Properties of Biomorphic Silicon Carbide

To further characterize biomorphic silicon carbide (bioSiC), the mechanical properties of bioSiC from multiple wood precursors were measured in compression and in flexure. The results of this testing were used in concert with the results presented in the previous chapter to correlate microstructure and phase composition to the mechanical properties of bioSiC. In this chapter, mechanical testing procedures and results are presented along with discussion on how these properties relate to the microstructure and phase composition of bioSiC.

### 4.1. Experimental Procedures

In order to identify bioSiC for potential applications, relevant properties must be measured. In many of the potential applications identified in chapter 2, knowledge of mechanical properties is essential. The mechanical properties pertinent to many of these applications include bulk properties such as compressive strength ( $\sigma_{comp}$ ), elastic modulus ( $E$ ), and fracture toughness ( $K_{IC}$ ) as well as specific properties of the solid phase of the material. These properties were measured for bioSiC from each precursor and synthetic SiC honeycomb in axial and transverse directions, and this section outlines the methods used to measure these properties.

For bioSiC, samples were machined from larger pieces (1 cm x 2 cm x 6 cm) of bioSi/SiC. This was done because all material was processed in a short five-week period in our collaborators' lab at the University of Seville in Spain and larger samples were more convenient to work with and required less machining time. This method was acceptable because infiltration of samples larger than those required for most mechanical testing will be necessary for most industrial applications and knowledge of the properties of materials of realistic sizes is essential.

The bioSi/SiC and SiC honeycomb samples were then professionally machined by PremaTech Advanced Ceramics (Worcester, MA) to ensure high dimensional tolerance and parallelism, which is not possible using locally available equipment. Unetched bioSi/SiC samples were sent for machining because they were less likely to be damaged during shipping than etched samples and because removal of residual Si was easier in smaller samples. All testing was conducted using a single universal testing machine (MTS Sintech 20/G, Norwood, MA). Following mechanical testing, fractographic analysis of tested samples was also conducted using scanning electron microscopy to determine crack paths and their dependence on microstructural features.

#### 4.1.1. Nanoindentation

Along with mechanical properties of bulk bioSiC and SiC honeycomb, specific properties of the solid portion of these materials were also measured using nanoindentation. In the bulk material, the effect of porosity and the effect of the solid portion of the material are often convoluted. Knowledge of specific properties can aid in determining those effects due to pore morphology and those due to the properties of the solid portion of the material. These specific

properties will also be used as inputs for finite element analysis, which will be the subject of the next chapter.

Nanoindentation was first introduced as a method for measuring hardness ( $H$ ) and elastic modulus ( $E$ ) in 1992 (Oliver and Pharr 1992; Pharr and Oliver 1992). In this method, a diamond Berkovich triangular pyramid is used to indent materials. During indentation loading and unloading, load and displacement are recorded. From these data,  $H$  can be calculated from (Oliver and Pharr 2004)

$$H = \frac{P_{\max}}{A} \quad (1)$$

where  $P_{\max}$  is the maximum load and  $A$  is the contact area which is given by an area function defined by previous calibration of the nanoindenter.  $E$  can also be calculated from the unloading portion of the curve using (Oliver and Pharr 2004)

$$S = \frac{2}{\sqrt{\pi}} E_{\text{effective}} \sqrt{A} \quad (2)$$

Here,  $S$  is the stiffness equal to the slope of the load-displacement curve and  $E_{\text{effective}}$  is the elastic modulus measured accounting for both the specimen and indenter compliance. From this,  $E$  of the sample can be solved for by (Oliver and Pharr 2004)

$$\frac{1}{E_{effective}} = \frac{1-\nu^2}{E} + \frac{1-\nu_{indenter}^2}{E_{indenter}} \quad (3)$$

where  $E_{indenter}$  and  $\nu_{indenter}$  are 1140 GPa and 0.07, respectively for the diamond indenter. A typical load-displacement curve from a ceramic material is shown in figure 4.1. Here, two distinct regions can be seen in the unloading curve. These regions correspond to (I) recovery of surface flexure and (II) recovery of the indentation depth (Page et al. 1992). From the unloading curve,  $E$  is measured from region I. To calculate  $E$ , values listed in the literature or values measured by pulse-echo for  $\nu$  were used. Pulse-echo is a method by which  $E$  and  $\nu$  can be calculated based on the speed of sound through a material.

Nanoindentation is ideal for determining the properties of specific areas that can not be measured using conventional mechanical testing. For this reason, it has been utilized by other researchers to measure the properties of the thin films (Li et al. 1993; Pharr and Oliver 1992; Sjoström et al. 1995) and interfaces (Urena et al. 2005). More recently, nanoindentation has also been used to measure the properties of the solid component of porous materials such as porous Si (Bellet et al. 1996), cement (Constantinides and Ulm 2004), bone (Hengsberger et al. 2002; Rho et al. 1997; Turner et al. 1999), and wood (Wimmer et al. 1997).

The system used to perform nanoindentation tests was the Hysitron TriboIndenter (Minneapolis, MN). Testing regions were first identified using an optical microscope. Unlike other nanoindenters, this system also has additional capabilities that allowed for imaging and roughness measurements of the exact spot to be indented.

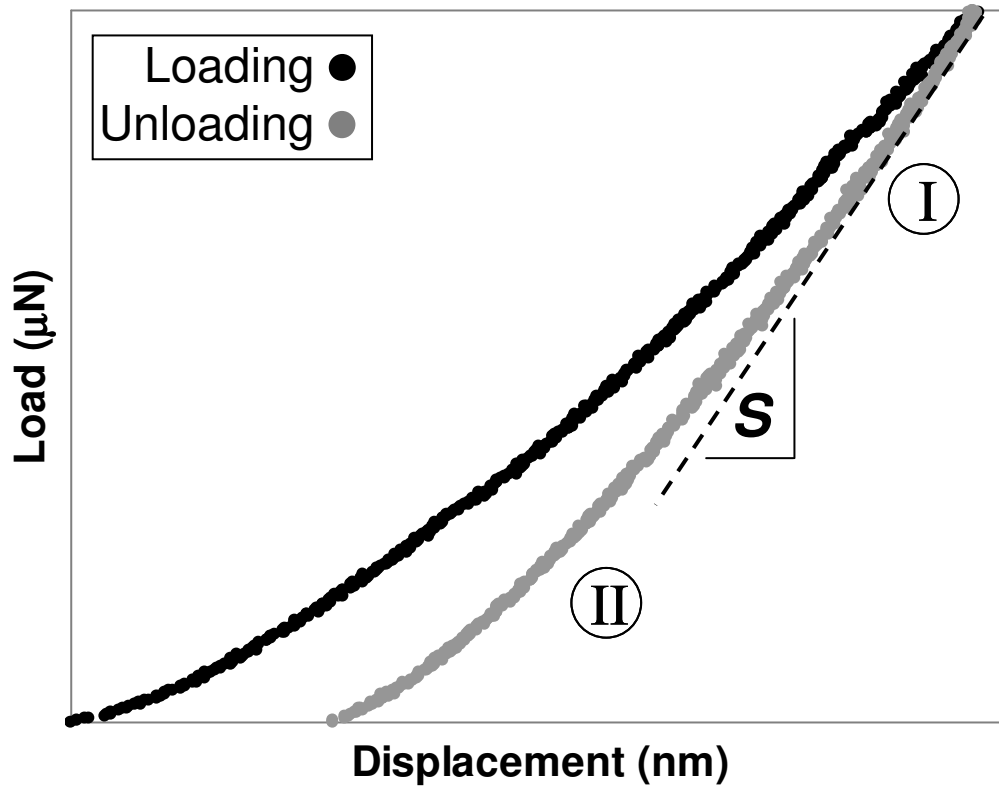


**Figure 4.1. Typical load-displacement curve from nanoindentation of a ceramic material showing regions of (I) surface flexure recovery and (II) indentation depth recovery where  $S$  is stiffness.**

This was especially useful for measurements on porous bioSiC as specific areas suitable for nanoindentation could be identified prior to testing and indentations could be examined after testing.

Prior to indentation, all samples were polished to a finish of 0.1  $\mu\text{m}$  to ensure flat surfaces for indentation and mounted on aluminum disks with super glue.  $E$  and  $H$  of standard samples were measured along with bioSiC samples which were indented in axial and transverse planes at various loads. At least 16 indentations were made on each material. Indentations were made using loads between 3 and 10 mN to depths of 75-200 nm where the area function was known to be accurate.

#### 4.1.2. Compressive Strength and Elastic Modulus

Compression samples with dimensions of approximately 4 mm x 4 mm x 8 mm were machined to measure both  $\sigma_{comp}$  and  $E$  for beech, mahogany, poplar, red oak, and sapele bioSiC as well as SiC honeycomb. Samples were tested in compression because of the relatively simple shapes necessary and to avoid sample gripping during testing, which is necessary for tensile testing. For each type of bioSiC and SiC honeycomb, samples were machined such that the long axis was parallel to the axial or transverse (radial or tangential for bioSiC) principal direction. This was done in order to test the effect of pore orientation on the mechanical properties. At least 3 samples were tested for each type of bioSiC and SiC honeycomb in each of the three principal orientations.

Samples were compressed at a rate of 0.1 mm/minute in a fixture consisting of two stainless steel platens in a sleeve to ensure the platens were aligned and parallel (figure 4.2).

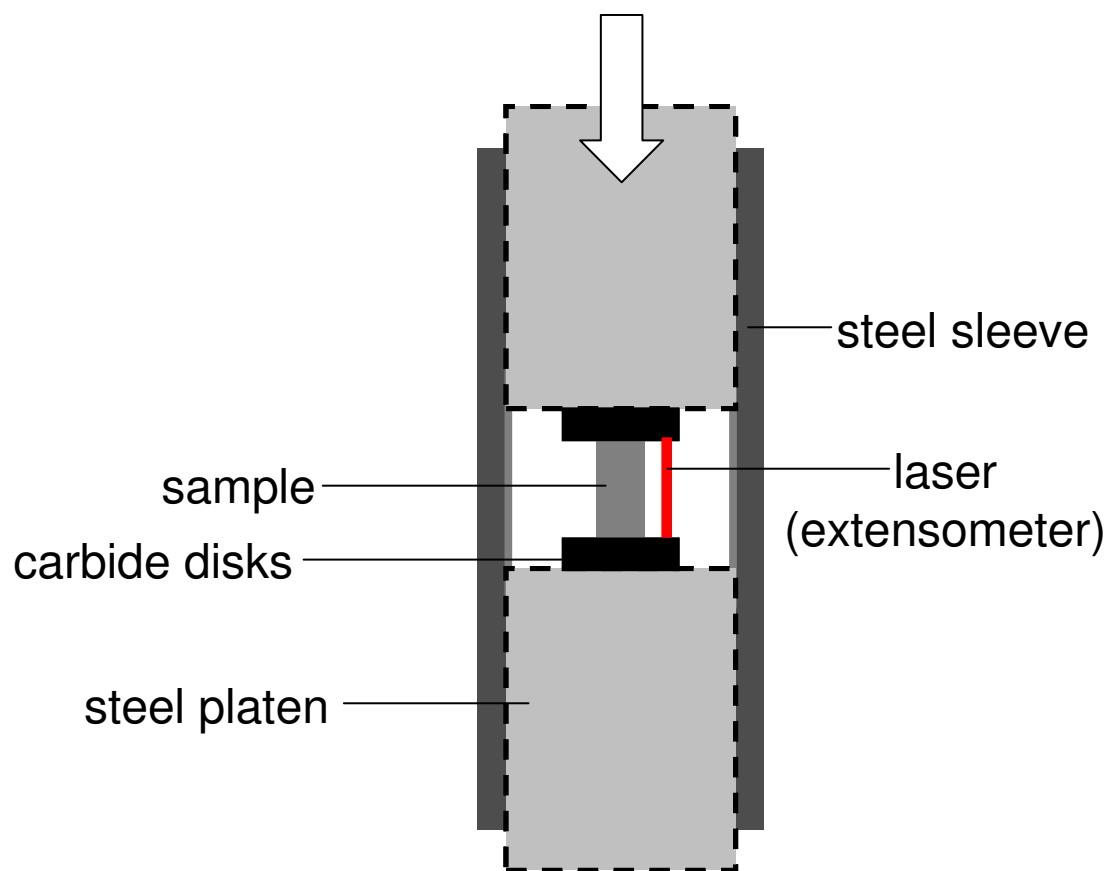


**Figure 4.2. Schematic of experimental setup used for compressive testing.**

This was done to prevent damage of the platens by the samples. During the test, a laser extensometer (LaserMike, Dayton, OH) was used to directly measure displacement of the sample. This method was used because the crosshead displacement does not exclude the test fixture and machine compliance. Following the test,  $\sigma_{comp}$  was taken to be the stress at which initial fracture occurred and  $E$  was measured from the stress versus strain plot for each sample. Following compression testing, fracture surfaces of several samples were also examined using SEM.

#### 4.1.3. Fracture Toughness

The single-edge notched beam (SENB) method was used to measure fracture toughness ( $K_{IC}$ ) of each type of bioSiC. Other methods for measuring  $K_{IC}$  were also evaluated including the chevron notch (CN) and the surface crack in flexure (SCF) methods. The CN method was not used because it required stable crack growth during testing which was difficult to achieve consistently, and the SCF method was not used because the crack width was limited by the pore size of the material which varied in each type of bioSiC.

For the SENB method, 3 mm x 4 mm x 25 mm samples were machined and tested in accordance with ASTM standard C1421-99 (C1421-99 1999). As with the compression samples, bars with the long axes parallel to the axial and transverse directions were tested. At least 3 samples were tested for each test condition. Notches of approximately 400  $\mu\text{m}$  were also machined into the 3 mm face of the samples. This width was chosen because it is larger than the sample pores so cracks could originate at the notches and not at a sample pore. The samples were tested at a rate of 0.15 mm/minute in three-point bending (figure 4.3).

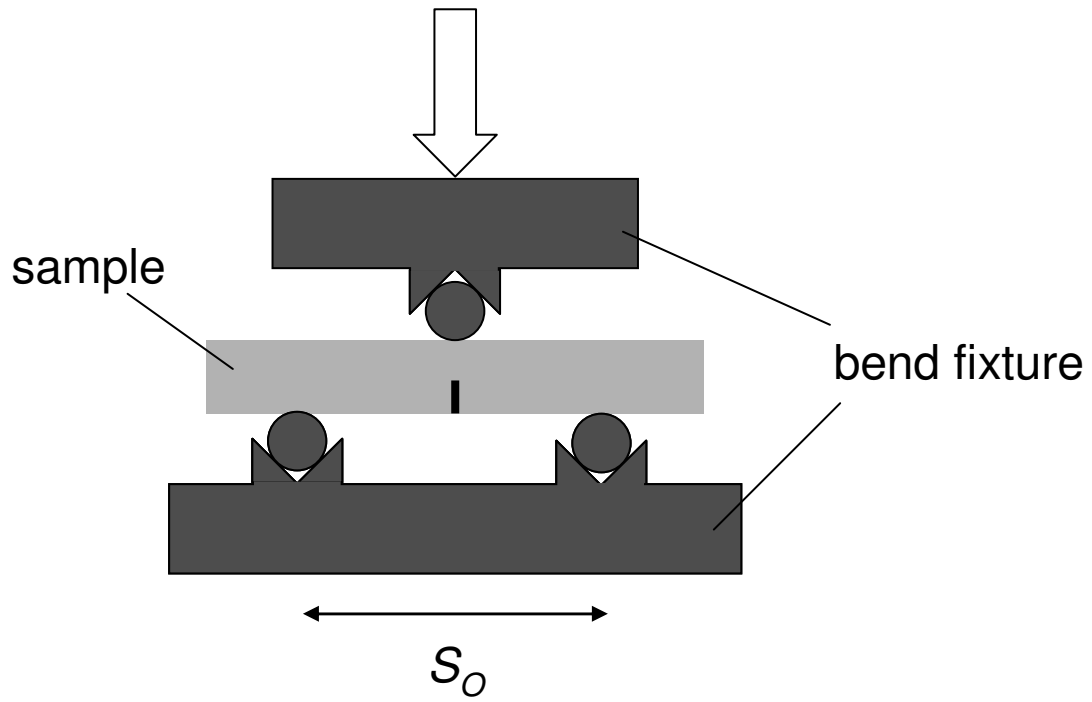


**Figure 4.3. Schematic of experimental setup used for fracture toughness testing.**

In accordance with the ASTM standard,  $K_{IC}$  was calculated from

$$K_{IC} = g \left[ \frac{P_{max} S_o}{BW^{3/2}} \right] \left[ \frac{3(a/W)^{1/2}}{2(1-a/W)^{3/2}} \right] \quad (4)$$

where  $P_{max}$  is the maximum load,  $S_o$  the outer span (20 mm),  $B$  and  $W$  the thickness and width, respectively, of the bar,  $a$  the notch length, and  $g$  is given by

$$g = \frac{1.99 - (a/W)(1-a/W)(2.15 - 3.93[a/W] + 2.7[a/W]^2)}{1 + 2(a/W)} \quad (5)$$

As with compression samples, fracture surfaces of tested samples were also examined using SEM.

#### 4.2. Nanoindentation Results and Discussion

As the mechanical properties of porous materials are a function of both pore morphology and pore wall material, knowledge of the properties of the solid portion of the material is essential. In the previous chapter, it was established that the solid portion of bioSiC was composed of both SiC and unreacted carbon. Nanoindentation was used to measure  $E$  for these phases and for the pore wall material of SiC honeycomb.

#### 4.2.1. Nanoindentation Results

Prior to analyzing the solid phases of bioSiC,  $E$  and  $H$  of several dense standard materials were measured to verify the nanoindenter values. These materials were fused quartz, sintered alumina, and sintered  $\alpha$ -SiC. The properties of  $\alpha$ -SiC also served as a good comparison to the values measured for the SiC phase in bioSiC as the  $E$  and  $H$  of  $\alpha$ -SiC are expected to be very similar to those of  $\beta$ -SiC (Gulden 1969). The measured values for these standards are shown in table 4.1, and a single indent is shown in figure 4.4. The values measured for each of the standard samples were in agreement with those in the literature and those measured by pulse-echo.

Measurements of  $E$  for both reaction-formed SiC and unreacted carbon were both made on bioSiC samples. It was important to use bioSiC and not simply pyrolyzed carbon to measure  $E$  for unreacted carbon because, while the carbon was not exposed to Si during the infiltration reaction, the high temperature heat treatment may change its properties. Using the imaging capabilities of the nanoindenter, flat areas in bioSiC samples could be identified and indented. The majority of the material was SiC but areas of unreacted carbon existed. As discussed in the previous chapter, these areas were most likely to occur in dense late wood regions and could be identified by the presence of distinct non-granular fiber and tracheid pores that are characteristic of the carbon scaffold.

Initially, indentations on bioSiC were made in the transverse orientation because the interior walls of vessel pores appeared to be smooth and dense, ideal for indentation as shown in figure 4.5. However,  $E_{SiC}$  measured in these planes,  $290.59 \pm 108.89$  GPa, was much lower than anticipated and highly variable. This was attributed to varying wall thickness and curvature.

**Table 4.1. Mechanical properties measured by nanoindentation of dense standard samples (error represents one standard deviation).**

	<b><i>E</i> (GPa)</b>	<b><i>H</i> (GPa)</b>
<b><i>Fused Quartz</i></b>	$72.01 \pm 1.88$	$9.66 \pm 0.61$
<b><i>Sintered Alumina</i></b>	$368.73 \pm 4.12$	$26.99 \pm .061$
<b><i>Sintered <math>\alpha</math>-SiC</i></b>	$411.51 \pm 38.35$	$38.50 \pm 5.83$

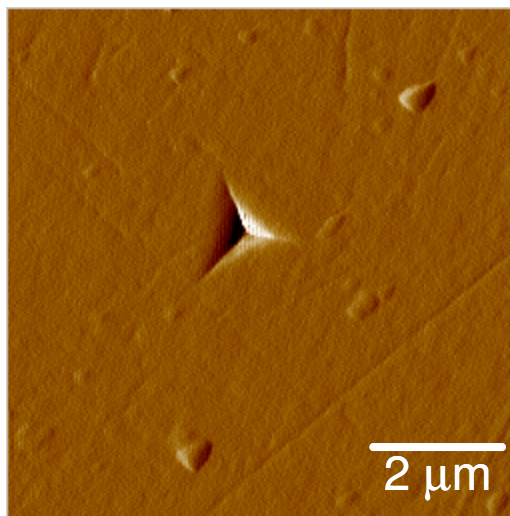


**Figure 4.4.** Single nanoindentation made using a Berkovich indenter on fused quartz.

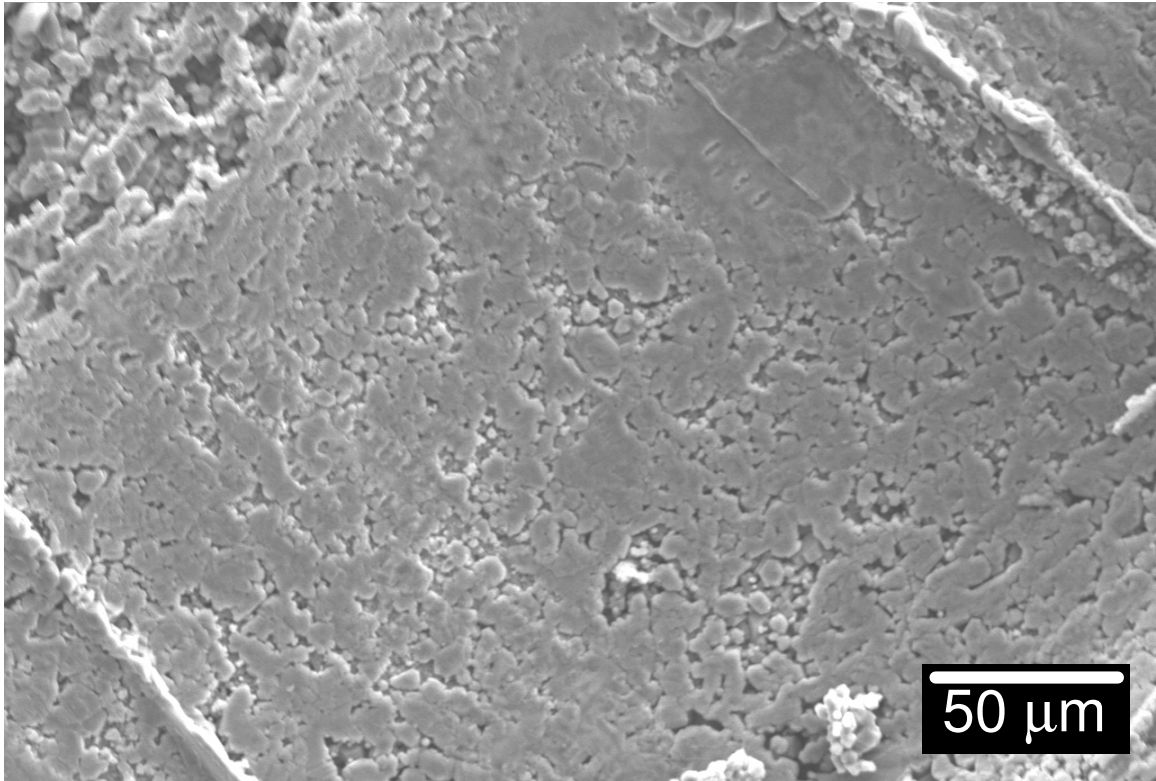


**Figure 4.5.** As-processed interior of a vessel pore in red oak bioSiC.

Further measurements were made in ground and polished axial planes where surfaces were flat and, because of the honeycomb-like microstructure, could be assumed to be much thicker than the depth of the indentation. For this reason, only measurements in axial planes were used to determine the properties of bioSiC phases.

It was expected that  $E_{SiC}$  would be independent of the type of wood precursor and this was verified by indentation in the axial planes of both NUDP (red oak) and UDP (beech) bioSiC. The  $E$  of unreacted carbon was measured in the axial plane of red oak bioSiC samples which possessed uninfiltreated patches in dense late wood regions as previously shown in figure 3.16. In addition to porous bioSiC, nanoindentation was also used to measure the specific properties of SiC honeycomb. As with the bioSiC, polished samples were indented in the axial plane. These bioSiC and SiC honeycomb  $E$  values are shown in table 4.2 and were calculated using  $\nu_{SiC}$  and  $\nu_{carbon}$  values of 0.16 and 0.17 (Gulden 1969; Kutz 2003), respectively.

**Table 4.2. Mechanical properties measured by nanoindentation on porous bioSiC phases and SiC honeycomb.**

	<b><i>E</i> (GPa)</b>	<b><i>H</i> (GPa)</b>
<b>Beech bioSiC</b>	417.13 ± 10.96	40.14 ± 1.25
<b>Red Oak bioSiC</b>	403.13 ± 40.80	37.00 ± 2.63
<b>Unreacted Carbon</b>	28.71 ± 2.68	4.94 ± 0.31
<b>SiC Honeycomb</b>	132.60 ± 94.09	16.62 ± 10.30

#### 4.2.2. Nanoindentation Discussion

The values measured for  $E_{SiC}$  and  $H_{SiC}$  were in agreement with those in the literature for  $\beta$ -SiC and those measured from the sintered  $\alpha$ -SiC standard (Gulden 1969).  $E_{carbon}$  and  $H_{carbon}$  were also found to be in agreement with literature values for amorphous carbon (Kutz 2003). As expected,  $E_{SiC}$  for both UDP and NUDP bioSiC were in agreement. It is also important to note that  $E_{carbon}$  is lower than  $E_{SiC}$  by over an order-of-magnitude. Unreacted carbon is present with SiC and, as will be shown in the following sections, its presence can drastically alter the mechanical properties of bioSiC.

Unlike bioSiC, the  $E$  and  $H$  values for SiC honeycomb are highly variable and much lower than expected given that the solid phase is entirely SiC. This is attributed to the distribution of porosity in this material. While the pore wall material in bioSiC is free of porosity, the same can not be said for SiC honeycomb. Previous image analysis results indicated that the wall material of SiC honeycomb was 44.17 % porous. As a result this porosity in the pore wall material of SiC honeycomb, valid nanoindentation measurements for the solid phase could not be made. This pore wall porosity will have a deleterious effect on  $E$  and  $H$  values, and the degree of this effect will depend on the porosity present in the region of each indent. This accounts for the lower than expected and highly variable values of  $E$  and  $H$  for SiC honeycomb.

### 4.3. Compressive Strength and Bulk Elastic Modulus Results and Discussion

Trees are massive organisms that require support of a tremendous load in compression. For this reason, nature has optimized the structure of wood to provide excellent mechanical properties in compression while still remaining lightweight and porous/conductive. Many

aspects of this optimized structure are retained in bioSiC and the performance in compression of bioSiC from five hardwood precursors and synthetic SiC honeycomb is presented in this section.

#### 4.3.1. Compressive Test Results

Compressive strength results in the axial and transverse directions for bioSiC and SiC honeycomb are shown as a function of porosity in figures 4.6(a) and 4.6(b), respectively. Elastic modulus was also measured in compression, and the results in the axial and transverse directions are shown as a function of porosity in, respectively, figures 4.7(a) and 4.7(b).

In addition to the experimentally measured  $E$  values, lines corresponding to the theoretically predicted values of  $E$  in the axial and transverse directions are also shown in figure 4.7. These theoretical lines come from the minimum solid area (MSA) model developed by Rice (Rice 1998), which predicts the mechanical properties of porous materials based on the calculated minimum solid area perpendicular to the direction of mechanical action. This model was chosen because it allows for comparison of the natural and non-regular microstructure of bioSiC to an ideal and regular structure.

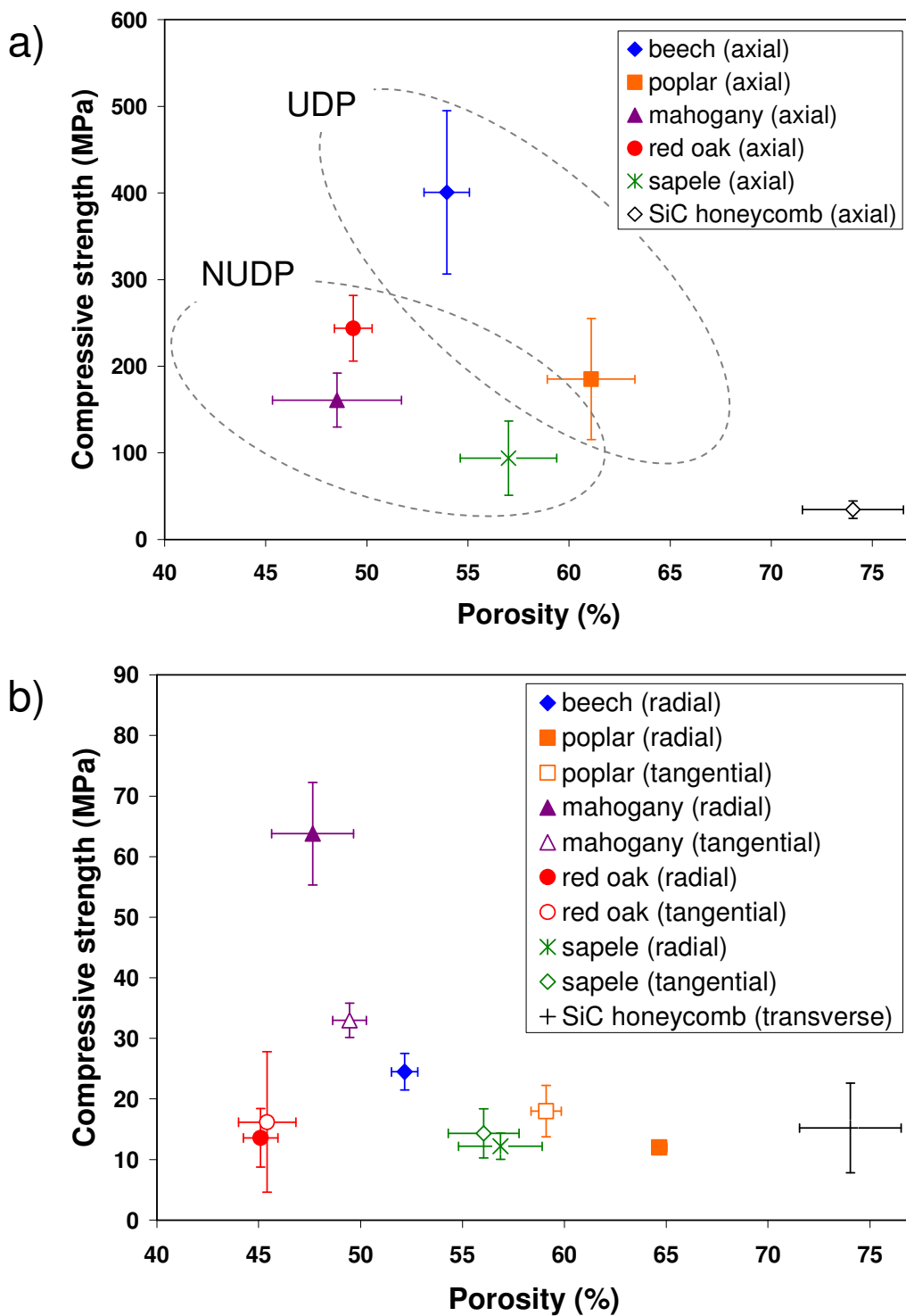


Figure 4.6. Compressive strength as a function of porosity for (a) axial and (b) transverse bioSiC and SiC honeycomb.

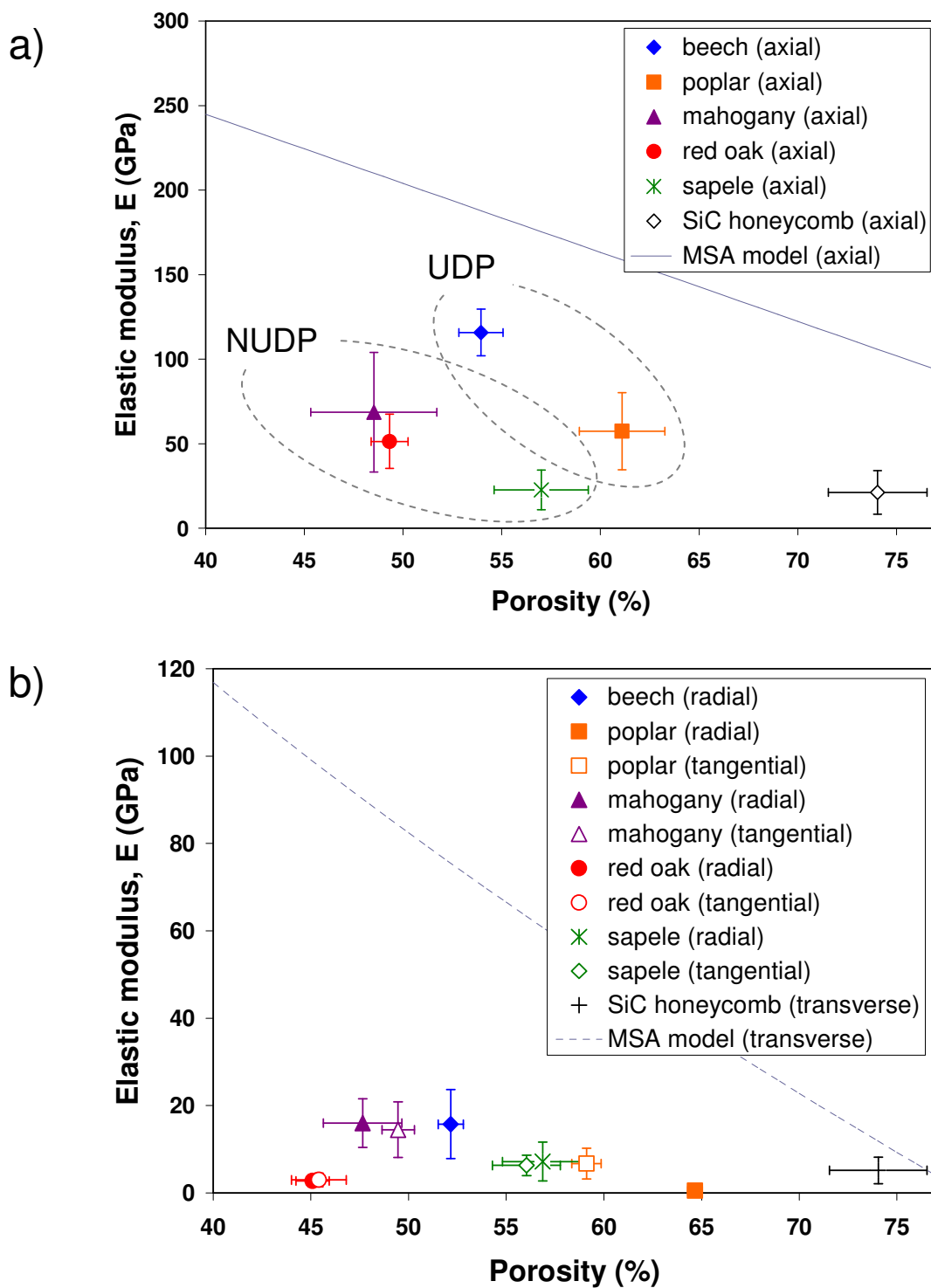


Figure 4.7. Elastic modulus as a function of porosity for (a) axial and (b) transverse bioSiC and SiC honeycomb.

For a material with aligned tubular pores of circular cross-section in a regular simple cubic-type arrangement,  $E$  is predicted in the axial and transverse directions, respectively, by

$$E_{\parallel} = E_o(1 - P) \quad (6)$$

$$E_{\perp} = E_o \left( 1 - \left[ \left( \frac{4}{\pi} \right) P \right]^{1/2} \right) \quad (7)$$

Here,  $P$  is the volume fraction of porosity and  $E_o$  is the elastic modulus of the solid phase. These models are derived by assuming that the relative elastic modulus ( $E/E_o$ ) is equal to the MSA fraction perpendicular to the loading direction. In figure 4.7, the  $E_o$  is taken to be 408 GPa, the value of  $E_{SiC}$  measured by nanoindentation.

The most obvious and expected trend seen in figures 4.6 and 4.7 is the decrease of  $\sigma_{comp}$  and  $E$  with increasing porosity. This is intuitive as elimination of solid material would lead to a reduction in strength and stiffness. In addition to porosity, orientation also plays a role in the compressive properties of bioSiC and SiC honeycomb. For both  $\sigma_{comp}$  and  $E$ , the properties in the axial direction are greater than those in the transverse directions by nearly an order of magnitude. While the MSA model does predict higher values of  $E$  in the axial orientation, experimental values for bioSiC and SiC honeycomb in both the axial and transverse directions fall well below the model predictions.

As mentioned in chapter 2, most of the mechanical property data in the literature is for bioSiC with residual Si (bioSi/SiC). The  $E$  values measured here are on average about half those

reported in the literature for bioSi/SiC (Singh and Salem 2002). This is not surprising as the residual Si serves to reinforce the bioSiC. Similarly,  $\sigma_{comp}$  values measured in this work are about 20% those reported in the literature for bioSi/SiC (Arellano-Lopez and Martinez-Fernandez 2004). Although there are no strength data in the literature for Si melt-infiltrated bioSiC without excess Si, the values measured here do agree with  $\sigma_{comp}$  values for bioSi/SiC measured above the softening temperature of Si (Martinez-Fernandez et al. 2003; Munoz et al. 2002; Varela-Feria et al. 2002).

The bioSiC data for axial compression shown in figures 4.6(a) and 4.7(a) are also categorized as either UDP or NUDP. By grouping these data by precursor type, it is evident that axial  $\sigma_{comp}$  and  $E$  of bioSiC from UDP precursors is, for a given porosity, greater than that of bioSiC from NUDP precursors. No such difference in properties between precursor types is present in the transverse directions. In these directions, for both  $\sigma_{comp}$  and  $E$ , UDP and NUDP bioSiC tend to follow the same trends, with the exception of red oak bioSiC. There is also no significant difference between radial and tangential bioSiC from the same precursor. Also evident is the range of porosities for samples from a single type of precursor. As explained in the previous chapter, this is a result of natural variation of porosity in the wood precursors.

For the most part, SiC honeycomb follows similar trends to bioSiC in terms of dependence on porosity and orientation. Unexpectedly,  $E$  values for SiC honeycomb also fall below values predicted by the MSA model in both the axial and transverse directions. This is surprising because the structure of SiC honeycomb is much more regular than bioSiC and similar to the porous structure assumed by the model.

### 4.3.2. Compressive Test Discussion

#### *Axial Compression*

In addition to a difference in mechanical properties due to orientation, there is also an effect in the axial direction due to precursor type that is independent of porosity. As was done with the volume fraction of unreacted carbon, these data from axial compressive testing can be normalized by

$$\text{normalized } \sigma_{comp} = \frac{\sigma_{comp}}{1-P} \quad (8)$$

$$\text{normalized } E = \frac{E}{1-P} \quad (9)$$

and the range of the difference between the two sample means can be calculated using equation 11 from chapter 3, as shown in table 4.3(a) and (b). From these equations, it can be said with at least 95% confidence that, for a given porosity, bioSiC from UDP precursors is stronger and stiffer in compression than bioSiC from NUDP precursors. In compression, failure is a result of accumulated crack damage and not of the largest flaw as it is in tension (Adams and Sines 1976; Adams and Sines 1977). As a result, the lower  $\sigma_{comp}$  of the NUDP bioSiC in the axial direction cannot be explained simply by the fact that there are larger pores in these materials. However, the difference in  $\sigma_{comp}$  and  $E$  between UDP and NUDP bioSiC is hypothesized to be influenced by the amount of unreacted carbon in the materials.

**Table 4.3. Normalized (a) compressive strength and (b) elastic modulus data showing significant differences between UDP and NU DP bioSiC.**

a)

	$\sigma_{comp}/(1-P)$	Std. Dev.	n	Confidence Level	Range of Diff. between Sample Means
UDP bioSiC	671	272	10	95%	169
NU DP bioSiC	323	136	17		

b)

	$E/(1-P)$	Std. Dev.	n	Confidence Level	Range of Diff. between Sample Means
UDP bioSiC	200	71	10	95%	53
NU DP bioSiC	92	57	17		

The mechanical properties of porous materials are not only a function of pore morphology but also of the properties of the solid phase of the material. As discussed in the previous chapter, there is unreacted carbon in all bioSiC samples. By apparent  $E$  values from nanoindentation, it is shown that  $E_{carbon}$  is lower than  $E_{SiC}$  by an order of magnitude. Greil et al. measured  $\sigma_{comp}$  for amorphous carbon scaffolds from wood (Greil et al. 1998), and these values were significantly lower than those measured here for bioSiC. Hence, the presence of the weaker and more compliant unreacted carbon phase would lead to a reduction in  $\sigma_{comp}$  and  $E$ . As established in chapter 2, the amount of unreacted carbon is greater in NU DP bioSiC than UDP bioSiC. Due to the deleterious nature of this phase, it can be concluded that this is the cause for the greater reduction in  $\sigma_{comp}$  and  $E$  for NU DP bioSiC.

The presence of unreacted carbon is also responsible, in part, for experimental values of  $E$  being less than those predicted by the MSA model. Using values for  $E$  established from nanoindentation and the rule of mixtures, it is possible to determine an effective  $E_{SiC-C}$  for the SiC-unreacted carbon composite solid phase of bioSiC. The upper and lower bounds of  $E_{SiC-C}$  for this two-phase composite are predicted from the rule of mixtures, respectively, by

$$E_{SiC-C(upper)} = E_{bioSiC}V_{bioSiC} + E_{carbon}V_{carbon} \quad (10)$$

$$E_{SiC-C(lower)} = \frac{E_{bioSiC}E_{carbon}}{V_{bioSiC}E_{carbon} + V_{carbon}E_{bioSiC}} \quad (11)$$

Here,  $V$  is volume fraction,  $E_{SiC-C(upper)}$  corresponds to the condition where both phases are parallel to the loading direction, and  $E_{SiC-C(lower)}$  corresponds to the condition where both phases are perpendicular to the loading direction. Using these equations and the unreacted carbon volume fractions from chapter 2, the upper and lower bound for  $E_{SiC-C}$  were calculated for each bioSiC. These values and the porosities measured by Archimedes' method were then used with the MSA model to more accurately predict  $E_{bioSiC}$ , and these values are compared with experimental values in table 4.4 and figure 4.8. From this table, the deleterious effect of unreacted carbon on  $E_{SiC-C}$  is clear. However, from figure 4.8, it is apparent that many of the experimental values still fall well below the values predicted by the MSA model, even when the lower bound  $E_{SiC-C}$  from the rule of mixtures is used. This would indicate some deviation from the ideal structure assumed by the MSA model in bioSiC. Reasons for this additional reduction in properties from the model prediction are presented in the next chapter.

In addition, values for  $E$  and  $\sigma_{comp}$  in the axial direction for the SiC honeycomb are also well below those predicted by the MSA model. This cannot be accounted for by the presence of unreacted carbon and SiC honeycomb has a regular microstructure similar to the one assumed by the model.

**Table 4.4. Comparison of experimental elastic modulus values for axial bioSiC and values predicted by the MSA model (equation 6) using the rule of mixtures (equations 10 and 11) to account for unreacted carbon.**

	<b>AXIAL COMPRESSION</b>						
	<b>Experiment</b>			<b>Rule of Mixtures</b>		<b>MSA Model</b>	
	<b>Porosity</b>	<b>E<sub>axial</sub></b>	<b>vol. frac. C</b>	<b>E<sub>cl</sub></b>	<b>E<sub>ct</sub></b>	<b>E // upper</b>	<b>E // lower</b>
<b><i>Beech</i></b>	53.95%	115.80	11.54%	364.57	161.65	167.88	74.44
<b><i>Poplar</i></b>	61.10%	57.40	8.40%	376.49	193.46	146.45	75.25
<b><i>Mahogany</i></b>	48.53%	68.60	35.41%	273.94	71.86	141.00	36.98
<b><i>Red Oak</i></b>	49.32%	51.40	13.82%	355.91	144.42	180.37	73.19
<b><i>Sapele</i></b>	57.01%	22.70	11.65%	364.15	160.73	156.55	69.10

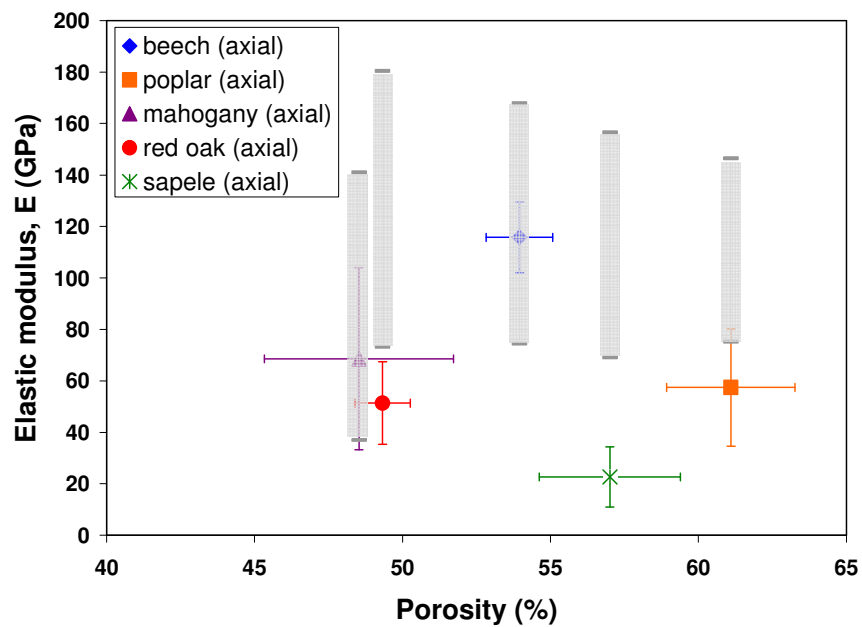


**Figure 4.8.** Plot of  $E$  as a function of porosity in the axial direction with gray bars showing the upper and lower bound MSA values when unreacted carbon is accounted for using the rule of mixtures.

However, the volume fraction of porosity in SiC honeycomb can account for these low values. Above a porosity of 70%, materials are considered cellular. Porous and cellular materials differ because, at high porosities, pores begin to interact and with each other and properties are no longer governed by the MSA model. Instead, the properties are governed by the model developed by Gibson and Ashby (Gibson and Ashby 1997), where

$$E \approx E_o(1-P)^n \quad (12)$$

Because the square pores of SiC honeycomb are tubular and the wall porosity is not, the constant  $n$  in equation 12 is likely between 1 ( $n_{axial\ honeycomb}$ ) and 2 ( $n_{foam}$ ). This would give an expected  $E$  value as low as 27.5 GPa, which is lower than that predicted by the MSA model and very close to the experimental value of  $21.2 \pm 12.9$  GPa.

### *Transverse Compression*

As mentioned above, in transverse compression, each type of UDP and NUDP bioSiC follow the same trend for  $\sigma_{comp}$  and  $E$  with respect to porosity with the exception of red oak bioSiC. In this orientation, the  $\sigma_{comp}$  and  $E$  values for red oak bioSiC are much lower than expected. This can be explained by the nature of the porosity in this material. As shown in figure 3.7 (i), red oak is a ring porous wood and the porosity in the resulting bioSiC is extremely inhomogeneous with large vessel pores and small fiber and tracheid pores segregated into bands. The vessel pore bands are highly porous and serve as easy fracture paths. This results in a lower value of  $E$  and fracture of this material at lower than expected loads. This effect is not seen in

axial compression because the pore bands are in a parallel-type orientation and stress is redistributed to the denser bands. However, in transverse compression, these pore bands are loaded in a series-type orientation and  $\sigma_{comp}$  and  $E$  are limited by the high porosity bands.

Aside from red oak bioSiC, the difference in  $\sigma_{comp}$  and  $E$  in the axial direction between UDP and NUDP bioSiC that was attributed to differing carbon contents is absent in the transverse direction. This is due to the way  $E$  scales with solid phase  $E$  ( $E_o$ ) in the axial and transverse orientations. This becomes clear by plotting  $E$  as predicted by the MSA model as a function of  $E_o$  for constant porosity in the axial and transverse orientations (figure 4.9). From figure 4.9, it is clear that axial properties are more sensitive to changes in  $E_o$  than are transverse properties. In the axial orientation, deformation occurs by compression of the solid phase, and properties of the bulk material are more sensitive to changes in the properties of the solid phase. In transverse orientation, the material has lower  $\sigma_{comp}$  and  $E_{effective}$  because properties are determined by pore wall bending and are less sensitive to changes in the properties of the solid phase. For this reason, the differing carbon contents in UDP and NUDP bioSiC do not cause a significant difference in  $\sigma_{comp}$  and  $E$  in the transverse orientation. This difference in deformation mechanisms also explains the lower values for  $\sigma_{comp}$  and  $E$  in the transverse orientation.

While unreacted carbon does not separate UDP and NUDP bioSiC in the transverse orientation, its presence does, in part, explain why experimental  $\sigma_{comp}$  and  $E$  values are lower than those predicted by the MSA model.

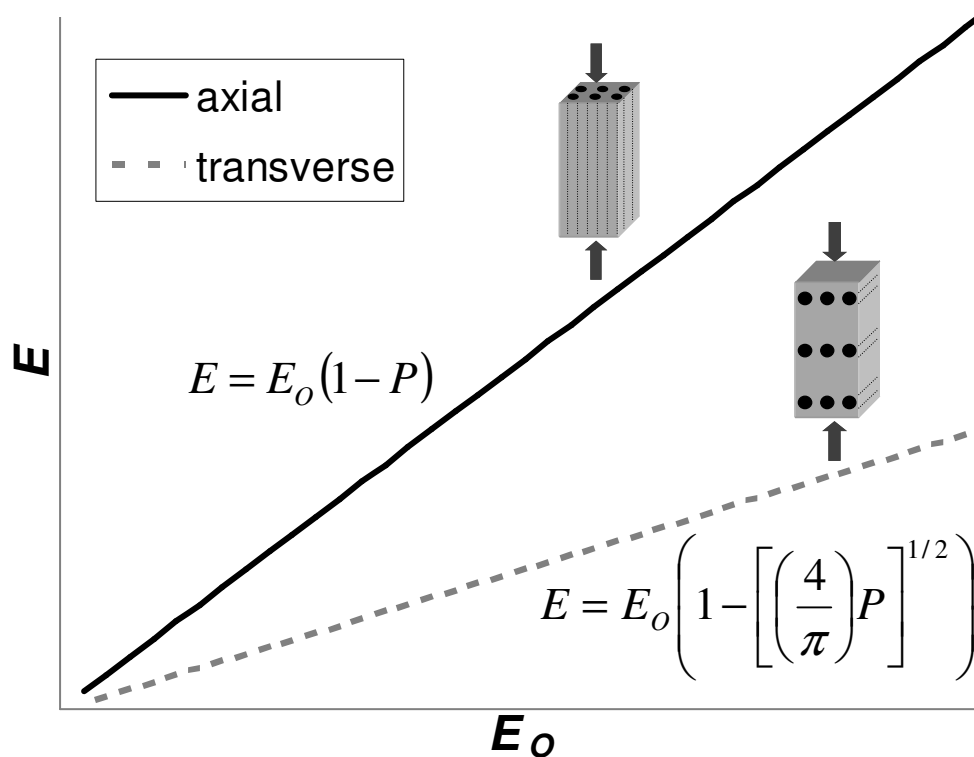


**Figure 4.9. Bulk elastic modulus as a function of solid phase elastic modulus for constant porosity (50%) as predicted by the MSA model.**

Again using the rule of mixtures, the upper and lower bounds of solid phase  $E$  given the previously quantified carbon contents were compared to experimental values (table 4.5 and figure 4.10). As in the axial direction, figure 4.10 shows that experimental  $E$  values still fall below even the lower bound  $E_{bioSiC}$  predicted by the MSA model. This indicates that unreacted carbon accounts for only a portion of the reduction in  $\sigma_{comp}$  and  $E$  in the transverse direction. Reasons for the additional reduction in  $\sigma_{comp}$  and  $E$  will be presented in the next chapter.

The lower than expected results for  $E_{bioSiC}$  in the transverse direction are not entirely negative. One previously proposed application for bioSiC was as a bioimplant, and transverse  $E_{bioSiC}$  values are very close to those reported for cortical bone (Fan et al. 2002; Weiner et al. 1999). This similarity in  $E$  is crucial for bone replacement in order to avoid a phenomenon known as stress shielding, which occurs when load is transferred from natural bone to an implant. This results in atrophy of the bone surrounding and often occurs with high  $E$  ceramic implants (Black 1999).

Transverse values of  $\sigma_{comp}$  and  $E$  for SiC honeycomb also fall below the values predicted by the MSA model. This is again due to the cellular nature of SiC honeycomb. In the transverse direction,  $E$  is also controlled by equation 12 with an expected value of  $n$  between 2 ( $n_{foam}$ ) and 3 ( $n_{transverse\ honeycomb}$ ). This predicts an  $E$  values as low as 7.1 GPa, which is very close to the experimental value of  $5.2 \pm 3.03$  GPa.

**Table 4.5. Comparison of experimental elastic modulus values for transverse bioSiC and values predicted by the MSA model (equation 7) using the rule of mixtures (equations 10 and 11) to account for unreacted carbon.**

	<b>TRANSVERSE COMPRESSION</b>						
	<b>Experiment</b>			<b>Rule of Mixtures</b>		<b>MSA Model</b>	
	<b>Porosity</b>	<b><math>E_{\text{transverse}}</math></b>	<b>vol. frac. C</b>	<b><math>E_{\text{cl}}</math></b>	<b><math>E_{\text{ct}}</math></b>	<b>E // upper</b>	<b>E // lower</b>
<b><i>Beech (radial)</i></b>	52.16%	15.75	11.54%	364.57	161.65	67.47	29.92
<b><i>Poplar (radial)</i></b>	64.66%	0.55	8.40%	376.49	193.46	34.88	17.92
<b><i>Poplar (tangential)</i></b>	59.11%	6.75	8.40%	376.49	193.46	49.87	25.63
<b><i>Mahogany (radial)</i></b>	47.65%	16.00	35.41%	273.94	71.86	60.57	15.89
<b><i>Mahogany (tangential)</i></b>	49.46%	14.50	35.41%	273.94	71.86	56.55	14.83
<b><i>Red Oak (radial)</i></b>	45.09%	2.80	13.82%	355.91	144.42	86.24	34.99
<b><i>Red Oak (tangential)</i></b>	45.41%	3.00	13.82%	355.91	144.42	85.28	34.61
<b><i>Sapele (radial)</i></b>	56.89%	7.20	11.65%	364.15	160.73	54.23	23.93
<b><i>Sapele (tangential)</i></b>	56.04%	6.33	11.65%	364.15	160.73	56.55	24.96

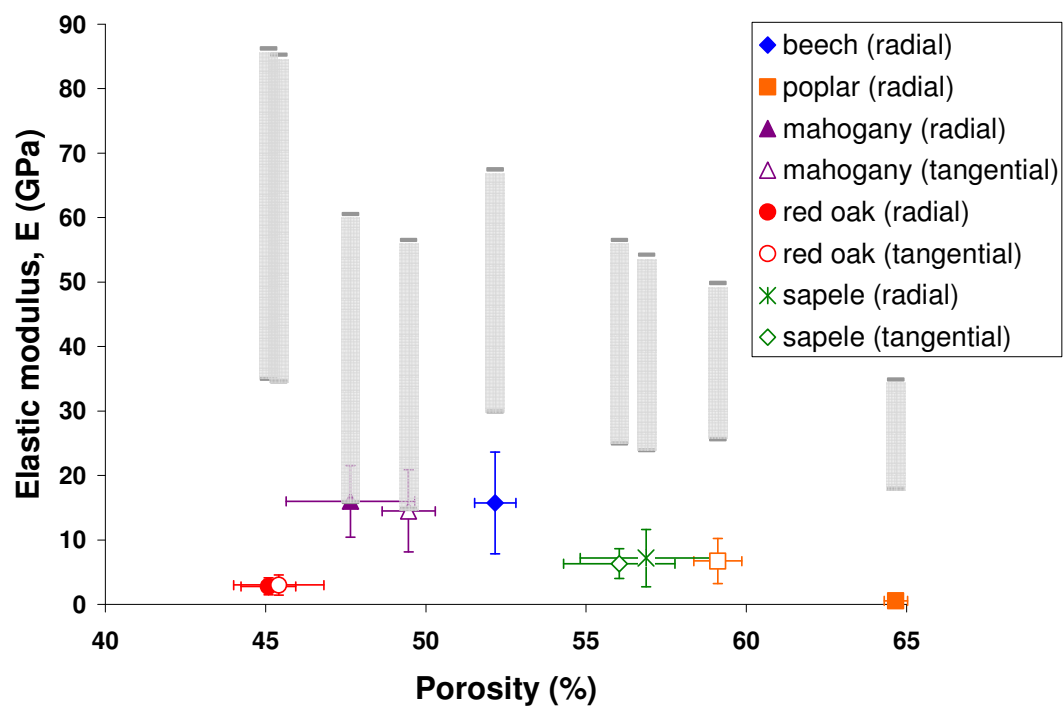


**Figure 4.10. Plot of  $E$  as a function of porosity in the transverse direction with gray bars showing the upper and lower bound MSA values when unreacted carbon is accounted for using the rule of mixtures.**

### *Fractographic Analysis*

The fracture surfaces of compressive samples were examined after testing to determine crack paths and their dependence on microstructural features and phase composition in bioSiC. This analysis shows evidence of a preferred crack path as fracture in both axial and transverse orientations always occurred in planes parallel to the axial direction.

In the axial orientation, samples tend to fracture parallel to the loading axis with no crack deflection as shown in figure 4.11. Here, “half” vessel pores are visible on the fracture surface indicating that cracks propagated in porous planes as expected and predicted by the MSA model. In transverse loading, fracture paths are influenced by precursor features such as growth rings and rays which result from changes in growth rate and grouped alignment of pores in wood. Growth rings and rays are manifest as density gradients in bioSiC and can serve as sources for crack deflection. Additionally, unreacted carbon with lower  $\sigma_{comp}$  than SiC is most likely to be present in the lower porosity regions of these density gradients. Consequently, in transverse loading, cracks tend to deflect perpendicular to the loading axis or follow the path of growth rings or rays. This is shown in fracture profiles in figure 4.12 and is especially clear in red oak bioSiC (figure 4.12(d)) because of the extreme inhomogeneity between vessel pore and fiber and tracheid pore bands. These density gradients exist in both the radial and tangential samples and the crack paths in both are very similar. As shown in figure 4.13, the fracture surfaces of transverse samples are very similar to those of axial samples. This again shows evidence of the preferred crack path in planes parallel to the axial direction.

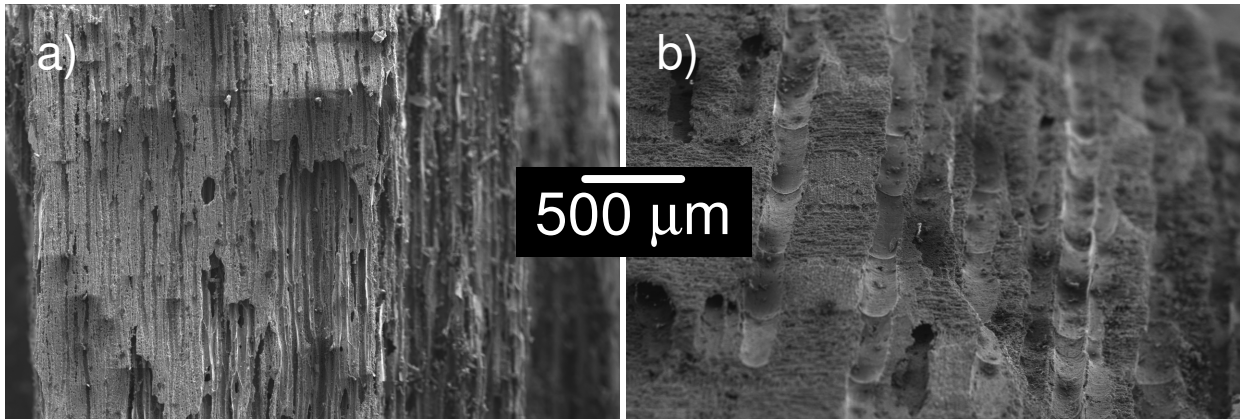


**Figure 4.11. SEM micrographs of fracture surfaces of UDP (poplar) and NUDP (sapele) axial bioSiC samples tested in compression.**

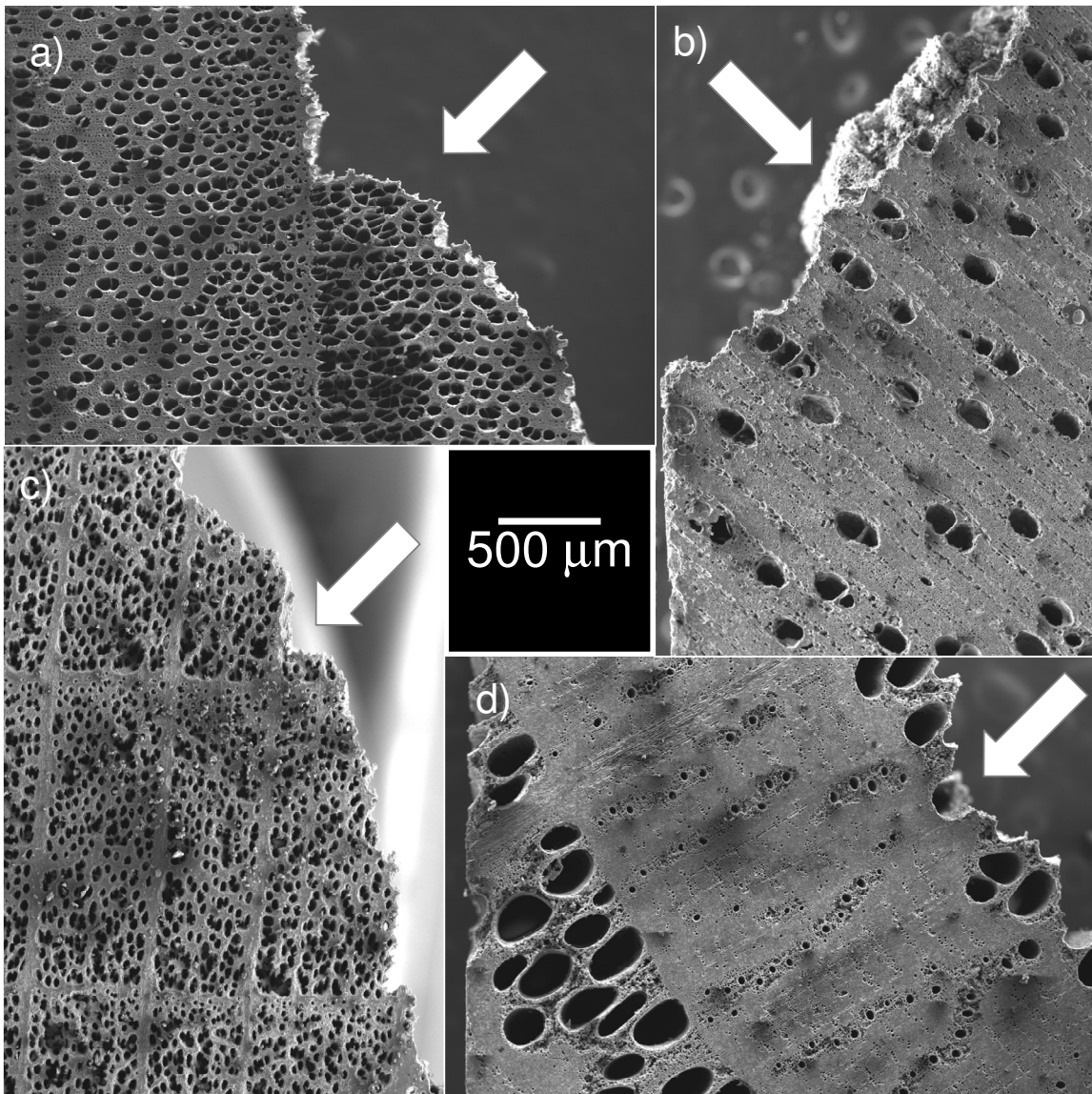


**Figure 4.12. SEM micrographs of fractured compression samples of (a) poplar, (b) mahogany, (c) beech, and (d) red oak bioSiC (arrows point to fracture surfaces).**

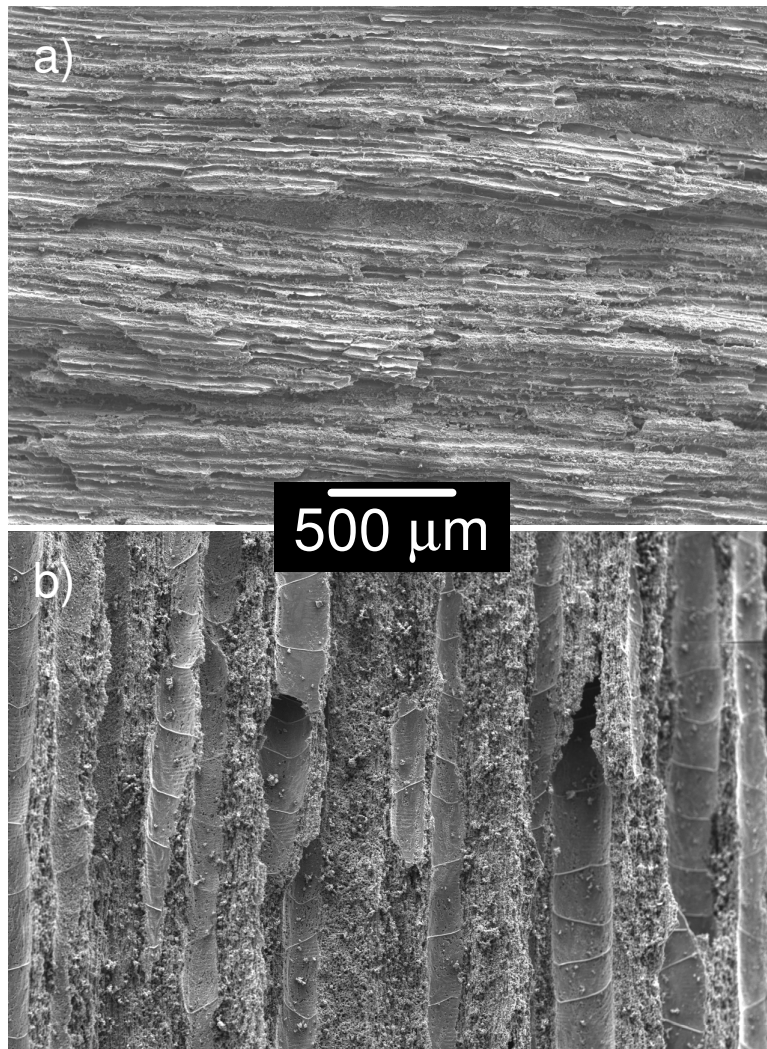


**Figure 4.13. SEM micrographs of fracture surfaces from transverse (a) poplar and (b) red oak bioSiC samples tested in compression.**

Fracture surfaces and profiles of axial and transverse SiC honeycomb samples are also shown in figure 4.14. In this material, cracks again traveled through porous regions of the material. In the transverse orientation, cracks tended to follow square pore diagonals (figure 4.14(b)), most likely because the corners of these pore served as stress concentrators.

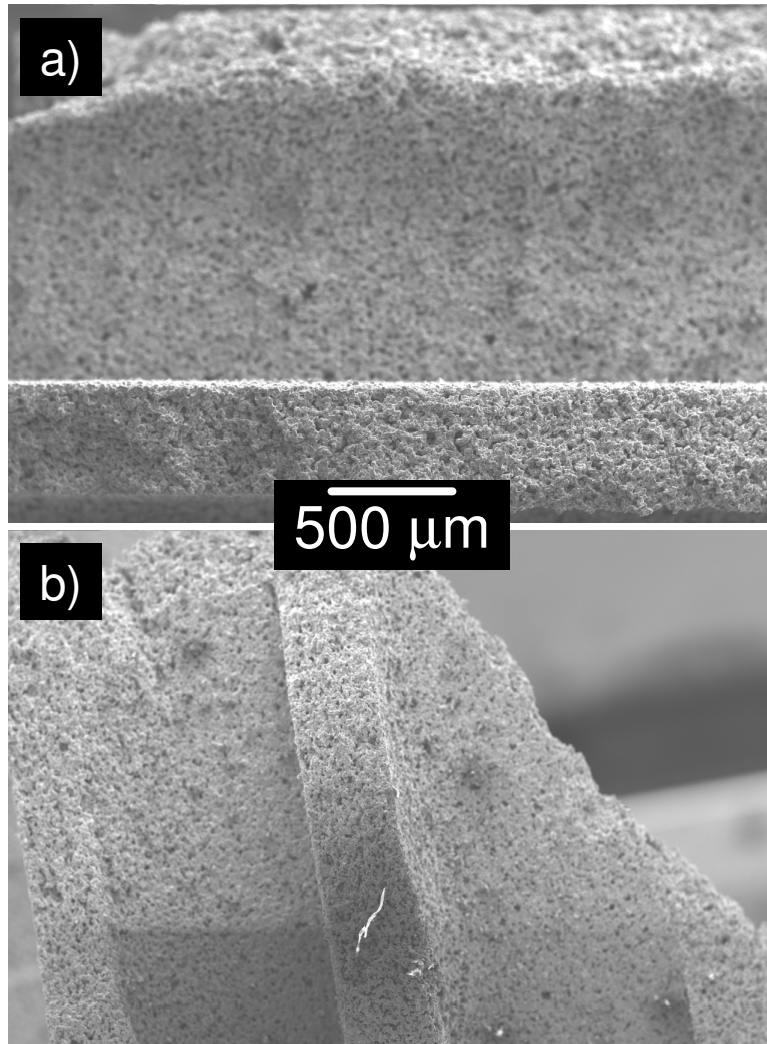


**Figure 4.14. SEM micrographs of (a) fracture surface and (b) profile of SiC honeycomb samples tested in compression.**

#### 4.4. Fracture Toughness Results and Discussion

In addition to excellent compressive properties, wood is also a relatively tough material (Gibson 1992). Much of this toughness comes from the compliance of the phases that make up wood. While the structure of wood is retained in bioSiC, the compliant organic phases of wood have been replaced by brittle inorganic phases. This section presents the results of fracture toughness testing and the effects of this retained wood structure.

##### 4.4.1. Fracture Toughness Results

As with  $\sigma_{comp}$  and  $E$ ,  $K_{IC}$  results for bioSiC and SiC honeycomb also show a strong dependence on orientation in addition to porosity. The results for axial and transverse orientations are shown in figure 4.15. It is clear from these results that bioSiC is significantly tougher in the axial orientation than the transverse orientation. In SENB testing, cracks propagate from the notches with the crack plane parallel to the notch. As a result, cracks propagate in planes parallel to the axial direction in transverse samples and perpendicular to the axial direction in axial samples. Transverse samples correspond to the conditions where the tubular pores are aligned vertically with the notch or horizontally with the notch as shown in figure 4.16.

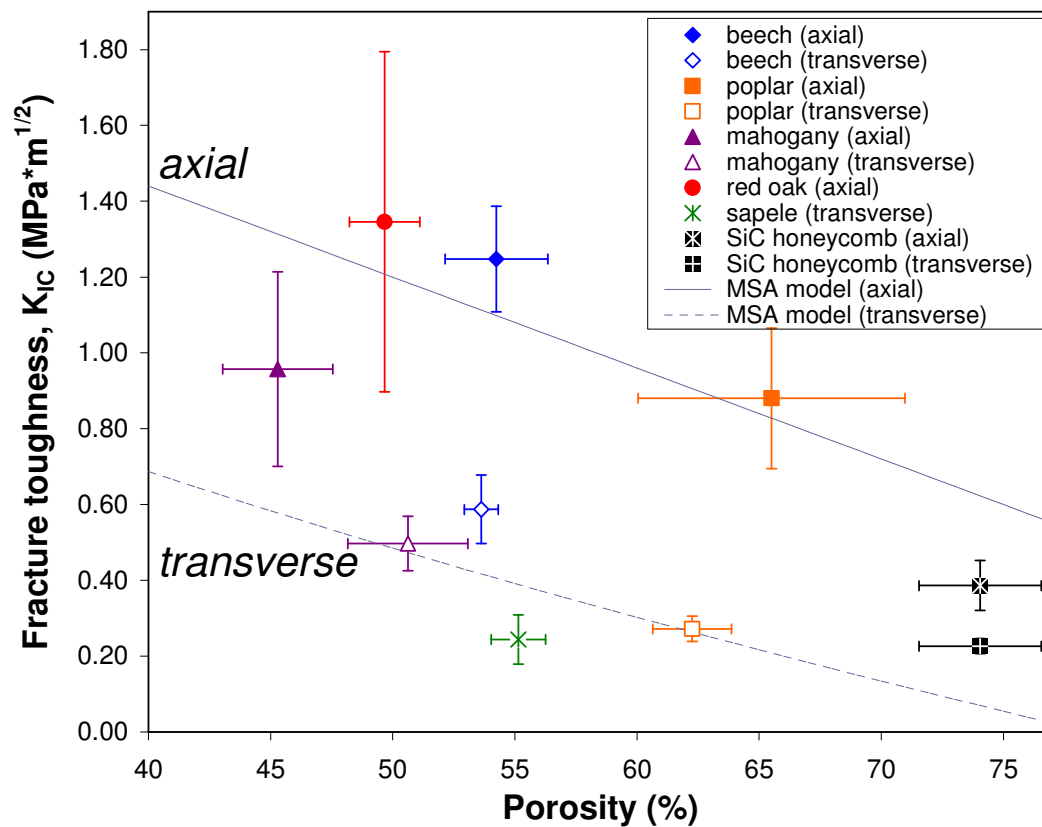
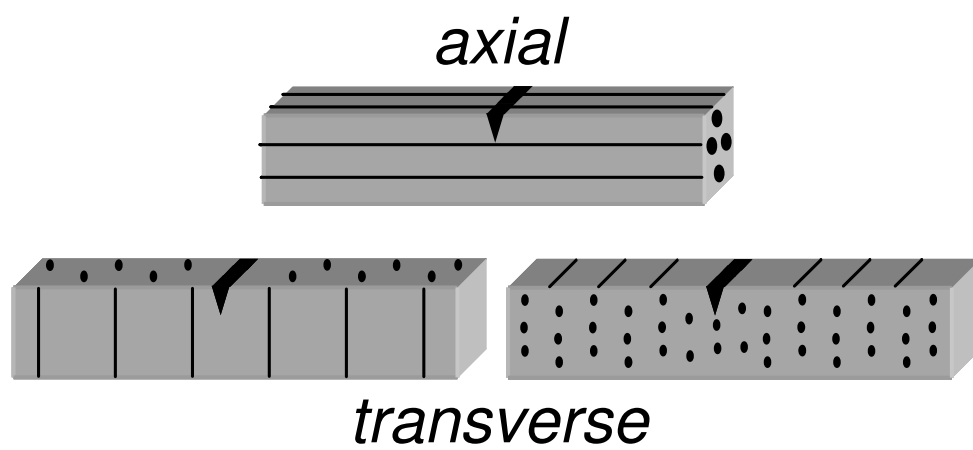


Figure 4.15. Fracture toughness of bioSiC and SiC honeycomb (axial and transverse orientations) as a function of porosity.



**Figure 4.16.** Schematics of axial and transverse bioSiC fracture toughness samples.

The MSA model was also used to model  $K_{IC}$ , and the values predicted by the model are also shown in figure 4.15. For  $K_{IC}$ , MSA model values in the axial and transverse directions are given, respectively by

$$K_{IC_A} = K_{IC_o}(1 - P) \quad (13)$$

$$K_{IC_T} = K_{IC_o} \left( 1 - \left[ \left( \frac{4}{\pi} \right) P \right]^{1/2} \right) \quad (14)$$

Here,  $K_{IC}$  is taken to be the toughness of SiC ( $2.4 \text{ MPa} \times \text{m}^{1/2}$ ) (Faber and Evans 1983). These equations are similar to those of  $E$  as the dependence of  $K_{IC}$  on porosity is the same as that of  $E$  (Rice 1998).

For  $K_{IC}$  of bioSiC, values in the axial and transverse orientations tend to agree with those predicted by the MSA model. As with  $\sigma_{comp}$  and  $E$ , there are no data in the literature on  $K_{IC}$  of bioSiC without residual Si. The  $K_{IC}$  values reported for axial and transverse samples of beech bioSi/SiC are approximately 20 % higher than the values measured here (Hou et al. 2006). This is again due to the presence of residual Si instead of pore space. Unlike bioSiC,  $K_{IC}$  values for SiC honeycomb are very similar in the axial and transverse orientations and do not agree with the MSA model.

#### 4.4.2. Fracture Toughness Discussion

Unlike  $\sigma_{comp}$  and  $E$ , there is no difference between UDP and NUDP bioSiC. This is true in both the transverse orientation and the axial orientation where properties are more dependent on the properties of the solid portion of the material. In addition, the experimentally measured values of  $K_{IC}$  agree with those predicted by the MSA model. These trends can both be explained by the fact that  $K_{IC}$  of amorphous carbon is at least as high as that of SiC (Li and Bhushan 1999). Hence, the presence of unreacted carbon has little effect on the fracture toughness of bioSiC and the measured values agree with the MSA model.

Although there is no effect from the presence of unreacted carbon, there is an effect from orientation on  $K_{IC}$  of bioSiC. This again has to do with the preferred crack path that exists in bioSiC. In the transverse samples, cracks are allowed to propagate in preferred planes parallel to the axial orientation. There is no distinction between the two transverse orientations shown in figure 4.16 because this condition holds in both. In the axial samples, cracks are forced to propagate in non-preferred planes perpendicular to the axial orientation. This path is much more tortuous as cracks are deflected by the previously discussed density gradients resulting from natural wood features.

Again as a result of the cellular nature of SiC honeycomb, experimental values do not agree with those predicted by the MSA model. In the case of  $K_{IC}$ , values are given by the Gibson and Ashby model by

$$K_{IC} \approx K_{IC_0} (1 - P)^{3/2} \quad (15)$$

in both the axial and transverse directions. This predicts a value of  $0.34 \text{ MPa} \times \text{m}^{1/2}$ , which is in reasonable agreement with experimental values.

### *Fractography*

As with compressive samples, fracture surfaces of toughness samples were also examined to determine crack paths. Similarly, the natural features of wood again played a role in crack propagation. Fracture surfaces from both axial and transverse bioSiC samples are shown in figure 4.17. From these images, the orientation of the crack plane relative to the axial direction is evident. From the fractured red oak bioSiC sample shown in figure 4.18, clear evidence of crack deflection by the density gradients resulting from segregated pore bands in the wood precursor is apparent. Fractured axial and transverse SiC honeycomb samples are shown in figure 4.19. Because of the lack of similar density gradients, no such crack deflections are observed in this material.

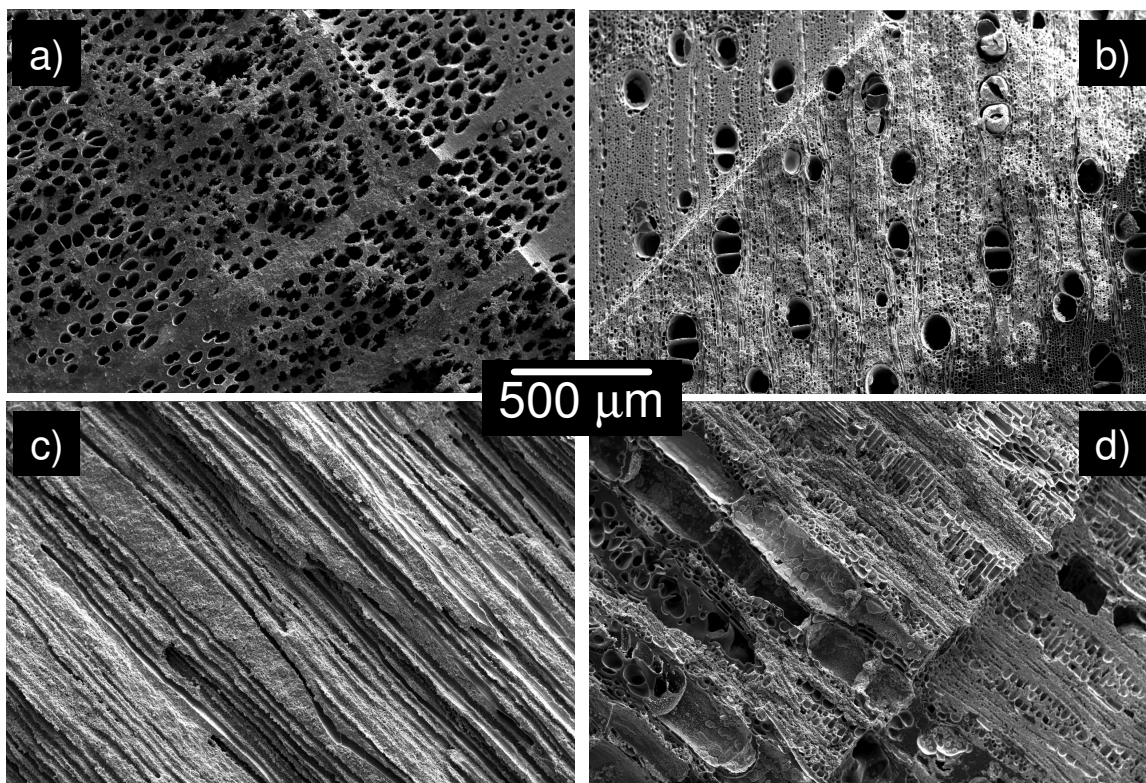


**Figure 4.17. SEM micrographs of fracture surfaces of axial (a) beech and (b) mahogany, and transverse (c) poplar and (d) sapele bioSiC fracture toughness samples.**

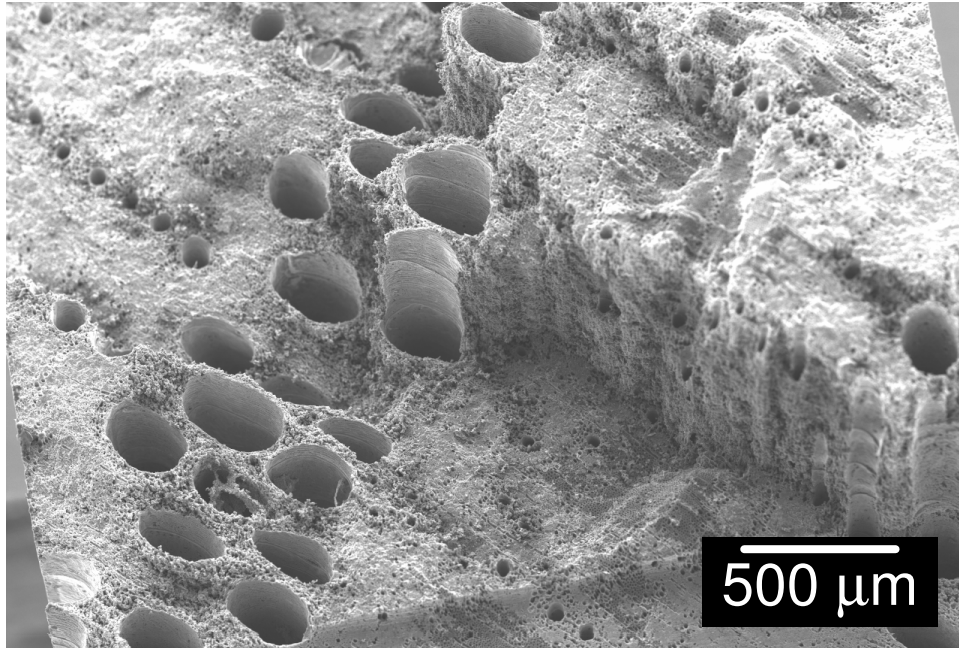


**Figure 4.18. SEM micrograph of fracture surface of axial fracture toughness red oak bioSiC sample.**

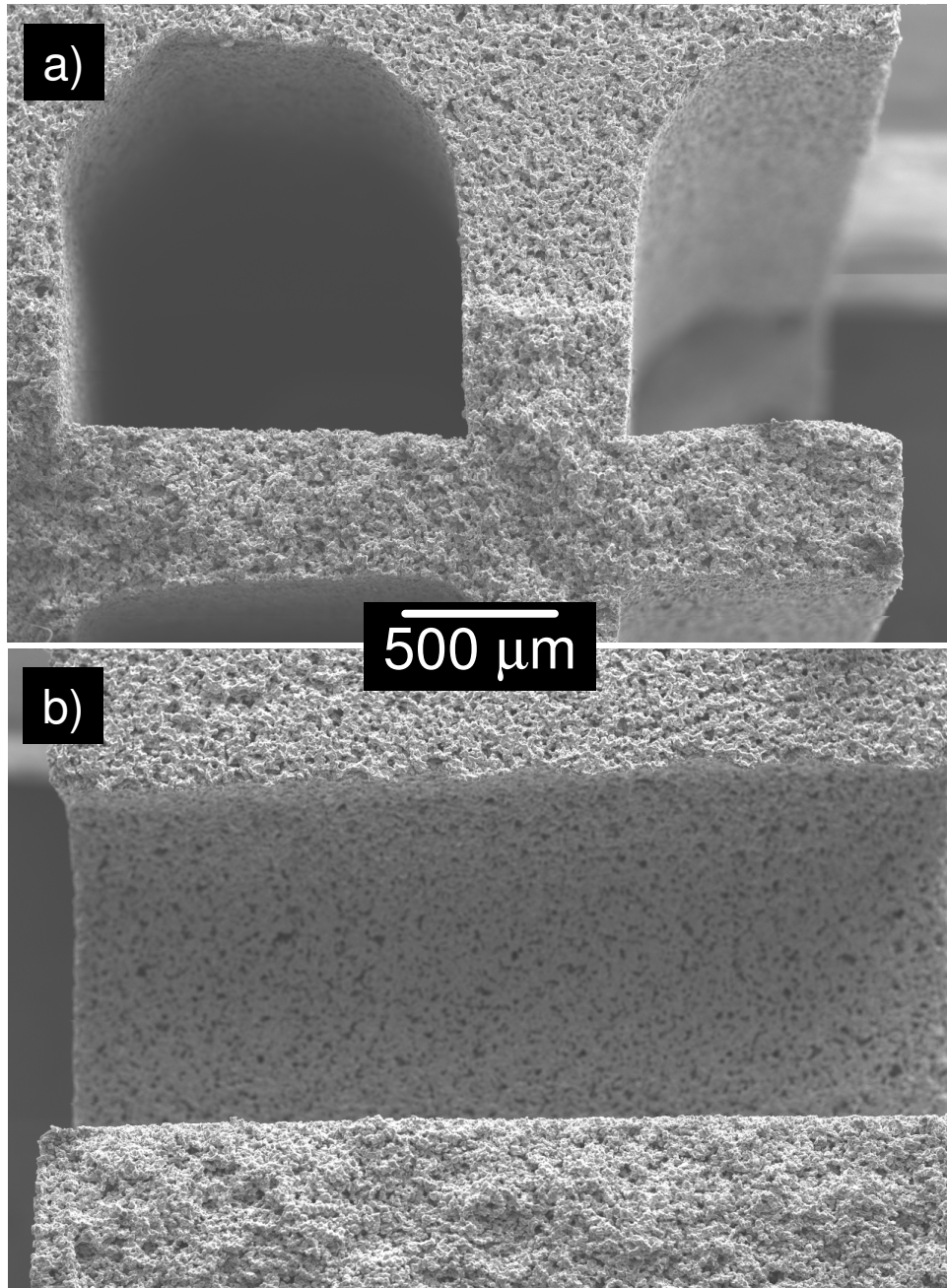


**Figure 4.19. SEM micrographs of fracture surface of (a) axial and (b) transverse SiC honeycomb fracture toughness samples.**

#### 4.5. Summary

In order to establish structure-mechanical property relationships, bulk and specific mechanical properties of bioSiC and SiC honeycomb were measured and related to results presented in the previous chapter. These results were also compared against model predictions based on an ideal microstructure, and the mechanical properties of bioSiC were found to be a function of porosity, orientation, and phase composition.

The  $E$  of unreacted carbon was found to be an order-of-magnitude lower than that of SiC. For a given porosity in axial compression, this led to a lower  $E$  and  $\sigma_{comp}$  for NUDP bioSiC when compared to UDP bioSiC and caused results for all bioSiC to fall below model values. The presence of unreacted carbon was accounted for using the rule-of-mixtures. However, values were still below those predicted by the model indicating that the results cannot be explained by the presence of unreacted carbon alone. Toughness of bioSiC was found to agree with the model as  $K_{IC}$  values for SiC and unreacted carbon are very similar. BioSiC was also found to have a preferred crack path in the axial plane. For SiC honeycomb, mechanical property values were found to agree with the Gibson and Ashby model for cellular materials as the fraction of porosity in these materials was above 70%.

# 5

## Finite-Element Analysis of Mechanical Behavior in Biomorphic Silicon Carbide

In addition to mechanical testing of bioSiC and SiC honeycomb, mechanical behavior was also analyzed using finite-element analysis. This analysis provided additional knowledge of mechanical behavior and helped to explain many of the trends seen in mechanical testing. Along with finite-element analysis of bioSiC microstructures, idealized microstructures were also created to isolate and gauge the effect of certain microstructural features on mechanical behavior. The methods used and the results of finite-element analysis are presented in this chapter along with discussion on how these results relate to previous analyses.

### **5.1. Object-Oriented Finite-Element Analysis**

By using finite-element analysis, the mechanical behavior of materials can be modeled and the effect of specific microstructural features can be determined. In the case of bioSiC, there are several microstructural and compositional variables that may affect mechanical behavior, and their roles are difficult to determine by mechanical testing alone. These variables include: pore volume, pore orientation, pore shape, pore size, pore alignment, pore distribution, and phase composition. Because of these variables and the natural, complex microstructure of bioSiC, a two-dimensional object-oriented finite-element analysis system (OOF) developed by researchers at the National Institute of Standards and Technology (NIST) was utilized (Langer et al. 2000;

Langer et al. 2001). While many finite-element analysis programs exist, OOF was chosen because it is designed to allow virtual mechanical testing on real microstructures. From this testing, macroscopic mechanical properties and their dependence on microstructure can be determined.

#### 5.1.1. Creation of Finite-Element Mesh

Finite-element meshes were created in a program called ppm2oof, which works in tandem with OOF (Langer et al. 2000). The mesh is created from a digitized image, like a micrograph. Material properties such as elastic modulus can then be set by the selection of pixels in the image and the assignment of properties using OOF elements. There are several tools in ppm2oof that aid in the selection of image pixels based on gray-scale value. In the case of bioSiC, digitized SEM micrographs were used and a threshold was set to create a black-and-white image where black pixels corresponded to pore space and white pixels represented solid material. Following the assignment of properties, a uniform finite-element mesh is created. Based on the assignment of properties in the image, this mesh can be intelligently adapted to closely match the original image using different ppm2oof functions to recreate the image in the finite-element mesh. This sequence is shown in figure 5.1.

The advantage of the dual-program OOF system over other finite-element programs is in the ability to create finite-element meshes that mimic real microstructures instead of model microstructures. This is especially useful for a complex material such as bioSiC.

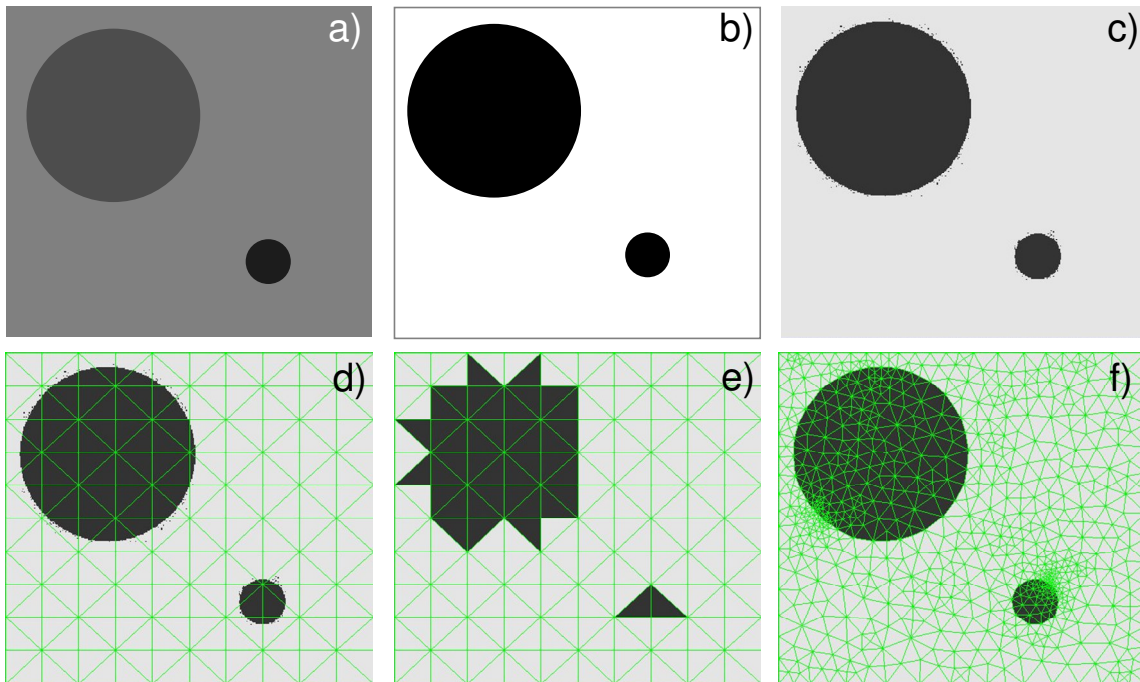


**Figure 5.1. Sequence used to create a finite-element mesh in OOF beginning with a a) digitized image to which a b) threshold is applied followed by the c) assignment of properties. Finally a d) grid is created forming a e) coarse finite-element mesh that is adapted to the image resulting in the f) final mesh.**

### 5.1.2. Virtual Mechanical Testing

Following the creation of the finite-element mesh in ppm2oof, OOF can be used to perform virtual mechanical tests using the mesh. The assignment of properties to pixels in an image in ppm2oof is done by the use of OOF elements. There are several different elements in OOF that are used to simulate the behavior of different material phases. These include elements that can be used to simulate porosity, crystallographic anisotropy, or brittleness. The elements used in the modeling of bioSiC were the empty element, which simulates pore space, the isotropic element, which simulates the properties of an isotropic linear elastic material, and the Griffith2 element, which simulates a brittle element capable of “virtual fracture.”

While no property inputs are necessary for empty elements, both isotropic and Griffith2 elements require inputs to assign mechanical properties. For the isotropic element, elastic modulus ( $E$ ), and Poisson’s ratio ( $\nu$ ) are input and the condition of plane stress or plane strain must be specified. Given the honeycomb-like structure of bioSiC, plane strain was assumed as this corresponds to a very thick specimen. Under this assumption, OOF calculates the stiffness matrix using  $E$  and  $\nu$  as

$$\frac{E(1-\nu)}{(1+\nu)(1-2\nu)} \begin{pmatrix} 1 & \frac{\nu}{1-\nu} & 0 \\ \frac{\nu}{1-\nu} & 1 & 0 \\ 0 & 0 & \frac{1-2\nu}{2(1-\nu)} \end{pmatrix}$$

The Griffith2 element includes assignment of these properties as well as others in order to allow elements to fail under the Griffith criterion to simulate brittle fracture. The Griffith criterion states that a crack will propagate if the elastic energy in a body is enough to create a new surface and is given for an elliptical crack by

$$\sigma_c = \left( \frac{2E\gamma_s}{\pi a} \right)^{1/2} \quad (1)$$

Here,  $\sigma_c$  is critical stress,  $\gamma_s$  is the specific surface energy, and  $a$  is the half crack length. In addition to  $E$  and  $\nu$ , the Griffith2 element also includes  $\gamma_s$  and two “knockdown” factors. While OOF elements cannot actually fracture, if the Griffith criterion is met, elements are mutated during testing by multiplying the rotated stiffness matrix by the specified knockdown factors and redistributing load to the other elements, thus allowing elements to quasi-fracture.

In order to perform virtual mechanical tests in OOF, boundary conditions can be set and displacements can be imposed. The mesh is then equilibrated and the response of the material is dictated by the assigned elements and properties. Outputs include both qualitative and quantitative data such as images of stress distribution and fracture, as well as effective values of  $E$ . These data can be coupled with mechanical testing results to further analyze the mechanical behavior of bioSiC.

### 5.1.3. Materials Analysis by OOF

Finite-element analysis has previously been used by other researchers to analyze the mechanical behavior of bioSiC (Fey et al. 2005). However, this work used a simple model structure to represent the microstructure of bioSiC and only analyzed properties in the transverse direction. In contrast to an idealized model-structure, using an object-oriented program such as OOF enables the creation of finite-element meshes based on real microstructures and may better model the properties of the real material.

OOF has been used in the past by many researchers to model both thermal and mechanical behavior of materials. For example, Zimmerman et al. used OOF to model fracture of a textured ceramic (Zimmerman et al. 2001) and Saigal et al. used it to analyze the effect of interface properties on microcracking (Saigal et al. 1998). Additionally, OOF has been used to model the effects of porosity on the mechanical properties of glass (Cannillo et al. 2003), functionally graded ceramics (Cannillo et al. 2006), and plasma-sprayed coatings (Wang et al. 2003). As a result of the heterogeneous-nature of these materials, the microstructure-based meshing capability of OOF was essential.

## 5.2. Experimental Plan

From the results of mechanical testing, it is clear that the presence of unreacted carbon has a negative effect on  $\sigma_{comp}$  and  $E$  of bioSiC. However, these results also indicate that other variables affect the properties of bioSiC and cause them to differ from a porous SiC material with a more ideal microstructure. To determine these additional factors, OOF was used to analyze mechanical behavior as a function of microstructure for real bioSiC micrographs as well

as idealized porous structures in both axial and transverse orientations. Idealized structures were used in order to isolate microstructural features and determine their effect on mechanical behavior. For the properties of the solid component of the material, the phase composition and nanoindentation results presented previously were used. Additionally, Griffith2 elements were also used to simulate fracture in bioSiC to further analyze the effects of microstructure on fracture paths. Initially for the porous phase, empty elements were used. However, for many of the high porosity meshes, OOF was unable to solve for the mechanical properties of the material. This was due to the large discrepancy between the matrix stiffness and the pore space, which prevents convergence of the OOF solver (Reid 2006). To avoid this, the pore space in all materials was represented by isotropic elements with properties assigned to represent pore space ( $E = 0.1$  GPa and  $\nu = 0$ ). To verify this method, OOF meshes that were solvable when empty elements were used to represent pore space were also tested using isotropic elements for pore space. This method was validated as the  $E_{effective}$  values reported for both cases were in agreement. As with mechanical testing, OOF tests were performed in compression with the top and bottom surfaces of the virtual material fixed in order to simulate compressive testing.

### **5.3. Mechanical Behavior of BioSiC in Axial Compression**

In the previous chapter, it was concluded that the deleterious effects of unreacted carbon on the properties of bioSiC were, in part, responsible for lower than expected experimental values of  $\sigma_{comp}$  and  $E$  for NUDP bioSiC in axial compression when compared to UDP bioSiC. Additionally, the fact that measured properties for both UDP and NUDP bioSiC in axial compression were lower than those predicted by the MSA model was also attributed, in part, to

the presence on unreacted carbon. However, when the properties of this phase were accounted for using the rule-of-mixtures, experimental values were still lower than expected. This indicates that additional factors, such as deviation of the structure from the assumptions of the model, are responsible for the behavior of bioSiC in axial compression.

### 5.3.1. Effective Axial Elastic Modulus

To determine the effects of the structure of bioSiC on the properties in axial compression, ppm2oof was used to create finite-element meshes from micrographs of transverse bioSiC planes. Examples of these micrographs are shown in figure 5.2. From these images, it is clear that, while anisotropic tubular pores are present in this plane, the diameter and alignment of these pores are not constant. A threshold was applied to these images to create a two-phase material so that the large vessel pores were isolated and the rest of the material was considered to be solid. A finite-element mesh based on the two-phase image was then created using ppm2oof. The meshes corresponding to the micrographs from each bioSiC are also shown in figure 5.2. Using image analysis, the porosities of the finite-element mesh images were measured and found to be in agreement with the two-phase micrographs and the previously determined vessel porosities, indicating the finite-element meshes were representative of the bioSiC microstructures.

These finite-element meshes were assigned properties using isotropic elements for both the solid component and the pore space ( $E_{pore} = 0.1$  GPa,  $\nu_{pore} = 0$ ). As with image analysis, it was difficult to image both large vessel pores and small fiber and tracheid pores and still have a representative image. Additionally, meshing images of higher resolution or very small features created extremely large files or led to over meshing of individual image pixels.

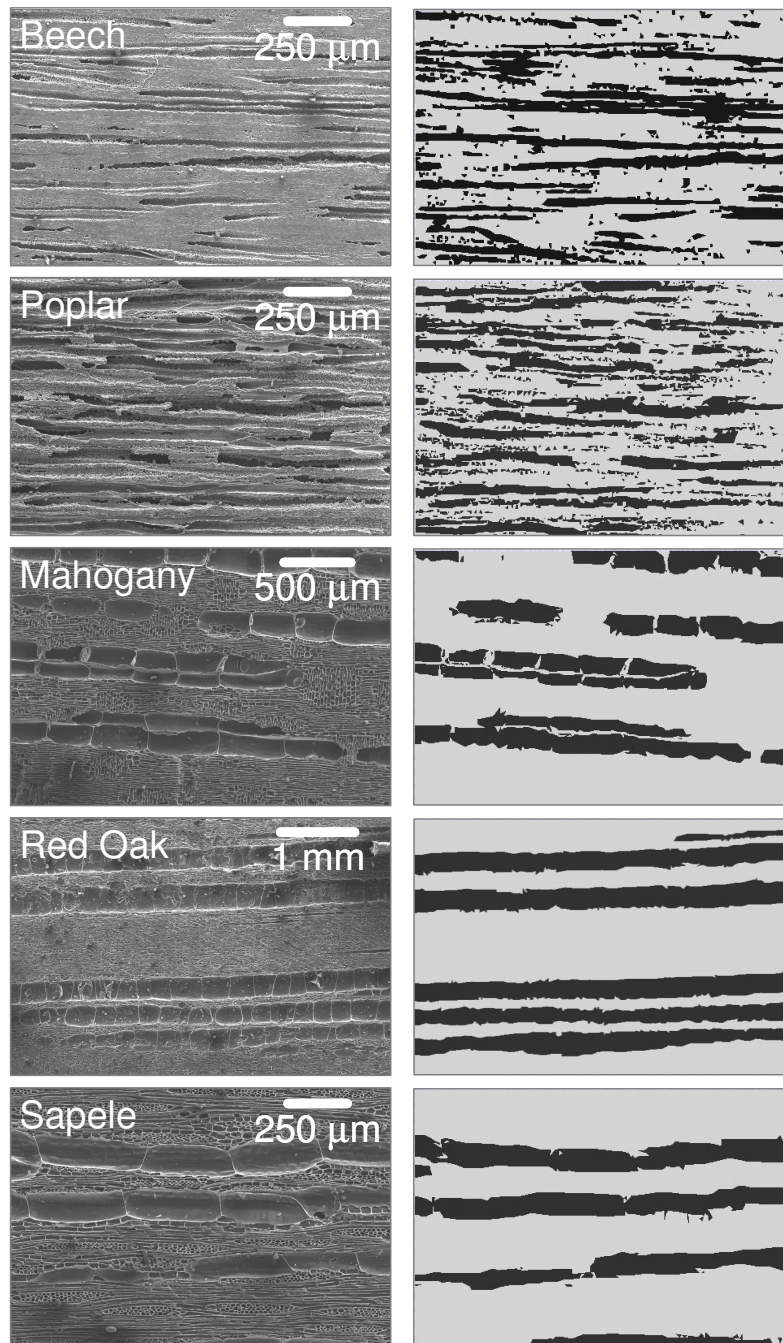


**Figure 5.2. SEM micrographs of transverse bioSiC planes and corresponding finite-element meshes for analysis of axial mechanical behavior.**

For this reason, effective  $E$  values determined from higher magnification images of fiber and tracheid pores (figure 5.3) were used for  $E_{solid}$ . The image selected to represent each bioSiC was selected based on the previously measured fiber and tracheid porosity. To account for this small pore porosity, figure 5.3(a) was used to represent beech bioSiC, figure 5.3(b) was used to represent poplar, mahogany, and red oak bioSiC, and figure 5.3(c) was used to represent sapele bioSiC. The porosities of these images are very similar to those measured by image analysis for fiber and tracheid porosity. In order to account for the unreacted carbon content in each bioSiC, the solid phase of the finite-element meshes shown in figure 5.3 was assigned an  $E$  value based on the effective  $E$  values calculated by the rule-of-mixtures (table 4.4). Accounting for unreacted carbon using this procedure, the upper and lower bound  $E_{effective}$  values calculated for the fiber and tracheid portion of each bioSiC are shown in table 5.1.

The values in table 5.1 were then used as the inputs for the solid phase properties in meshes based on more representative micrographs. This method allows for the creation of representative finite-element meshes with properties that account for both solid phases (SiC and unreacted carbon) as well as all porosity (vessel porosity and fiber and tracheid porosity). The results of OOF modeling for the meshes shown in figure 5.2, as well as values measured by mechanical testing, are shown in table 5.2. Here, an upper and lower-bound  $E_{effective}$  are shown, based on the values calculated for the fiber and tracheid porous regions. Accounting for unreacted carbon and the true structure of bioSiC, the experimental values are within the range of the OOF values. These results illustrate the ability of OOF to model the complex and non-regular microstructure of bioSiC.

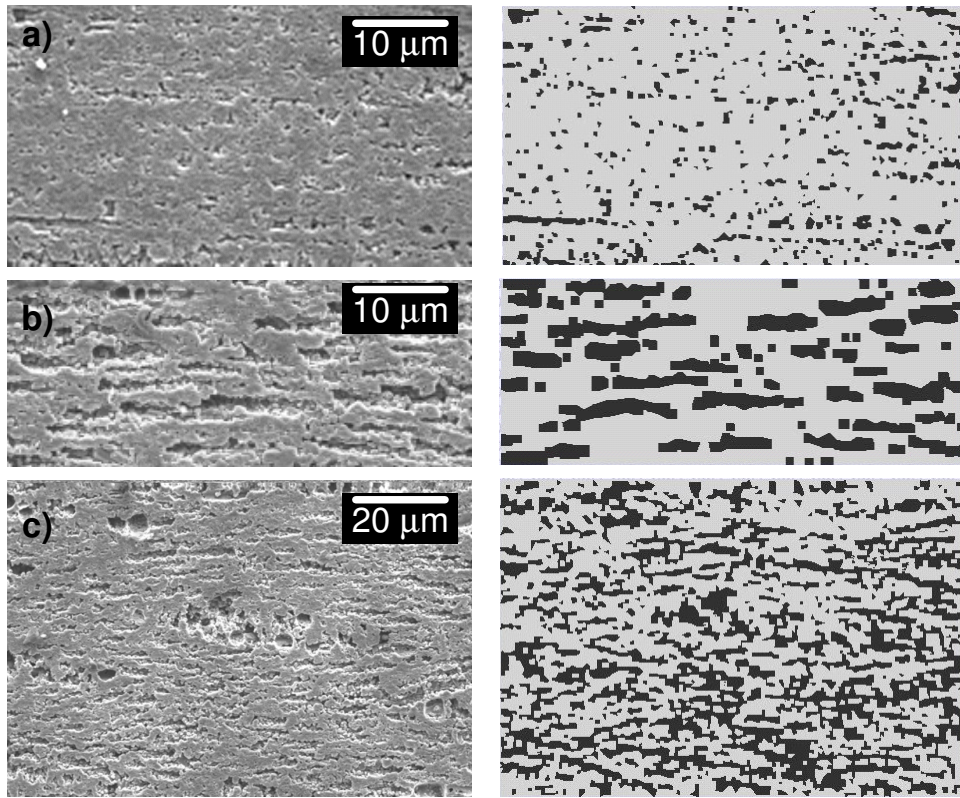


**Figure 5.3. SEM micrographs of bioSiC fiber and tracheid porosity in the transverse plane and the corresponding finite-element meshes.**

**Table 5.1. Upper and lower-bound axial elastic moduli calculated with OOF using the rule-of-mixtures values for solid phase elastic modulus.**

<b>FIBER AND TRACHEID POROSITY (AXIAL)</b>			
<b>BioSiC</b>	<b>vol. frac C in Solid (%)</b>	<b><math>E_{effective}</math> upper (GPa)</b>	<b><math>E_{effective}</math> lower (GPa)</b>
<i>Beech</i>	11.54	293.44	130.16
<i>Poplar</i>	8.40	175.46	90.41
<i>Mahogany</i>	35.41	127.81	33.88
<i>Red Oak</i>	13.82	165.9	67.62
<i>Sapele</i>	11.65	43.25	21.24

**Table 5.2. Experimental and OOF values for axial elastic moduli calculated accounting for all porosity and unreacted carbon content.**

<b>BioSiC</b>	<b>Porosity (%)</b>	<b>Mech. Test.</b>	<b>OOF Results</b>	
		<b><math>E_{axial}</math> (GPa)</b>	<b><math>E_{effective}</math> upper (GPa)</b>	<b><math>E_{effective}</math> lower (GPa)</b>
<i>Beech</i>	53.95	115.80	127.37	55.68
<i>Poplar</i>	61.10	57.40	73.58	38.71
<i>Mahogany</i>	48.53	68.60	80.88	21.75
<i>Red Oak</i>	49.32	51.40	96.01	39.68
<i>Sapele</i>	57.01	22.70	29.69	14.59

In addition to these results, the relative elastic moduli ( $E/E_o$ ) of the bioSiC meshes in figure 5.2 were also determined assuming the same  $E_{solid}$  for each bioSiC. These results are compared with those predicted by the MSA model in table 5.3. It is important to note that  $E_{effective}$  for each bioSiC is still below the value predicted by the MSA model. Again, this is due to the naturally derived microstructure of bioSiC. The curvature of the channels and changes in pore channel diameter would be expected to cause a reduction in  $E_{effective}$  when compared to a material with straight channels of constant diameter, as assumed by the MSA model.

The significance of bioSiC microstructure on the measured properties can further be illustrated by figure 5.4, where the  $\sigma_{yy}$  stress distributions of two finite-element meshes from red oak bioSiC compressed in the  $Y$  direction are shown. Although figure 5.4(b) is more porous, it actually has a greater value of  $E$  than the less porous mesh in figure 5.4(a) due to the curved channels and nodes in the microstructure. These irregularities in the microstructure of bioSiC come from two sources, the primary one being the wood precursor. Wood is a natural material and trees often grow in a nonlinear fashion resulting in an irregular microstructure. These characteristics of the wood precursor are retained in bioSiC, which result in the microstructure shown in figure 5.2. In addition to the precursor, warping of the carbon scaffold can cause additional curvature of the pore channels. This warping is caused by the volume change that takes place during pyrolysis.

**Table 5.3. Relative axial elastic moduli calculated for each bioSiC using OOF and the MSA model (only vessel porosities shown and used for OOF and MSA  $E/E_o$ ).**

<b>BioSiC</b>	<b>Porosity (%)</b>	<b><i>OOF</i> <math>E/E_o</math></b>	<b><i>MSA Model</i> <math>E/E_o</math></b>
<i>Beech</i>	34	0.36	0.66
<i>Poplar</i>	38	0.41	0.62
<i>Mahogany</i>	26	0.49	0.74
<i>Red Oak</i>	36	0.57	0.64
<i>Sapele</i>	25	0.69	0.75

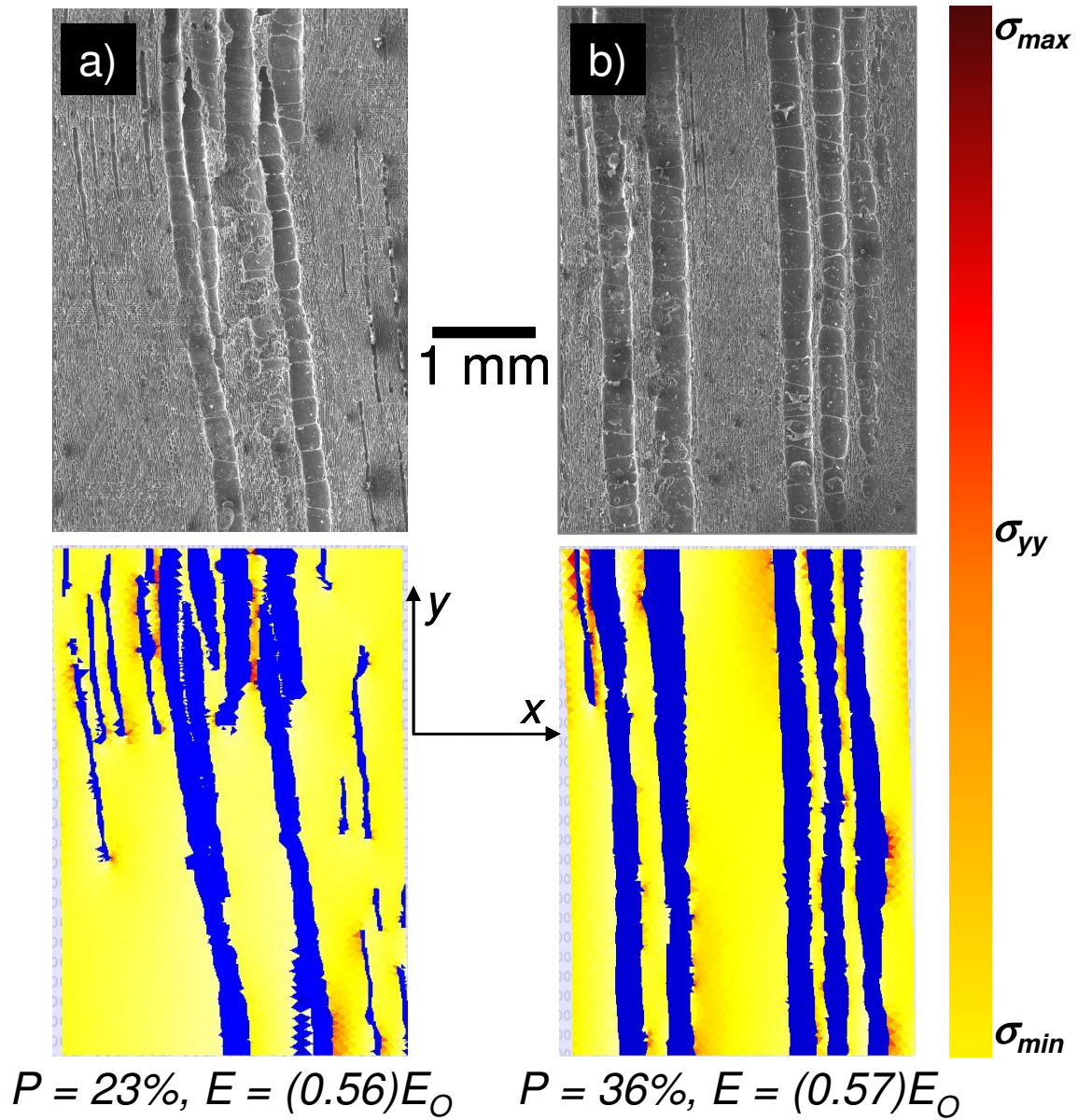
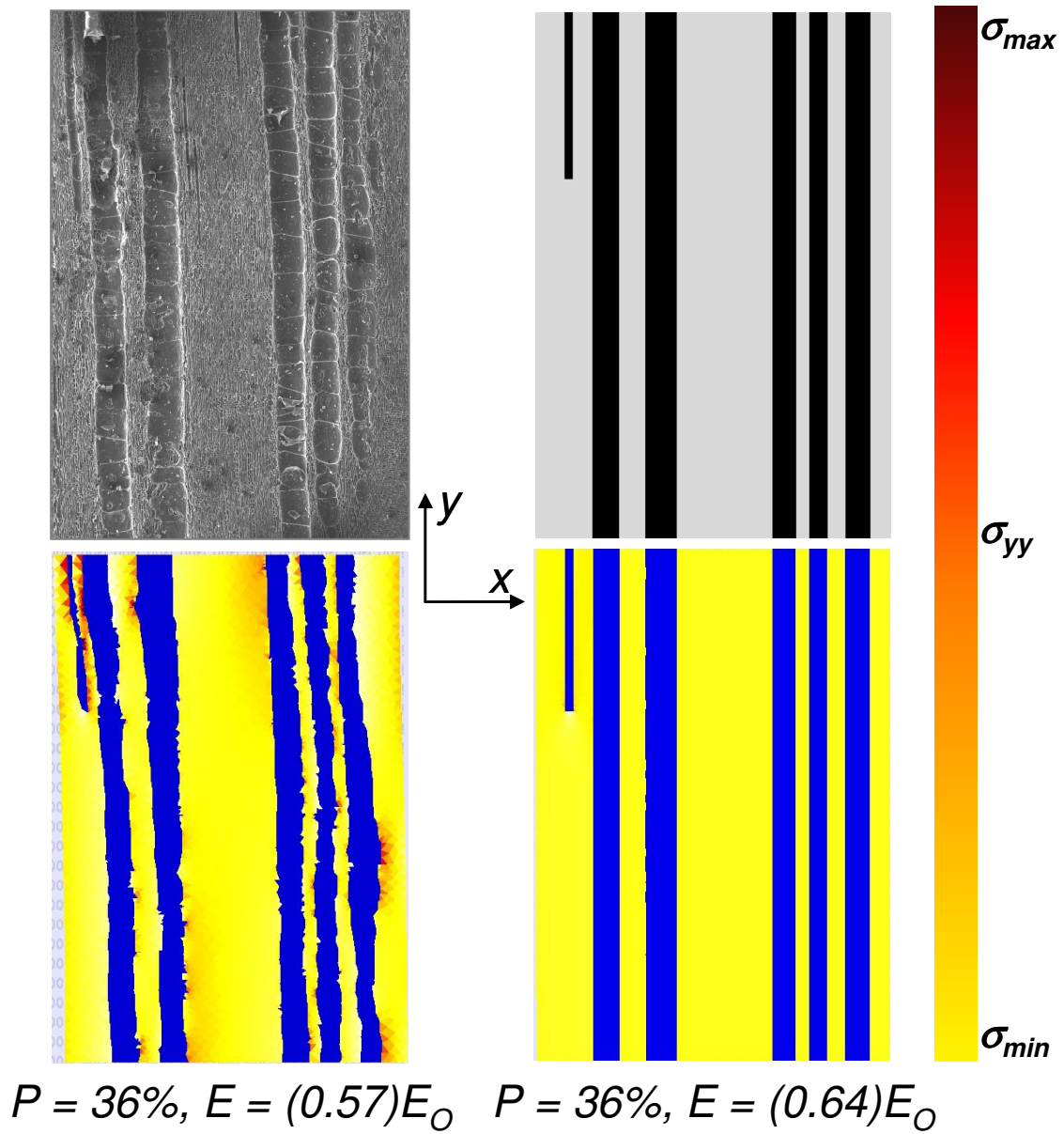


Figure 5.4. SEM micrographs and corresponding stress distributions of axial red oak bioSiC samples compressed in the  $Y$  direction (pore space shown in blue).

The MSA model assumes an ideal microstructure of perfectly straight tubular pores without the irregularities seen in bioSiC. Figure 5.5 shows the  $\sigma_{yy}$  stress distribution for a mesh with an idealized version of the porosity in figure 5.4(b) subjected to the same compressive loading conditions. Here, porosity of the two images is equivalent and, because there are no nodes or curvature in the tubular porosity, the stress concentrators observed in the bioSiC meshes are absent. As expected, the relative  $E$  measured for the idealized mesh is in agreement with the value of  $E/E_o = 0.64$  predicted by the MSA model. It is important to note that, had the finite-element mesh been based on a model microstructure instead of an actual micrograph, the effects of the irregularities in bioSiC would have been omitted.



**Figure 5.5.** SEM micrograph and idealized image of red oak bioSiC compressed in the  $Y$  direction with corresponding stress distributions (pore space shown in blue).

### 5.3.2. Pore Channel Misalignment

As mentioned above, pore channel curvature and changes in channel diameter serve to reduce  $E_{effective}$  for bioSiC in the axial direction. This effect occurs because these irregularities misalign the load bearing solid phase in bioSiC so that it is no longer parallel to the direction of applied stress. The degree of this effect can be illustrated by creating idealized microstructures of parallel tubular pores as shown in figure 5.6. The porosity in each of these images is 50% and the direction of pore alignment relative to the direction of applied stress is varied. Meshes based on each of these images were created and OOF was used to test these meshes in axial compression. The results of this testing are shown in figure 5.7 in a plot of  $E/E_o$  as a function of the angle of misalignment ( $\theta$ ) of these pore channels to the loading axis in these meshes. As this plot is based on two-dimensional structures, a more accurate representation may be given by a model for fiber reinforced composites where the “fiber” is pore space. This model is given by

$$\frac{1}{E} = \frac{\cos^4 \theta}{E_1} + \frac{\sin^4 \theta}{E_2} + \left( \frac{1}{G} - \frac{2\nu}{E_1} \right) \cos^2 \theta \sin^2 \theta \quad (2)$$

where  $E_1$  and  $E_2$  are, respectively, the axial and transverse properties and  $G$  is the shear modulus (12 GPa) . From these plots, it is clear that even slight misalignment from parallel can result in a very large change in  $E$  as a significant reduction is seen for even small misalignment angles.

This very significant effect helps to explain why experimental values of  $E$  in the axial direction for both UDP and NUDP bioSiC fall well below those predicted by the MSA model.

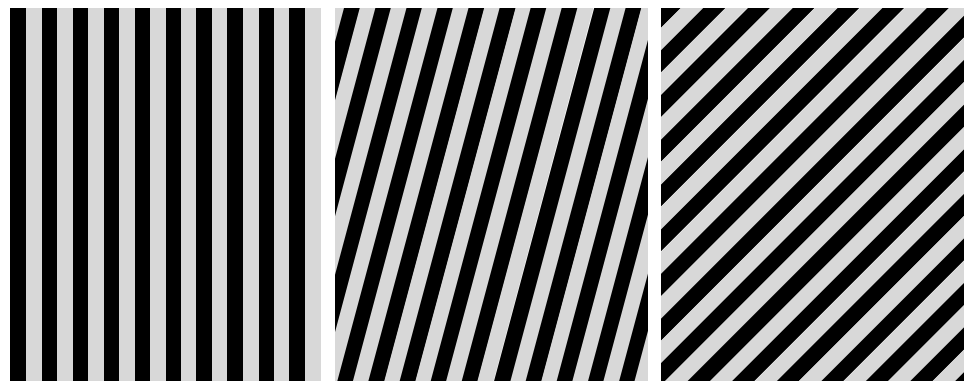


**Figure 5.6. Idealized microstructures of tubular pores at various alignment angles.**

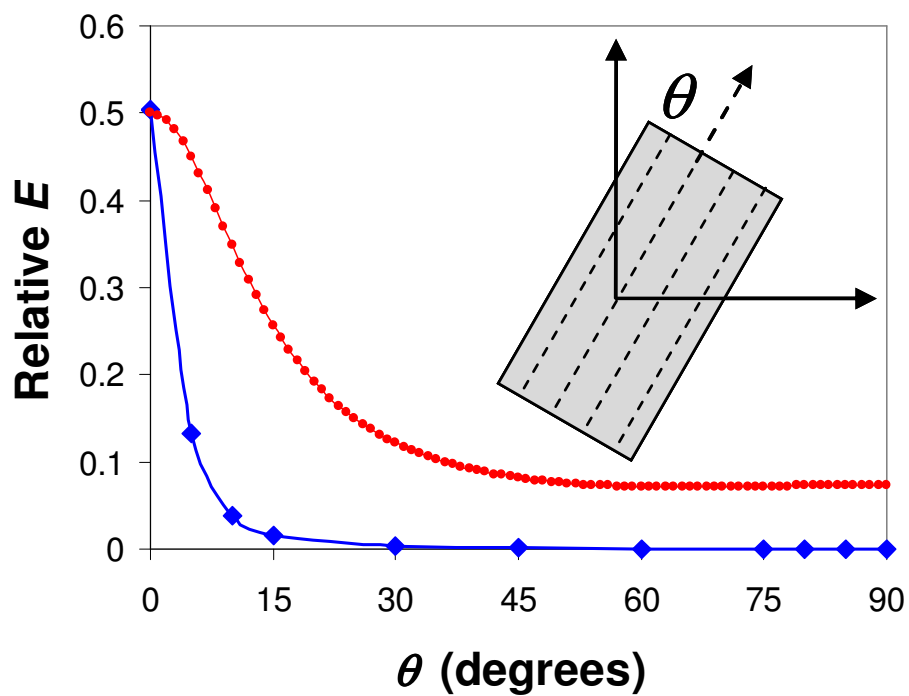


Figure 5.7. Plot of relative elastic modulus as a function of angle of alignment to stress axis from OOF data and equation 2.

### 5.3.3. Stress Distribution and Fracture of BioSiC in Axial Compression

Qualitative results from axial OOF testing are presented in figure 5.8, which shows the  $\sigma_{xx}$  stress distributions for the finite-element meshes for each bioSiC when compressed in the  $X$  direction. Off axis stress distributions ( $\sigma_{yy}$  and  $\sigma_{xy}$ ) are also shown in figures 5.9 and 5.10, respectively. It is apparent from figure 5.8 that irregularities such as curves and nodes in the tubular porosity of bioSiC act as stress concentrators. Along with unreacted carbon, these stress concentrators would be likely to reduce  $\sigma_{comp}$  in bioSiC. As expected, the stress distributions in figures 5.9 and 5.10 are more or less constant.

In addition to  $E_{effective}$  and stress distributions, fracture was also modeled in axial compression by OOF using Griffith2 elements and compared to experimental observations. For the Griffith2 elements, a value of  $7.1 \text{ J/m}^2$  was used for  $\gamma_s$ , which was calculated from (Courtney 2000)

$$K_{IC} = [E(2\gamma_s)]^{1/2} \quad (3)$$

where  $K_{IC} = 2.4 \text{ MPa}\cdot\text{m}^{1/2}$  and  $E = 408 \text{ GPa}$ , both values for SiC. To allow for quasi-fracture, values of  $1.0 \times 10^{-6}$  and  $2.0 \times 10^{-6}$  were used for knockdown factors 1 and 2, respectively (Fuller 2006). A compressive strain of 1.5 % was applied in 0.05 % increments in the axial direction to each of the bioSiC meshes to induce fracture. When elements fracture, the rotated stiffness matrix is multiplied by the first knockdown factor and the stress is redistributed. This process is repeated until no more elements satisfy the Griffith criterion, and the strain is then incremented.

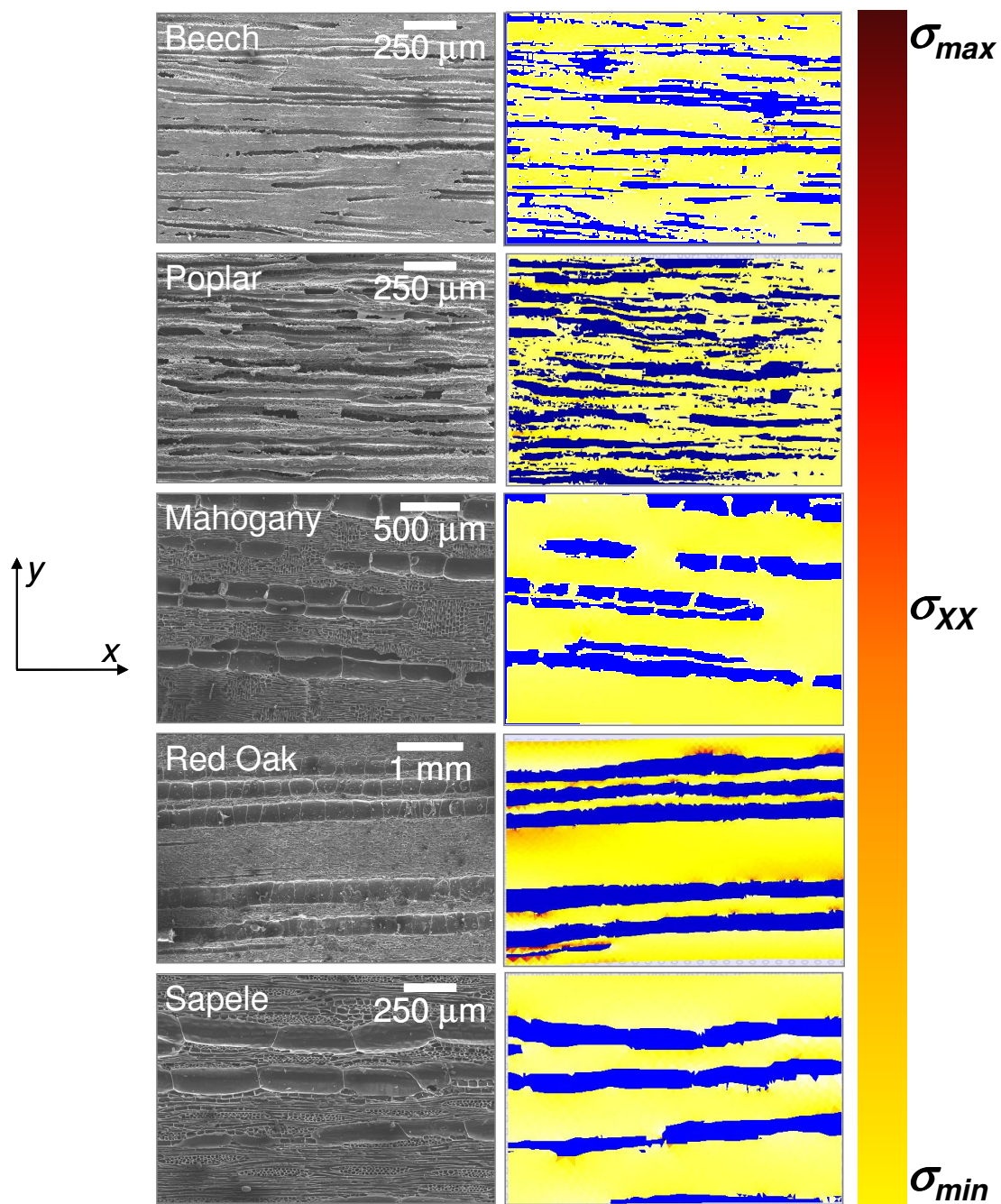


**Figure 5.8. SEM micrographs and corresponding stress distributions ( $\sigma_{xx}$ ) of axial bioSiC samples compressed in the X direction (pore space shown in blue, scale from -33.06 to 5.55 MPa).**

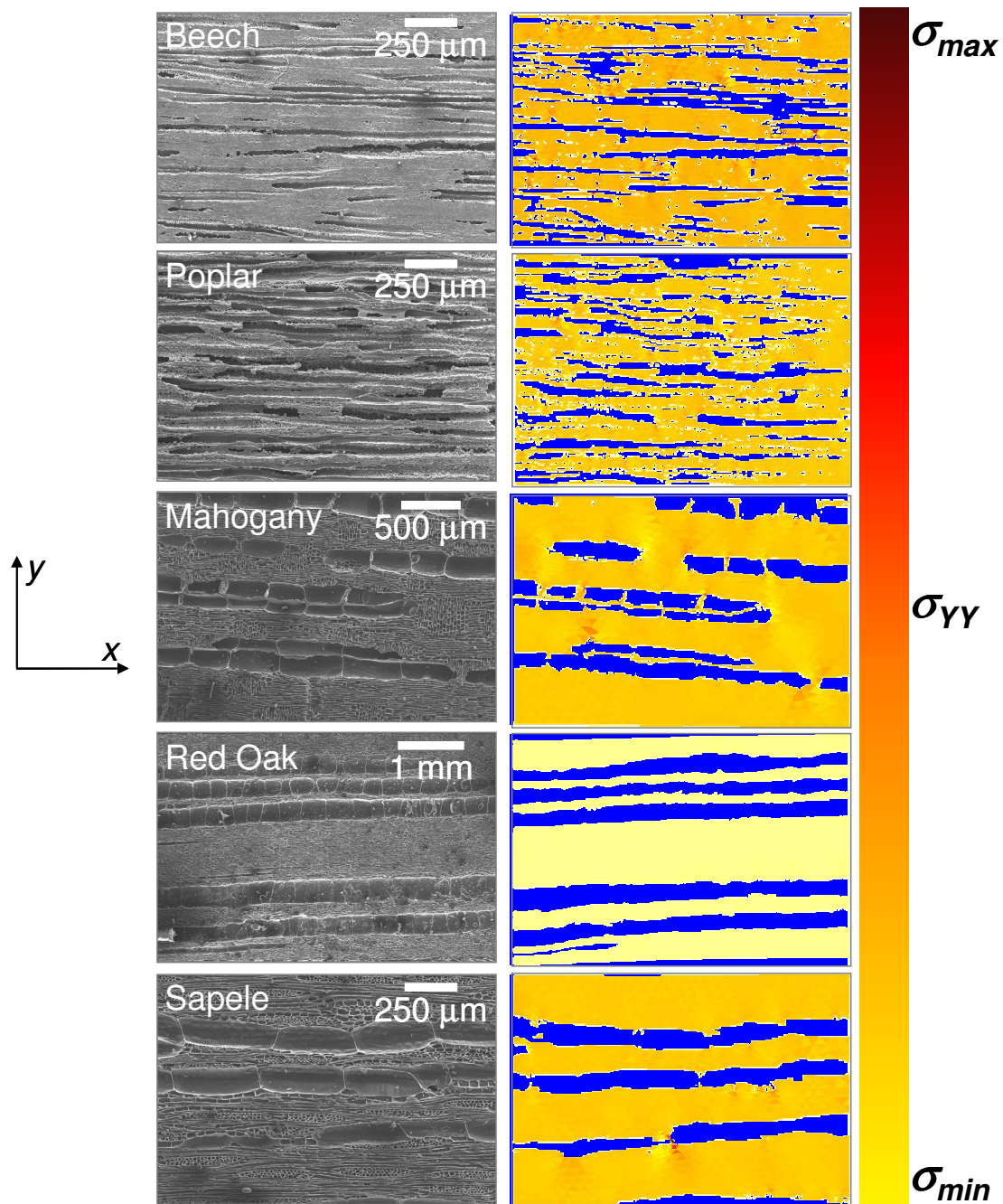


**Figure 5.9.** SEM micrographs and corresponding stress distributions ( $\sigma_{yy}$ ) of axial bioSiC samples compressed in the X direction (pore space shown in blue, scale from -15.00 to 10.00 MPa).

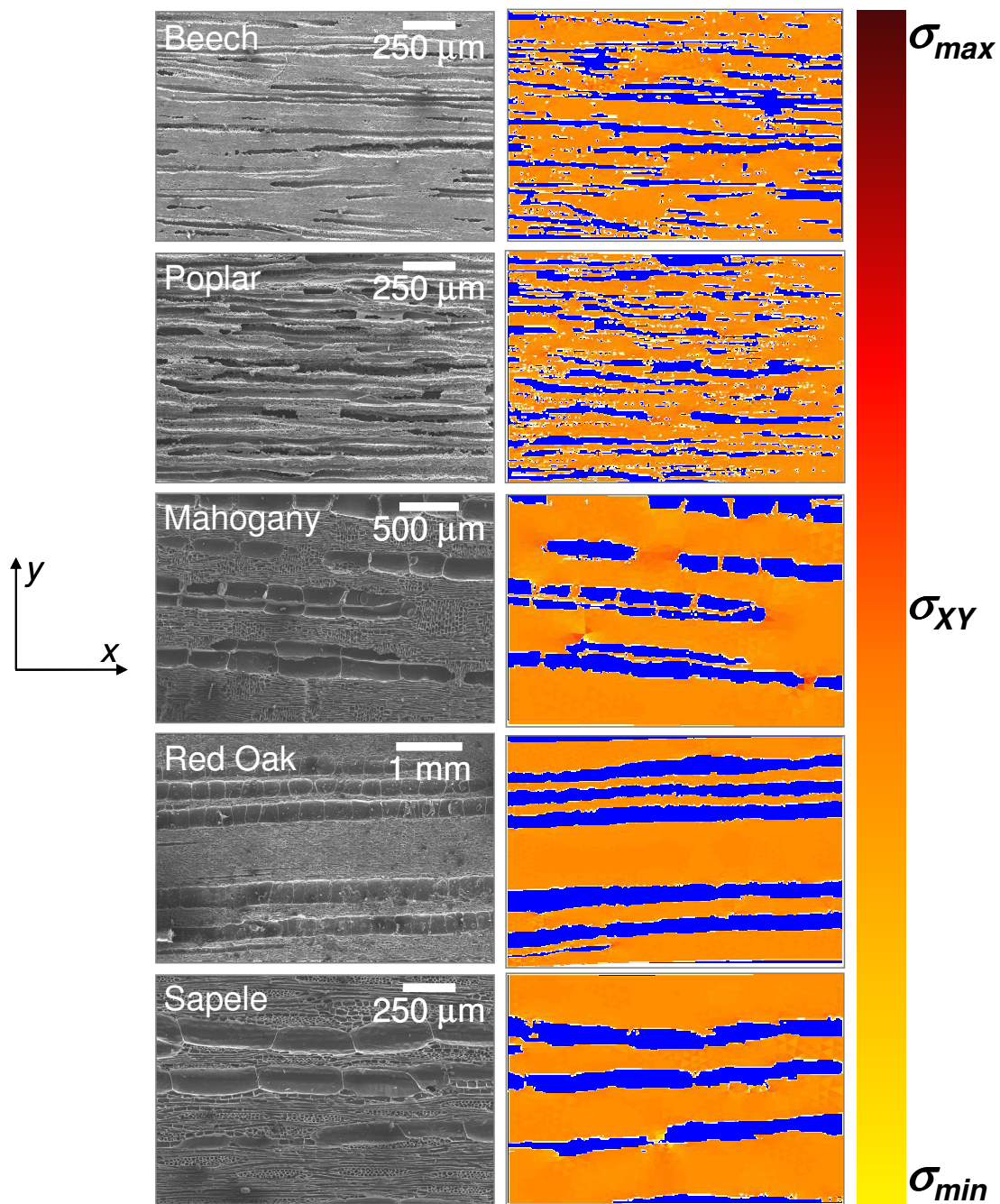


**Figure 5.10. SEM micrographs and corresponding stress distributions ( $\sigma_{xy}$ ) of axial bioSiC samples compressed in the X direction (pore space shown in blue, scale from -10.00 to 13.00 MPa).**

The second knockdown factor is applied to an element if it again satisfies the Griffith criterion after being fractured once, and it results in a reduction of the shear stresses across the fracture plane. Images of these virtually fractured bioSiC materials compressed in the  $X$  direction are shown in figure 5.11. The black elements in these images correspond to those that have fractured. From these images, it can be observed that many areas of failed elements tend to lie adjacent to inflection points in the curves of pore channels. This corresponds to locations of the previously shown stress concentrations (figure 5.8). Fracture is most likely to initiate at these stress concentrators and create fracture surfaces as shown in figure 5.11. From mechanical testing, images of fracture surfaces (figure 4.11) show half vessel pores and give an indication of the preferred fracture path in bioSiC. Many of the images in figure 5.11 show similar behavior with fractured areas adjacent and parallel to pore channels. Fractured material is also shown between pore channels and usually corresponds to channel irregularities where stress concentration was highest. These areas correspond to propagation of cracks between pore channels, which leads the multi-faceted surface seen in figure 4.11(a). Additionally, damage is heavier in lower density regions with high concentrations of vessel pores.

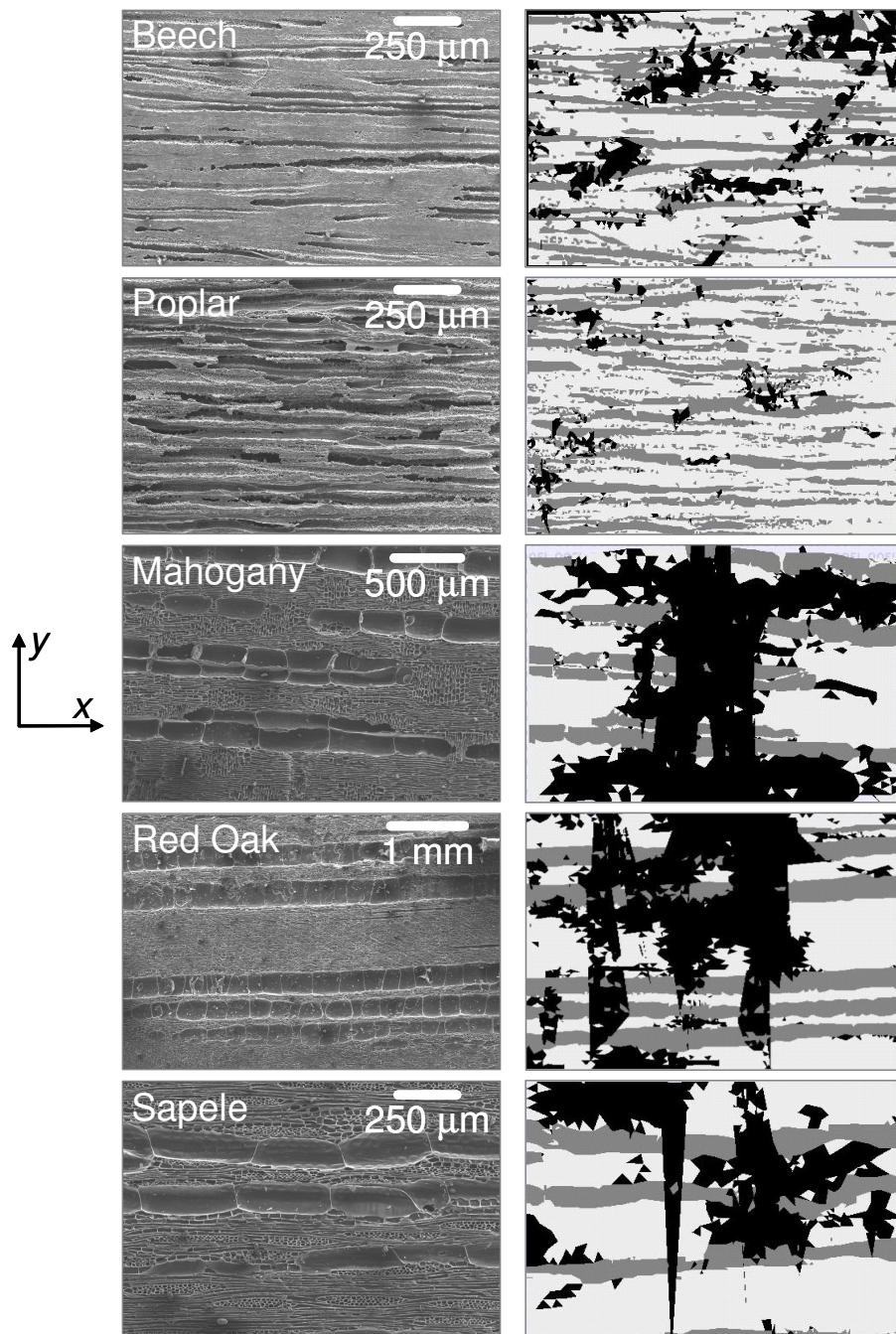


**Figure 5.11.** SEM micrographs and corresponding virtual fracture images of axial bioSiC compressed in the  $X$  direction (black elements are fractured).

#### 5.4. Mechanical Behavior of BioSiC in Transverse Compression

As with axial compression, the mechanical properties of bioSiC in transverse compression also fell well below the values predicted by the MSA model. This was partially attributed to the presence of unreacted carbon but, as in the case of axial compression of bioSiC, the lower than expected properties could not be entirely attributed to this phase. For axial compression, misalignment of channels and irregularities in the natural microstructure of bioSiC were determined to be responsible for deviations in mechanical behavior from those predicted for an ideal microstructure. However, this cannot explain the behavior of bioSiC in transverse compression because the tubular pores are aligned perpendicular to the applied stress and small deviations from this have little effect on the mechanical properties. To determine the cause of the lower than expected mechanical properties, finite-element analysis of bioSiC microstructures and idealized microstructures using OOF was conducted and the results are presented here.

##### 5.4.1. Effective Transverse Elastic Modulus

Similar to the modeling of axial compression, a threshold was applied to axial plane SEM micrographs of each type of bioSiC to model transverse compression. These micrographs and the resulting finite-element meshes are shown in figure 5.12. Higher magnification micrographs were again used to determine an effective  $E$  for the fiber and tracheid porous area that was difficult to mesh on representative images. The images and the resulting finite-element meshes are shown in figure 5.13. These images were also used for image analysis of fiber and tracheid areas.

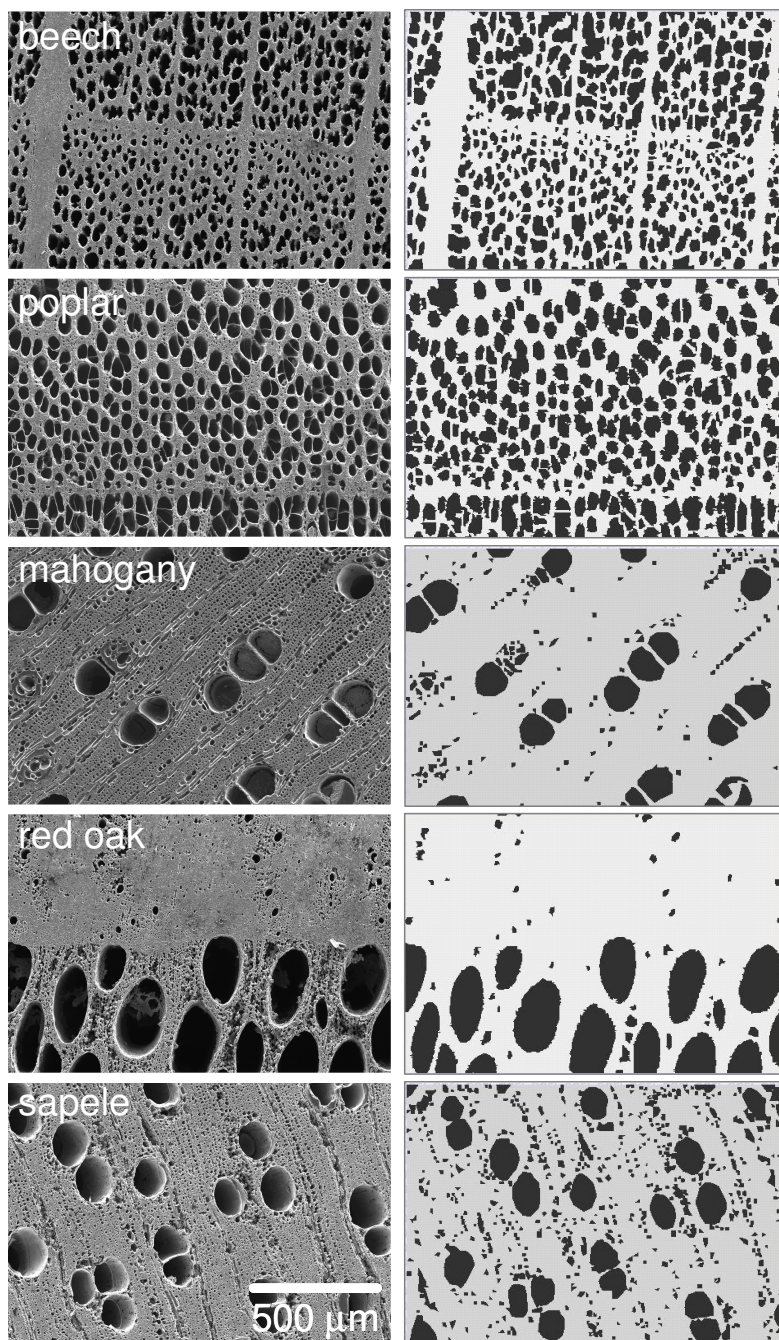


**Figure 5.12. SEM micrographs of axial bioSiC planes and corresponding finite-element meshes for analysis of transverse mechanical behavior.**

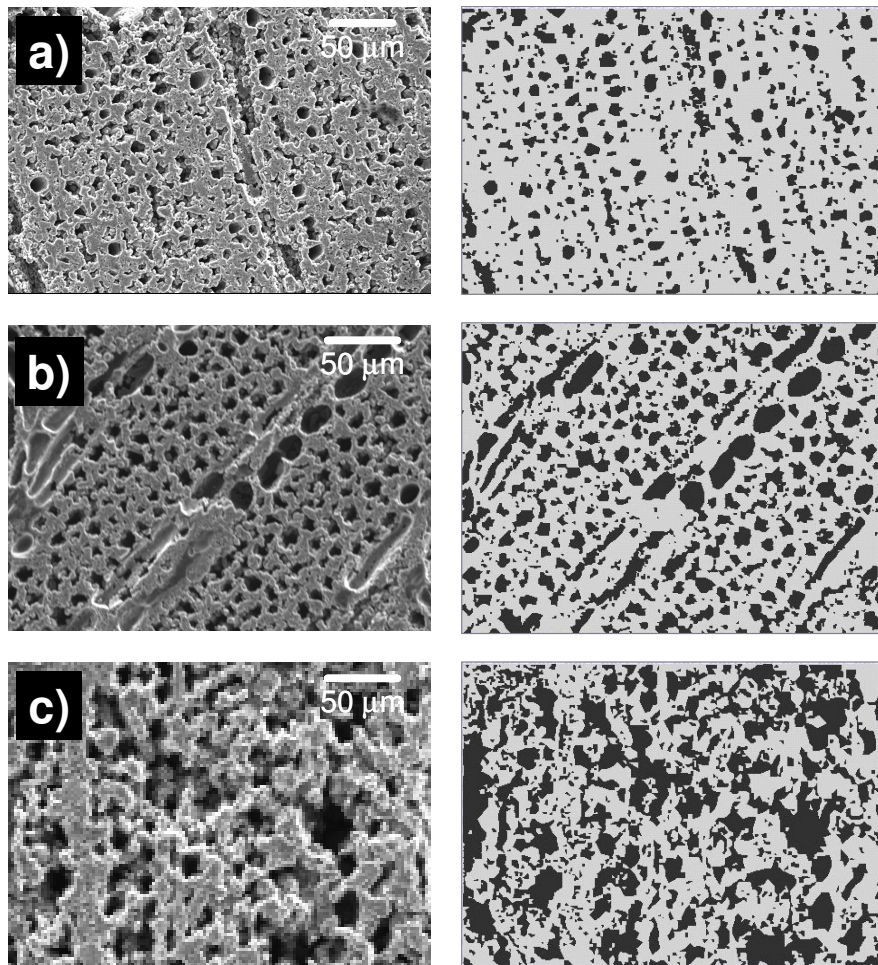


**Figure 5.13. SEM micrographs of bioSiC fiber and tracheid porosity in the axial plane and the corresponding finite-element mesh.**

To account for this small pore porosity, figure 5.13(a) was used to represent beech bioSiC, figure 5.13(b) was used to represent poplar, mahogany, red oak bioSiC, and sapele bioSiC, and figure 5.13(c) was also used to represent red oak bioSiC as will be explained later. Unreacted carbon was also accounted for in the assigned properties of the solid material by using the  $E$  values calculated from the previously determined carbon contents and the rule-of-mixtures. The upper and lower-bound  $E_{effective}$  values were determined based on the carbon content of each bioSiC and these values are shown in table 5.4. These values were then applied to the more representative bioSiC meshes shown in figure 5.12, and  $E$  values calculated by OOF using these meshes are shown in table 5.5. Also shown in these results are the mechanical testing values for  $E$  measured in transverse compression. For simplicity, porosity and  $E$  are the average of radial and tangential values for each bioSiC. By taking into account both the carbon content and the actual structure of each bioSiC, the experimental results fall within the range of OOF values with the exception of red oak bioSiC. The  $E$  value for red oak measured by mechanical testing falls below the range of values calculated by OOF, and this can be explained by the pore bands in this material. In red oak bioSiC, not only is there a difference in the distribution of vessel porosity but also in the distribution of fiber and tracheid porosity, as shown in figure 5.14. While the tested meshes accurately represent the vessel porosity in red oak bioSiC, they do not accurately represent the fiber and tracheid porosity. To account for this, the porous and dense bands in red oak bioSiC can be treated separately by the finite-element meshes also shown in figure 5.14.

**Table 5.4. Upper and lower-bound transverse elastic moduli calculated with OOF using the rule of mixtures values for solid phase elastic modulus.**

<b><i>FIBER AND TRACHEID POROSITY (TRANSVERSE)</i></b>			
<b>BioSiC</b>	<b>vol. frac C in Solid (%)</b>	<b><math>E_{effective}</math> upper (GPa)</b>	<b><math>E_{effective}</math> lower (GPa)</b>
<i>Beech</i>	11.54	48.95	22.36
<i>Poplar</i>	8.40	49.19	26.28
<i>Mahogany</i>	35.41	36.46	10.36
<i>Red Oak</i>	13.82	46.94	20.07
<i>Sapele</i>	11.65	48.76	22.22

**Table 5.5. Experimental and OOF values for transverse elastic moduli calculated accounting for all porosity and unreacted carbon content.**

<b>BioSiC</b>	<b>Porosity (%)</b>	<b>Mech. Test.</b>	<b>OOF Results</b>	
		<b><math>E_{transverse}</math> (GPa)</b>	<b><math>E_{effective}</math> upper (GPa)</b>	<b><math>E_{effective}</math> lower (GPa)</b>
<i>Beech</i>	52.16	15.75	17.35	8.08
<i>Poplar</i>	61.89	3.65	11.35	3.33
<i>Mahogany</i>	48.56	15.25	21.18	6.13
<i>Red Oak</i>	45.25	2.90	23.15	10.05
<i>Sapele</i>	56.47	6.77	17.41	4.31

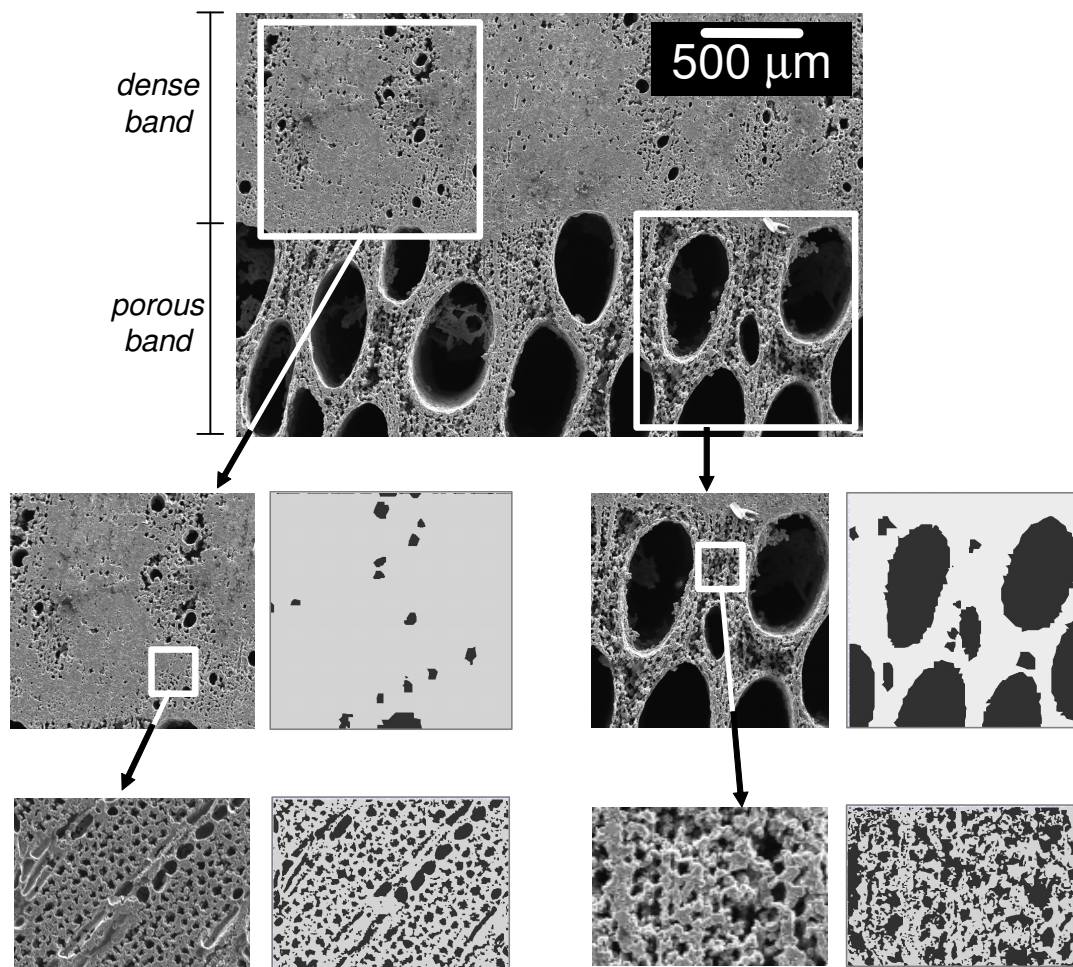


**Figure 5.14. SEM micrographs and finite-element meshes illustrating the procedure used to determine  $E_{effective}$  for dense and porous bands of red oak bioSiC.**

Using this method, upper and lower bounds for each band can be determined and these values are shown in table 5.6. The  $E$  values for these bands can be combined again using the rule-of-mixtures given by

$$E = \frac{E_{dense} E_{porous}}{V_{dense} E_{dense} + V_{porous} E_{porous}} \quad (4)$$

and the upper and lower bound values for  $E$  of red oak bioSiC are 4.68 GPa and 1.82 GPa, respectively. In equation 4,  $V_{dense}$  and  $V_{porous}$  are 0.62 and 0.37 as given by the lengths of each band (determined by image analysis). This range agrees with the experimental value of  $2.90 \pm 1.37$  GPa.

**Table 5.6. Upper and lower bound results for red oak bioSiC bands using rule-of-mixtures to account for unreacted carbon.**

	<b><math>E_{effective}</math> upper (GPa)</b>	<b><math>E_{effective}</math> lower (GPa)</b>
<i>dense red oak bioSiC</i>	42.38	18.41
<i>porous red oak bioSiC</i>	3.03	1.17

#### 5.4.2. Pore Effects on Transverse Properties

As in the axial direction, even when the solid phase is assumed to be free of unreacted carbon, the properties of bioSiC are lower than expected. Again, this would indicate some deviation from the ideal structure assumed by the MSA model. Although the differences in the axial direction between the assumed ideal structure and the actual bioSiC structure have little effect in the transverse direction, idealized microstructures can also be used to determine the effect of pore properties on the properties of the bulk material in the transverse direction. The effects of these idealized microstructures can be related to the microstructures of bioSiC and the trends seen in these materials in transverse compression.

##### *Pore Size Effect*

While there are common features in the porosities of each type of bioSiC, differences unique to each precursor wood are also found in bioSiC. One such difference is pore size, which ranges from 3-300  $\mu\text{m}$  in five types of bioSiC tested. The effect of pore size was determined by creating idealized microstructures of varying pore size and constant porosity (15 %), examples of which are shown in figure 5.15. These were created using the *swiss cheese* function in OOF and simple drawing programs. OOF was used to determine  $E/E_o$  values from these meshes and there is essentially no difference between them. This is the expected result as volume of porosity and not pore size is expected to have a significant effect and mechanical property models for porous materials generally do not include a pore size term. The small difference between the small pore mesh and the other meshes is most likely due to slightly differing pore arrangements. This is discussed below.

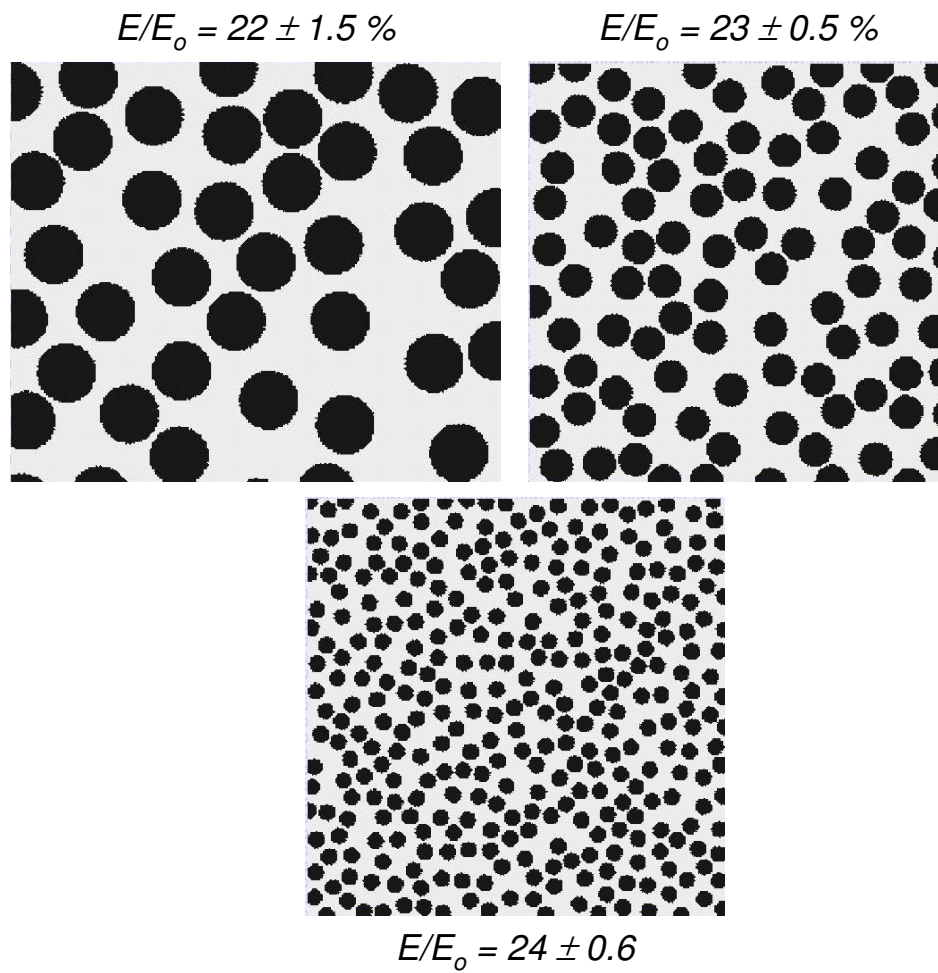


**Figure 5.15. Idealized microstructures and relative elastic moduli used to analyze the effect of pore size on mechanical behavior.**

### *Pore Arrangement*

While bioSiC is derived from a natural material and has a random arrangement of pores, the MSA model assumes a simple cubic-type arrangement. To test the effects of pore arrangement on transverse  $E$ , four simple microstructures with equal porosities and simple cubic and random arrangements were made as shown in figure 5.16, and the  $E/E_o$  values for these idealized microstructures are shown in table 5.7. The random microstructures in these figures have significantly lower  $E/E_o$  values and the difference between ordered and random porosity is greater at higher porosity. The effect of random porosity is also apparent in figure 5.17 where  $E_{effective}$  values for random idealized microstructures are plotted along with the values predicted by the MSA model as a function of porosity. From figure 5.17, it is clear that the deleterious effect of random pore arrangement is increased with increasing porosity.

When ordered, the distance between pores is maximized and constant. The reduction in  $E/E_o$  due to disorder is most likely due to interactions between pores that take place because distances between pores are no longer maximized. This reduction is expected to be more significant at higher porosity because separation distance between pores is smaller and disorder would lead to even more interaction between pores than would occur at lower pore volumes. At a porosity of approximately 50 %,  $E/E_o$  of the randomly arranged microstructure is 33 % less than that of the ordered microstructure. This effect helps to explain the why the experimental values fell below those predicted by the MSA model.

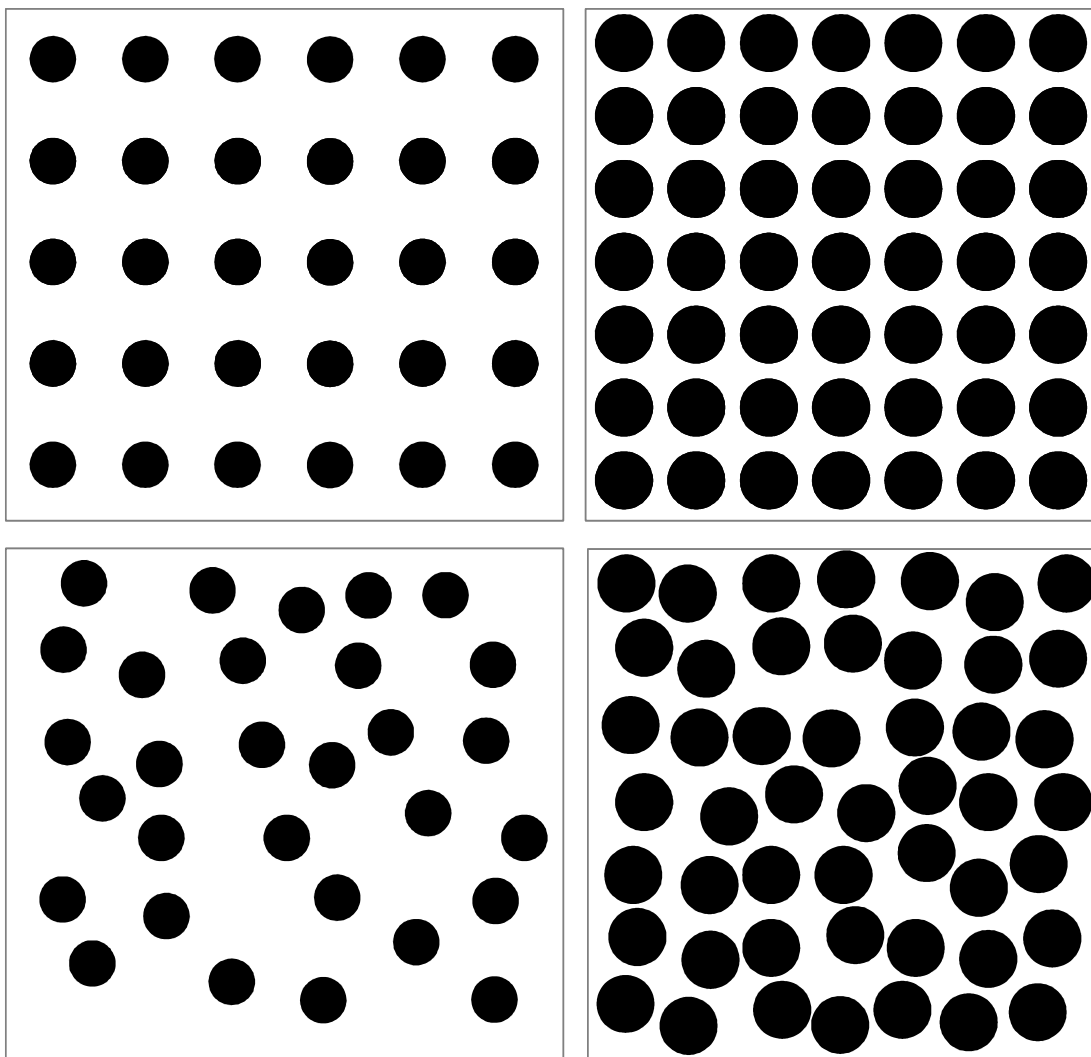


**Figure 5.16. Idealized microstructures to analyze the effect of pore arrangement on mechanical behavior.**

**Table 5.7. OOF results of relative elastic modulus as a function of pore arrangement.**

<b>Arrangement</b>	<b>Porosity (%)</b>	<b><math>E/E_o</math> (%)</b>
simple cubic	18	$67.1 \pm 1.2$
random	18	$63.7 \pm 0.8$
simple cubic	51	$32.7 \pm 0.2$
random	51	$25.4 \pm 1.2$

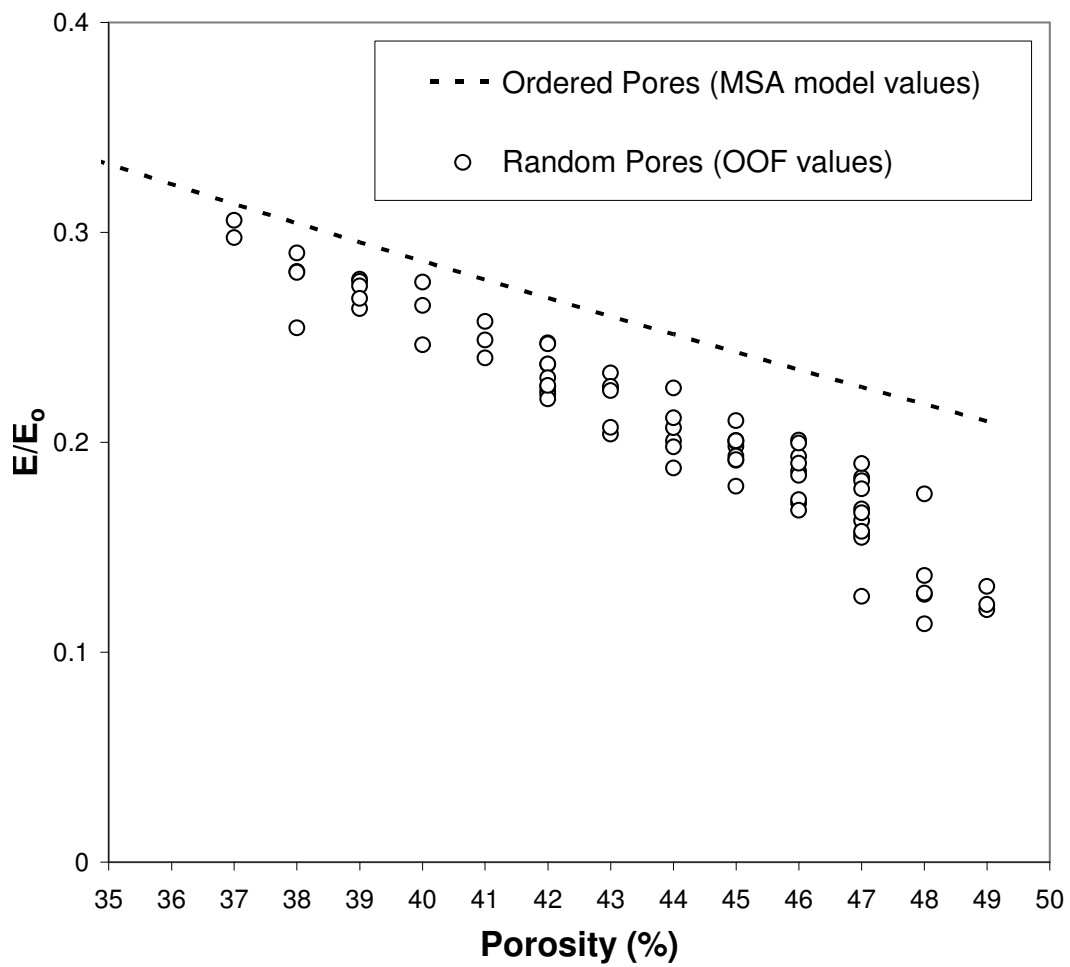


**Figure 5.17. Plot of relative elastic modulus as a function of porosity for ordered and random porosity.**

### *Pore Shape*

The MSA model also assumes circular pore channel cross-sections. However, bioSiC pores often have elliptical pore cross-sections. To determine the effect of pore shape, idealized microstructures with pores of elliptical cross-section were also created as shown in figure 5.18. The ratio of the major to minor axis size of the elliptical pores is equal to 1.35 and was chosen because it closely matches the ratio in bioSiC measured by image analysis. Also, the orientation of the major axes of the ellipses in bioSiC tends to be the same for all pores in a given sample and this is true of the idealized microstructures as well. These microstructures show elliptical pores in both random and simple cubic arrangements at two distinct porosities. The  $E/E_o$  results for these microstructures determined using OOF and circular pore microstructures are shown in table 5.8. From these results, it is clear that pore shape has a significant effect on  $E/E_o$  and this effect is greater as porosity increases. It is important to note that the orientation of the elliptical pores relative to the stress axis also affects the properties as  $E/E_o$  is higher for elliptical pores relative to circular pores when the stress axis is aligned with the major axes of the ellipses. However, the significance of this stiffening effect is reduced when randomized circular and elliptical microstructures are compared. In contrast, when compressed parallel to the minor axes,  $E/E_o$  of the ellipse microstructure is significantly lower than that of the circle microstructure. This dependence on orientation of the ellipse microstructure is discussed below.

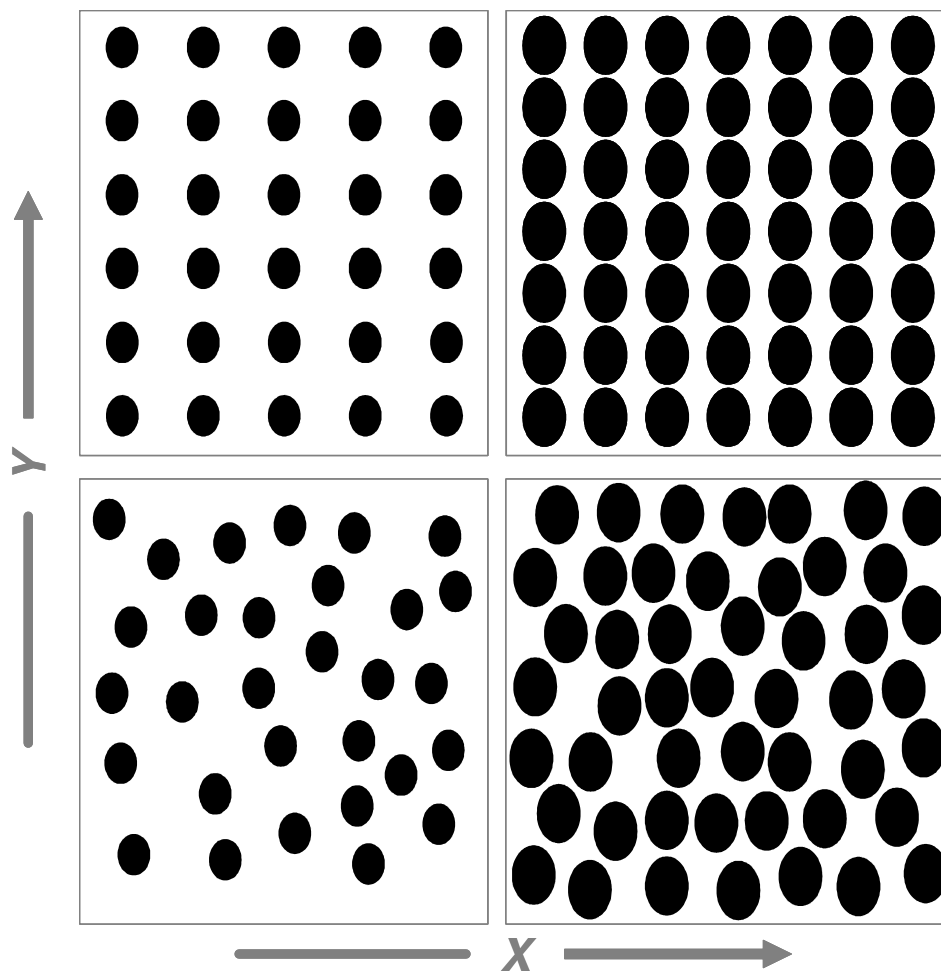


**Figure 5.18.** Idealized microstructures to analyze the effect of pore shape and arrangement on mechanical behavior.

**Table 5.8. Compiled OOF results of circular and ellipsoidal pores in ordered and random arrangements in  $X$  and  $Y$  orientations.**

<b>Pore Shape</b>	<b>Arrangement</b>	<b>Porosity (%)</b>	<b><math>E_y/E_o</math></b>	<b><math>E_x/E_o</math></b>
circle	simple cubic	18	0.66	0.68
circle	random	18	0.64	0.63
ellipse	simple cubic	18	0.72	0.62
ellipse	random	18	0.68	0.61
circle	simple cubic	51	0.33	0.33
circle	random	51	0.26	0.25
ellipse	simple cubic	51	0.41	0.18
ellipse	random	51	0.26	0.17

### *Pore Orientation*

From the results shown in table 5.8, it is clear that microstructures with elliptical pores oriented with the major axes parallel to the stress axis are significantly stiffer than materials with the stress axis parallel to the ellipse minor axes. In the case of bioSiC however, the pore orientation is likely to be somewhere between these two extremes. In order to determine how  $E_{effective}$  changes with orientation, microstructures of elliptical pores with varying angles of orientation were created. These microstructures, examples of which are shown in figure 5.19, have a constant porosity of 50% and a simple cubic arrangement. From these idealized microstructures,  $E/E_o$  as a function of angle of orientation ( $\alpha$ ) relative to the stress axis is shown in figure 5.20. These results show that the change of  $E/E_o$  with  $\alpha$  is not linear and is more sensitive to changes in  $\alpha$  away from the two extremes. Also important to note in figure 5.20 is the line corresponding to a material of the same porosity with circular pore cross-sections. This line intersects the elliptical line at approximately  $40^\circ$  and all higher angle values for the elliptical pores are below this line. This indicates that, while elliptical pores may result in an increase in  $E_{effective}$  over circular pores, they are more likely to cause a decrease in  $E_{effective}$ .

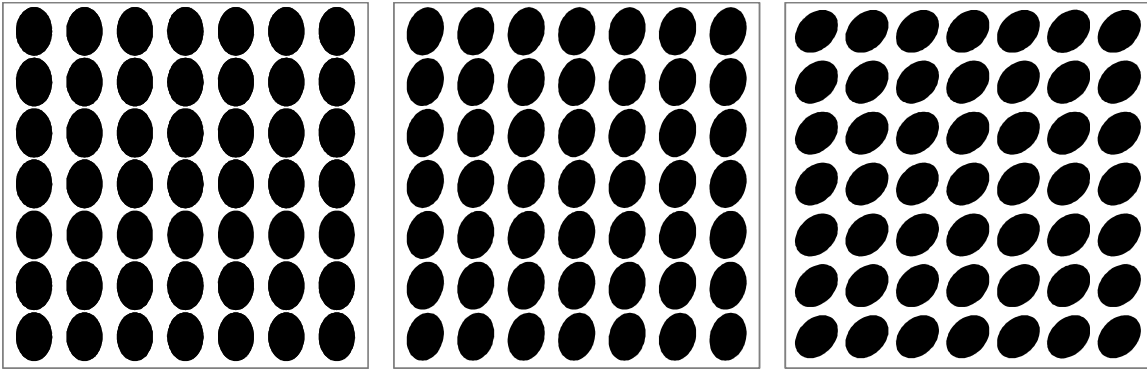


**Figure 5.19. Idealized microstructures to analyze the effect of elliptical pore orientation on mechanical behavior.**

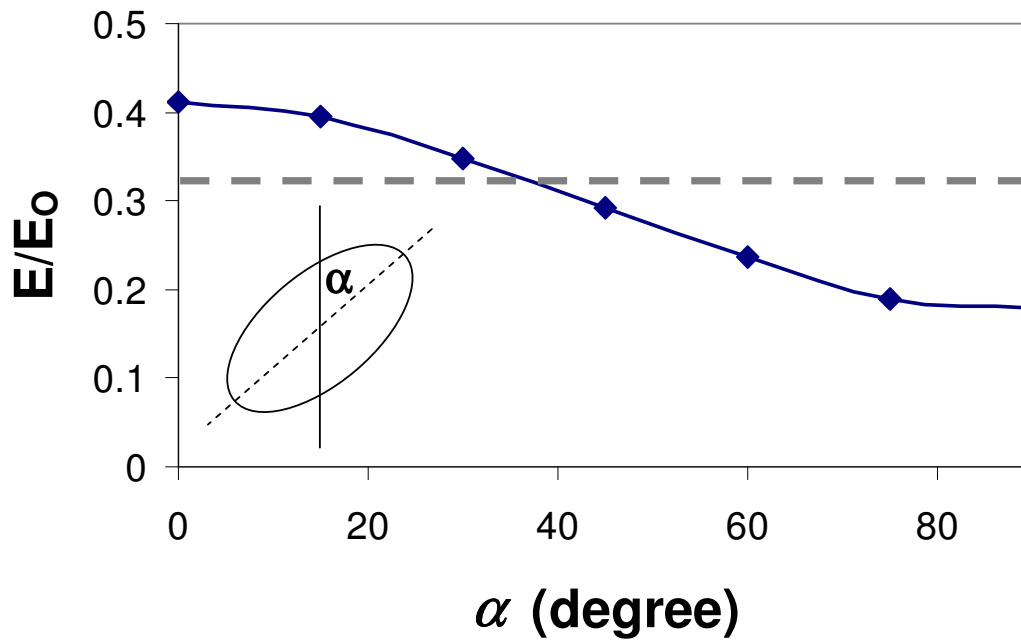
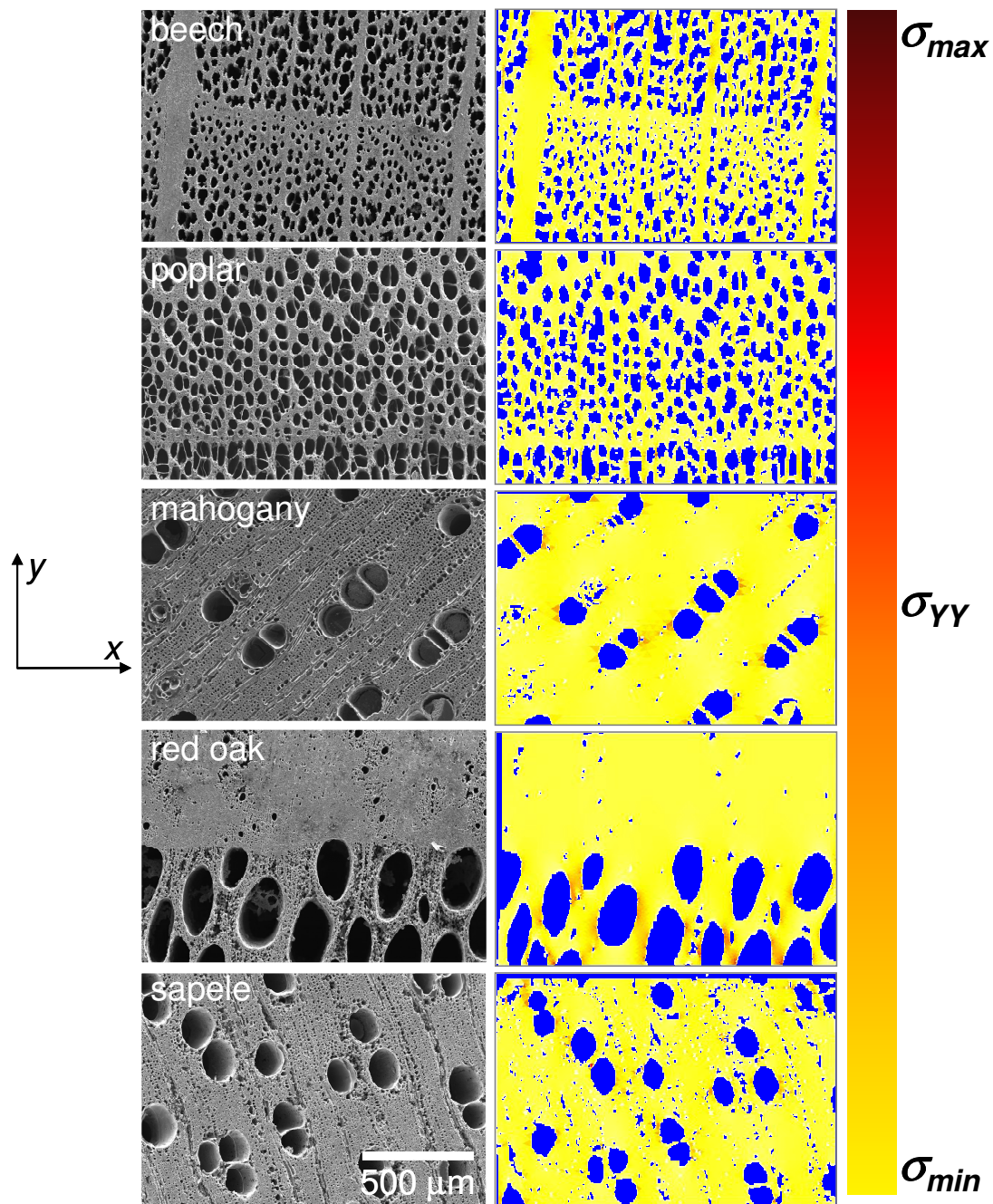


Figure 5.20. Plot of relative elastic modulus as a function of angle of orientation for transverse compression of elliptical pores ( $P = 50\%$ ).

From the idealized microstructures tested to simulate transverse compression, it is clear that pore arrangement, pore shape, and pore orientation all affect  $E$  in this direction. Due to interaction between pores, random pore arrangements had lower  $E$  when compared to ordered arrangements. Additionally, while elliptical cross-sectioned pores typically present in bioSiC may lead to an increase in  $E$  when compared to circular cross-sectioned pores, they were found to most likely result in a reduction in  $E$  due to orientation of the pore relative to the stress axis.

#### 5.4.3. Stress Distribution and Fracture of BioSiC in Transverse Compression

The stress ( $\sigma_{yy}$ ) distributions of bioSiC in transverse compression in the  $Y$  direction are shown in figure 5.21. Additionally, the  $\sigma_{xx}$  and  $\sigma_{xy}$  stress distributions are also shown in figures 5.22 and 5.23, respectively. As expected, pores in these materials create stress concentrators. This is especially clear in figure 5.21 in the porous bands of red oak bioSiC where the stress is concentrated in the thin walls of large pores. In contrast, in the more uniform UDP bioSiC materials, the stress is more evenly distributed throughout the microstructure with some stress concentration in smaller struts. Additionally, natural features of the wood precursor such as density gradients from growth rings and rays can also be seen to affect the stress distribution. Dense areas corresponding to rays in beech bioSiC also serve as areas of high stress because they are aligned with the stress axis. These stress concentrators likely result in strength reduction in bioSiC when compared to a material with more uniform stress distribution. Areas of high stress concentration also correspond to the fracture paths observed in mechanical testing samples. For example, red oak bioSiC failed in porous bands where stress concentration is highest.



**Figure 5.21. SEM micrographs and corresponding stress distributions ( $\sigma_{yy}$ ) of transverse bioSiC samples compressed in the Y direction (pore space shown in blue, scale from -30.00 to 7.00 MPa).**

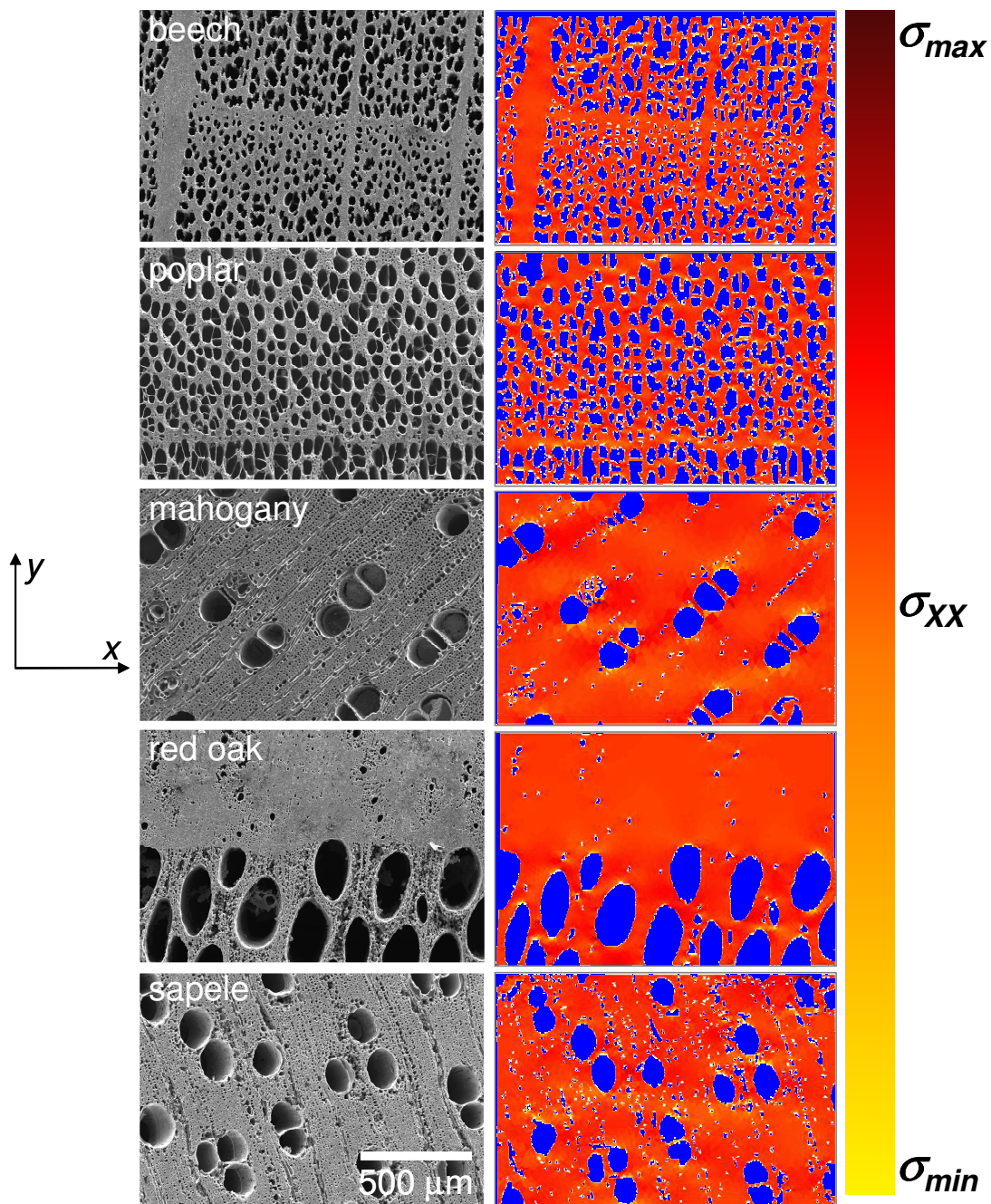


**Figure 5.22. SEM micrographs and corresponding stress distributions ( $\sigma_{xx}$ ) of transverse bioSiC samples compressed in the  $Y$  direction (pore space shown in blue, scale from -8.00 to 12.00 MPa).**

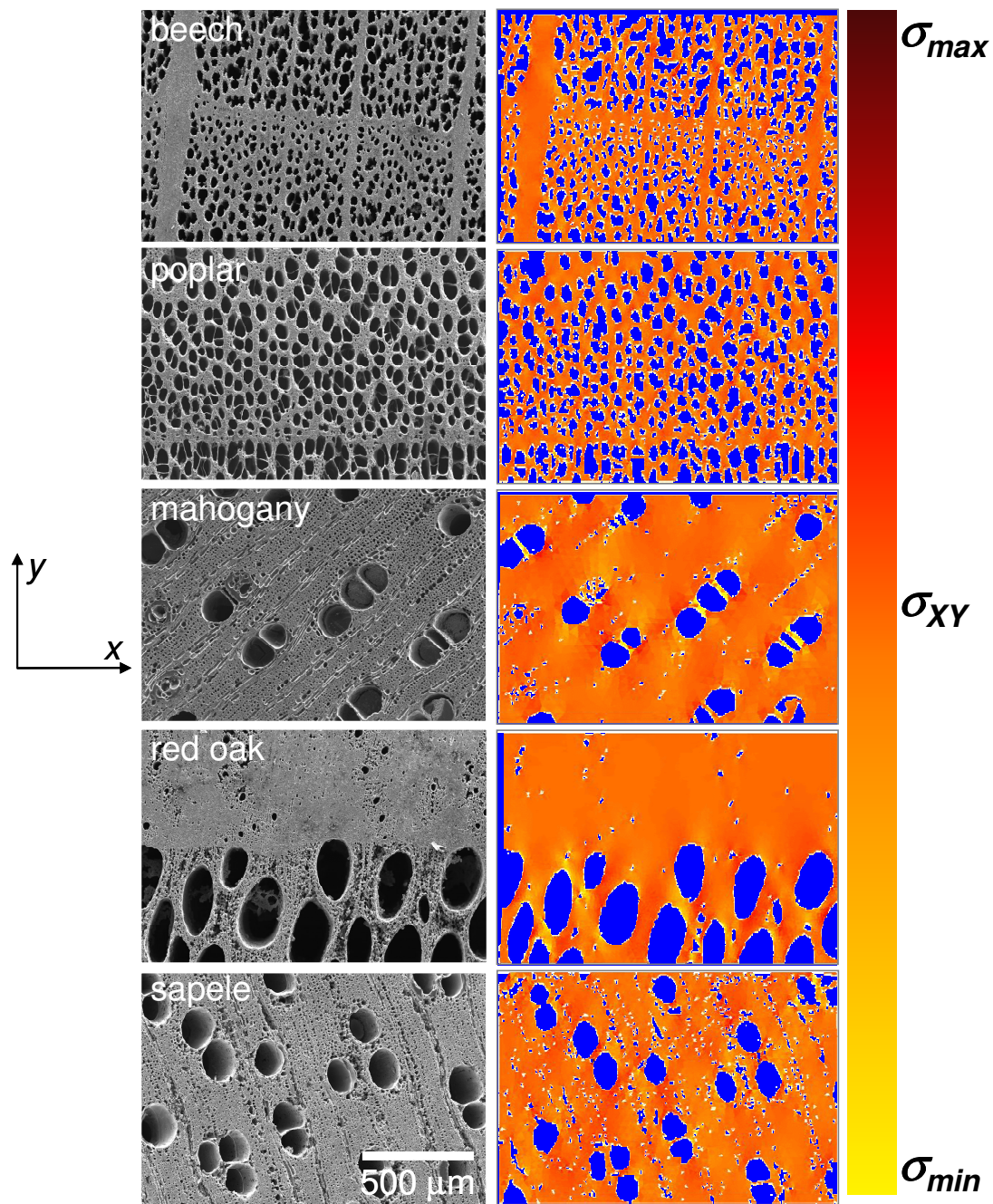


**Figure 5.23. SEM micrographs and corresponding stress distributions ( $\sigma_{xy}$ ) of transverse bioSiC samples compressed in the  $Y$  direction (pore space shown in blue, scale from -9.00 to 11.00 MPa).**

Also, vessels in mahogany and sapele act as stress raisers which correspond to the half vessel pores seen on bioSiC fracture surfaces. Finally, density gradients in beech and poplar bioSiC corresponding to rays and growth rings are regions of stress concentration and fracture in bioSiC tend to follow the paths of these gradients.

Griffith2 elements were also used in transverse compression to model fracture in bioSiC. The results of this virtual testing for compression in the *Y* direction are shown in figure 5.24. Fractured elements are again shown in black. Here, the effects of both the large vessel pores and the density gradients from features in the wood precursors are apparent. The fracture paths in sapele and mahogany bioSiC run between large vessel pores, which agree with experimental observation of half pore channels on the fracture surface and the previously described stress distributions. Also in agreement with experimental results and stress distribution images, the density gradients apparent in beech and poplar bioSiC are clearly preferred fracture paths, and fracture occurs in more porous areas. As was observed by fractography, because of these density gradients, cracks that are perpendicular to the stress axis form in beech and poplar bioSiC. The red oak material in figure 5.24 also shows a correspondence to experimental results (figure 4.18) as fracture occurs in the porous bands areas corresponding to rays.

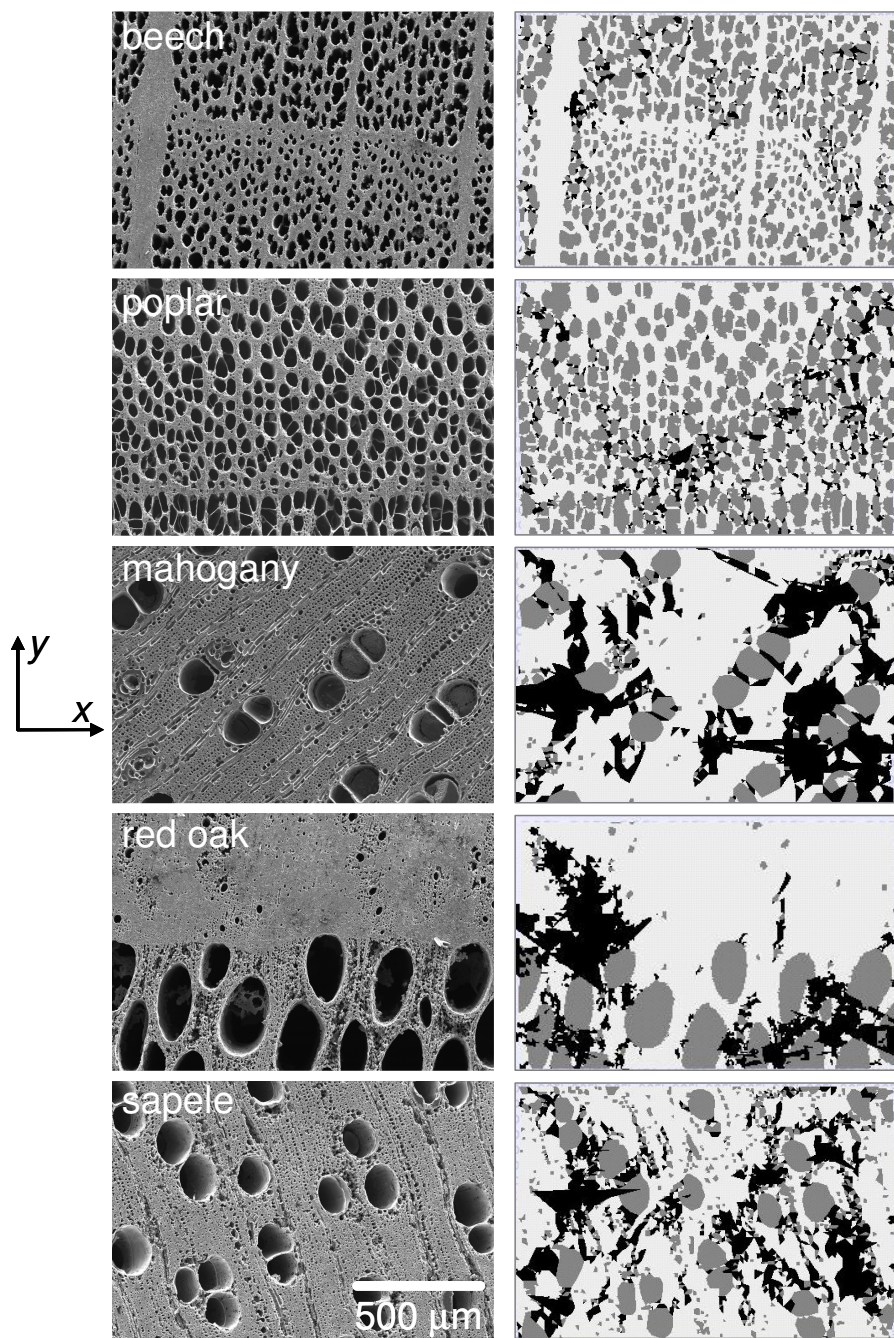


**Figure 5.24. SEM micrographs and corresponding virtual fracture images of transverse bioSiC compressed in the  $Y$  direction (black elements are fractured).**

## 5.5. Summary

Object-oriented finite-element analysis was used to evaluate the mechanical behavior of bioSiC. Finite-element meshes based on real bioSiC microstructures were created and used for virtual mechanical testing in axial and transverse compression. By accounting for the true structure and phase composition of bioSiC, OOF results were found to agree with experimental results. In axial compression, curvature and misalignment of pore channels was found to significantly reduce  $E$ . In transverse compression, pore shape, pore orientation, and arrangement of pores were all found to be aspects of bioSiC porosity that resulted in lower than expected values of  $E$ . Additionally, fracture in bioSiC was modeled using OOF and, as in experimental analysis, pores and density gradients in bioSiC played a role in determining fracture paths.

# 6

## Summary and Conclusions

Biomorphic silicon carbide (bioSiC) is a novel porous ceramic material derived directly from natural wood precursors. The work presented in this thesis describes characterization of structure, phase composition, and mechanical properties of this material. This includes experimental procedures, quantitative and qualitative data on several properties, and discussion on correlation and explanation of these properties. This chapter provides a summary of the work presented in this thesis as well as conclusions that can be drawn and their impact on use of this material for potential applications. Finally, suggestions for future work are described.

### **6.1. Summary**

BioSiC is a synthetic material with a microstructure that mimics that of wood, a natural porous material. This material is fabricated by beginning with a wood precursor. The wood is pyrolyzed in an inert atmosphere at 800 °C. Using a slow and controlled ramp rate, volatiles in wood are removed and the remaining components are decomposed into amorphous carbon. As a result of this controlled heat treatment, the naturally optimized microstructure of the wood precursor is retained after pyrolysis. The resulting carbon scaffold is then infiltrated with molten Si in vacuum at 1550 °C. The carbon and Si react via a multi-mechanism dissolution/precipitation reaction to form a Si/SiC composite material. The residual Si phase of

this material is then removed by a HF/HNO<sub>3</sub> acid solution leaving a porous SiC material that retains the optimized structure of the wood precursor.

Wood is an anisotropic porous material consisting mainly of tubular aligned pores. While all woods share certain basic aspects of microstructure, each wood possesses a unique combination of features including volume of porosity, pore size, and uniformity of pore distribution. As the microstructure of bioSiC is analogous to that of the wood precursor, it is important to understand how these features affect properties in order to identify this material for potential applications. To this end, the objective of this work was to establish fundamental structure-mechanical property relationships in bioSiC.

To achieve this goal, five wood precursors were chosen that covered a range of porosities, pore sizes, and pore size distributions. Additionally, a synthetic SiC honeycomb material was also analyzed as a more uniform comparison to bioSiC. The structure and phase composition of these materials were characterized through the fabrication process using a combination of SEM, XRD, EDS, helium pycnometry, density measurement, and image analysis. From this analysis, it was determined that, while changes in structure and porosity took place during processing, the anisotropic and bimodal porosity of wood was retaining in bioSiC. It was also clear from SEM and image analysis that the bioSiC from the five wood precursors could be divided into two categories. Material derived from beech or poplar wood was classified as uniformly distributed pore (UDP) bioSiC and mahogany, red oak, and sapele derived material was classified as non-uniformly distributed pore (NUDP) bioSiC. In UDP bioSiC, porosity was primarily composed of larger vessel pores which were homogeneously distributed in the material creating spatially uniform porosity. In NUDP bioSiC, porosity was primarily composed of

smaller fiber and tracheid pores and, because of the heterogeneous spatial distribution of porosity, areas of low porosity and areas of high porosity existed.

Along with pore morphology, the solid portions of bioSiC and SiC honeycomb were also analyzed. Although Si in stoichiometric excess was used during processing to promote complete conversion of the carbon scaffold to SiC, it was determined by density measurements that other phases were also present in these materials. These phases were hypothesized to be closed porosity, residual Si, or unreacted carbon. To resolve the phase composition of bioSiC, a procedure using pycnometry, Archimedes' method, and oxidizing heat treatments was developed. Using this methodology, it was determined that, while closed porosity and residual Si were not present, bioSiC from each precursor contained some unreacted carbon. The amount of unreacted carbon was quantified and determined to be present due to insufficient reaction times and pore channel closure resulting from volume expansion during processing. It was also noted that, for a given porosity, the carbon content of NUDP bioSiC was higher than that of UDP bioSiC.

Unlike bioSiC, SiC honeycomb was composed of uniformly distributed tubular pores of a single size. While the pore wall material of bioSiC was found to be a dense two-phase material, using density measurements and image analysis, this portion of SiC honeycomb was found to consist of SiC and open and closed porosity.

Following characterization of structure and phase composition, mechanical properties of bioSiC from each precursor wood and SiC honeycomb were measured. Specific properties, elastic modulus ( $E$ ) and hardness ( $H$ ), of the pore wall material in bioSiC and SiC honeycomb were also measured using nanoindentation. Measurements of the SiC and unreacted carbon

phases in bioSiC indicated that  $E_{SiC}$  was greater than  $E_{carbon}$  by over an order-of-magnitude. While  $E_{SiC}$  values of bioSiC phases agreed with values in the literature, values for SiC honeycomb were far below those reported for SiC. This was attributed to the porosity present in the pore wall material of SiC honeycomb.

In addition to specific properties, strength ( $\sigma_{comp}$ ) and  $E$  of bulk bioSiC and SiC honeycomb were measured in compression and fracture toughness ( $K_{IC}$ ) was measured in flexure using the single-edge notched beam method (SENB). The results of compressive testing showed effects from volume of porosity, orientation, and phase composition. As expected, both  $\sigma_{comp}$  and  $E$  of bioSiC and SiC honeycomb decreased with increasing porosity. Also as expected because of the anisotropic nature of the porosity in these materials, properties in the axial direction were greater than those in the transverse direction by nearly an order-of-magnitude because of the differing deformation mechanisms in each orientation. In the axial direction, compression of the solid portion of a material determines  $\sigma_{comp}$  and  $E$  while pore wall bending determines the properties in the transverse direction. In the axial direction, compressive testing results also indicated that, for a given porosity, UDP bioSiC was significantly stronger and stiffer than NUDP bioSiC. This was attributed to the higher unreacted carbon content in NUDP materials, which, as shown by literature values and nanoindentation, was lower in  $\sigma_{comp}$  and  $E$  by an order-of-magnitude (Greil et al. 1998b). This distinction between UDP and NUDP bioSiC was not present in the transverse direction because the properties scale with a reduced fraction of  $E$  due to bending.

As with  $\sigma_{comp}$  and  $E$ , values for  $K_{IC}$  also showed dependence on porosity and orientation.  $K_{IC}$  decreased with increasing porosity and was significantly higher for cracks propagating in

directions perpendicular to the axial direction than those propagating parallel to it. This difference was a result of tortuous crack paths and crack deflection in planes perpendicular to the axial direction in bioSiC. This was evident from fractographic analysis of samples tested in compression, which showed a preferred crack path in planes parallel to the axial direction. Additionally, features such as rays and growth rings that are present in the wood precursors are manifest as density gradients in bioSiC and cause crack deflection in the transverse direction. Unlike  $\sigma_{comp}$  and  $E$ , values of  $K_{IC}$  showed no dependence on the presence of unreacted carbon as  $K_{IC}$  for both SiC and unreacted carbon were nearly equal (Li and Bhushan 1999).

The properties of SiC honeycomb did not agree with the trends seen for bioSiC. This was attributed to the high pore volume of this material ( $74.04 \pm 2.50 \%$ ). For materials with porosities greater than approximately 70 %, properties are dictated by interaction between pores and these are referred to as cellular materials. The properties of SiC honeycomb were in agreement with those predicted by the cellular material model developed by Gibson and Ashby (1997).

The properties measured in compression were also compared to the minimum solid area (MSA) model, which predicts values for mechanical properties of porous materials based on an assumed microstructure. Even after accounting for the presence of unreacted carbon in bioSiC, experimental values fell below those predicted by the model, indicating that mechanical properties in compression were dependent on factors other than pore volume, orientation, and phase composition. For this reason and to further analyze mechanical behavior in bioSiC, object-oriented finite-element analysis (OOF) was also utilized.

Using OOF, two-dimensional finite-element meshes were created to model the properties of bioSiC in the axial and transverse directions. These meshes closely resembled the structure of bioSiC and, when accounting for both SiC and unreacted carbon phases using the rule of mixtures, gave a range of  $E$  values into which experimental values of bioSiC fell. Using OOF, the properties of bioSiC were found to also be a function of pore alignment, pore shape, and pore arrangement. In the axial direction, nodes and curves in pore channels were determined to serve as stress concentrators that were not present in materials without these irregularities. Using an idealized axial microstructure, OOF results showed that even small misalignments of pore channels from parallel to the stress axis caused by microstructural irregularities result in significant reductions in  $E$ . In the transverse direction, when compared to an ordered simple cubic-type arrangement,  $E$  for a material with an idealized microstructure of randomly arranged pores was significantly lower. Additionally, the elliptical shape of the cross-sections of bioSiC pores was also found to most likely result in a reduction in  $E$ .

Fracture paths were also modeled using OOF and were also found to correspond with experimental fractographic analysis. These showed a preferred crack path in planes parallel to the axial direction and that density gradients in bioSiC serve as crack deflectors and determine crack paths.

## **6.2. Conclusions**

The objective of this work was to determine fundamental structure-mechanical property relationships so that bioSiC can be identified for specific applications. There are a myriad of wood precursors from which to choose and it was important to characterize specific features and

determine their effect on the final bioSiC material as this would allow for not only the identification of bioSiC for specific applications but also bioSiC from a particular wood species. These relationships were established by correlation of mechanical properties to structural properties and phase composition. Several significant conclusions can be drawn from the work described in this thesis.

Previous researchers have established that the properties of bioSiC are a function of both porosity and orientation (Arellano Lopez et al. 2004; Greil et al. 1998a; Greil et al. 1998b; Martinez Fernandez et al. 2003; Martinez Fernandez et al. 2000; Varela Feria et al. 2002). However, little work has been done to determine mechanical properties of this material as a function of other microstructural properties. Also, previous work has only acknowledged the presence of unreacted carbon (Zollfrank and Sieber 2004) in bioSiC and not analyzed its effect on mechanical properties.

In the work presented in this thesis, the structure and phase composition of bioSiC from several wood precursors has been characterized. A procedure was developed to quantify the amount of unreacted carbon present in this material, and it was found that the carbon content of NUDP bioSiC is higher than that of UDP bioSiC. Unreacted carbon was found in dense areas of small pores with thick pore walls that are more prevalent in NUDP bioSiC and likely occurred because of channel choking. This effect was directly related to the microstructure of the material and independent of the total volume of porosity. The unreacted carbon was also found to cause lower than expected values of  $E$  because it was an order-of-magnitude less stiff than SiC as measured by nanoindentation. In contrast, unreacted carbon had little effect on  $K_{IC}$  values.

Along with phase composition, the natural wood-like microstructure of bioSiC also affected mechanical properties. In the axial direction, channel misalignment and curvature served to lower  $E$  and nodes and other irregularities in microstructure served as stress concentrators. The random pore arrangement, elliptical pore shape, and pore orientation were also found to lower  $E$  in bioSiC. Mechanical properties of bioSiC were also compared to the minimum solid area (MSA) model for porous materials. All of these factors and those listed above indicate that the mechanical properties of bioSiC are a functional of microstructural variables in addition to porosity and orientation. As the MSA model is based on an idealized tubular microstructure, it serves as an upper limit and, because non-ideal natural precursors are used, it is unlikely the properties of bioSiC will ever approach this limit.

The knowledge of structure-mechanical property relationships can aid in the identification of bioSiC for potential applications. Based on the pore size distribution in the material, the likelihood that significant amounts of unreacted carbon will be present in the final material can be assessed. In addition, the effects of orientation and porosity on  $\sigma_{comp}$ ,  $E$ ,  $K_{IC}$ , and fracture path can also be hypothesized for potential applications. Using this information, not only can the viability of bioSiC for an application be evaluated, but a specific wood species can be chosen as a precursor to give the desired properties in the final porous SiC material. For example, for refractory applications where high strength, stiffness, and stability in air is important, poplar or beech bioSiC would be ideal because of the relatively low amounts of unreacted carbon in these materials. In contrast, for a filtration application that requires porosity on the order of 100  $\mu\text{m}$  or more, sapele or mahogany bioSiC would be better candidate materials because they possess larger pores.

### 6.3. Suggestions for Future Work

While this thesis contributes to understanding of structure-mechanical property relationships in bioSiC, several areas for future analysis can be suggested. In addition to the characterization done here, three-dimensional characterization of structure would also be beneficial. Characterization by techniques such as mercury porosimetry or serial sectioning would provide a better understanding of the structure and volume of bioSiC porosity. Additionally, three-dimensional finite-element analysis would also serve as a more realistic way to model the properties of bioSiC. While 3-D finite-element analysis programs exist, a microstructure-based program such as OOF would be ideal.

Along with  $E$  and  $H$ , additional characterization of unreacted carbon would increase understanding of its effect on bioSiC. One possible area of future work would be the use of transmission electron microscopy (TEM) and atomic force microscopy (AFM) to analyze the interface between unreacted carbon and SiC phases in bioSiC. Also, analysis of the changes in density and crystal structure of unreacted carbon with heat treatment, as this material is amorphous and subject to changes in these properties at elevated temperatures, would be beneficial in understanding the effect of unreacted carbon on bioSiC.

An alternative focus of future work would be in better processing techniques to minimize the amount of unreacted carbon present in bioSiC. Processing at lower temperatures may allow for better Si infiltration of the carbon scaffold as the reaction would be slower which reduces the likelihood of channel choking prior to complete infiltration. Also, longer processing times at higher temperatures would reduce diffusion times and may decrease the fraction of unreacted carbon. Other alternative processing methods include gas phase or sol-gel Si sources instead of

liquid. In addition to the elimination of unreacted carbon, alternative methods to toxic and dangerous HF/HNO<sub>3</sub> acid etching for Si removal would greatly increase the viability of bioSiC for industrial applications. Possible alternatives include carbon felt-wicking or high temperature oxidation of residual Si.

A final suggestion for future work would be the use of a more similar control SiC honeycomb-type material. The porosity of the synthetic honeycomb material used here was much higher than that of bioSiC and the properties of this material were therefore governed by other factors. Possible alternatives would be a corrugated cardboard derived material that can be processed in a manner similar to bioSiC or a lower porosity extruded SiC honeycomb material.

## References

Adams, M., and Sines, G. (1976). "Methods for Determining the Strength of Brittle Materials in Compressive Stress States." *Journal of Testing and Evaluation*, 4(6), 383-396.

Adams, M., and Sines, G. (1977). "A Statistical, Micromechanical Theory of the Compressive Strength of Brittle Materials." *Journal of the American Ceramic Society*, 62(3-4), 126-131.

Arellano Lopez, A. R. d., and Martinez Fernandez, J. (2004). "Biomorphic SiC: A New Engineering Ceramic Material." *International Journal of Applied Ceramic Technology*, 1(1), 1-12.

Arellano Lopez, A. R. d., Martinez Fernandez, J., Varela Feria, F. M., Orlova, T. S., Goretta, K. C., Mora, F. G., Chen, N., and Routbort, J. L. (2004). "Erosion and Strength Degradation of Biomorphic SiC." *Journal of the European Ceramic Society*, 24, 861-870.

Ashby, M. F., F.R.S., Easterling, K. E., Harrysson, R., and Maiti, S. K. (1985). "The Fracture and Toughness of Woods." *Proceedings of the Royal Society of London A*, 398, 261-280.

Ashby, M. F., Gibson, L. J., Wegst, U., and Olive, R. (1995). "The Mechanical Properties of Natural Materials. I. Material Property Charts." *Proceedings of the Royal Society of London A*, 450, 123-140.

ASTM C373-88. (1999). "Standard Test Method for Determination of Water Absorption, Bulk Density, Apparent Porosity, and Apparent Specific Gravity of Fired Whiteware Products." ASTM International

Bauer, T., and Eschrich, W. (1997). "Mechanical Pressure Inhibits Vessel Development of Xylogenic Cambial Derivatives of Beech (*Fagus sylvatica* L.)." *Trees*, 11, 349-355.

Bellet, D., Lamagnere, P., Vincent, A., and Brechet, Y. (1996). "Nanoindentation Investigation of the Young's Modulus of Porous Silicon." *Journal of Applied Physics*, 80(7), 3772-3776.

Ben-Nissan, B. (2003). "Natural Bioceramics: From Coral to Bone and Beyond." *Current Opinion in Solid State & Materials Science*, 7, 283-288.

Black, J. (1999). *Biological Performance of Materials*, Marcel Dekker, Inc., New York.

Brezny, R., and Green, D. J. (1990). "The Effect of Cell Size on the Mechanical Behavior of Cellular Materials." *Acta Materialia*, 38(12), 2517-2526.

Byrne, C. E., and Nagle, D. C. (1997a). "Carbonization of Wood for Advanced Materials Applications." *Carbon*, 35(2), 259-266.

Byrne, C. E., and Nagle, D. C. (1997b). "Carbonized Wood Monoliths - Characterization." *Carbon*, 35(2), 267-273.

Callister, W. D. (2003). *Materials Science and Engineering: An Introduction*, John Wiley & Sons, New York.

Cannillo, V., Leonelli, C., Manfredini, T., and Montorsi, M. (2003). "Computational Simulations for the Assessment of the Mechanical Properties of Glass with Controlled Porosity." *Journal of Porous Materials*, 10, 189-200.

Cannillo, V., Manfredini, T., Montorsi, M., Siligardi, C., and Sola, A. (2006). "Microstructure-Based Modelling and Experimental Investigation of Crack Propagation in Glass-Alumina Functionally Graded Materials." *Journal of the European Ceramic Society*, 26, 3067-3073.

Canny, M. (1998). "Transporting Water in Plants." *American Scientist*, 86, 152-159.

Carlos, A. d., Borrajo, J. P., Serra, J., Gonzalez, P., Liste, S., and Leon, B. (2005). "In Vitro Cytotoxicity Testing of Wood-Based Biomimetic SiC Ceramics." *Key Engineering Materials*, 284-286, 581-584.

Chakrabarti, O. P., Maiti, H. S., and Majumdar, R. (2004). "Biomimetic Synthesis of Cellular SiC Based Ceramics from Plant Precursor." *Bulletin of Materials Science*, 27(5), 467-470.

Cheng, H.-M., Endo, H., Okabe, T., Saito, K., and Zheng, G.-B. (1999). "Graphitization Behavior of Wood Ceramics and Bamboo Ceramics as Determined by X-ray Diffraction." *Journal of Porous Materials*, 6, 233-237.

Chiang, Y.-M., Messner, R. P., and Terwilliger, C. D. (1991). "Reaction-Formed Silicon Carbide." *Materials Science and Engineering A*, 144, 63-74.

Constantinides, G., and Ulm, F.-J. (2004). "The Effect of Two Types of C-S-H on the Elasticity of Cement-Based Materials: Results from Nanoindentation and Micromechanical Modeling." *Cement and Concrete Research*, 34, 67-80.

Courtney, T. H. (2000). *Mechanical Behavior of Materials*, McGraw Hill, Boston.

Davis, M. E. (2002). "Ordered Porous Materials for Emerging Applications." *Nature*, 417, 813-821.

Di, Z., Xian-qing, X., Tong-xiang, F., Bing-he, S., Sakata, T., Mori, H., and Okabe, T. (2003). "Microstructure and Properties of Ecoceramics/Metal Composites with Interpenetrating Networks." *Materials Science and Engineering A*, 351, 109-116.

Dinwoodie, J. M. (1989). *Wood: Nature's Cellular, Polymeric Fibre-Composite*, The Institute of Metals, Brookfield, Vermont.

Esposito, L., Sciti, D., Piancastelli, A., and Bellosi, A. (2004). "Microstructure and Properties of Porous b-SiC Templated from Soft Woods." *Journal of the European Ceramic Society*, 24, 533-540.

Faber, K. T., and Evans, A. G. (1983). "Intergranular Crack-Deflection Toughening in Silicon Carbide." *Journal of the American Ceramic Society*, 66(6), C94-C96.

Fan, Z., Swadener, J. G., Rho, J. Y., Roy, M. E., and Pharr, G. M. (2002). "Anisotropic Properties of Human Tibial Cortical Bone as Measured by Nanoindentation." *Journal of Orthopaedic Research*, 20, 806-810.

Fey, T., Sieber, H., and Greil, P. (2005). "Stress Distribution in Biomorphous SiC-Ceramics Under Radial Tensile Loading." *Journal of the European Ceramic Society*, 25, 1015-1024.

Fitzgerald, T. J., Michaud, V. J., and Mortensen, A. (1995). "Processing of Microcellular SiC Foams II: Ceramic Foam Production." *Journal of Materials Science*, 30, 1037-1045.

Forest Products Laboratory, p. (1990). *Wood Engineering Handbook*, Prentice-Hall, Englewood Cliffs.

Franklin, R. E. (1951). "Crystallite Growth in Graphitizing and Non-Graphitizing Carbons." *Proceedings of the Royal Society of London A*, 209, 196-218.

Fuller Jr., E. R. (2006). "OOF Griffith element." V. S. Kaul, personal communication.

Gibson, E. J. (1992). "Wood: A Natural Fibre Reinforced Composite." *Metals and Materials*, 6, 333-336.

Gibson, L. J. (2005). "Biomechanics of Cellular Solids." *Journal of Biomechanics*, 38, 377-399.

Gibson, L. J., and Ashby, M. F. (1997). *Cellular Solids: Structure and Properties*, Cambridge University Press, Cambridge.

Gibson, L. J., Ashby, M. F., Karam, G. N., Wegst, U., and Shercliff, H. R. (1995). "The Mechanical Properties of Natural Materials. II. Microstructures for Mechanical Efficiency." *Proceedings of the Royal Society of London A*, 450, 141-162.

Gonzalez, P., Borrajo, J. P., Serra, J., Liste, S., Chiussi, S., Leon, B., Semmelmann, K., Carlos, A. d., Varela-Feria, F. M., Martinez-Fernandez, J., and Arellano-Lopez, A. R. d. (2004). "Extensive Studies on Biomorphous SiC Ceramics Properties for Medical Applications." *Key Engineering Materials*, 254-256, 1029-1032.

Gonzalez, P., J., S., Liste, S., Chiussi, S., Leon, B., Perez-Amor, M., Martinez-Fernandez, J., Arellano-Lopez, A. R. d., and Varela-Feria, F. M. (2003). "New Biomorphous SiC Ceramics Coated with Bioactive Glass for Biomedical Applications." *Biomaterials*, 24, 4827-4832.

Green, D. J., and Colombo, P. (2003). "Cellular Ceramics: Intriguing Structures, Novel Properties, and Innovative Applications." *MRS Bulletin*, April, 296-300.

Greil, P. (2001). "Biomorphous Ceramics from Lignocellulosics." *Journal of the European Ceramic Society*, 21, 105-118.

Greil, P., Lifka, T., and Kaindl, A. (1998a). "Biomorphic Cellular Silicon Carbide Ceramics from Wood: I. Processing and Microstructure." *Journal of the European Ceramic Society*, 18, 1961-1973.

Greil, P., Lifka, T., and Kaindl, A. (1998b). "Biomorphic Cellular Silicon Carbide Ceramics from Wood: II. Mechanical Properties." *Journal of the European Ceramic Society*, 18, 1975-1983.

Gulden, T. D. (1969). "Mechanical Properties of Polycrystalline Beta-SiC." *Journal of the American Ceramic Society*, 52(11), 585-590.

Hase, T., Suzuki, H., and Iseki, T. (1976). "Formation Process of  $\beta$ -SiC During Reaction-Sintering." *Journal of Nuclear Materials*, 59, 42-48.

Hasselmann, D. P. H., and Fulrath, R. M. (1965). "Effect of Cylindrical Porosity on Young's Modulus of Polycrystalline Brittle Materials." *Journal of the American Ceramic Society*, 545.

Hengsberger, S., Kulik, A., and Zysset, P. (2002). "Nanoindentation Discriminates the Elastic Properties of Individual Human Lamellae Under Dry and Physiological Conditions." *Bone*, 30(1), 178-184.

Herzog, A., Vogt, U., Kaczmarek, O., Klingner, R., Richter, K., and Thoemen, H. (2006). "Porous SiC Ceramics Derived from Tailored Wood-Based Fiberboards." *Journal of the American Ceramic Society*, 89(5), 1499-1503.

Hou, G., Jin, Z., and Qian, J. (2006). "Effect of Holding Time on the Basic Properties of Biomorphic SiC Ceramic Derived from Beech Wood." *Materials Science and Engineering A*, in press.

Huang, J. S., and Gibson, L. J. (1991). "Fracture Toughness of Brittle Honeycombs." *Acta Materialia*, 39(7), 1617-1626.

Kaul, V. S., Faber, K. T., Sepulveda, R., Arellano-Lopez, A. R. d., and Martinez-Fernandez, J. (2006). "Precursor Selection and its Role in the Mechanical Properties of Porous SiC Derived from Wood." *Materials Science and Engineering A*, 428, 225-232.

Kelly, A. (2006). "Why Engineer Porous Materials?" *Philosophical Transactions of the Royal Society A*, 364(5-14), 5-14.

Kingery, W. D., Bowen, H. K., and Uhlmann, D. R. (1976). *Introduction to Ceramics*, Wiley, New York.

Klett, J. (2000). "Process for Making Carbon Foam." US patent # 6033506.

Kutz, M. (2003). *Standard Handbook of Biomedical Engineering & Design*, McGraw-Hill, New York.

Langer, S. A., Carter, W. C., and Fuller Jr., E. R. (2000). "OOF."  
<http://www.ctcms.nist.gov/oof/>.

Langer, S. A., Fuller, E. R., and Carter, W. C. (2001). "OOF: An Image-Based Finite-Element Analysis of Material Microstructures." *Computing in Science and Engineering*, 15-23.

Li, D., Chung, Y., Wong, M., and Sproul, W. (1993). "Nanoindentation Studies of Ultrahigh Strength Carbon Nitride Thin-Films." *Journal of Applied Physics*, 74(1), 219-223.

Li, J.-G., and Hausner, H. (1991). "Wettability of Silicon Carbide by Gold, Germanium and Silicon." *Journal of Materials Science Letters*, 10, 1275-1276.

Li, X., and Bhushan, B. (1999). "Evaluation of Fracture Toughness of Ultra-Thin Amorphous Carbon Coatings Deposited by Different Deposition Techniques." *Thin Solid Films*, 355-356, 330-336.

Liu, Z., Tonziang, F., and Zhang, D. (2005). "Synthesis of Biomorphous Nickel Oxide from a Pinewood Template and Investigation on a Hierarchical Porous Structure." *Journal of the American Ceramic Society*.

Martinez Fernandez, J., Munoz, A., Arellano Lopez, A. R. d., Varela Feria, F. M., Dominguez Rodriguez, A., and Singh, M. (2003). "Microstructure-Mechanical Properties Correlation in Siliconized Silicon Carbide Ceramics." *Acta Materialia*, 51, 3259-3275.

Martinez Fernandez, J., Varela Feria, F. M., and Singh, M. (2000). "High Temperature Compressive Mechanical Behavior of Biomorphic Silicon Carbide Ceramics." *Scripta Materialia*, 43, 813-818.

Munoz, A., Martinez-Fernandez, J., and Singh, M. (2002). "High Temperature Compressive Mechanical Behavior of Joined Biomorphic Silicon Carbide Ceramics." *Journal of the European Ceramic Society*, 22, 2727-2733.

Oliver, W. C., and Pharr, G. M. (1992). "An Improved Technique for Determining Hardness and Elastic Modulus Using Load and Displacement Sensing Indentation Experiments." *Journal of Materials Research*, 7(6), 1564-1583.

Oliver, W. C., and Pharr, G. M. (2004). "Measurement of Hardness and Elastic Modulus by Instrumented Indentation: Advances in Understanding and Refinements to Methodology." *Journal of Materials Research*, 19(1), 3-20.

Ota, T., Imaeda, M., Takase, H., Kobayashi, M., Kinoshita, N., Hirashita, T., Miyazaki, H., and Hikichi, Y. (2000). "Porous Titania Ceramic Prepared by Mimicking Silicified Wood." *Journal of the American Ceramic Society*, 83(6), 1521-1523.

Ota, T., Takahashi, M., Hibi, T., Ozawa, M., Suzuki, S., and Hikichi, Y. (1995). "Biomimetic Process for Producing SiC "Wood". " *Journal of the American Ceramic Society*, 78(12), 3409-3411.

Page, T. F., Oliver, W. C., and McHargue, C. J. (1992). "The Deformation Behavior of Ceramic Crystals Subjected to Very Low Load (Nano)indentations." *Journal of Materials Research*, 7(2), 450-473.

Pappacena, K. E., Wang, H., Porter, W. D., and Faber, K. T. (2006). "Thermal Conductivity of Porous Silicon Carbide from Wood Precursors." in preparation for the Journal of the American Ceramic Society.

Pharr, G. M., and Oliver, W. C. (1992). "Measurement of Thin-Film Mechanical-Properties Using Nanoindentation." MRS Bulletin, 17(7), 28-33.

Presas, M., Pastor, J. Y., Llorca, J., Arellano-Lopez, A. R. d., Martinez-Fernandez, J., and Sepulveda, R. E. (2005). "Mechanical Behavior of Biomorphic Si/SiC Porous Composites." Scripta Materialia, 53, 1175-1180.

Qian, J.-M., Wang, J.-P., and Jin, Z.-H. (2003). "Preparation and Properties of Porous Microcellular SiC Ceramics by Reactive Infiltration of Si Vapor into Carbonized Basswood." Materials Chemistry and Physics, 82, 648-653.

Qian, J.-M., Wang, J.-P., Qiao, G.-J., and Jin, Z.-H. (2004a). "Preparation of Porous SiC Ceramic with a Woodlike Microstructure by Sol-Gel and Carbothermal Reduction Processing." Journal of the European Ceramic Society, 24, 3251-3259.

Qian, J., Wang, J., and Jin, Z. (2004b). "Preparation of Biomorphic SiC Ceramic by Carbothermal Reduction of Oak Wood Charcoal." Materials Science and Engineering A, 371, 229-235.

Rambo, C. R., Cao, J., and Sieber, H. (2004). "Preparation and Properties of Highly Porous, Biomorphic YSZ Ceramics." Materials Chemistry and Physics, 87, 345-352.

Rambo, C. R., and Sieber, H. (2005). "Novel Synthetic Route to Biomorphic Al<sub>2</sub>O<sub>3</sub> Ceramics." Advanced Materials, 17(8), 1088-1091.

Rasband, W. (2005). "Image J." <http://rsb.info.nih.gov/ij/>.

Raven, P. H., Evert, R. F., and Curtis, H. (1976). Biology of Plants, Worth Publishers, Inc., New York.

Reid, A. C. E. (2006). "OOF help." V. S. Kaul, personal communication.

Rho, J., Tsui, T. Y., and Pharr, G. M. (1997). "Elastic Properties of Human Cortical and Trabecular Lamellar Bone Measured by Nanoindentation." *Biomaterials*, 18(20), 1325-1330.

Rice, R. W. (1998). *Porosity of Ceramics*, Marcel Dekker, Inc., New York.

Robbins, H., and Schwartz, B. (1959). "Chemical Etching of Silicon 1. The System HF, HNO<sub>3</sub>, and H<sub>2</sub>O." *Journal of the Electrochemical Society*, 106(6), 505-508.

Saggio-Woyansky, J., Scott, C. E., and Minnear, W. P. (1992). "Processing of Porous Ceramics." *American Ceramic Society Bulletin*, 71(11), 1674-1682.

Saigal, A., Fuller Jr., E. R., Langer, S. A., Carter, W. C., Zimmerman, M. H., and Faber, K. T. (1998). "Effect of Interface Properties on Microcracking of Iron Titanate." *Scripta Materialia*, 38(9), 1449-1453.

Sangsuwan, P., Orejas, J. A., Gatica, J. E., Tewari, S. N., and Singh, M. (2001). "Reaction-Bonded Silicon Carbide by Reactive Infiltration." *Industrial Engineering Chemical Research*, 40, 5191-5198.

Scace, R. I., and Slack, G. A. (1959). "Solubility of Carbon in Silicon and Germanium." *Journal of Chemical Physics*, 30(6), 1551-1555.

Schulte-Fischedick, J., Zern, A., Mayer, J., Ruhle, M., Frieb, M., Krenkel, W., and Kochendorfer, R. (2002). "The Morphology of Silicon Carbide in C/C-SiC Composites." *Materials Science and Engineering A*, 332, 146-152.

Schwartzwalder, K., Somers, H., and Somers, A. V. (1963). "Method of Making Porous Ceramic Articles." United States.

Sepulveda, P., and Binner, J. G. P. (1999). "Processing of Cellular Ceramics by Foaming and In Situ Polymerisation of Organic Monomers." *Journal of the European Ceramic Society*, 19, 2059-2066.

Shanti, N. O., Araki, K., and Halloran, J. W. (2006). "Particle Redistribution During Dendritic Solidification of Particle Suspensions." *Journal of the American Ceramic Society*, 89(8), 2444-2447.

Singh, M., and Salem, J. A. (2002). "Mechanical Properties and Microstructure of Biomorphic Silicon Carbide Ceramics Fabricated from Wood Precursors." *Journal of the European Ceramic Society*, 22, 2709-2717.

Singh, M., and Yee, B.-M. (2004). "Reactive Processing of Environmentally Conscious, Biomorphic Ceramics from Natural Wood Precursors." *Journal of the European Ceramic Society*, 24, 209-217.

Sjostrom, H., Stafstrom, S., Boman, M., and Sundgren, J. (1995). "Superhard and Elastic Carbon Nitride Thin-Films Having Fullerene-like Microstructure." *Physical Review Letters*, 75(7), 1336-1339.

Studart, A. R., Gonzenback, U. T., Tervoot, E., and Gauckler, L. J. (2006). "Processing Routes to Macroporous Ceramics: A Review." *Journal of the American Ceramic Society*, 89(6), 1771-1789.

Tang, M. M., and Bacon, R. (1964). "Carbonization of Cellulose Fibers - I Low Temperature Pyrolysis." *Carbon*, 2, 211-220.

Turner, C. H., Rho, J., Takano, Y., Tsui, T. Y., and Pharr, G. M. (1999). "The Elastic Properties of Trabecular and Cortical Bone Tissues are Similar: Results from Two Microscopic Measurement Techniques." *Journal of Biomechanics*, 32, 437-441.

Urena, A., Rams, J., Escalera, M., and Sanchez, M. (2005). "Characterization of Interfacial Mechanical Properties in Carbon Fiber/Aluminum Matrix Composites by the Nanoindentation Technique." *Composites Science and Technology*, 65(13), 2025-2038.

Varela Feria, F. M., Fernandez, J. M., Lopez, A. R. d. A., and Singh, M. (2002). "Low Density Biomorphic Silicon Carbide: Microstructure and Mechanical Properties." *Journal of the European Ceramic Society*, 22, 2719-2725.

Vogli, E., Mukerji, J., Hoffman, C., Kladny, R., Sieber, H., and Greil, P. (2001). "Conversion of Oak to Cellular Silicon Carbide Ceramic by Gas-Phase Reaction with Silicon Monoxide." *Journal of the American Ceramic Society*, 84(6), 1236-1240.

Vogli, E., Sieber, H., and Greil, P. (2002). "Biomorphic SiC-Ceramic Prepared by Si-Vapor Phase Infiltration of Wood." *Journal of the European Ceramic Society*, 22, 2663-2668.

Vyshnyakova, K., Yushin, G., Pereselentseva, L., and Gogotsi, Y. (2006). "Formation of Porous SiC Ceramics by Pyrolysis of Wood Impregnated with Silica." *International Journal of Applied Ceramic Technology*, 3(6), 485-490.

Wang, Y., Tan, S., and Jiang, D. (2004). "The Effect of Porous Carbon Preform and the Infiltration Process on the Properties of Reaction-Formed SiC." *Carbon*, 42, 1833-1839.

Wang, Z., Kulkarni, A., Deshpande, S., Nakamura, T., and Herman, H. (2003). "Effects of Pores and Interfaces on Effective Properties of Plasma Sprayed Zirconia Coating." *Acta Materialia*, 51, 5319-5334.

Warren, C. (2004). "Corning SiC Honeycomb." V. Kaul, personal communication.

Weiner, S., Traub, W., and Wagner, D. H. (1999). "Lamellar Bone: Structure-Function Relations." *Journal of Structural Biology*, 126, 241-255.

Whalen, T. J., and Anderson, A. T. (1975). "Wetting of SiC, Si<sub>3</sub>N<sub>4</sub>, and Carbon by Si and Binary Si Alloys." *Journal of the American Ceramic Society*, 58(9-10), 396-399.

Wilkes, T. E., Young, M. L., Sepulveda, R., Dunand, D. C., and Faber, K. T. (2006). "Composites By Aluminum Infiltration of Porous Silicon Carbide Derived from Wood Precursors." *Scripta Materialia*, 55, 1083-1086.

Wimmer, R., Lucas, B., Tsui, T., and Oliver, W. (1997). "Longitudinal Hardness and Young's Modulus of Spruce Tracheid Secondary Walls Using Nanoindentation Technique." *Wood Science and Technology*, 31(2), 131-141.

Yang, J.-F., Ohji, T., Kanzaki, S., Diaz, A., and Hampshire, S. (2002). "Microstructure and Mechanical Properties of Silicon Nitride Ceramics with Controlled Porosity." *Journal of the American Ceramic Society*, 85(6), 1512-1516.

Zhang, W., Zhang, D., Fan, T., Ding, J., Guo, Q., and Ogawa, H. (2006). "Morphosynthesis of Hierarchical ZnO Replica Using Butterfly Wing Scales as Templates." *Microporous and Mesoporous Materials*, 92, 227-233.

Zimmerman, M. H., Baskin, D. M., Faber, K. T., Fuller Jr., E. R., Allen, A. J., and Keane, D. T. (2001). "Fracture of a Textured Anisotropic Ceramic." *Acta Materialia*, 49, 3231-3242.

Zollfrank, C., and Sieber, H. (2004). "Microstructure and Phase Morphology of Wood Derived Biomorphous SiSiC-Ceramics." *Journal of the European Ceramic Society*, 24, 495-506.

Zollfrank, C., and Sieber, H. (2005). "Microstructure Evolution and Reaction Mechanism of Biomorphous SiSiC Ceramics." *Journal of the American Ceramic Society*, 88(1), 51-58.

Zollfrank, C., Travitzky, N., Sieber, H., Selchert, T., and Greil, P. (2005). "Biomorphous SiSiC/Al-Si Ceramic Composites Manufactured by Squeeze Casting: Microstructure and Mechanical Properties." *Advanced Engineering Materials*, 7, 743-746.